Division of Research & Innovation

Analysis of Laterally Loaded Long or Intermediate Drilled Shafts of Small or Large Diameter in Layered Soil

Final Report

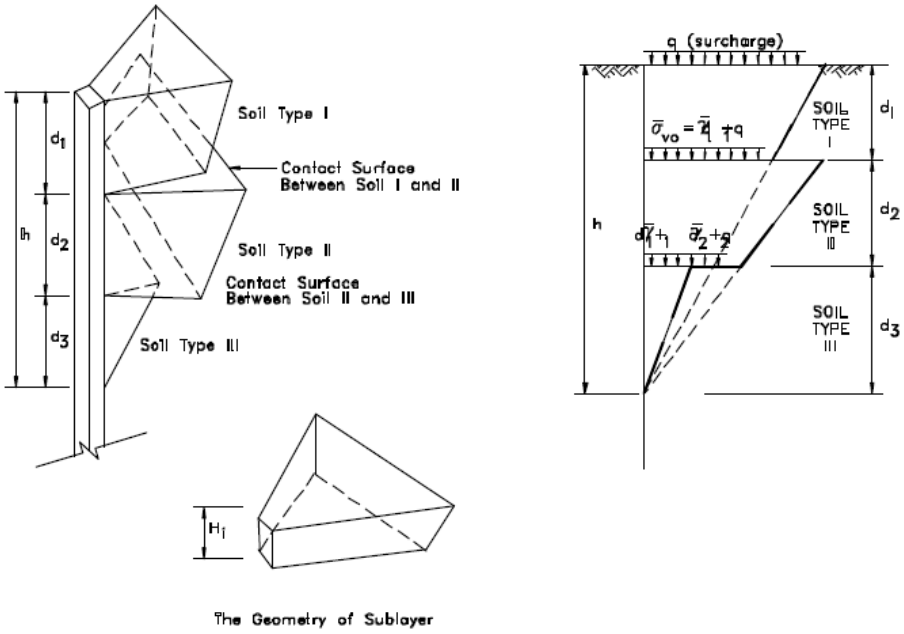

The Geometry of Sublayer

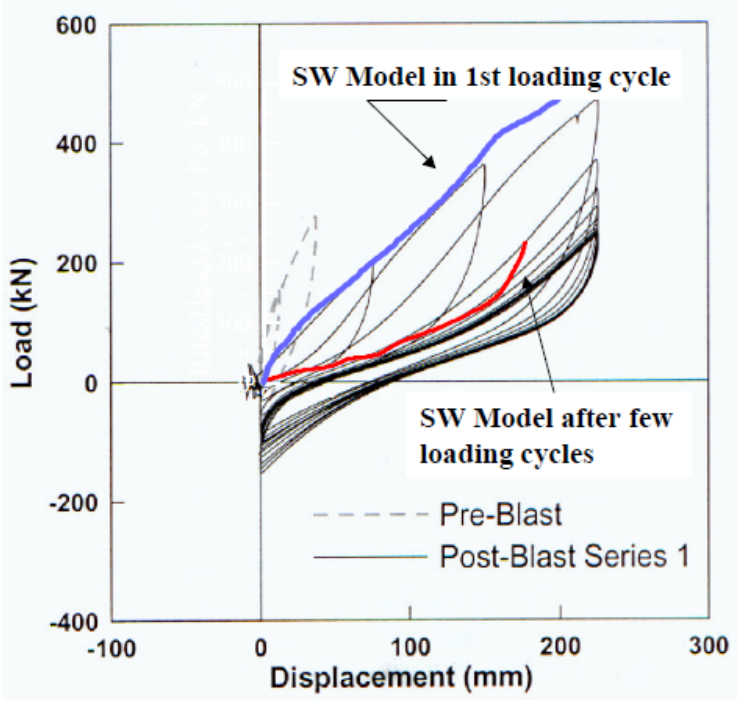

Report CA04-0252
December 2008

Analysis of Laterally Loaded Long or Intermediate Drilled Shafts of Small or Large Diameter in Layered Soils

Final Report

Report No. CA04-0252

December 2008

Prepared By:

Department of Civil and Environmental Engineering
University of Nevada, Reno
Reno, NV 89557

Prepared For:

California Department of Transportation
Engineering Services Center
1801 30th Street
Sacramento, CA 95816

California Department of Transportation
Division of Research and Innovation, MS-83
1227 O Street
Sacramento, CA 95814

DISCLAIMER STATEMENT

This document is disseminated in the interest of information exchange. The contents of this report reflect the views of the authors who are responsible for the facts and accuracy of the data presented herein. The contents do not necessarily reflect the official views or policies of the State of California or the Federal Highway Administration. This publication does not constitute a standard, specification or regulation. This report does not constitute an endorsement by the Department of any product described herein.

STATE OF CALIFORNIA DEPARTMENT OF TRANSPORTATION

TECHNICAL REPORT DOCUMENTATION PAGE

TR0003 (REV. 10/98)

1. REPORT NUMBER	2. GOVERNMENT ASSOCIATION NUMBER	3. RECIPIENT'S CATALOG NUMBER
CA04-0252		

4. TITLE AND SUBTITLE	5. REPORT DATE
Analysis of Laterally Loaded Long or Intermediate Drilled Shafts of Small or Large Diameter in Layered Soil	December, 2008
	6. PERFORMING ORGANIZATION CODE
7. AUTHOR(S)	8. PERFORMING ORGANIZATION REPORT NO.
Mohamed Ashour, Gary Norris, Sherif Elfass	UNR / CCEER 01-02
9. PERFORMING ORGANIZATION NAME AND ADDRESS	10. WORK UNIT NUMBER
Department of Civil & Environmental Engineering University of Nevada Reno, NV 89557-0152	11. CONTRACT OR GRANT NUMBER DRI Research Task No. 0252 Contract No. 59A0348
12. SPONSORING AGENCY AND ADDRESS	13. TYPE OF REPORT AND PERIOD COVERED
California Department of Transportation Engineering Services Center 1801 30th Street Sacramento, CA 95816 California Department of Transportation Division of Research and Innovation, MS-83 1227 O Street Sacramento, CA 95814	Final Report 14. SPONSORING AGENCY CODE 913

15. SUPPLEMENTAL NOTES

This report may also be referenced as report UNR / CCEER 01-02 published by the University of Nevada, Reno.

16. ABSTRACT

Strain wedge (SW) model formulation has been used, in previous work, to evaluate the response of a single pile or a group of piles (including its pile cap) in layered soils to lateral loading. The SW model approach provides appropriate prediction for the behavior of an isolated pile and pile group under lateral static loading in layered soil (sand and/or clay). The SW model analysis covers the entire range of soil strain or pile deflection that may be encountered in practice. The method allows development of p-y curves for the single pile based on soil-pile interaction by considering the effect of both soil and pile properties (i.e. pile size, shape, bending stiffness, and pile head fixity condition) on the nature of the p-y curve.

This study has extended the capability of the SW model in order to predict the response of laterally loaded large diameter shafts considering 1) the influence of shaft type (long, intermediate or short) on the lateral shaft response; 2) the nonlinear behavior of shaft material (steel and/or concrete) and its effect on the soil-shaft-interaction; 3) developing (partial or complete) liquefaction in the surrounding soil profile based on far and near-field induced pore water pressure; and 4) vertical side shear resistance along the shaft wall that has a significant contribution to the lateral shaft response.

The incorporation of the nonlinear behavior of shaft material, soil liquefaction and vertical side shear resistance has a significant influence on the nature of the calculated p-y curves and the associated t-z curves. Contrary to the traditional Matlock-Reese p-y curve that was established for small diameter long (slender) piles and does not account for soil liquefaction and the variation in the shaft bending stiffness, the current approach for large diameter shafts can provide the p-y curve based on varying liquefaction conditions, vertical and horizontal shear resistance along the shaft, and the degradation in shaft flexural stiffness. In addition, the technique presented allows the classification and the analysis of the shaft as long, intermediate or short based on soil-shaft interaction.

17. KEY WORDS	18. DISTRIBUTION STATEMENT	
Laterally Loaded Deep Foundations, Drilled Shafts, Strain Wedge Model, Layered Soils, Nonlinear Behavior of Shaft Material, Liquefaction, Vertical Side Shear	No restrictions. This document is available to the public through the National Technical Information Service, Springfield, VA 22161	
19. SECURITY CLASSIFICATION (of this report)	20. NUMBER OF PAGES	21. PRICE
Unclassified	219 Pages	

ANALYSIS OF LATERALLY LOADED LONG OR INTERMEDIATE DRILLED SHAFTS OF SMALL OR LARGE DIAMETER IN LAYERED SOIL

(FINAL)

CCEER 01-02

Prepared by:

Mohamed Ashour
Research Assistant Professor

Gary Norris
Professor of Civil Engineering

and

Sherif Elfass
Research Assistant Professor

University of Nevada, Reno
Department of Civil Engineering

Prepared for:

State of California
Department of Transportation

Contract No. 59A0348

June 2004

ACKNOWLEDGMENTS

The authors would like to thank Caltrans for its financial support of this project. The authors would also like to acknowledge Dr. Saad El-Azazy, Mr. Anoosh Shamsabadi, Dr. Abbas Abghari, Mr. Angel Perez-Copo, Mr Steve McBride, Mr. Bob Tanaka and Mr. Tom Schatz for their support and guidance as the Caltrans monitors for this project.

DISCLAIMER

The contents of this report reflect the views of the authors who are responsible for the facts and accuracy of the data presented herein. The contents do not necessarily reflect the official views or policies of the State of California or the Federal Highway Administration. This report does not constitute standard specifications, or regulations.

ABSTRACT

Strain wedge (SW) model formulation has been used, in previous work, to evaluate the response of a single pile or a group of piles (including its pile cap) in layered soils to lateral loading. The SW model approach provides appropriate prediction for the behavior of an isolated pile and pile group under lateral static loading in layered soil (sand and/or clay). The SW model analysis covers the entire range of soil strain or pile deflection that may be encountered in practice. The method allows development of p-y curves for the single pile based on soil-pile interaction by considering the effect of both soil and pile properties (i.e. pile size, shape, bending stiffness, and pile head fixity condition) on the nature of the p-y curve.

This study has extended the capability of the SW model in order to predict the response of laterally loaded large diameter shafts considering 1) the influence of shaft type (long, intermediate or short) on the lateral shaft response; 2) the nonlinear behavior of shaft material (steel and/or concrete) and its effect on the soil-shaft-interaction; 3) developing (partial or complete) liquefaction in the surrounding soil profile based on far- and near-field induced porewater pressure; and 4) vertical side shear resistance along the shaft wall that has a significant contribution to the lateral shaft response.

The incorporation of the nonlinear behavior of shaft material, soil liquefaction and vertical side shear resistance has a significant influence on the nature of the calculated p-y curves and the associated t-z curves. Contrary to the traditional Matlock-Reese p-y curve that was established for small diameter long (slender) piles and does not account for soil liquefaction and the variation in the shaft bending stiffness, the current approach for large diameter shafts can provide the p-y curve based on varying liquefaction conditions, vertical and horizontal shear resistance along the shaft, and the degradation in shaft flexural stiffness. In addition, the technique presented allows the classification and the analysis of the shaft as long, intermediate or short based on soil-shaft interaction.

TABLE OF CONTENTS

CHAPTER 1

INTRODUCTION

The problem of a laterally loaded large diameter shafts has been under investigation and research for the last decade. At present, the p-y method developed by Matlock (1970) and Reese (1977) for slender piles is the most commonly used procedure for the analysis of laterally loaded piles/shafts. The confidence in this method is derived from the fact that the p-y curves employed have been obtained (back calculated) from a few full-scale field tests. Many researchers since have attempted to improve the performance of the p-y method by evaluating the p-y curve based on the results of the pressuremeter test or dilatometer test.

The main drawback with the p-y approach is that p-y curves are not unique. Instead the p-y relationships for a given soil can be significantly influenced by pile properties and soil continuity and are not properly considered in the p-y approach. In addition, the p-y curve has been used with large diameter long/intermediate/short shafts, which is a compromise. The SW model proposed by Norris (1986) analyzes the response of laterally loaded piles based on a representative soil-pile interaction that incorporates pile and soil properties (Ashour et al. 1998). The SW model does not require p-y curves as input but instead predicts the p-y curve at any point along the deflected part of the loaded pile using a laterally loaded soil-pile interaction model. The effect of pile properties and surrounding soil profile on the nature of the p-y curve has been presented by Ashour and Norris (2000). However, the current SW model still lack the incorporation of the vertical side shear resistance that has growing effect on the lateral response of large diameter piles/shafts. In addition, many of the large diameter shafts could be designed as long shafts and in reality they behave as intermediate shafts. Compared to the long shaft characteristics, the intermediate shaft should maintain softer response. It is customary to use the traditional p-y curves for the analysis of all types of piles/shafts (short/intermediate/long) which carries significant comprise.

The lateral response of piles/shafts in liquefied soil using the p-y method is based on the use of traditional p-y curve shape for soft clay corresponding to the undrained residual strength (S_r) of liquefied sand. Typically S_r is estimated using the standard penetration test (SPT) corrected blowcount, $(N_1)_{60}$, versus residual strength developed by Seed and Harder (1990). For a given $(N_1)_{60}$ value, the estimated values of S_r associated with the lower and upper bounds of this relationship vary considerably. Even if a reasonable estimate of S_r is made, the use of S_r with the clay curve shape does not correctly reflect the level of strain in a liquefied dilative sandy material. The p-y relationship for a liquefied soil should be representative of a realistic undrained stress-strain relationship of the soil in the soil-pile interaction model for developing or liquefied soil. Because the traditional p-y curve approach is based on static field load tests, it has been adapted to the liquefaction condition by using the soft clay p-y shapes with liquefied sand strength values.

In the last several years, the SW model has been improved and modified through a number of research phases with Caltrans to accommodate:

- a laterally loaded pile with different head conditions that is embedded in multiple soil layers (report to Caltrans, Ashour et al. 1996)
- nonlinear modeling of pile materials (report to Caltrans, Ashour and Norris 2001);
- pile in liquefiable soil (report to Caltrans, Ashour and Norris 2000); and
- pile group with or without cap (report to Caltrans, Ashour and Norris 1999)

The current report focuses on the analysis of large diameter shafts under lateral loading and the additional influential parameters, such as vertical side shear resistance, compared to piles. It also addresses the case of complete liquefaction and how the completely liquefied soil rebuilds significant resistance due to its dilative nature after losing its whole strength. The assessment of the t-z curve along the length of shaft and its effect on the shaft lateral response is one of the contributions addressed in this report

The classification of the shaft type whether it behaves as short, intermediate or long shaft has a crucial effect on the analysis implemented. The mechanism of shaft deformation and soil reaction is governed by shaft type (geometry, stiffness and head conditions) as presented in Chapter 2.

The assessment of the vertical side shear due to the shaft vertical movement induced by either axial or lateral loading is presented in Chapter 3 and 4. New approach for the prediction of the t-z curve in sand and clay is also presented. Since the lateral resistance of the shaft base has growing effect on the short/intermediate shaft lateral response, a methodology to evaluate the shaft base resistance in clay/sand is also presented in Chapters 3 and 4.

The SW model relates one-dimensional BEF analysis (p-y response) to a three-dimensional soil pile interaction response. Because of this relation, the SW model is also capable of determining the maximum moment and developing p-y curves for a pile under consideration since the pile load and deflection at any depth along the pile can be determined. The SW model has been upgraded to deal with short, intermediate and long shafts using varying mechanism. The degradation in pile/shaft bending stiffness and the effect of vertical side shear resistance are also integrated in the assessed p-y curve. A detailed summary of the theory incorporated into the SW model is presented in Chapter 5.

Soil (complete and partial) liquefaction and the variation in soil resistance around the shaft due to the lateral load from the superstructure are presented in Chapter 6. Based on the results obtained from the Treasure Island field test (sponsored by Caltrans), it is obvious that none of the current techniques used to analyze piles/shafts in liquefied soils reflects the actual behavior of shafts under developing liquefaction. New approach is presented in Chapter 6 to assess the behavior of liquefied soil and will be incorporated in the SW model analysis as seen in Chapter 8.

The nonlinear behavior of shaft material (steel and concrete) is a major issue in the analysis of large diameter shafts. Such nonlinear behavior of shaft material should be reflected on the nature of the p-y curve and the formation of a plastic hinge as presented in Chapter 7.

Several case studies are presented in this study to exhibit the capability of the SW model and how the shaft classification, shaft material modeling (steel and/or concrete) and soil liquefaction can be all implemented in the SW model analysis. Comparisons with field results and other techniques also are presented in Chapter 8.

CHAPTER 2

CLASSIFICATION AND CHARACTERIZATION OF LARGE DIAMETER SHAFTS

2.1 SHAFT CLASSIFICATION

The lateral load analysis procedures differ for short, intermediate and long shafts. The short, intermediate and long shaft classifications are based on shaft properties (i.e. length, diameter and bending stiffness) and the soil conditions described as follows. A shaft is considered "short" so long as it maintains a lateral deflection pattern close to a straight line. A shaft classified as "intermediate" under a given combination of applied loads and soil conditions may respond as a "short" shaft for the same soil profile for a different combination of applied loads and degraded soil properties (e. g. a result of soil liquefaction).

The shaft is defined as "long" when $L/T \geqslant 4$. L is the shaft length below ground surface and T is the relative stiffness defined as $T = (EI/f)^{0.2}$ where f is the coefficient of subgrade reaction (F/L^3). The computer Shaft treats the given shaft as a short shaft. The value of relative stiffness, T, varies with EI and f. For a short shaft, the bending stiffness (EI) in the analysis could have a fixed value (linear elastic). The coefficient of subgrade reaction, f, varies with level of deflection and decreases with increasing lateral load. The chart (Fig. 2-1) attributable to Terzaghi (DM 7.2, NAVFAC 1982) and modified by Norris (1986) provides average values of f as a function of soil properties only (independent of pile shape, EI, head fixity, etc).

The shaft behaves as an "intermediate" shaft when $[4 > (L/T) > 2]$. When an intermediate shaft is analyzed as a long shaft it results in overestimated lateral response. It should be noted that the classification of the shaft type in the present study (i.e. evaluation of its relative stiffness, T) is based on the initial bending stiffness of the shaft and an average of the coefficient of subgrade reaction (f) including the free-field liquefaction effect.

The shaft classification for the same shaft my change according to the level loading and the conditions (e.g. liquefied or non-liquefied) of the surrounding soils. In addition, shaft stiffness also varies with level of loading and the induced bending moment along the shaft. Therefore, the criterion mentioned above is not accurate and does not reflect the actual type of shaft with the progressive state of loading. For example, a shaft could behave as a long shaft under static loading and then respond as an intermediate shaft under developing liquefaction. Such response is due to the changing conditions of the surrounding soil. The analysis carried out in this study changes according to the type of shafts.

2.2 FOUNDATION STIFFNESS MATRIX

The structural engineer targets the shaft-head stiffness (at the base of the column) in 6 degrees of freedom as seen in Figs. 2-2 through and 2-4. In reality, the bending stiffness (EI) of the cross section varies with moment. In order to deal with an equivalent linear elastic behavior, a constant reduced bending stiffness (EI_r) for the shaft cross section can be used to account for the effect of the cracked concrete section under applied loads. However, it is very difficult to identify the appropriate reduction ratio for the shaft stiffness at a particular level of loading. The technique presented in this report allows the assessment of the displacement and rotational stiffness based on the varying bending stiffness of the shaft loaded. Such nonlinear modeling of shaft material reflects a realistic representation for the shaft behavior according to the level of loading, and the nonlinear response of shaft material and the surrounding soil The structural engineer can also replace the nonlinear shaft-head stiffnesses shown in Figs. 2-3 and 2-4 by using the shaft foundation and the p-y curve resulting from the presented technique along with the superstructure (complete solution) to model the superstructure-soil-shaft behavior as shown in Fig 2-6.

2.3 LARGE DIAMETER SHAFT

The computer programs LPILE/COM624P have been developed using lateral load tests performed on long slender piles. The Vertical Shear Resistance (V_v) acting along the pile or shaft perimeter has no significant influence on the lateral response of shafts and piles of diameters less than 3 feet. However, V_v contributes significantly to the capacity of large diameter shafts. The shaft analysis presented in this report accounts for the Horizontal and

Vertical Shear Resistance (V_h and V_v) acting along the sides of large diameter shafts in addition to base resistance (Fig. 2-7). The t-z curve for soil (sand, clay, c-φ soil and rock) is evaluated and employed in the analysis to account for the vertical shear resistance.

It should be noted herein that there are basic differences between the traditional p-y curves used with LPILE/COM624P and the Strain Wedge (SW) model technique employed in the current Shaft analysis.

- The traditional p-y relationships used in LPILE/COM624P do not account for the vertical side shear (V_v) acting along the sides of large diameter shafts because these relationships were developed for piles with small diameters where side shear is not significant.
- The traditional p-y relationships used in LPILE/COM624P were developed for long piles and not for intermediate/short shafts or piles. The p-y relationships for long piles are stiffer than those of short piles/shafts and their direct use in the analysis of short shafts is not realistic.
- The traditional p-y relationships for sand used in LPILE/COM624P are multiplied, without any explanation, by an empirical correction factor of 1.55 (Morrison and Reese, 1986)
- The bending stiffness of the pile/shaft has a marked effect on the nature of the resulting p-y curve relationship. The traditional p-y relationships used in LPILE/COM624P do not consider this effect. That is, the traditional p-y relationships used in LPILE/COM624P were developed for piles with diameters less than 3 feet that have much lower values of bending stiffness (EI) than the large diameter shafts.
- The traditional p-y curves for sand, developed about 30 years ago, is based on a static load test of a 2-ft diameter long steel pipe pile. They do not consider soil liquefaction.
- The traditional p-y curves have no direct link with the stress-strain relationship of the soil. Therefore, it is not feasible to incorporate the actual stress-strain behavior of liquefied soil in the traditional p-y curve formula.
- The traditional p-y curve cannot account for the varying pore water pressure in liquefied soil. It can only consider the pore water pressure ratio (r_u) in the free field (away from the shaft) by reducing the effective unit weight of soil by a ratio equal to r_u. Because of

this limitation, the traditional p-y curve, even after modification via r_u, is incapable of modeling the increase in pore water pressure around the shaft from the added superstructure loading.

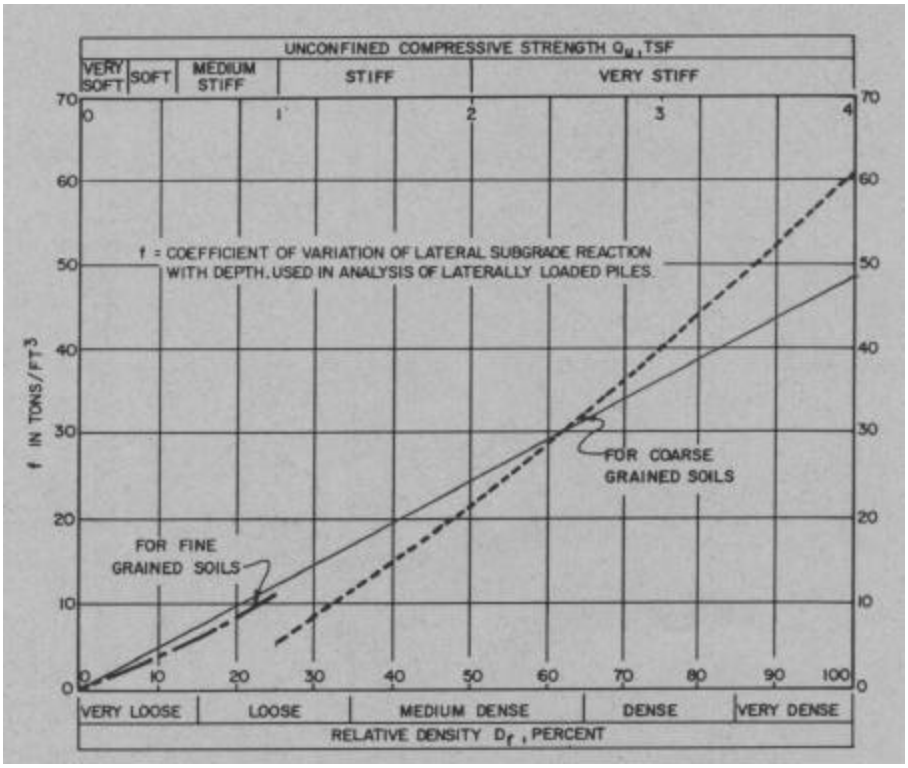

Fig. 2-1 f vs. q_u for Fine Grained Soil and f vs. D_r for Coarse Grained Soils

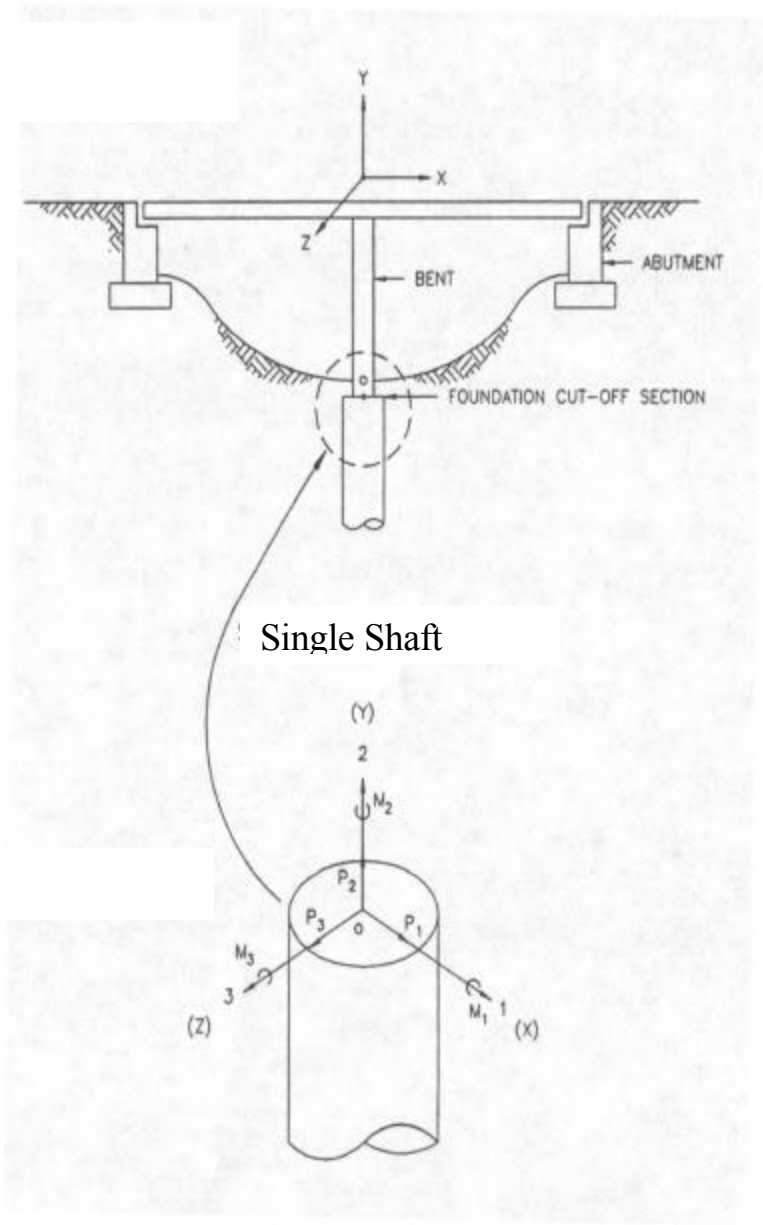

Fig. 2-2 Bridge Shaft Foundation and Its Global Axes

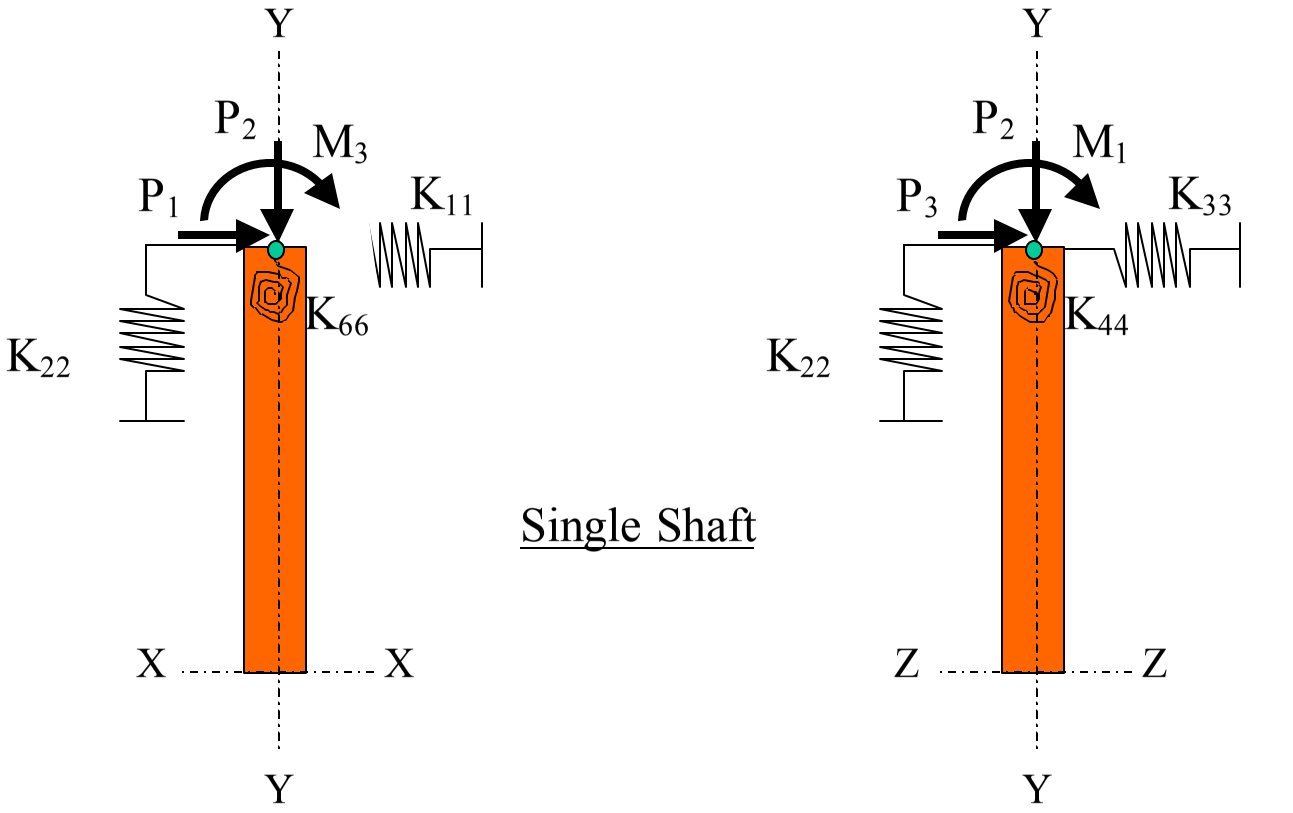

A) Loading in the X-X Direction (Axis 1)

B) Loading in the Z-Z Direction (Axis 3)

Fig. 2-3 Foundation Stiffnesses for a Single Shaft

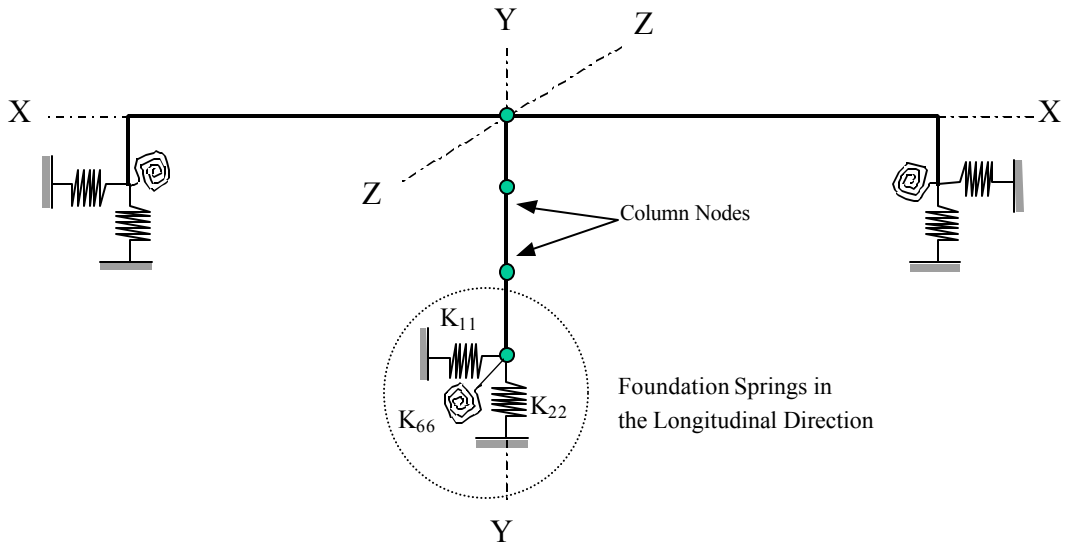

Fig. 2-4 Foundation Springs at the Base of a Bridge Column in The X-X Direction.

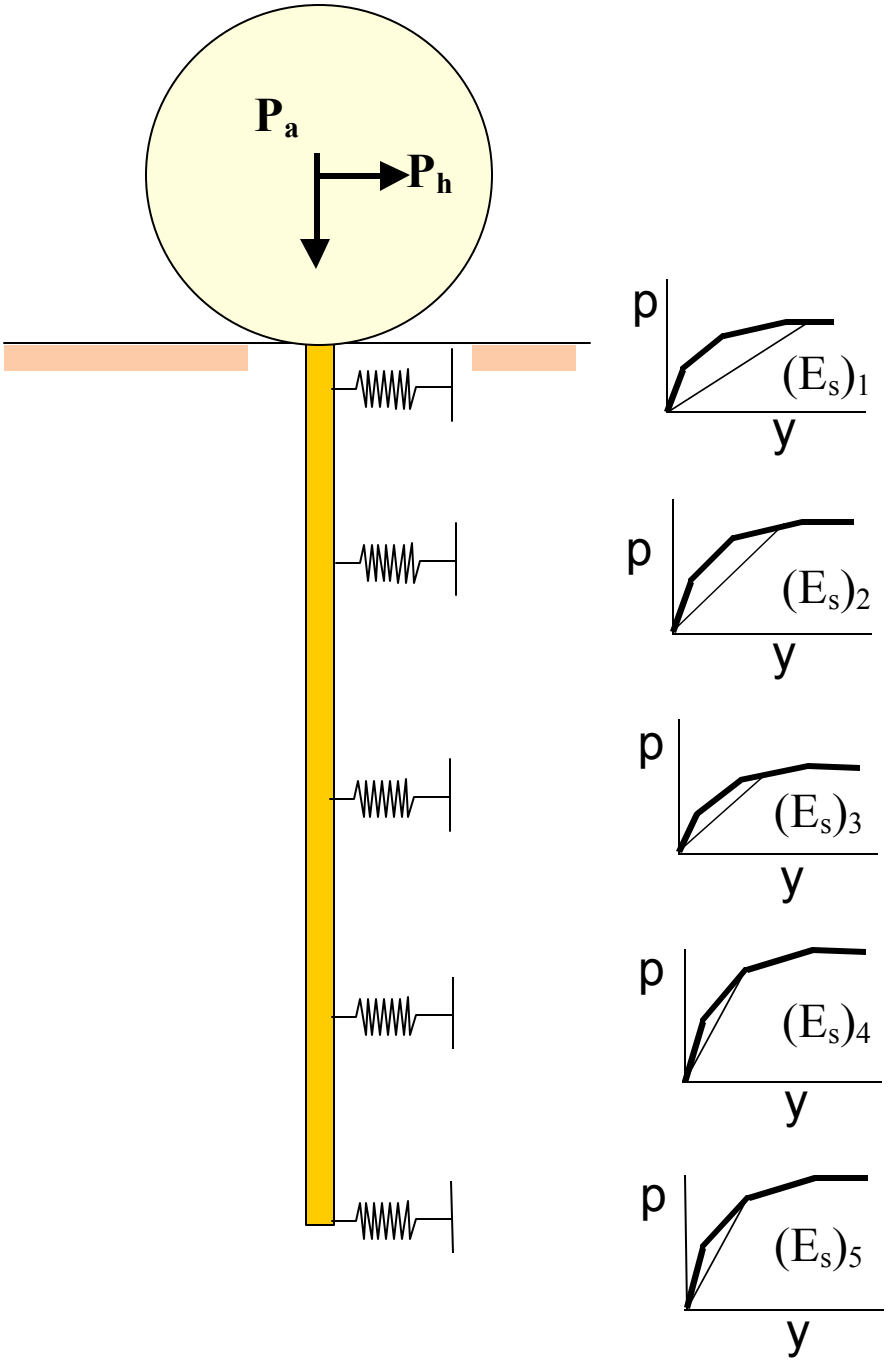

Fig. 2-6 Superstructure-Shaft-Soil Modeling as a Beam on Elastic Foundation (BEF)

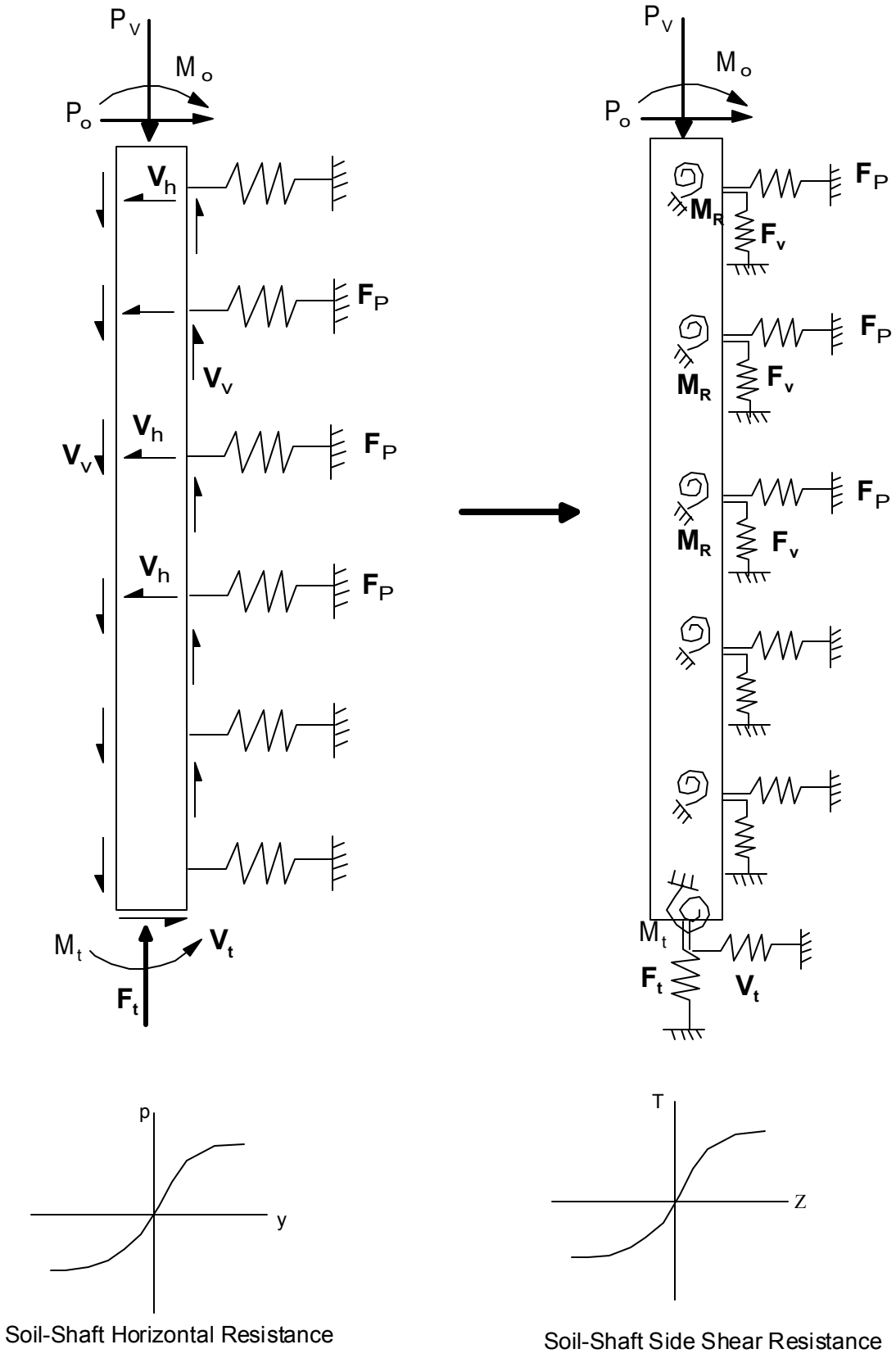

Fig. 2-7 Configuration of a Large Diameter Shaft

CHAPTER 3

VERTICAL SIDE SHAER AND PILE POINT TIP RESISTANCE OF A PILE / SHAFT IN CLAY

3.1 INTRODUCTION

The primary focus of this chapter is the evaluation of the vertical side shear induced by the vertical displacement accompanying the deflection of a laterally loaded shaft. The prediction of the vertical side shear of a laterally loaded shaft is not feasible unless a relationship between the vertical shaft displacement and the associated shear resistance is first established. The most common means to date is the t-z curve method proposed by Seed and Reese (1957). The associated curves were developed using experimental data from the vane shear test to represent the relationship between the induced shear stress (due to load transfer) and vertical movement (z) along the side of the pile shaft (Fig. 3-1). Other procedures are available to generate the t-z curve along the pile shaft (Coyle and Reese 1966; Grosch and Reese 1980; Holmquist and Matlock 1976 etc.). Most of these procedures are empirical and based on field and experimental data. Others are based on theoretical concepts such as the methods presented by Randolph and Worth (1978), Kraft et al. (1981) in addition to the numerical techniques adopted by Poulos and Davis (1968), Butterfield and Banerjee (1971), and the finite element method.

It should be noted that any developed t-z relationship is a function of the pile/shaft and soil properties (such as shaft diameter, cross section shape and material, axial stiffness, method of installation and clay shear stress-strain-strength). This requires the incorporation of as many soil and pile properties as useful and practical in the suggested analysis.

Coyle and Reese (1966) presented an analytical method to assess the load transfer relationship for piles in clay. The method is addressed in this chapter and requires the use of a t-z curve such as those curves suggested by Seed and Reese (1957), and Coyle and Reese (1966) shown in Figs. 3-1 and 3-2. However, the t-z curve presented by Seed

and Reese (1957) is based on the vane shear test, and the t-z curve developed by Coyle and Reese (1966) is based on data obtained from a number of pile load tests from the field (Fig. 3-2).

The current chapter presents a procedure for evaluating the change in the axial load with depth for piles in clay called "friction" piles since most of the axial load is carried by the shaft (as opposed to the pile point). The load transfer mechanism presented by Coyle and Reese (1966) is used in the proposed analysis in association with the t-z curve developed herein. In fact, the axially loaded pile analysis is just a means to develop the nonlinear t-z curves for clay that will be used later to assess the vertical side shear resistance of a laterally loaded large diameter shaft undergoing vertical movement at its edges as it rotates from vertical.

3.2 LOAD TRANSFER AND PILE SETTLEMENT

In order to construct the load transfer and pile-head movement in clay under vertical load, the t-z curve for that particular soil should be assessed. The load transferred from shaft skin to the surrounding clay soil is a function of the diameter and the surface roughness of the shaft, clay properties (cohesion, type of consolidation and level of disturbance) in addition to the shaft base resistance. The development of a representative procedure allows the assessment of the t-z curve in soil (sand and/or clay) that leads to the prediction of a nonlinear vertical load-settlement response at the shaft head. Such a relationship provides the mobilized shaft-head settlement under axial load and the ration of load displacement or vertical pile head stiffness.

The procedure developed by Coyle and Reese (1966) to assess the load-settlement curve is employed in this section. However, such a procedure requires knowledge of the t-z curves (theoretical or experimental) that represent the load transfer to the surrounding soil at a particular depth for the pile movement (z).

The following steps present the procedure that is employed to assess the load transfer and pile movement in clay soil:

1. Based on Skempton assumptions (1951), assume a small shaft base resistance, q_P (small percentage of $q_{net} = 9\ C$).

$$q_P = 9\ C_m = 9\ C\ SL = SL\ q_{net} \quad (3\text{-}1)$$

$$Q_P = q_P\ A_{base} = SL\ q_{net}\ A_{base} \quad (3\text{-}2)$$

C is equal to the clay undrained shear strength, S_u. A_{base} is the area of the pile tip (shaft base).

2. Using the SL evaluated above and the stress-strain relationship presented in Chapter 5 [Norris (1986) and Ashour et al. (1998)], compute the induced axial (deviatoric) soil strain, ε_P and the shaft base displacement, z_P

$$z_P = \varepsilon_P\ B \quad (3\text{-}3)$$

where B the diameter of the shaft base. See Section 3-3 for more details.

3. Divide the pile length into segments equal in length (h_s). Take the load Q_B at the base of the bottom segment as (Q_P) and movement at its base (z_B) equal to (z_P). Estimate a midpoint movement for the bottom segment (segment 4 as seen in Fig. 3-3). For the first trial, the midpoint movement can be assumed equal to the shaft base movement.

4. Calculate the elastic axial deformation of the bottom half of this segment,

$$z_{elastic} = \frac{Q_B h_s / 2}{E A_{base}} \quad (3\text{-}4)$$

The total movement of the midpoint in the bottom segment (segment 4) is equal to

$$z = z_T + z_{elastic} \quad (3\text{-}5)$$

5. Based on the soil properties of the surrounding soil (S_u and ε_{50}), use a Ramberg-Osgood formula (Eqn. 3-6) to characterize the backbone response (Richart 1975).

$$\frac{z}{z_r} = \frac{\gamma}{\gamma_r} = \frac{\tau}{\tau_{ult}} \left[1 + \beta \left(\frac{\tau}{\tau_{ult}} \right)^{R-1} \right] \qquad (3\text{-}6)$$

z = total midpoint movement of a pile/shaft segment

γ = average shear strain in soil adjacent to the shaft segment

τ = average shear stress in soil adjacent to the shaft segment

γ_r is the reference strain, as shown in Fig. 3-4, and equals to G_i / τ_{ult}

z_r = shaft segment movement associated to γ_r

ε_{50} = axial strain at SL = 0.5 (i.e. $\sigma_d = S_u$). ε_{50} can be obtained from the chart provided in Chapter 5 using the value of S_u.

β and R-1 are the fitting parameters of the a Ramberg-Osgood model given in Eqn. 3-7. These parameters are evaluated in section 3.2.1.

6. Using Eqn. 3-6 which is rewritten in the form of Eqn. 3-7, the average shear stress level ($SL_t = \tau / \tau_{ult}$) in clay around the shaft segment can be obtained iteratively based on movement z evaluated in Eqn. 3-5.

$$\frac{z}{z_r} = \frac{\gamma}{\gamma_r} = SL_t \left[1 + \beta (SL_t)^{R-1} \right] \qquad \text{(Solved for } SL_t\text{)} \qquad (3\text{-}7)$$

7. Shear stress at clay-shaft contact surface is then calculated, i.e.

$$\tau = SL_t \, \tau_{ult} \qquad \text{or} \qquad \tau = SL_t \, \alpha \, C \qquad (3\text{-}8)$$

where α is the ratio of C_A/C that expresses the variation in the cohesion of the disturbed clay (C_A) due to pile installation and freeze, as seen in Fig. 3-5 (DM7.2 , 1986). It should be noted that the drop in soil cohesion is accompanied by a drop in the initial shear modulus (G_i) of the clay

8. The axial load carried by the shaft segment in skin friction / adhesion (Q_s) is expressed as

$$Q_s = \pi\ B\ H_s\ \tau \tag{3-9}$$

9. Calculate the total axial load (Q_i) carried at the top of the bottom segment (i = 4).

$$Q_i = Q_s + Q_B \tag{3-10}$$

10. Determine the elastic deformation in the bottom half of the bottom segment assuming a linear variation of the load distribution along the segment.

$$Q_{mid} = (Q_i + Q_B) / 2 \tag{3-11}$$

$$z_{elastic} = \left(\frac{Q_{mid} + Q_B}{2} H_s \right) / EA = \frac{(Q_i + 3 Q_B)\, H_s}{8\, EA} \tag{3-12}$$

11. Compute the new midpoint movement of the bottom segment.

$$z = z_P + z_{elastic} \tag{3-13}$$

12. Compare the z value calculated from step 11 with the previously evaluated estimated movement of the midpoint from step 4 and check the tolerance.

13. Repeat steps 4 through 12 using the new values of z and Q_{mid} until convergence is achieved

14. Calculate the movement at the top of the segment i= 4 as

$$z_i = z_B + \frac{Q_i + Q_B}{2} \frac{H_s}{AE}$$

15. The load at the base (Q_B) of segment i = 3 is taken equal to Q_4 (i.e. Q_{i+1}) while z_B of segment 3 is taken equal to z_4 and steps 4-13 are repeated until convergence for segment 3 is obtained. This procedure is repeated for successive segments going up until reaching the top of the pile where pile head load Q is Q_l and pile top

movement δ is z_1. Based on presented procedure, a set of pile-head load-settlement coordinate values ($Q - \delta$) can be obtained on coordinate pair for each assumed value of Q_T. As a result the load transferred to the soil along the length of the pile can be calculated for any load increment.

16. Knowing the shear stress (τ) and the associated displacement at each depth (i.e. the midpoint of the pile segment), points on the t-z curve can be assessed at each new load.

3.3 DEVELOPED t-z CURVE RELATIONSHIP

For a given displacement (z), the mobilized shear stress (τ) at the shaft-soil interface can be expressed as a function of the ultimate shear strength (τ_{ult}) via the shear stress level (SL_t).

$$SL_t = \tau / \tau_{ult} \tag{3-14}$$

The shear displacement of the soil around the pile decreases with increasing distance from the pile wall (Fig. 3-6). Based on a model study (Robinsky and Morrison 1964) of the soil displacement pattern adjacent to a vertically loaded pile, it has been estimated (Norris, 1986) that the average shear strain, γ, within a zone of B/2 wide adjacent to the pile accounts for 75% of the shear displacement, z, as shown in Fig. 3-7. A linear shear strain, γ, in the influenced zone (B/2) can be expressed as

$$g = \frac{0.75\ z}{B/2} = \frac{1.5z}{B} \tag{3-15}$$

Therefore,

$$z = \frac{gB}{1.5} \tag{3-16}$$

As seen in Fig. 3-7 and because z is directly related to γ based on shaft diameter (Eqn.3-16), note that

$$\frac{z_{50}}{z_f} = \frac{\gamma_{50}}{\gamma_f} \tag{3-17}$$

where z_{50} and γ_{50} are the shaft displacement and the associated shear strain in the soil at $SL_t = 0.5$ (i.e. $\tau = 0.5\ \tau_{ult}$). z_f and γ_f are the shaft displacement and the associated shear strain at failure where $SL_t = 1.0$ (i.e. $\tau = \tau_{ult}$). Therefore, the variation in the shear strain (γ) occurs in concert with the variation in shaft displacement z (Fig. 3-4). It should be noted that soil shear modulus (G) exhibits its lowest value next to the pile skin and increases with distance away from the pile to reach it is maximum value (G_i) at γ and $z \cong 0$ (Fig. 3-6). Contrary to the shear modulus, the vertical displacement (z) and the shear strain (γ) reach their maximum value in the soil adjacent to the pile face and decrease with increasing radial distance from the pile.

3.3.1 Ramberg-Osgood Model for Clay

With the above mentioned transformation of the t-z curves to τ-γ curves, a Ramberg-Osgood model represented by Eqn. 3-6 can be used to characterize the t-z curve.

$$\frac{z}{z_r} = \frac{\gamma}{\gamma_r} = \frac{\tau}{\tau_{ult}} \left[1 + \beta \left(\frac{\tau}{\tau_{ult}} \right)^{R-1} \right] \tag{3-18}$$

At $\tau/\tau_{ult} = 1$ then

$$\beta = \frac{\gamma_f}{\gamma_r} - 1 \tag{3-19}$$

At $\tau/\tau_{ult} = 0.5$ and $\gamma = \gamma_{50}$, then

$$R - 1 = \frac{\log \left(\dfrac{2\,\dfrac{\gamma_{50}}{\gamma_r} - 1}{\beta} \right)}{\log (0.5)} = \frac{\log \left(\dfrac{2\,\dfrac{\gamma_{50}}{\gamma_r} - 1}{\dfrac{\gamma_f}{\gamma_r} - 1} \right)}{\log (0.5)} \tag{3-20}$$

The initial shear modulus (G_i) and the shear modulus (G_{50}) at SL = 0.5 can be determined via their direct relationship with the normal stress-strain relationship and Poisson's ratio (ν)

$$G_i = \frac{E_i}{2(1+\nu)} = \frac{E_i}{3} \qquad \nu \text{ for clay} = 0.5 \tag{3-21}$$

and

$$G_{50} = \frac{E_{50}}{2(1+\nu)} = \frac{E_{50}}{3} = \frac{S_u}{3\,\varepsilon_{50}} \tag{3-22}$$

As seen in Fig. 3-4,

$$\gamma_r = \frac{S_u}{G_i} = \frac{\tau_{ult}}{G_i} \tag{3-23}$$

$$\gamma_{50} = \frac{0.5\,S_u}{G_{50}} \tag{3-24}$$

The shear strain at failure (γ_f) is determined in terms of the normal strain at failure (ε_f), i.e.

$$\gamma_f = \frac{\varepsilon_f}{(1+\nu)} = \frac{\varepsilon_f}{1.5} \tag{3-25}$$

The normal stress-strain relationship of clay (σ_d - ε) is assessed based on the procedure presented in Chapter 5 that utilizes ε_{50} and S_u of clay. The initial Young's modulus of clay (E_i) is determined at a very small value of the normal strain (ε) or stress level (SL). In the same fashion, ε_f is evaluated at SL = 1 or the normal strength $\sigma_{df} = 2S_u$.

3.4 PILE TIP (SHAFT BASE) RESISTANCE IN CLAY

In regard to the pile tip resistance ($Q_T - z_T$) response, the concept of Skempton's characterization (1951) is used as follows,

$$Q_T = q_{net} A_{base} = 9 C A_{base}$$

where clay cohesion, C, represents the undrained shear strength, S_u. The stress level (SL = σ_d / σ_{df}) in clay is proportional to the pressure level (PL = q/q_{net}). Different from the strain-deflection relationship established by Skempton (1951) for strip footing ($y_{50} = 2.5 \varepsilon_{50} B$), the vertical soil strain (ε_1) beneath the base of the shaft is expressed as

$$\varepsilon_1 = \frac{\Delta\sigma_1}{E} + \nu \frac{\Delta\sigma_2}{E} + \nu \frac{\Delta\sigma_3}{E}$$

for $\sigma_2 = \sigma_3$ and $\nu = 0.5$, then

$$\varepsilon_1 = \frac{\Delta\sigma_1 - \Delta\sigma_3}{E} + (1 - 2\nu) \frac{\Delta\sigma_3}{E}$$

$$\varepsilon_1 = \frac{\Delta\sigma_1 - \Delta\sigma_3}{E} = \frac{\Delta\sigma_d}{E}$$

Therefore, for a constant Young's modulus (E) with depth, the strain or ε_1 profile has the same shape as the elastic ($\Delta\sigma_1 - \Delta\sigma_3$) variation or Schmertmann's I_z factor (Schmertmann 1970, Schmertmann et al. 1979 and Norris 1986). Taking ε_1 at depth B/2 below the shaft base (the peak of the I_z curve), the shaft base displacement (z_T) is a function of the area of the triangular variation (Fig. 3-9), or

$$z_T = \varepsilon B \qquad (3\text{-}26)$$

Dealing with different values for the pile tip resistance, the associated deviatoric stress (ε) and base movement (a function of strain, ε) can be determined (given the stress-strain, $\sigma_d - \varepsilon$ relationship of the clay immediately below pile tip) in order to construct the pile point load-point displacement curve.

3.5 PROCEDURE VALIDATION

3.5.1 Comparison with the Seed-Reese t-z Curve in Soft Clay (California Test)

The test reported by Seed and Reese (1957) was conducted in the San Francisco Bay area of California. As shown in Fig. 3-10, the soil conditions at that site consisted of 4 ft of

fill, 5 ft of sandy clay, and around 21 ft of organic soft clay “bay mud”. The water table was approximately 4 ft below ground.

Several 6-in.-diameter pipe piles (20 to 22 ft long) were driven into the above soil profile. The pipe pile had a coned tip and maximum load of 6000 lb. The top 9 ft of the nonhemogeneous soil was cased leaving an embedment in clay of 13 ft.

A number of disturbed and undisturbed unconfined compression tests were conducted to determine the unconfined compressive strength of clay (Fig. 3-11). Seven loading tests were performed on the same pile at different periods of time that ranged from 3 hours to 33 days. As shown in Fig. 3-12, the ultimate bearing capacity of the clay reached a stable and constant value (6200 lb) by the time of the seventh test. As a result, Coyle and Reese (1966) considered the results of the seventh load test as representative for stable load transfer-pile movement response.

Coyle and Reese (1966) used the data obtained from the current field test conducted by Seed and Reese (1957) to compute the values of the load transfer response and pile movement at different depths as seen in Fig. 3-13. Figure 3-14 exhibits an equivalent set of the t-z curves at the same depths that are constructed by using the procedure presented herein and based on the undrained compressive strength of clay that is described by the dashed line shown in Fig. 3-11. The good agreement between the experimental and predicted t-z curves can be seen in the comparison presented in Fig. 3-15. Such agreement speaks to capability of the technique presented. The predicted t-z curve at the deepest two points (20 and 22 feet below ground) and seen in Fig. 3-15 can be improved by a slight increase in the undrained compressive strength utilized.

The good agreement between the predicted and experimental t-z curves resulted in an excellent assessment for load distribution (due to shear resistance) along the pile. Fig. 3-16 shows the assessed load distribution and tip resistance that are based on the procedure presented and induced in 1000-lb axial load increments up to an axial load of 6000 lb. A

comparison between the measured and predicted load distributions along the pile is shown in Fig. 3-17.

The measured pile head load-settlement curves under seven cases of axial loads are shown in Fig. 3-18. The loading tests were performed at different periods of time after driving the pile. As mentioned earlier, the seventh test (after 33 days of driving the pile) is considered for the validation of the procedure presented. Reasonable agreement can be observed between the predicted and measured pile head load-settlement curve (Fig. 3-18).

It should be noted that Seed and Reese (1957) established a procedure that allows the assessment of the pile load-settlement curve and the distribution of the pile skin resistance based on the data collected from vane shear test shown in Fig. 3-1. In addition, some assumptions should be made for the point load movement in order to get good agreement with the actual pile response. Seed and Reese (1957) presented explanation for the lack of agreement between their calculated and measured data. The undrained compressive strength collected using the vane shear test was the major source of that disagreement.

3.6 SUMMARY

The procedure to evaluate the t-z and load-settlement curves for a pile in clay presented here is based on elastic theory and Ramberg-Osgood characterization of the stress-strain behavior of soil. This procedure allows the assessment of the mobilized resistance of the pile using the developed t-z curve and the pile point load-displacement relationship. The results obtained in comparison with the field data show the capability and the flexible nature of the suggested technique. Based on the comparison study presented in this chapter, the good agreement between the measured and predicted load transfer along the pile, pile movement, pile-head settlement and pile tip resistance shows the consistency of the technique's assumptions. The findings in this chapter will be employed in Chapter 5 to evaluate the vertical side shear resistance induced by the lateral deflection of a large diameter shaft and its contribution to the lateral resistance of the shaft.

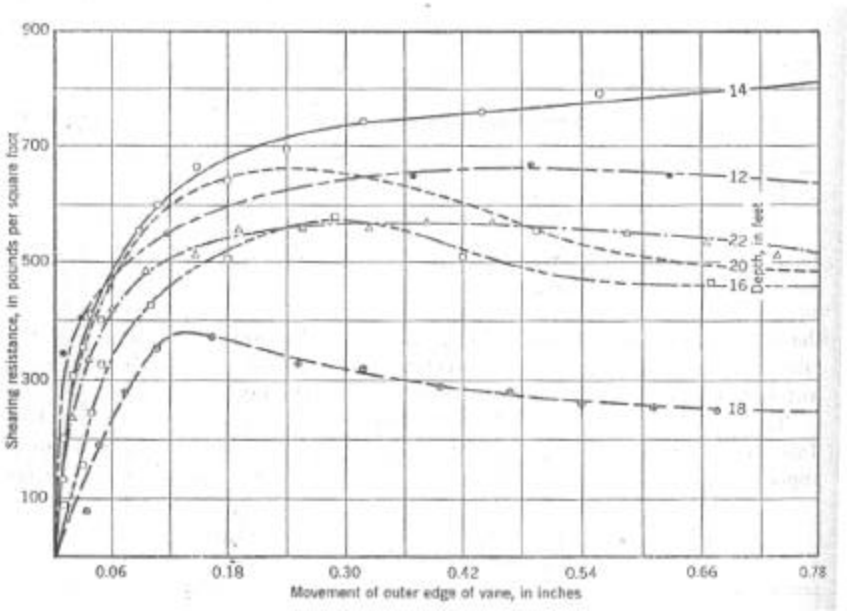

Fig. 3-1 Shear Resistance vs. Movement Determined by the Vane Shear Test (Seed and Reese 1957)

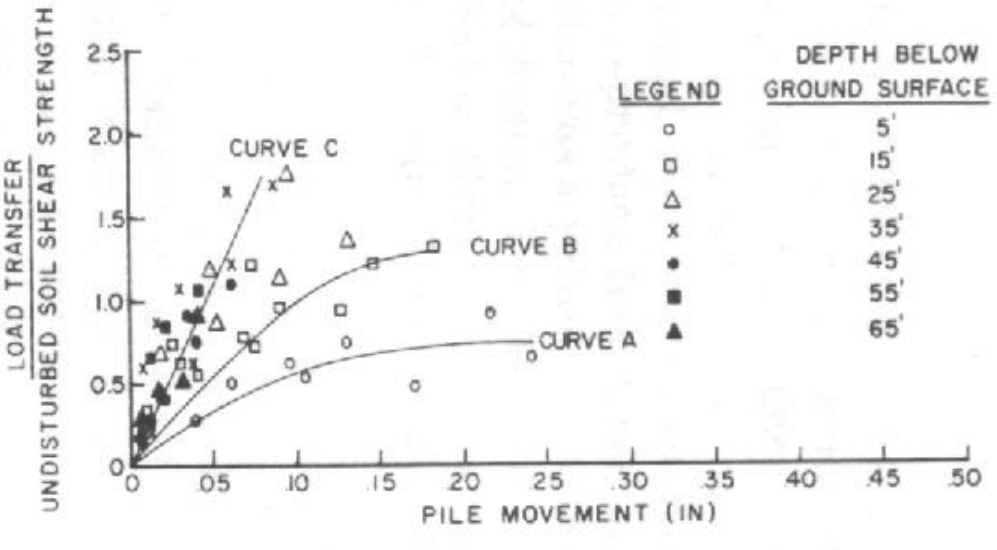

Fig. 3-2 Ratio of Load Transfer to Soil Shear Strength Vs. Pile Movement for a Number of Field Tests (Coyle and Reese 1966)

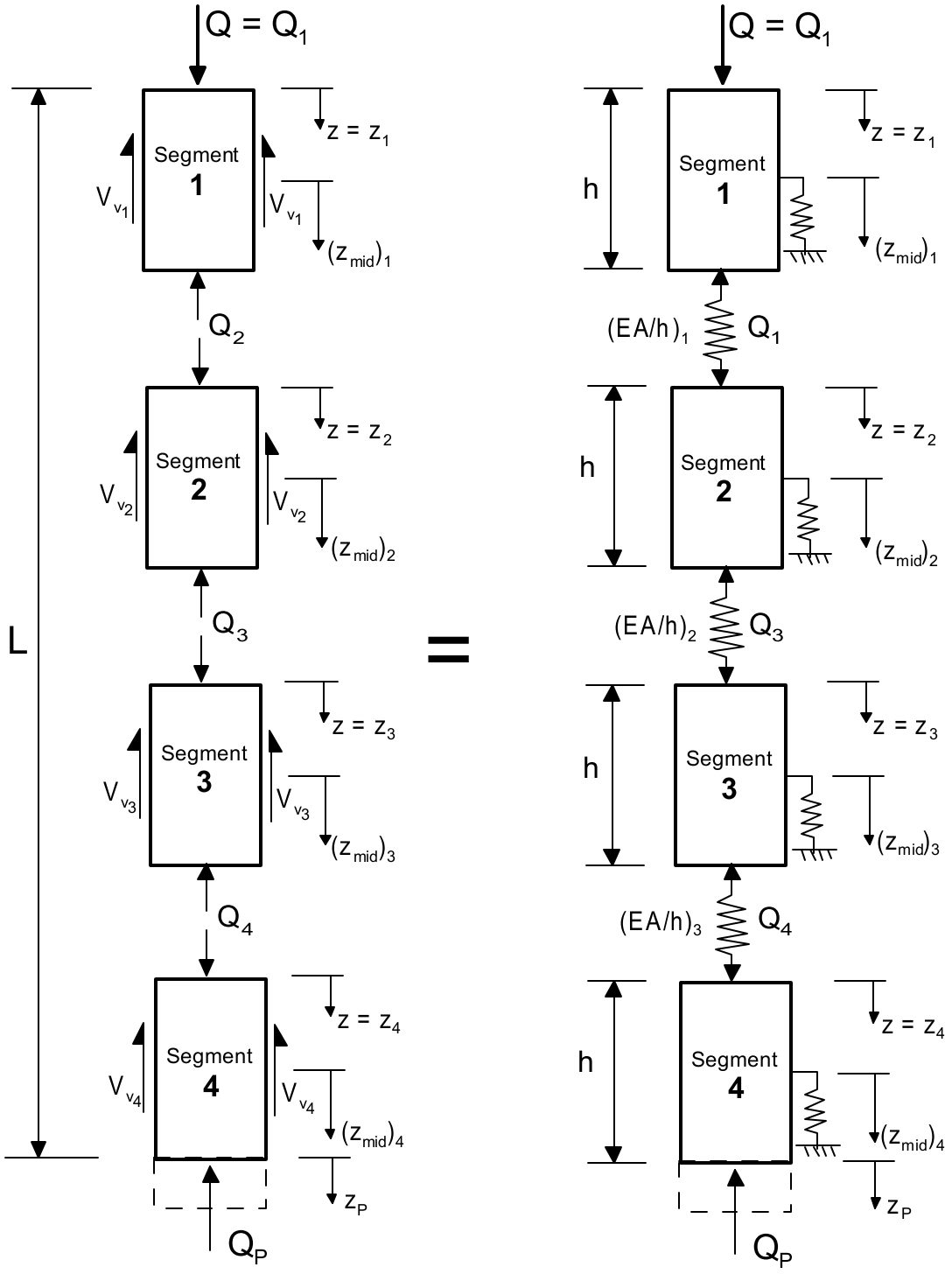

Fig. 3-3 Modeling Axially Loaded Pile Divided into Segments

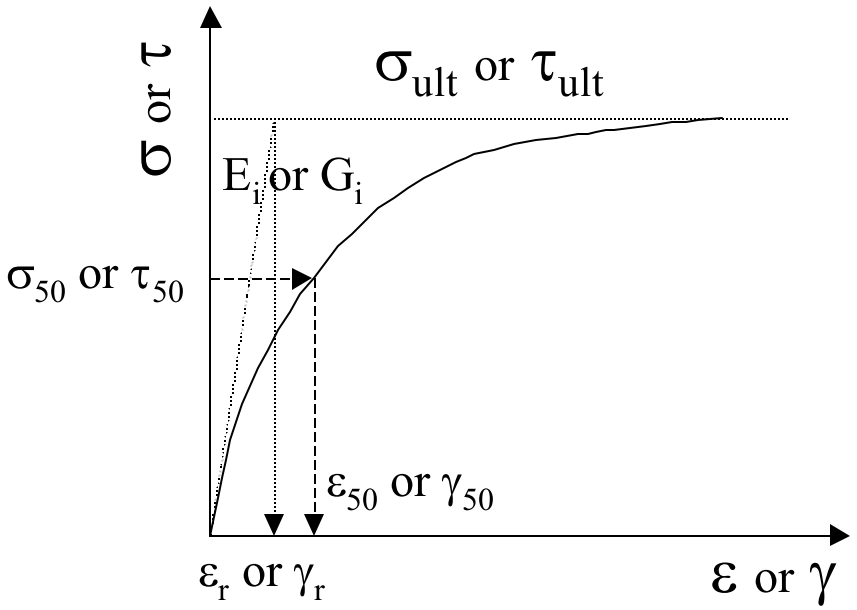

Fig. 3-4 Basic (Normal or Shear) Stress-Strain Curve

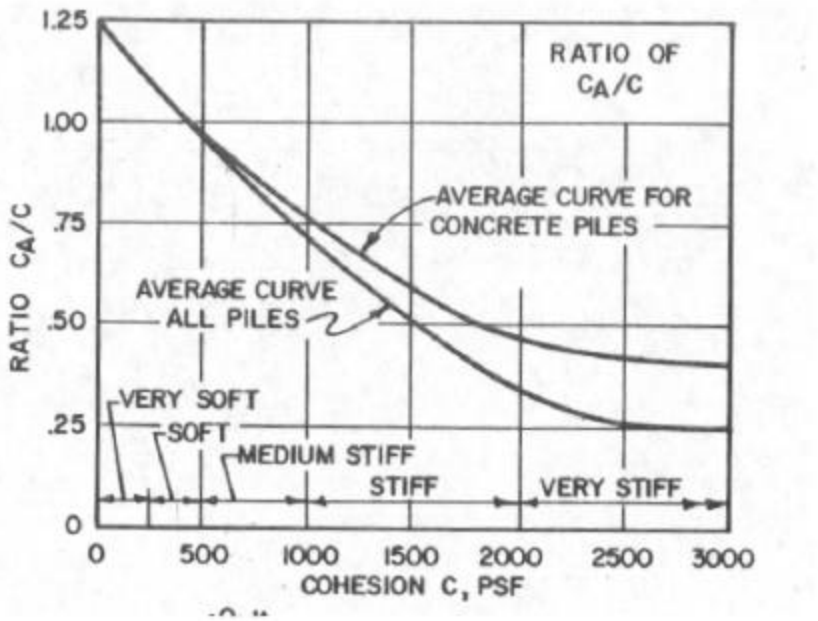

Fig. 3-5 Changes in Clay Cohesion Adjacent to the Pile Due to Pile Installation (DM7.2 1986)

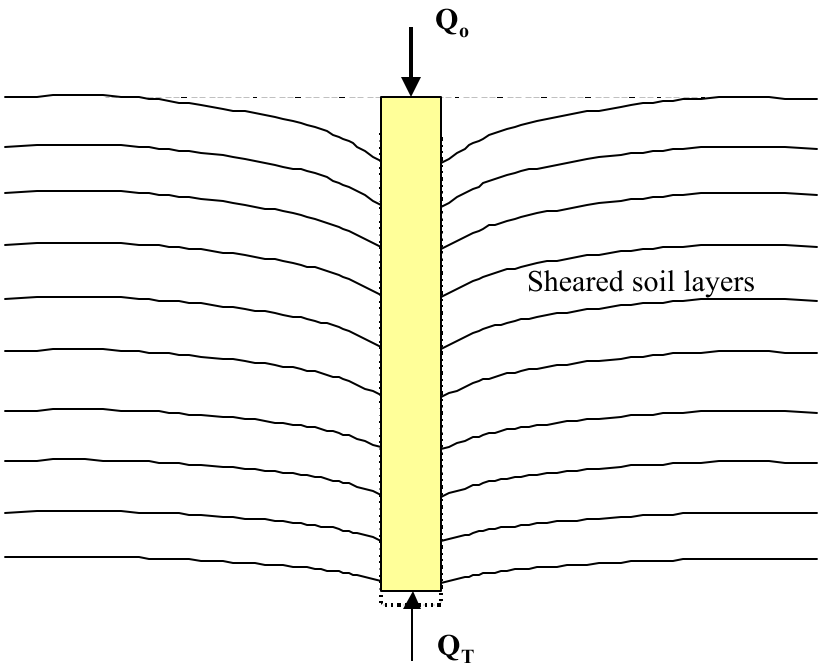

Fig. 3-6 Soil Layer Deformations Around Axially Loaded Pile

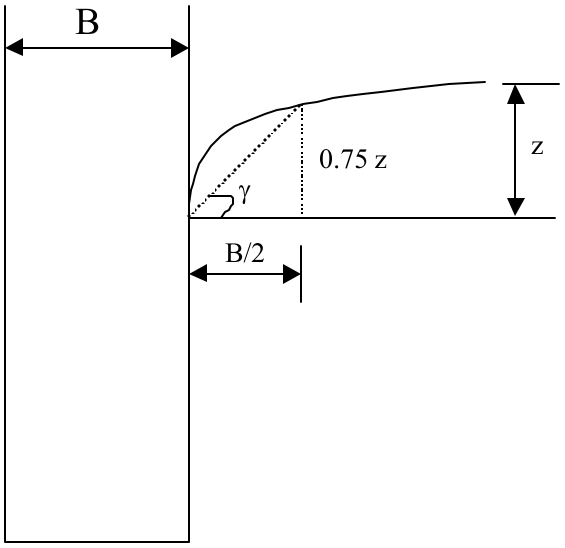

Fig. 3-7 Idealized Relationship Between Shear Strain in Soil (γ) and Pile Displacement (Z) (Norris, 1986)

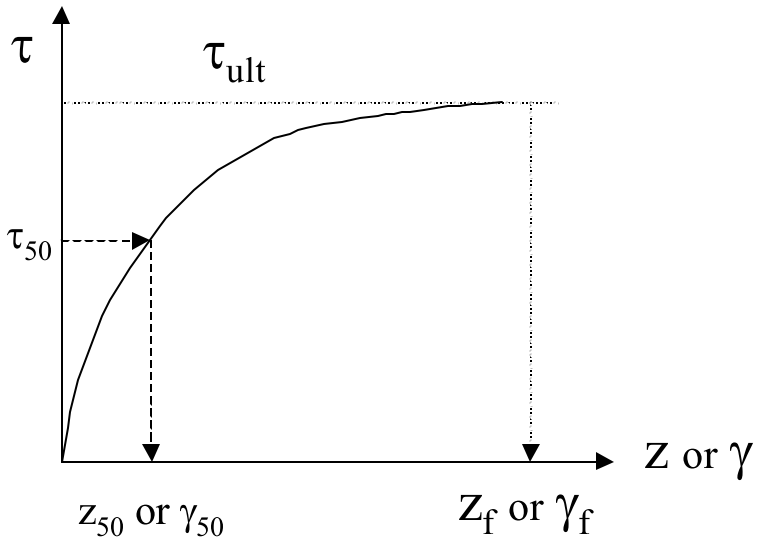

Fig. 3-8 Soil Shear Resistance Vs. Shear Strain (γ) or Pile Movement (z)

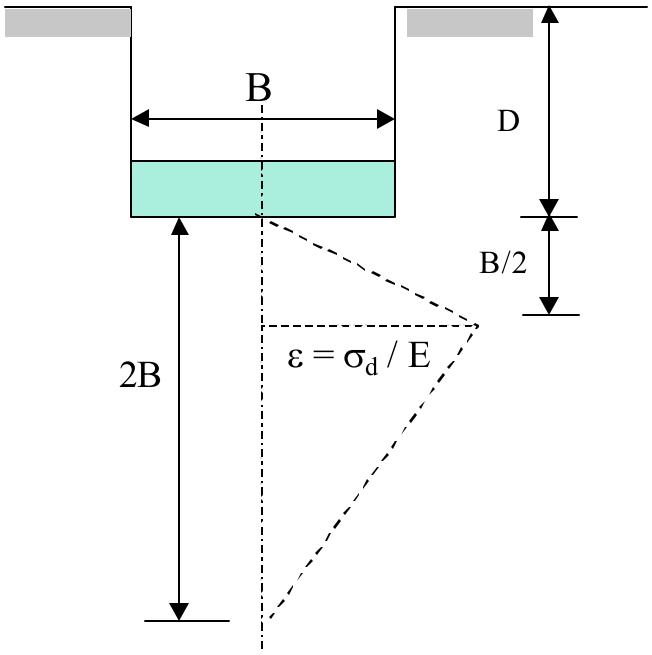

Fig. 3-9 Schmertmann Strain Distribution Below Foundation Base (after Norris, 1986)

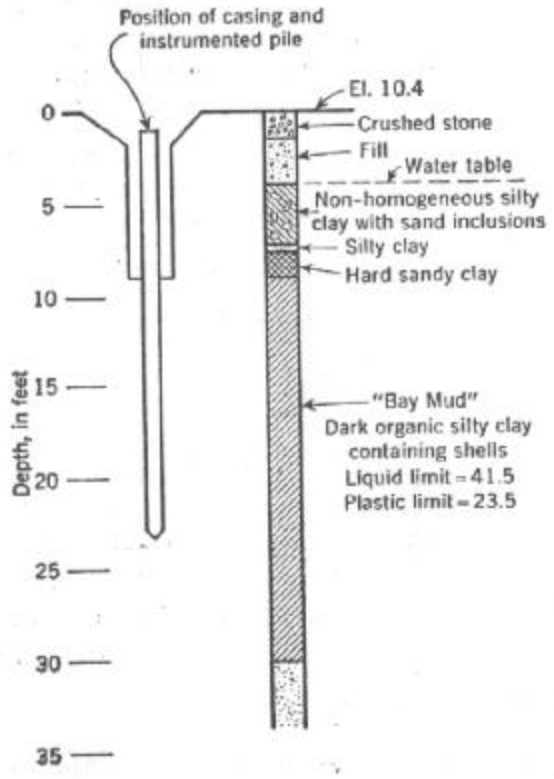

Fig. 3-10 Driven Pile and Soil Profile for California Test (Seed and Reese 1957)

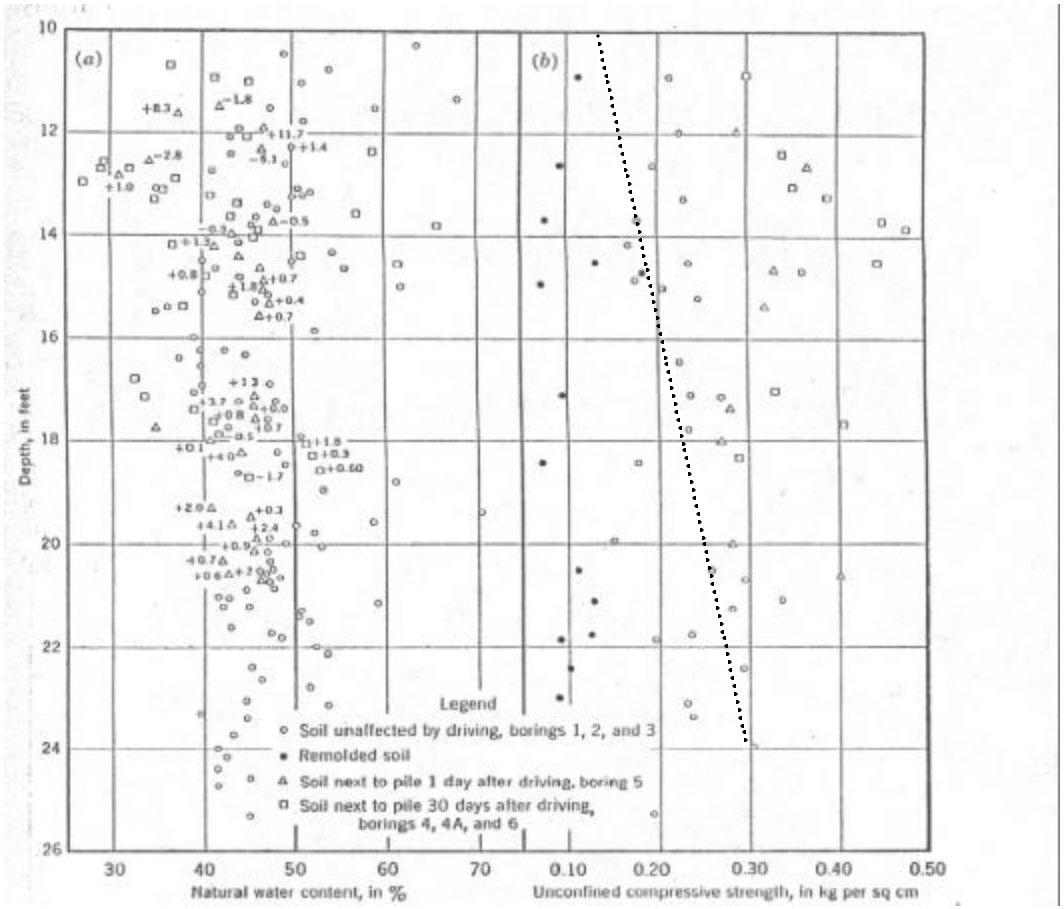

Fig. 3-11 Results of Soil Tests for the Undrained Shear Strength of the Bay Mud in California Test (Seed and Reese 1957)

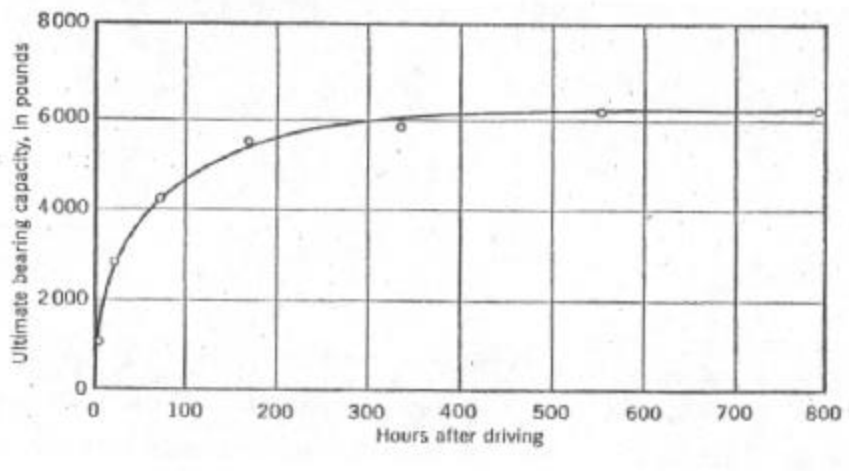

Fig. 3-12 Variation of the Clay Bearing Capacity with Time
(California Test, Seed and Reese 1957)

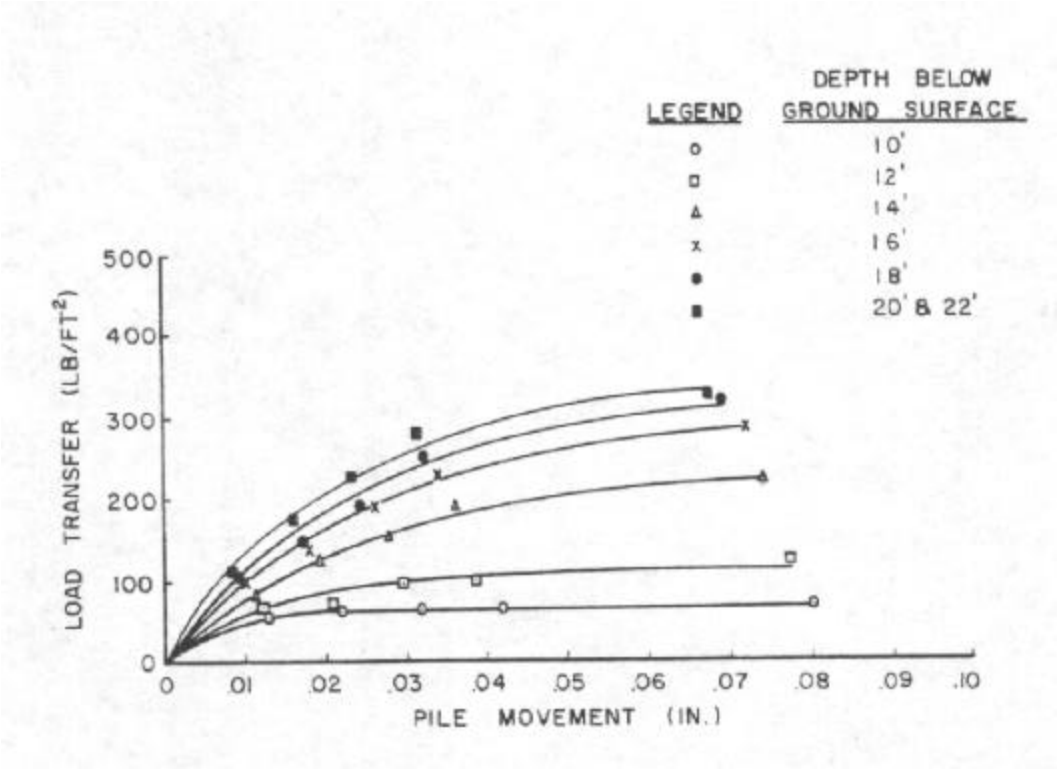

Fig. 3-13 Measured Load Transfer (τ) – Pile Movement (z) Curve for California Test
(Coyle and Reese 1966)

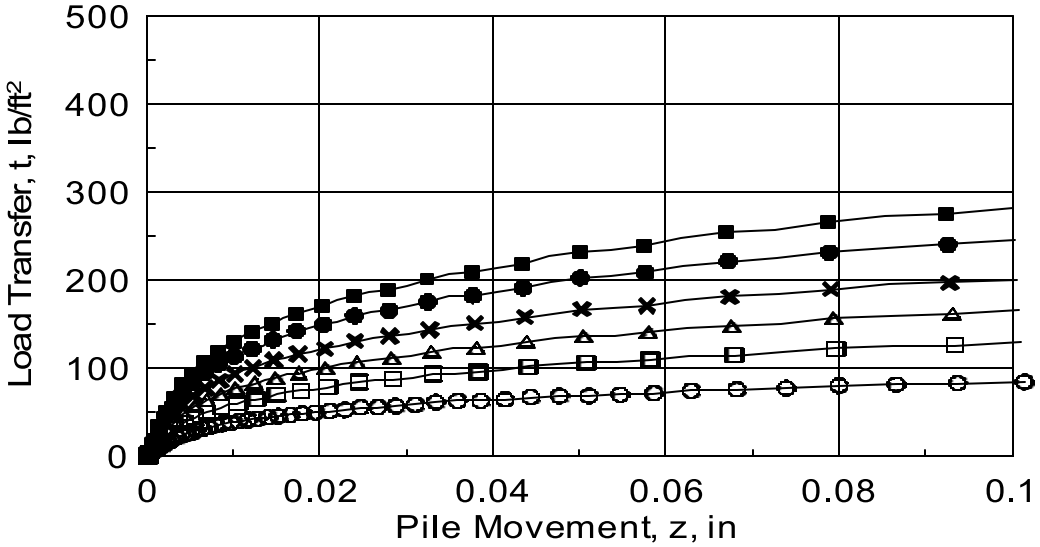

Fig. 3-14 Predicted Load Transfer (τ) – Pile Movement (z) Curve for California Test Using the Suggested Procedure

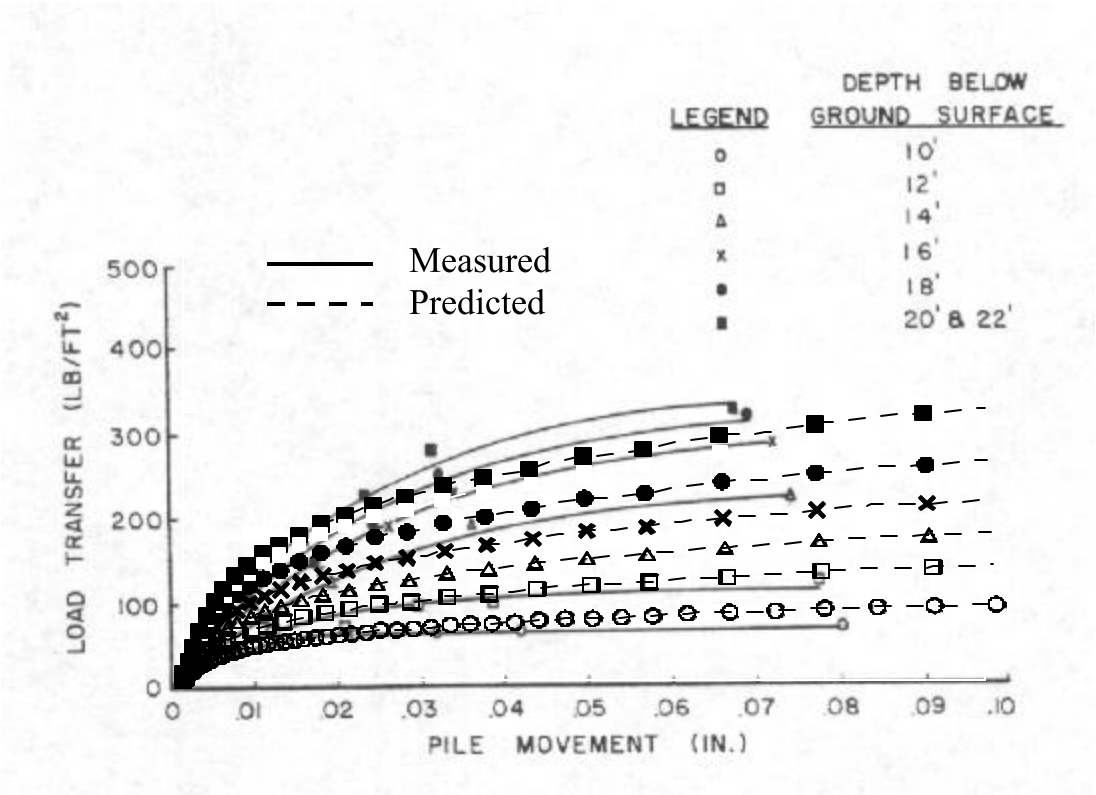

Fig. 3-15 Comparison Between Measured and Predicted Load Transfer (τ) – Pile Movement (z) Curve for the California Test

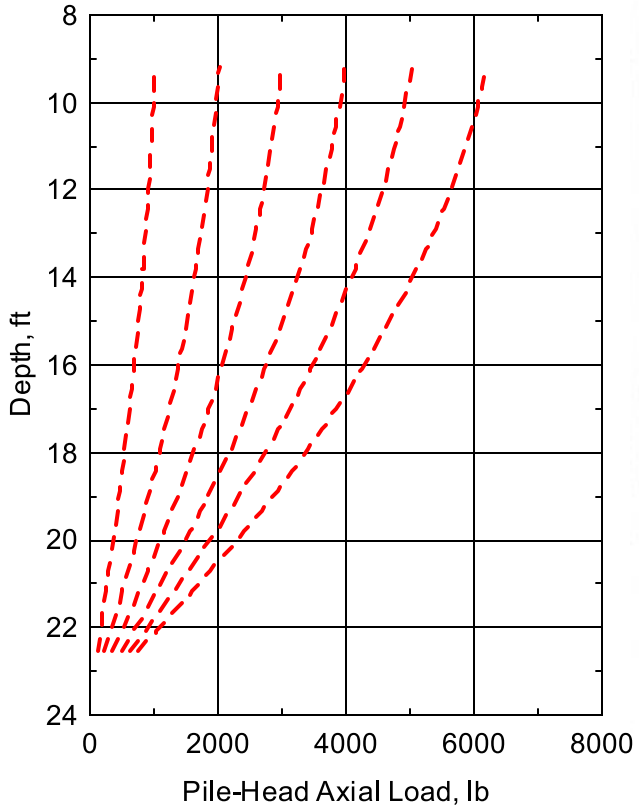

Fig. 3-16 Predicted Load Distribution along the Pile in California Test

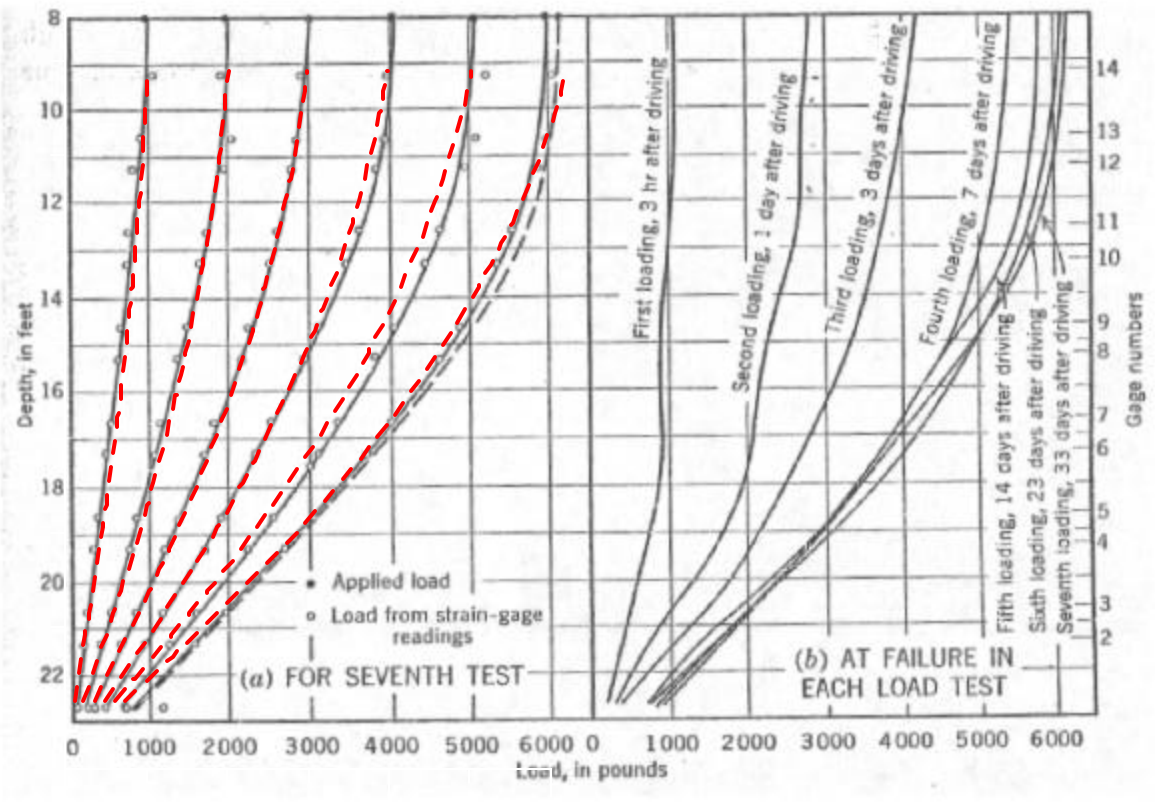

Fig. 3-17 Comparison of Measured and Predicted Load Distribution along the Pile in California Test (Seed and Reese 1957)

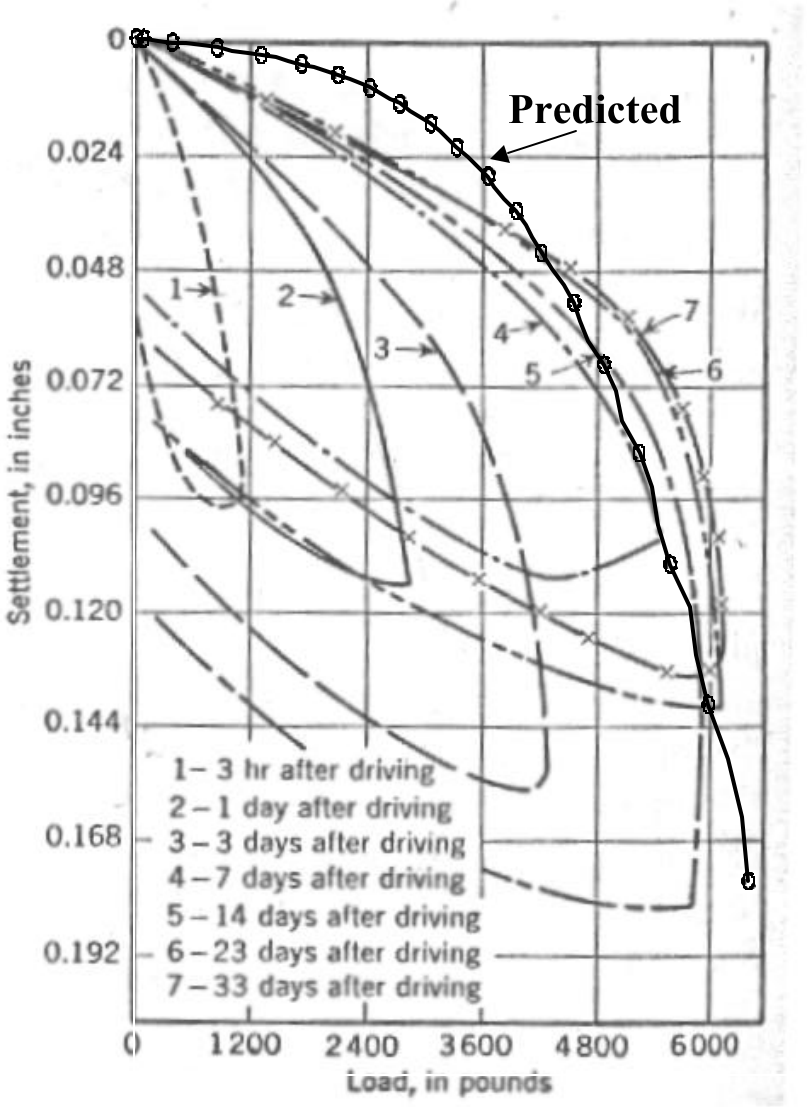

Fig. 3-18 Pile-Head Load-Settlement Curves for Seven Loading Tests at Different Time Periods for the California Test in Comparison with the Predicted Results

CHAPTER 4

VERTICAL SIDE SHAER AND POINT RESISTANCE OF PILE/SHAFT IN SAND

4.1 INTRODUCTION

The friction pile in cohesionless soil gains its support from the pile tip resistance and the transfer of load via the pile wall along its length. It has been suggested that the load transferred by skin friction pile can be neglected which is not always the case. The load transferred via the pile wall depends on the diameter and length of the pile, the surface roughness, and soil properties. It should also be mentioned that both pile point and skin resistances are interdependent.

The assessment of the mobilized load transfer of a pile in sand depends on the success in developing a representative t-z relationship. This can be achieved via empirical relationships (Kraft et al. 1981) or numerical methods (Randolph and Worth, 1978). The semi-empirical procedure presented in this chapter employs the stress-strain relationship of sand and findings from experimental tests. The t-z curve obtained based on the current study will be used in Chapter 5 to account for the vertical side shear resistance that develops with the laterally loaded large diameter shafts.

The method of slices presented in this chapter reflects the analytical portion of this technique that allows the assessment of the attenuating shear stress/strain and vertical displacement within the vicinity of the driven pile. As a result, the load transfer and the t-z curve can be assessed using a combination between the tip and side resistances of the pile.

PILE POINT (SHAFT BASE) RESISTANCE AND SETTLEMENT ($Q_P - z_P$) IN SAND

It is evident that the associated pile tip resistance manipulates the side resistance of the pile shaft. As presented in the analysis procedure, the pile tip resistance should be assumed at the first step. As a result, the shear resistance and displacement of the upper segments of the pile can be

computed based on the assumed pile tip movement. This indicates the need for a practical technique that allows the assessment of the pile tip load-displacement relationship under a mobilized or developing state. Most of the available techniques provide the ultimate pile tip resistance that is independent of the specified settlement. In other words, the pile tip settlement at the ultimate tip resistance is a function of the pile diameter (e.g. 5 to 10% of pile tip diameter). Thereafter, a hyperbolic curve is used to describe the load-settlement curve based on the estimated ultimate resistance and settlement of the pile tip.

Elfass (2001) developed an approach that allows the assessment of the mobilized pile tip resistance in sand and the accompanying settlement over the whole range of soil strain up to and beyond soil failure. In association with the pile side shear resistance technique presented in Section 4-2, the approach established by Elfass (2001) will be employed in the current study to compute the pile tip load-settlement in sand.

The failure mechanism developed by Elfass (2001) assumes four failure zones represented by four Mohr circles as shown in Fig. 4.1. This mechanism yields the bearing capacity (q) and its relationship with the deviatoric stress (σ_d) of the last (fourth Mohr circle) as shown in Fig 4-2. .

$$\sigma_d = 0.6\, q \qquad (4\text{-}1)$$

The pile tip resistance (Q_P) is given as,

$$Q_P = q\, A_{base} = \frac{\sigma_d}{0.6} A_{base} \qquad (4\text{-}2)$$

where A_{base} is the cross sectional area of the pile tip (shaft base).

As seen in Fig. 4-1, the Mohr Columb strength envelope is nonlinear and requires the evaluation of the secant angle of the fourth circle (φ_{IV}) tangent to the curvilinear envelope. The angle of the secant line tangent to first circle (φ_I) at effective overburden pressure can be obtained from the field blow data count (SPT test) or a laboratory triaxial test at approximately 1 tsf (100 kPa) confining pressure. Due to the increase in the confining pressure ($\overline{\sigma}_3$) from one circle to the

next, the friction angle (φ) decreases from φ_I at $(\bar{\sigma}_3)_I$ to φ_{IV} at $(\bar{\sigma}_3)_{IV}$ based on the following Bolton (1986) relationship modified by Elfass (2001) (Fig. 4-3)

$$\varphi_{peak} = \varphi_{min} + \varphi_{diff} \tag{4-3}$$

$$\varphi_{diff} = 3I_R = 3D_R\left\{10 - \ln\left[\left(\frac{2+\tan^2(45+\varphi/2)}{3}\right)\frac{\bar{\sigma}_3}{p}\right]\right\} - 1 \tag{4-4}$$

$\bar{\sigma}_3$ is in kPa. φ_{min} is the lowest friction angle that φ may reach at high confining pressure, as shown in Fig. 4-4 and Dr is inputted as its decimal value.

Knowing the sand relative density (D_r) and the associated friction angle under the original confining pressure $(\bar{\sigma}_3 = \bar{\sigma}_{vo})$, the reduction in the friction angle (Δφ) due to the increase of the confining pressure from $\bar{\sigma}_{vo}$ to $(\bar{\sigma}_3)_{IV}$ can be evaluated based on Eqns. 4-3 and 4-4, as described in the following steps:

1. Based on Eqn. 4-4, calculate $(\varphi_{diff})_I$ at the original confining pressure $(\bar{\sigma}_3 = \bar{\sigma}_{vo})$

$$(\varphi_{diff})_I = 3D_R\left\{10 - \ln\left[\left(\frac{2+\tan^2(45+\varphi_I/2)}{3}\right)\frac{\bar{\sigma}_{vo}}{p}\right]\right\} - 1 \tag{4-5}$$

2. Assume a value for the deviatoric stress (σ_d) of the fourth circle (Fig. 4-2). As a result,

$$q = \frac{\sigma_d}{0.6} \tag{4-6}$$

$$(\bar{\sigma}_3)_{IV} = \bar{\sigma}_{vo} + q - \sigma_d = \bar{\sigma}_{vo} + 0.4q \tag{4-7}$$

3. Assume a reduction (Δφ = 3 or 4 degrees) in the sand friction angle at $(\bar{\sigma}_3 = \bar{\sigma}_{vo})$ due to the increase in the confining pressure from $\bar{\sigma}_{vo}$ to $(\bar{\sigma}_3)_{IV}$, as seen in Fig. 4-4. Therefore,

$$\varphi_{IV} = \varphi_I - \Delta\varphi \tag{4-8}$$

4. As presented by Elfass (2001) and shown in Fig. 4-4, φ changes in a linear pattern with the logarithmic increase of $\bar{\sigma}_3$. The friction angle φ_{IV} associated with the confining pressure $(\bar{\sigma}_3)_{IV}$ can be calculated as

$$\varphi_{IV} = \varphi_I - \Delta\varphi \log \frac{(\bar{\sigma}_3)_{IV}}{\bar{\sigma}_{vo}} \tag{4-9}$$

5. According to the computed friction angle (φ_{IV}), use Eqn. 4-4 to evaluate $(\varphi_{diff})_{IV}$.

$$(\varphi_{diff})_{VI} = 3D_R \left\{10 - \ln\left[\left(\frac{2 + \tan^2(45 + \varphi_{IV}/2)}{3}\right)(\bar{\sigma}_3)_{IV}\right]\right\} - 1 \tag{4-10}$$

6. Having the values of $(\varphi_{diff})_I$ and $(\varphi_{diff})_{IV}$, a revised value for Δφ can be obtained.

$$\Delta\varphi = (\varphi_{diff})_I - (\varphi_{diff})_{IV} \tag{4-11}$$

7. Compare the value of Δφ obtained in step 6 with the assumed Δφ in step3. If they are different, take the new value and repeat the steps 3 through 7 until the value of φ_{IV} converges and the difference in Δφ reached is within the targeted tolerance.

8. Using the calculated values of φ_I and φ_{IV}, the deviatoric stress at failure can be expressed as

$$\sigma_{df} = (\bar{\sigma}_3)_{IV}\left(\tan^2(45 + \varphi_{IV}/2) - 1\right) \tag{4-12}$$

9. The current stress level (SL) in soil (Zone 4 below pile tip) is evaluated as

$$SL = \frac{\tan^2(45 + \varphi_m/2) - 1}{\tan^2(45 + \varphi_{IV}/2) - 1} = \frac{\sigma_d}{\sigma_{df}} \quad ; \quad \sigma_d = SL\,\sigma_{df} \tag{4-13}$$

where

$$\varphi_m = \sin^{-1}\left(\frac{\sigma_d/2}{(\bar{\sigma}_3)_{IV} + \sigma_d/2}\right) \tag{4-14}$$

4.2.1 Pile Tip Settlement

As presented in Chapter 3 with clay soil, the pile tip displacement in sand can be determined based on the drained stress-strain relationship presented in Chapter 5 (Norris 1986 and Ashour et al. 1998). The soil strain (ε) below the pile tip is evaluated according to the following equations: Corresponding to a triaxial test at a given confining pressure ($\bar{\sigma}_3$) at a deviator stress (σ_d) and stress level (SL) as given by Eqns. 4-12 through 4-14.

$$\varepsilon = \frac{SL \; e^{3.707\, SL}}{\lambda} \; \varepsilon_{50} \tag{4-15}$$

The value 3.707 and λ represent the fitting parameters of the power function relationship, and ε_{50} symbolizes the soil strain at 50 percent stress level. λ is equal to 3.19 for SL less than 0.5 and λ decreases linearly with SL from 3.19 at 0.5 to 2.14 at SL equal to 0.8.

Equation 4-16 represents the final loading zone which extends from 80 percent to 100 percent stress level. The following equation is used to assess the strain (ε) in this range:

$$SL = \exp\left[\ln 0.2 + \frac{100\,\varepsilon}{(m\varepsilon + q)} \right] ; \qquad SL \geq 0.80 \tag{4-16}$$

where m=59.0 and q=95.4 ε_{50} are the required values of the fitting parameters.
The two relationships mentioned above are developed based on unpublished experimental results (Norris 1977).

For a constant Young's modulus (E) with depth, the strain or ε_1 profile has the same shape as the elastic ($\Delta\sigma_1$ - $\Delta\sigma_3$) variation or Schmertmann's I_z factor (Schmertmann 1970, Schmertmann et al. 1979 and Norris 1986). Taking ε_1 at depth B/2 below the shaft base (the peak of the I_z curve), the shaft base displacement (z_P) is a function of the area of the triangular variation (Fig. 3-9).

$$z_P = \varepsilon B \quad (4\text{-}17)$$

where B is the diameter of the pile point (shaft base). Dealing with different values for pile tip resistance (Eqn. 4-2), the associated deviatoric stress (Eqn. 4-1), stress level (Eqn. 4-13) and principal strain (ε) (Eqns. 4-15 and 4-16) can be used to assess base movement in order to construct the pile tip load-settlement ($Q_P - z_P$) curve.

4.2 LOAD TRANSFER ALONG THE PILE/SHAFT SIDE (VERTICAL SIDE SHEAR)

4.3.1 Method of Slices for Calculating the Shear Deformation and Vertical Displacement in Cohesionless Soil

The methodology presented in this chapter is called the method of slices. The soil around the pile/shaft is modeled as soil horizontal slices that deform vertically as shown in Fig. 4-5. The shear stress/strain caused by the shaft settlement (z) at a particular depth gradually decreases along the radial distance (r) from the pile wall. As seen in Fig. 4-6, the shear stress (τ) and strain (γ) experience their largest values (τ_{max} and γ_{max}) just at the contact surface between the shaft and the adjacent sand. Due to the shear resistance of sand, the induced shear stress/ strain decreases to zero and large radial distance (r).

Randolph and Worth (1978) and Kraft et al. (1981) assume the shear stress decreases with distance such that $\tau\, r = \tau_o r_o$ in which τ_o is the shear stress (τ_{max}) at the pile wall (r_o); and τ is the shear stress angular ring at distance r. However, Randolph and Worth (1978) argued this assumption and indicated that the shear stress decreases rapidly with the distance r. Based on this assumption, Terzaghi (1943) showed a more decreasing parabolic pattern (similar to the one shown in Fig. 4-7) for the horizontal variation of the shear stress caused by the axially loaded sheet pile embedded in a homogenous mass of soil. Robinsky and Morrison (1964) performed experimental tests on model piles embedded in sand that exhibited the parabolic deflection pattern seen in Fig. 4-7. The following relationship describes the attenuation in the shear stress (τ) in soil with the distance r for such a parabolic pattern.

$$\frac{\tau}{\tau_o} = \frac{r_o^2}{r^2} \tag{4-18}$$

In order to understand the slice method, the stress-strain conditions of a small soil element at the contact surface with the pile shaft is analyzed. Figure 4-8 shows the induced shear stress on the soil-pile contact surface.

The lateral earth pressure coefficient (K) varies, with the radial distance, from 1 at the pile wall (due to pile installation) to $K = K_o = 1 - \sin \varphi$ in the free-field where the z-movement-induced shear stress (τ) reaches zero. Therefore, the horizontal effective stress at the pile wall after installation (prior to loading of the pile) just equals the vertical effective overburden, $\bar{\sigma}_{vo}$ (i.e. lateral earth pressure coefficient K = 1). It should be noted that τ_o represents the τ_{max} induced at the pile wall. Accordingly, a Mohr circle with a center at $\bar{\sigma}_{vo}$ and a diameter of $2\tau_o$ ($\tau_{max} = \tau_o$) develops at $r = r_o$, as shown in Fig. 4-8. With radial distance from the pile, the horizontal normal stress (σ_h) and the deviator stress (σ_d) continue to drop from $\bar{\sigma}_{vo}$ and $2\tau_{max}$ at r_o to $\bar{\sigma}_{vo}(1-\sin\phi)$ and $\bar{\sigma}_{vo}(1-K_o)$ or $\bar{\sigma}_{vo} \sin\phi$ in the far-field (where τ due to z is 0). The corresponding shear strain ($\gamma = \gamma_{max}$) causes a major normal strain ε_1,

$$\varepsilon_1 = (1 + \nu)\,\gamma \tag{4-19}$$

In addition, the shear modulus (G) is related to the Young's modulus (E) at the given effective confining pressure ($\bar{\sigma}_3$) and normal strain (ε_1), i.e.

$$G = \frac{E}{2(1+\nu)} \tag{4-20}$$

The method of slices described in Fig. 4-10, is based on the shear stress variation concepts presented above. The proposed method of slices provides the radius of the soil ring (radial distance, r) over which the induced shear stress diminishes, as shown in Fig. 4-7.

As shown in Fig. 4-11 for soil ring 1, the horizontal stress (σ_h) on the soil-pile interface (inner surface of the first soil slice) is equal to $\overline{\sigma}_{vo}$. At the same time, the horizontal stress (σ_h) on the outer surface is expressed as

$$\sigma_h = \overline{\sigma}_{vo} - \Delta\tau \tag{4-21}$$

The horizontal (radial and tangential) equilibrium is based on the ring action for the whole ring of soil ($2\pi r$) around the pile. The vertical equilibrium is also conducted on a full ring of soil. The vertical equilibrium of the first soil ring (slice) adjacent to the pile wall is expressed by the following equations:

$$\sum F_y = 0 \tag{4-22}$$

$$R_B \cos\phi_B - R_T \cos\phi_T - \Delta T - W_1 = 0 \tag{4-23}$$

Therefore,

$$R_B \cos\phi_B - R_T \cos\phi_T - \Delta T - W_1 = 0 \tag{4-24}$$

and

$$W_1 = R_B \cos\phi_B - R_T \cos\phi_T - \Delta T \tag{4-25}$$

where ΔT represents the reduction in the vertical shear force along the radial width (Δr) of the horizontal soil ring.

The following steps explain the implementation of the method of slices:

1. Divide the pile length into a number of segments that are equal in length (H_s). Note that the effective stress ($\overline{\sigma}_{vo}$) (i.e. the initial confining stress) increases with depth for each pile segment.
2. Assume a shear stress developed at the soil-pile interface ($r = r_o$) equal to that at soil failure or τ_{ult}. It should be noted that there might be a slip condition (e.g. $\tau_{limit} = K\ \overline{\sigma}_{vo} \tan\delta$) at the soil pile interface that limits to a value τ_{limit} less than τ_{ult}.

3. Determine the developing confining pressure $\bar{\sigma}_3$ due to τ_{max} (Fig. 4-11)

$$\bar{\sigma}_3 = K_o \, \bar{\sigma}_{vo} = 1 - \sin \phi \qquad (4\text{-}26)$$

where φ the friction angle at failure.

4. Increase the radial distance (r) from r_o to r_1 by a small incremental amount (Δr). As a result, the vertical shear stress on the face of the slice at r_1 will drop to τ_1 as expressed in Eqn. 4-21.

5. The horizontal stress (σ_h) on the vertical face of the soil slice decreases with the attenuating shear stress (τ) as shown in Fig. 4-9 until it reaches the value of $\bar{\sigma}_3$ given in Eqn. 4-26. The Mohr circles shown in Fig. 4 describe the decrease in horizontal stress (σ_h) and the mobilized friction angle (φ_m) in association to the attenuation in the shear stress (τ) (and the vertical shear force, T, on a vertical unit length) acting on the vertical face of the soil ring, i.e.

$$\Delta T_1 = T_0 - T_1 = 2\pi \, (r_o \tau_o - r_1 \tau_1) \qquad (4\text{-}27)$$

$$R_T = \frac{\bar{\sigma}_{h1}}{\cos \phi_T} \pi \, (r_1^2 - r_o^2) \qquad (4\text{-}28)$$

$$R_B = \frac{\bar{\sigma}_{vo}}{\cos \phi_B} \pi \, (r_1^2 - r_o^2) \qquad (4\text{-}29)$$

It should be noted that $\bar{\sigma}_{vo}$ is the effective stress at the middle of the slice which is used as an average effective stress for the whole slice (i.e. with More circle). The angles φ_T and φ_B at the top and bottom of the first soil ring, respectively, are determined as follows,

$$\phi_B = \sin^{-1} \frac{\tau_o}{\bar{\sigma}_{vo}} \qquad (4\text{-}30)$$

$$\phi_T = \sin^{-1} \frac{\tau_1}{\bar{\sigma}_{vo} - \Delta\tau} \qquad \textit{where} \quad \Delta\tau = \tau_o - \tau_1 \qquad (4\text{-}31)$$

φ_B equals φ_T of the next slice (soil ring 2) where τ_1 and τ_2 are the vertical shear stresses at radii r_1 and r_2, respectively (Fig. 4-12).

6. Based on the induced shear stress (τ_o) on the inner face of the current soil ring (first ring) and its Mohr circle, calculate the associated shear strain (γ) that develop over the width (Δr) of the current soil ring. For each horizontal soil slice i (soil ring with a width Δr) and based on the induced shear stress (τ) as seen in Fig. 4-10, the normal strain and stress (ε and σ_d), and ν will be evaluated. Thereafter, determine the associating shear strain γ_i and vertical displacement z_i as follows,

$$\gamma_i = \frac{\varepsilon_i}{1+\nu} \tag{4-32}$$

where

$$\nu = 0.1 + 0.4\, SL_i$$

$$z_i = \gamma_i\, \Delta r_i \tag{4-33}$$

7. Repeat steps 1 through 6 for larger values of r (i.e. an additional soil ring) and calculate z_i for each soil slice (ring) until the induced vertical shear stress approaches zero at $r = r_f$.

8. Assess the total vertical displacement at the soil-pile contact ($\tau = \tau_{max}$ or τ_o) as follows,

$$z_f = \sum_{t=t_o}^{t=0} z_i \tag{4-34}$$

z_f represents the elastic vertical displacement at failure at the soil-pile contact that is needed to construct the Ramberg-Osgood model in the next sections.

It would be noticed that the soil ring is always in horizontal equilibrium. For example, the horizontal equilibrium for the first ring of soil can be expressed as

$$\sum F_x = 0$$

$$E_o + R_T \sin \phi_T - E_1 - R_B \sin \phi_B = 0 \tag{4-35}$$

where,

$$E_o = \bar{\sigma}_{vo} \, 2\pi r_o H_s \tag{4-37}$$

$$E_1 = \bar{\sigma}_v \, 2\pi r_1 H_s \tag{4-38}$$

$\bar{\sigma}_v$ varies from $\bar{\sigma}_{vo}$ at the sand-pile contact surface to $\bar{\sigma}_{vo}(1 - \sin\phi)$ at r_f where the induced shear stress (τ) = 0, as shown in Fig. 4-7.

4.3.2 Ramberg-Osgood Model for Sand

As presented in Chapter 3 with the clay soil, Ramberg-Osgood model represented by Eqn. 4-39 can be used to characterize the t-z curve.

$$\frac{z}{z_r} = \frac{\gamma}{\gamma_r} = \frac{\tau}{\tau_{ult}} \left[1 + \beta \left(\frac{\tau}{\tau_{ult}} \right)^{R-1} \right] \tag{4-39}$$

At $\tau/\tau_{ult} = 1$ then

$$\beta = \frac{\gamma_f}{\gamma_r} - 1 \tag{4-40}$$

At $\tau/\tau_{ult} = 0.5$ and $\gamma = \gamma_{50}$, then

$$R - 1 = \frac{\log \left(\dfrac{2\,\dfrac{\gamma_{50}}{\gamma_r} - 1}{\beta} \right)}{\log (0.5)} = \frac{\log \left(\dfrac{2\,\dfrac{\gamma_{50}}{\gamma_r} - 1}{\dfrac{\gamma_f}{\gamma_r} - 1} \right)}{\log (0.5)} \tag{4-41}$$

The initial shear modulus (G_i) at a very low SL and the shear modulus (G_{50}) at SL = 0.5 can be determined via their direct relationship with the normal stress-strain relationship and Poisson's ration (ν)

$$G_i = \frac{E_i}{2(1+\nu)} = \frac{E_i}{2.2} \qquad \nu \text{ for sand} = 0.1 \tag{4-42}$$

and

$$G_{50} = \frac{E_{50}}{2(1+\nu)} = \frac{E_{50}}{3} = \frac{\sigma_{df}/2}{3\varepsilon_{50}} \tag{4-43}$$

Therefore,

$$\gamma_r = \frac{\tau_{ult}}{G_i} = \frac{\sigma_{df}/2}{G_i} \tag{4-44}$$

The Poisson's ratio (ν) for sand varies 0.1 to 0.5 with the increasing values of SL as follows,

$$\nu = 0.1 + 0.4\,SL \tag{4-45}$$

The shear strain at failure (γ_f) is determined in terms of the normal strain at failure (ε_f).

$$\gamma_f = \frac{\varepsilon_f}{(1+\nu)} = \frac{\varepsilon_f}{1.5} \tag{4-46}$$

The normal stress-strain relationship of sand (σ_d - ε) is assessed based on the procedure presented in Chapter 5. The initial Young's modulus of clay (E_i) is determined at a very small value of the normal strain (ε) or stress level (SL). In the same fashion, ε_f is evaluated at SL = 1 or the normal strength σ_{df}. By knowing the values of γ_r, γ_{50} and γ_f, the constants β and R of the Ramberg-Osgood model shown in Eqn. 4-39 can be evaluated.

The Ramberg-Osgood model given in Eqn. 4-39 allows the assessment of the elastic vertical displacement that occurs at the soil-pile contact surface based on z_f obtained in Section 4-3-1. Equation 4-39 can be rewritten as follows,

$$\frac{z}{z_r} = \frac{\tau}{\tau_{ult}}\left[1 + \beta\left(\frac{\tau}{\tau_{ult}}\right)^{R-1}\right] \tag{4-47}$$

where,

$$\frac{z_r}{z_f} = \frac{g_r}{g_f} \qquad i.e. \qquad z_r = z_f \ \frac{g_r}{g_f} \tag{4-48}$$

4.3.3 Procedure Steps to Assess Load Transfer and Pile Settlement in Sand (t-z Curve)

The assessment of the load transfer and associated settlement of a pile embedded in sand requires the employment of t-z curve for that particular soil. The load transferred from pile shaft to the surrounding sand is a function of the diameter and the surface roughness of the pile skin and sand properties (effective unit weight, friction angle, relative density and confining pressure) in addition to the pile tip resistance. The development of a representative procedure allows the assessment of the t-z curve in soil (sand and/or clay) that leads to the prediction of a nonlinear load-settlement curve at the pile/shaft head. Such a relationship provides the mobilized pile-head settlement under axial load and vertical shear resistance.

A new procedure is developed in this chapter to assess pile/shaft skin resistance in sand in a mobilized fashion. The proposed procedure provides the deformation in sand around the pile in the radial zone affected by the pile movement (Fig. 4-1). At the same time, the horizontal degradation (attenuation) of the shear stress away from the pile is evaluated by the suggested analysis. As a result, the varying shear stress/strain, shear modulus and deformation in the radial distance away from the pile can be predicted based on reasonable assumptions.

The presented t-z curve is developed according to the induced displacement along the pile. The following steps present the procedure that is employed to assess the load transfer and pile movement in sand soil:

1. Based on the approach presented in Section 4-2 for the pile tip resistance, assume a small pile tip resistance, Q_P as given in Eqns (4-1 and 4-2)

2. Using the SL evaluated above and the stress-strain relationship presented in Eqns. 4-13 through 4-16, compute the induced axial (deviatoric) soil strain, ε_P and the shaft base displacement, $z_P = \varepsilon_P B$. B is the diameter of the shaft base.

3. Divide the pile length into segments equal in length (h_s). Take the load Q_B at the base of the bottom segment as (Q_P) and movement at its base (z_B) equal to (z_P). Estimate a midpoint movement for the bottom segment (segment 4 as seen in Fig. 4-13). For the first trial, the midpoint movement can be assumed equal to the shaft base movement.

4. Calculate the elastic axial deformation of the bottom half of this segment,

$$z_{elastic} = \frac{Q_B h_s / 2}{E A_{base}} \tag{4-49}$$

The total movement of the midpoint in the bottom segment (segment 4) is equal to

$$z = z_T + z_{elastic} \tag{4-50}$$

5. Based on the soil properties of the surrounding sand, use a Ramberg-Osgood formula to characterize the backbone response (Richart 1975).

$$\frac{z}{z_r} = \frac{\gamma}{\gamma_r} = \frac{\tau}{\tau_{ult}} \left[1 + \beta \left(\frac{\tau}{\tau_{ult}} \right)^{R-1} \right] \tag{4-51}$$

z = total midpoint movement of a pile/shaft segment

γ = average shear strain in soil adjacent to the shaft segment

τ = average shear stress in soil adjacent to the shaft segment

γ_r is the reference strain, as shown in Fig. 3-4, and given by Eqn. 4-44

z_r = shaft segment movement associated to γ_r

ε_{50} = axial strain at SL = 0.5. ε_{50} can be obtained from the chart provided in Chapter 5.

β and R-1 are the fitting parameters of the Ramberg-Osgood model given in Eqn. 4-52. These parameters are evaluated in section 4.2.1.

6. Using Eqn. 4-51 which is rewritten in the form of Eqn. 4-52, the average shear stress level (SL_t) in sand around the shaft segment can be obtained iteratively based on movement z evaluated in Eqn. 4-50.

$$\frac{z}{z_r} = \frac{g}{g_r} = SL_t \left[1 + b\left(SL_t\right)^{R-1}\right] \qquad \text{(Solved for } SL_t\text{)} \qquad (4\text{-}52)$$

7. Shear stress at soil-shaft contact surface is then calculated, i.e.

$$\tau = SL\ \sigma_{df}/2 \qquad (4\text{-}53)$$

8. The axial load carried by the shaft segment in skin friction / adhesion (Q_s) is expressed as

$$Q_s = \pi\ B\ h_s\ \tau \qquad (4\text{-}54)$$

9. Calculate the total axial load (Q_i) carried at the top of the bottom segment (i = 4).

$$Q_i = Q_s + Q_B \qquad (4\text{-}55)$$

10. Determine the elastic deformation in the bottom half of the bottom segment assuming a linear variation of the load distribution along the segment.

$$Q_{mid} = (Q_i + Q_B) / 2 \qquad (4\text{-}56)$$

$$z_{elastic} = \left(\frac{Q_{mid} + Q_B}{2}\ h_s\right) / EA = \frac{(Q_i + 3\,Q_B)\,h_s}{8EA} \qquad (4\text{-}57)$$

11. Compute the new midpoint movement of the bottom segment.

$$z = z_P + z_{elastic} \quad (4\text{-}58)$$

12. Compare the z value calculated from step 11 with the previously evaluated estimated movement of the midpoint from step 4 and check the tolerance.

14. Repeat steps 4 through 12 using the new values of z and Q_{mid} until convergence is achieved

15. Calculate the movement at the top of the segment i= 4 as

$$z_i = z_B + \frac{Q_i + Q_B}{2} \frac{h_s}{AE}$$

16. The load at the base (Q_B) of segment i = 3 is taken equal to Q_4 (i.e. Q_{i+1}) while z_B of segment 3 is taken equal to z_4 and steps 4-13 are repeated until convergence for segment 3 is obtained. This procedure is repeated for successive segments going up until reaching the top of the pile where pile head load Q is Q_1 and pile top movement δ is z_1. Based on presented procedure, a set of pile-head load-settlement coordinate values (Q - δ) can be obtained on coordinate pair for each assumed value of Q_T. As a result the load transferred to the soil along the length of the pile can be calculated for any load increment.

17. Knowing the shear stress (τ) and the associated displacement at each depth (i.e. the midpoint of the pile segment), points on the t-z curve can be assessed at each new load.

4.4 PROCEDURE VALIDATION

As reported by Vesic (1970), an 18-inch diameter steel pipe pile with 0.5-inch-thick walls was driven and tested in five stages. The bottom section has a 2-in thick flat steel plate at the base of the pile. Tests with this pile were performed at driving depths of 10, 20, 30, 40 and 50 ft. Figure, 4-14 shows the results of the standard penetration tests (SPT) at different locations at the test site. Figure 4-15 the particle size distribution curves of two different types of sands. The

fine sand curves in this figure refer to the material found mostly at the top 5 ft of the soil profile. It should be noted that the frictions angles shown in Table 4-1 is a little bit relatively high compared to the associated $(N_1)_{60}$.

Table 4-1 – Suggested Soil Data for Current Soil Profile

Soil layer #	Soil type	Thickness (ft)	γ (pcf)	$(N_1)_{60}$	ϕ (deg.)	ε_{50}**
1	Sand	10	110	9	30	0.009
2	Sand	10	60	15	32	0.007
3	Sand	10	60	19	35	.006
4	Sand	10	66	24	39	.004
5	Sand	10	66	32	42	0.003

Figure 4-16 exhibits a comparison between the measured and computed data at the depths 20, 40 and 50 ft below ground. Good agreement between the measured and computed axial pile load can be seen in Fig. 4-16.

4.5 SUMMARY

This Chapter presents a procedure that allows the assessment of the t-z and load-settlement curves for a pile in sand. The methodology employed is based on the elastic theory, stress-strain relationship, and the method of slices for the vertical equilibrium. The results obtained incorporate the pile tip and side resistance in a mobilized fashion. The results obtained in comparison with the field data show the capability of the suggested technique. The findings of this chapter will be employed in Chapter 5 to evaluate the vertical side shear resistance induced by the lateral deflection of a large diameter shaft and its contribution to the lateral resistance of the shaft.

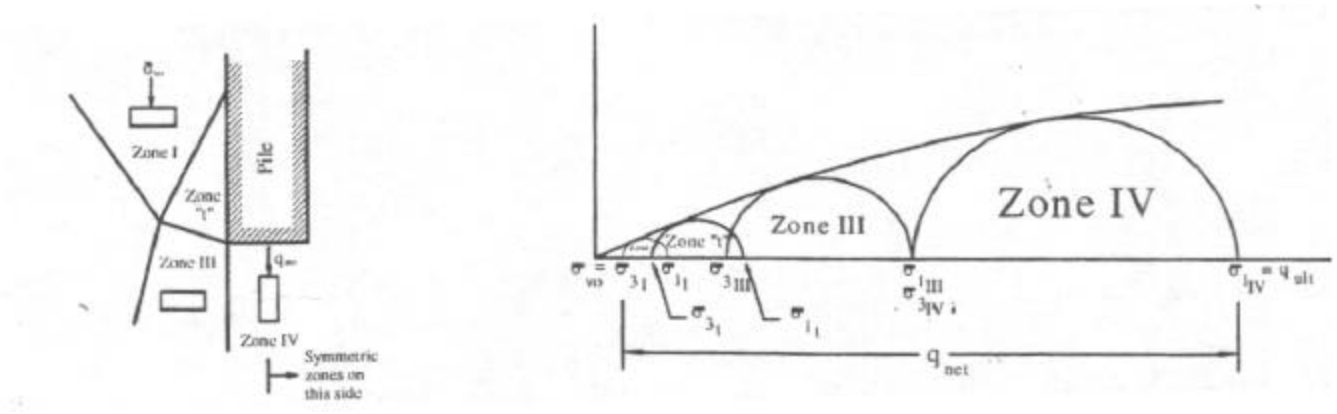

Fig. 4-1 Failure Mechanism of Sand Around Pile Tip (Elfass, 2001)

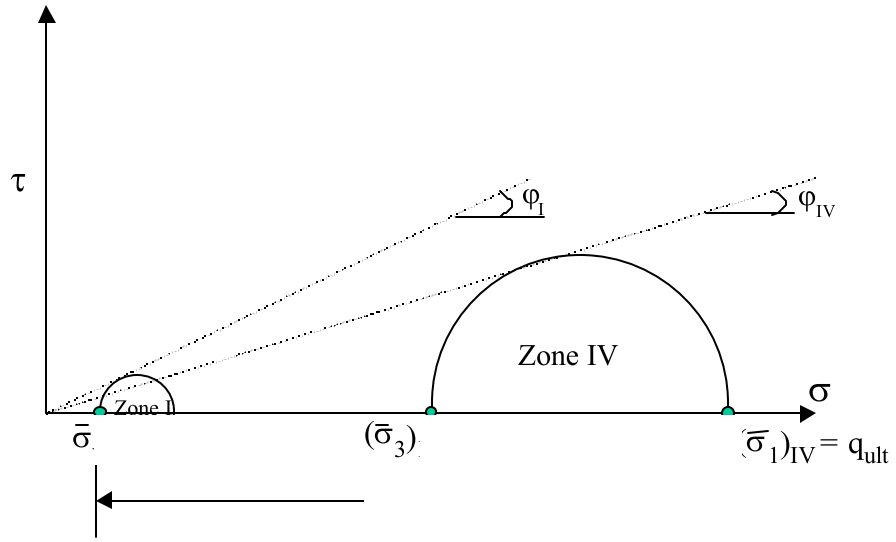

Fig. 4-2 Relationship Between Bearing Capacity (q_{net}) of Pile Tip in Sand and the Deviatoric Stress (σ_d) (after Elfass, 2001)

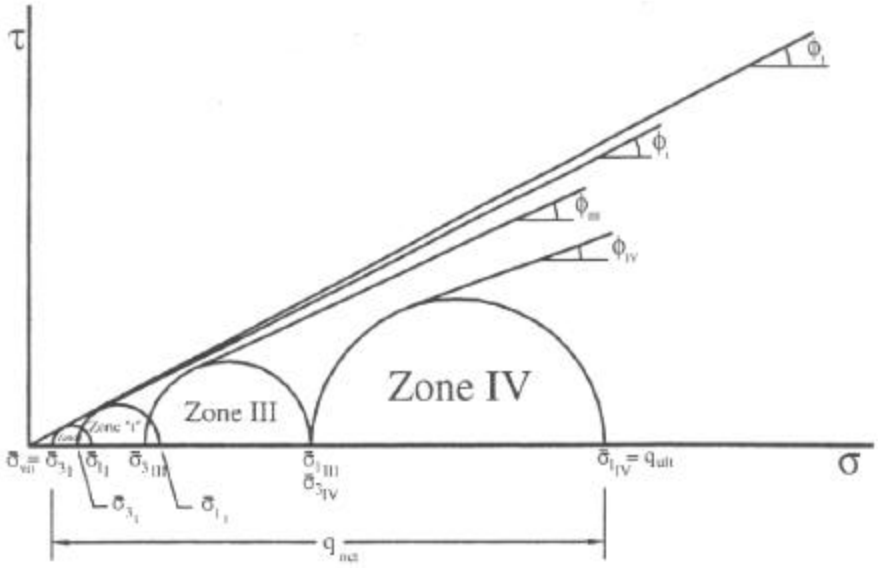

Fig. 4-3 Degradation in the Secant Friction Angles of Circles Tangent to a Curvilinear Envelope of Sand Due to the Increase in the Confining Pressure (Elfass, 2001)

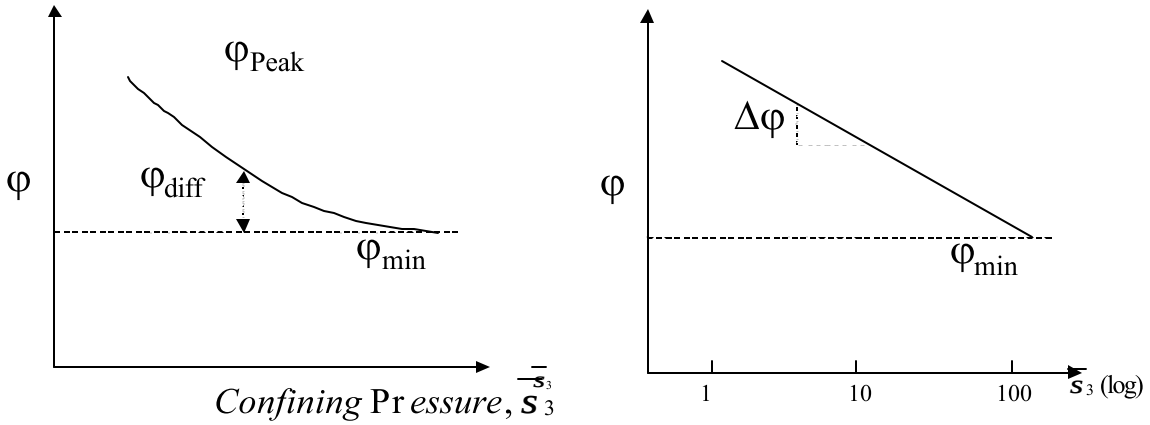

Fig. 4-4 Changes of Friction Angle (φ) with the Confining Pressure

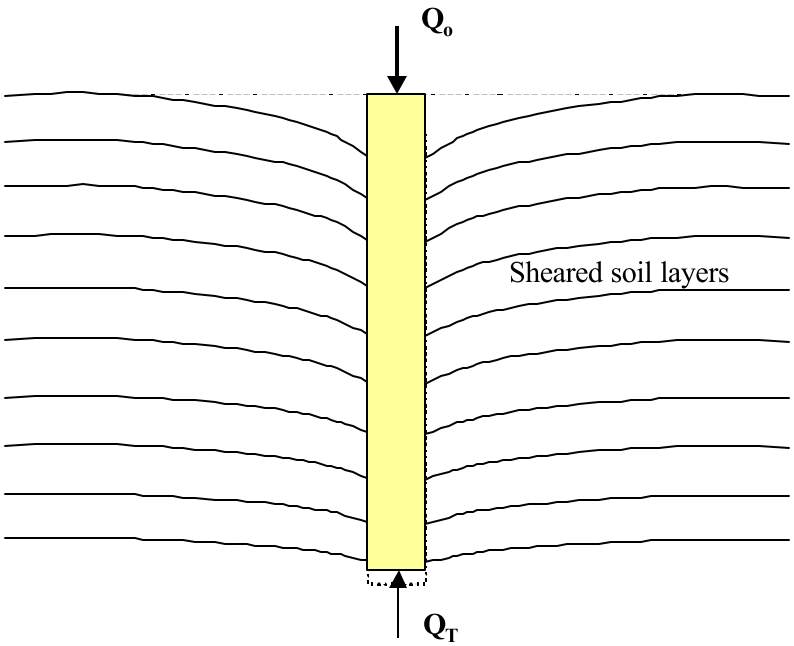

Fig. 4-5 Soil Deformation in the Vicinity of Axially Loaded Pile.

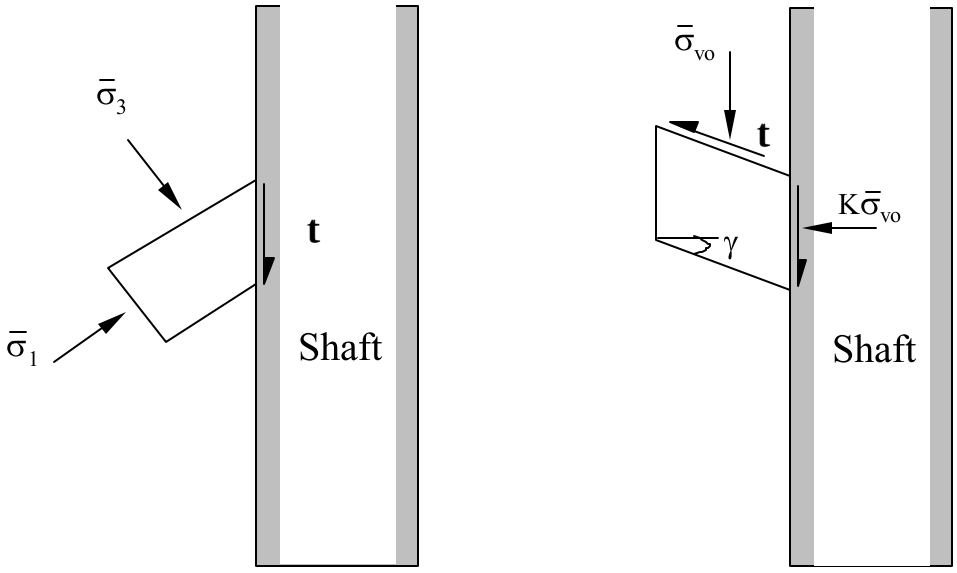

Fig. 4-6 Shear Stress/Strain at Soil-Pile Interface.

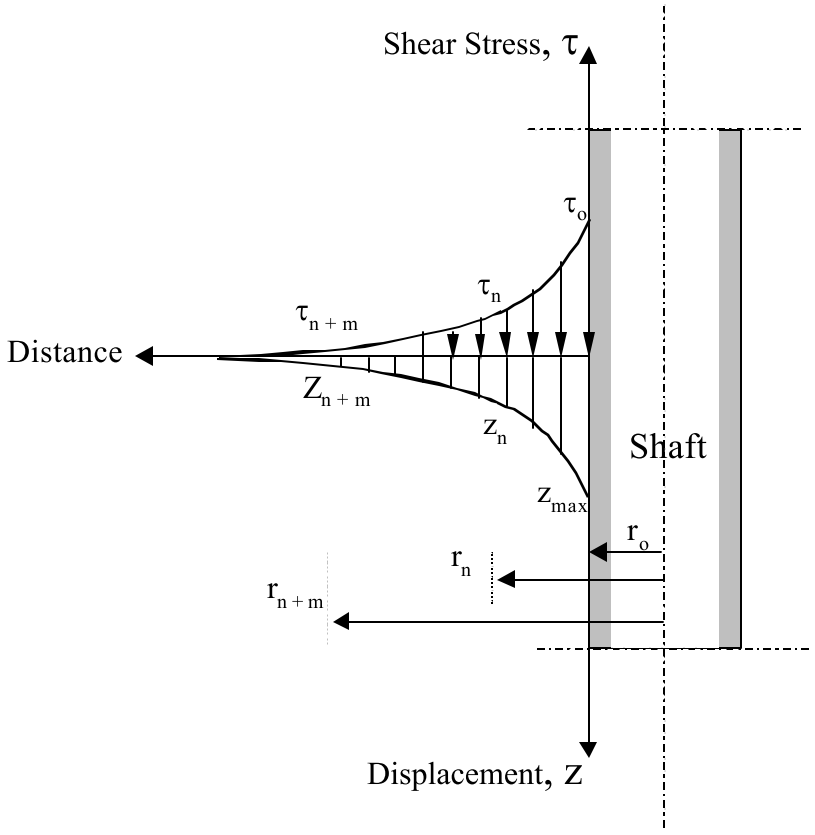

Fig. 4-7 Shear and Displacement Attenuation with the Radial Distance from the Pile Wall.

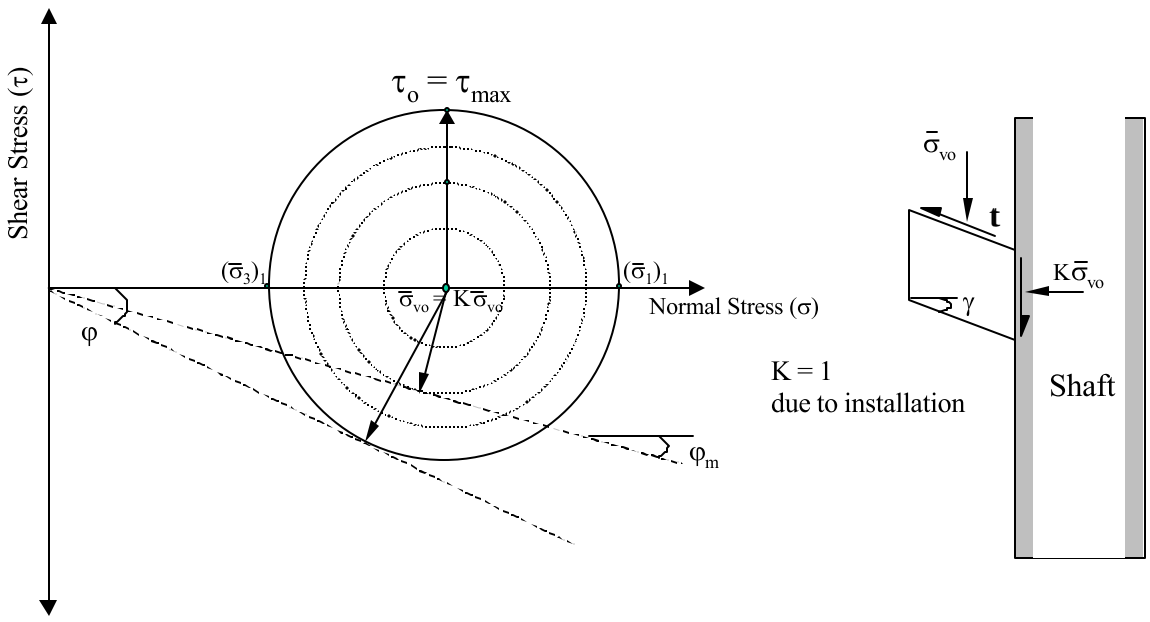

Fig. 4-8 Growth of Shear Stress at the Soil-Pile Contact Surface (Pile Wall) Due to Pile Movement

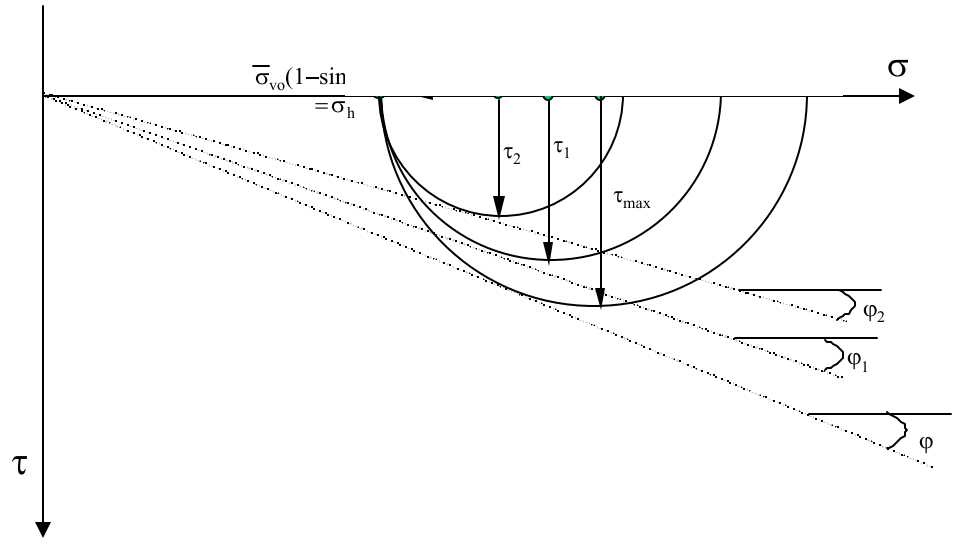

Fig. 4-9 Mohr Circles that Represent the Radial Attenuation of Shear and Normal Stresses For a Given Displacement z at the Pile Wall

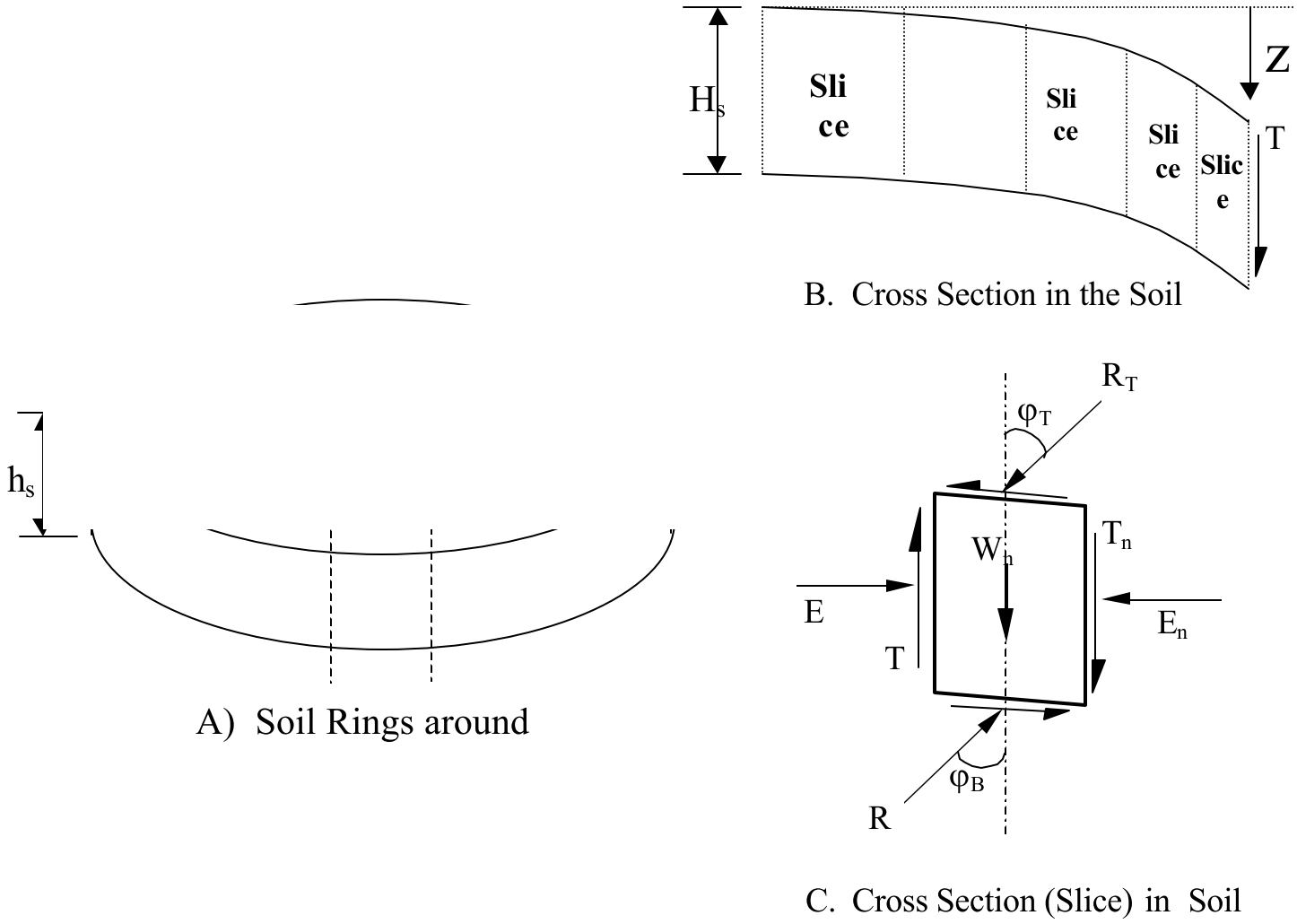

Fig. 4-10 Soil Rings Around the Pile and the Applying forces on Each Soil Ring (Slice)

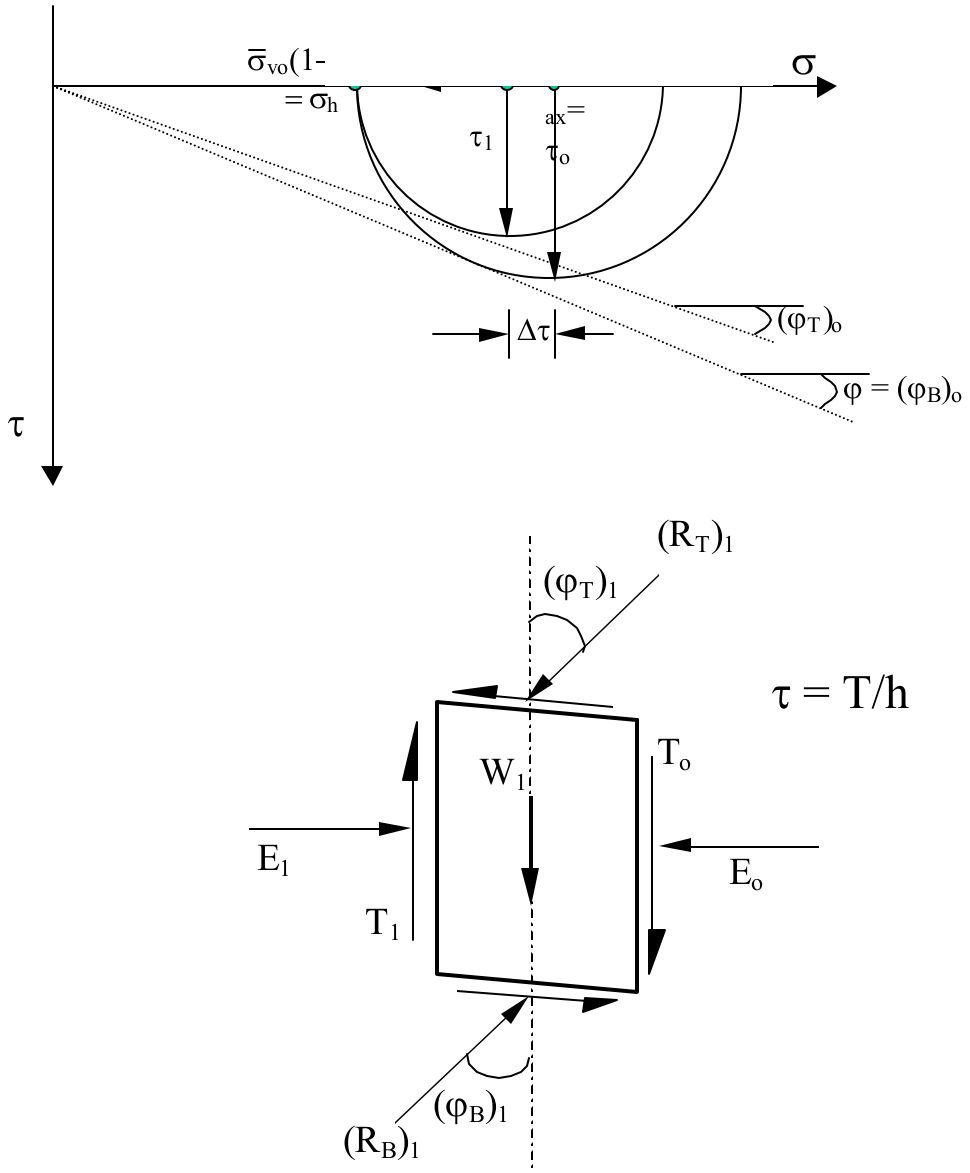

Fig. 4-11 Forces and Stresses Applied on the Soil Ring (Slice) Number 1

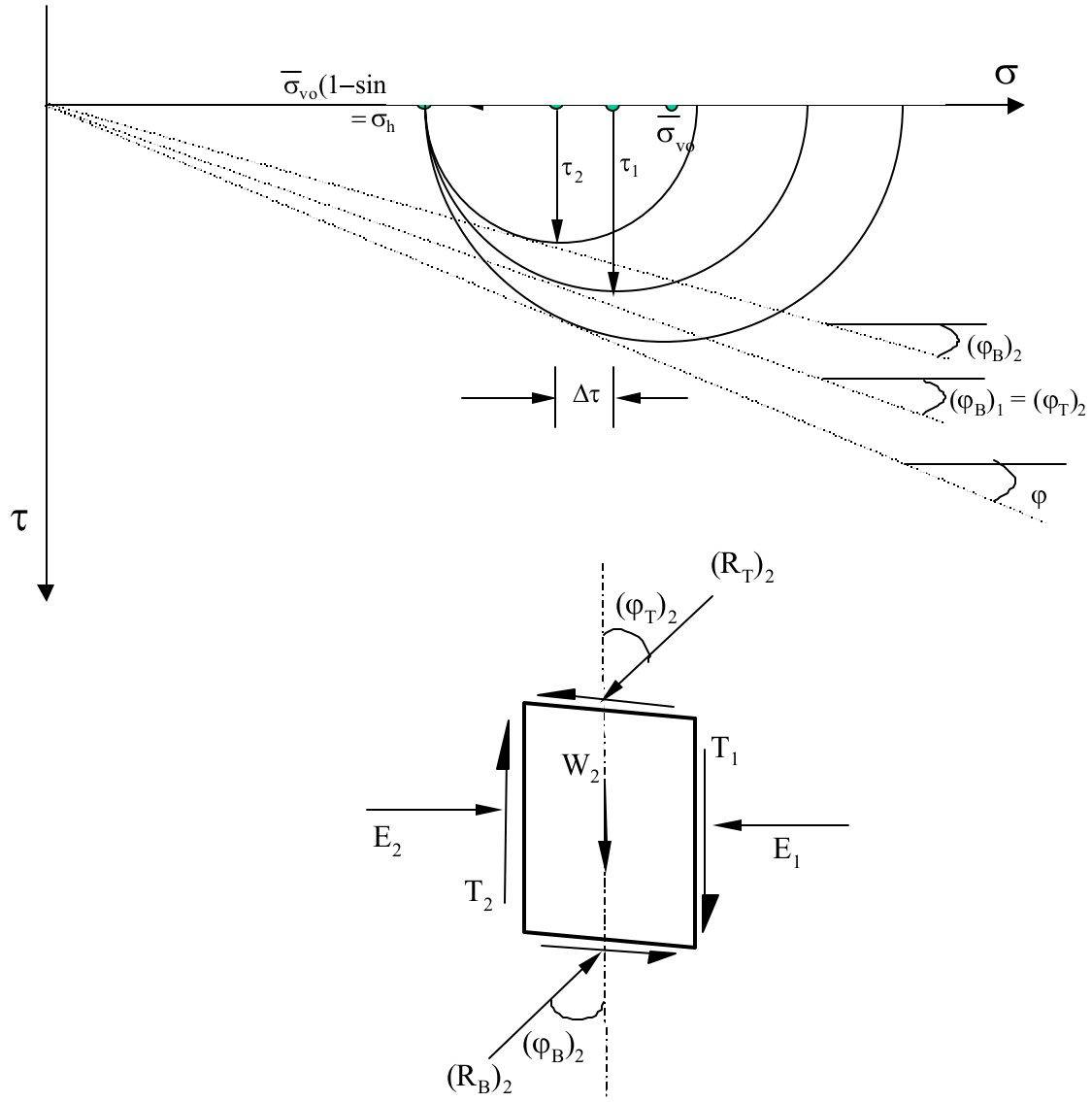

Fig. 4-12 Forces and Stresses Applied on the Soil Ring (Slice) Number 2

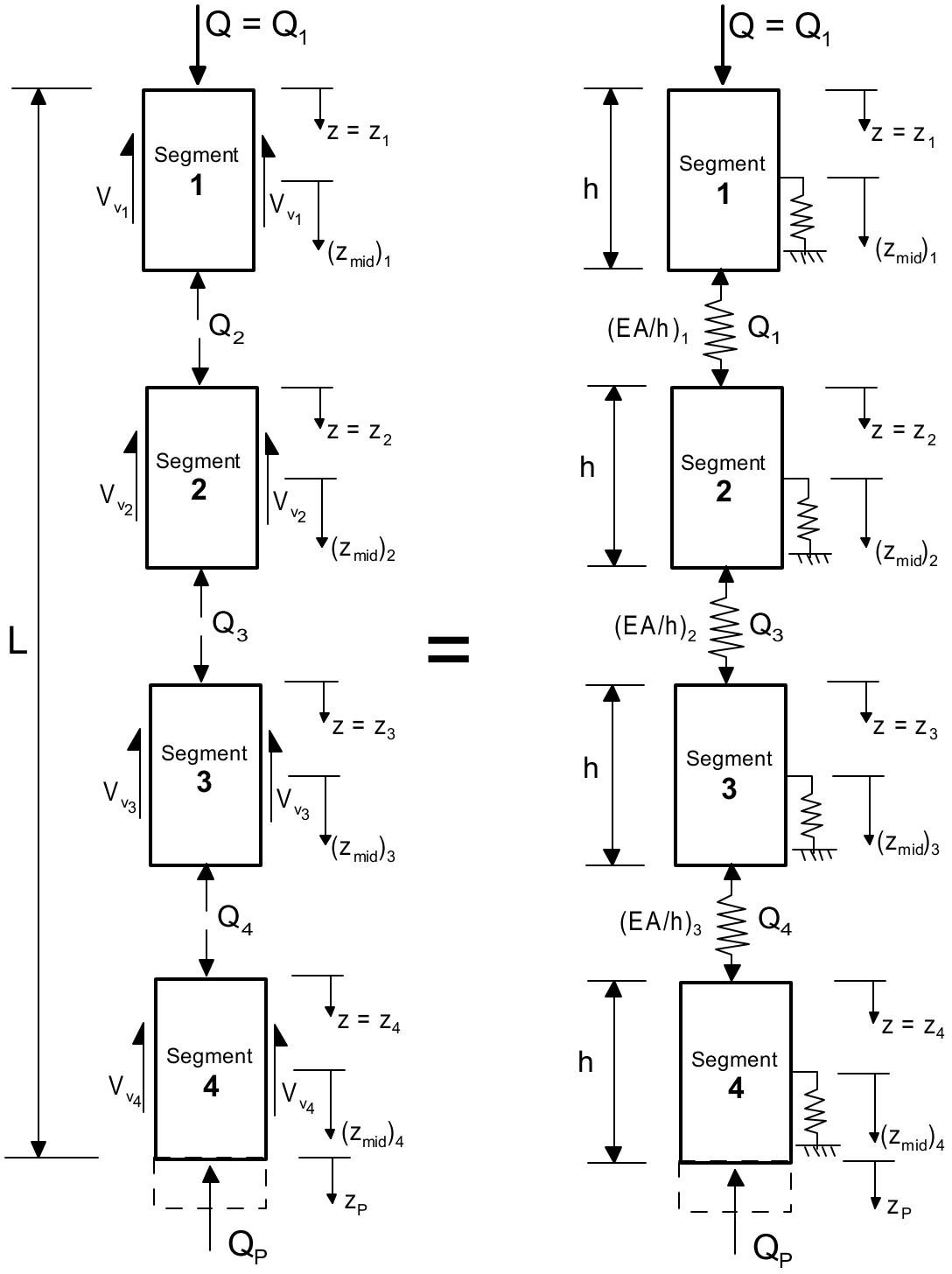

Fig. 4-13 Modeling Axially Loaded Pile Divided into Segments

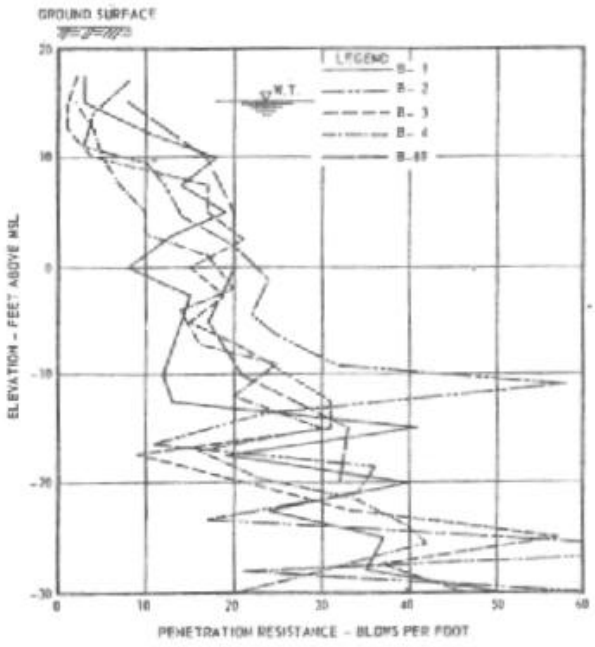

Fig. 4-14 Results of the Standard Penetration Tests (SPT) at Different Locations (Vesic, 1970)

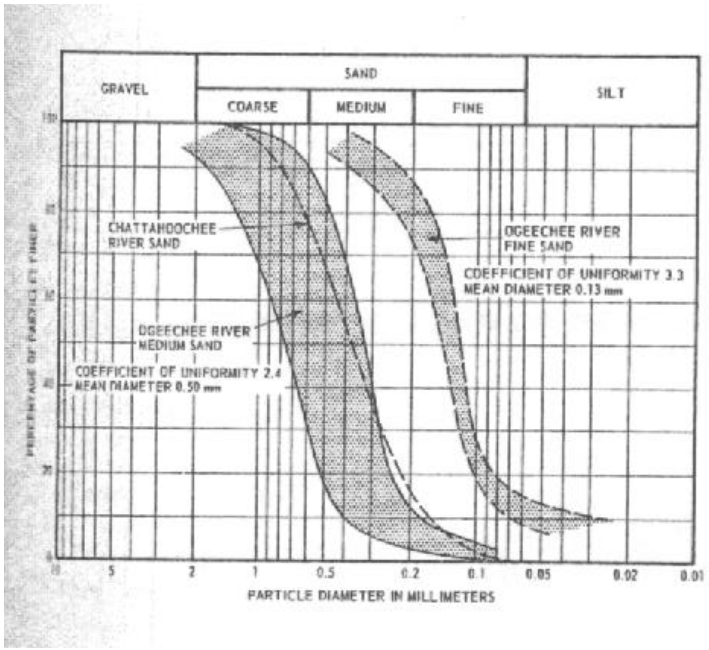

Fig. 4-15 Particle Size Distribution of Sands at Test Site

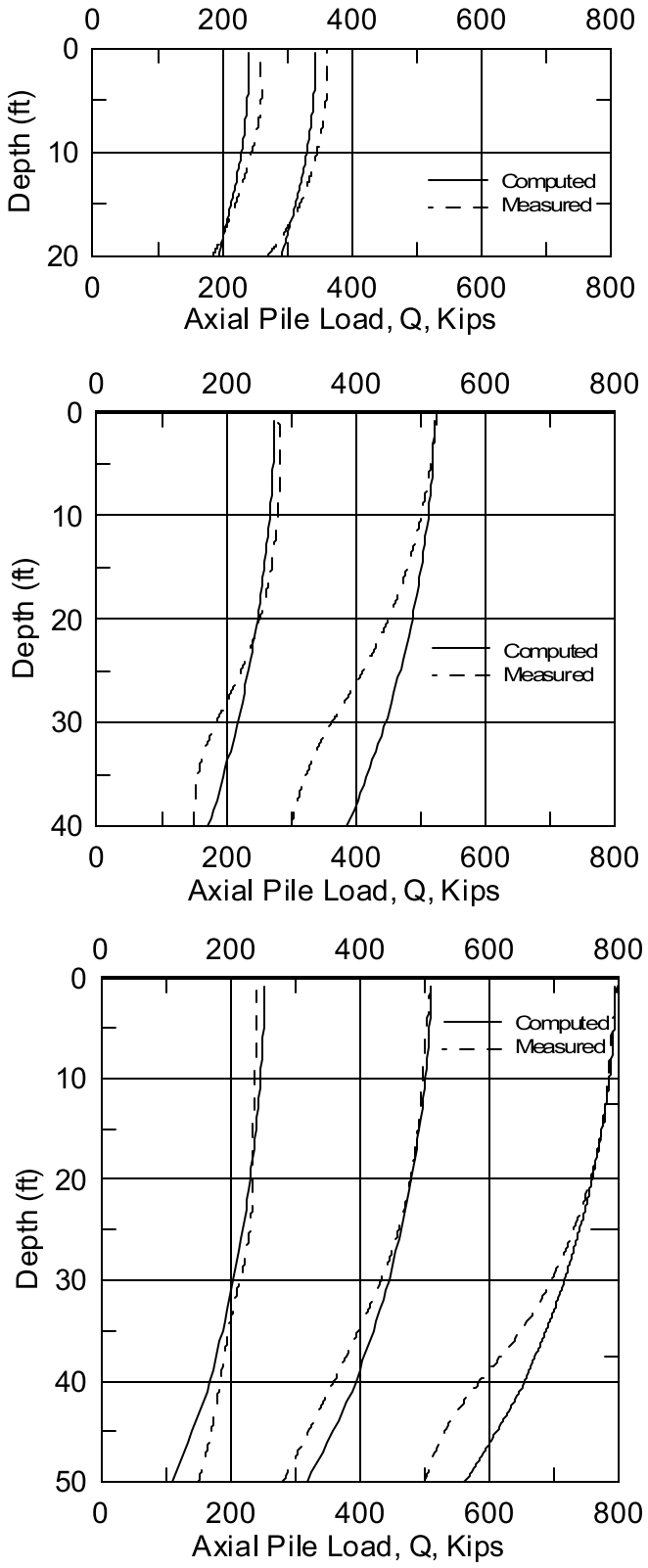

Fig. 4-16 A Comparison Between Measured and Computed Axial Pile Load at Different Depths (After Vesic, 1970)

CHAPTER 5

LATERAL LOADING OF A SHAFT IN LAYERED SOIL USING THE STRAIN WEDGE MODEL

5.1 INTRODUCTION

The strain wedge (SW) model is an approach that has been developed to predict the response of a flexible pile under lateral loading (Norris 1986, Ashour et al. 1996 and Ashour et al. 1998). The main concept associated with the SW model is that traditional one-dimensional Beam on Elastic Foundation (BEF) pile response parameters can be characterized in terms of three-dimensional soil-pile interaction behavior. The SW model was initially established to analyze a free-head pile embedded in one type of uniform soil (sand or clay). However, the SW model has been improved and modified through additional research to accommodate a laterally loaded pile embedded in multiple soil layers (sand and clay). The SW model has been further modified to include the effect of pile head conditions on soil-pile behavior. The main objective behind the development of the SW model is to solve the BEF problem of a laterally loaded pile based on the envisioned soil-pile interaction and its dependence on both soil and pile properties.

The problem of a laterally loaded pile in layered soil has been solved by Reese (1977) as a BEF based on modeling the soil response by p-y curves. However, as mentioned by Reese (1983), the nonlinear p-y curve employed does not account for soil continuity and pile properties such as pile stiffness, pile cross-section shape and pile head conditions.

The SW model was initially developed to assess the response of a laterally loaded long (slender) pile (diameter < 3 ft). As a result, the effect of the vertical side shear (Vv) along the side of a large diameter shaft should be integrated in the SW model analysis to account for such a significant parameter in the analysis of large diameter shafts (Fig. 5-1). In addition, the characterization of the intermediate and short shafts should be incorporated in the SW model analysis to cover broader aspects of the shaft/pile analysis.

5.2 THE THEORETICAL BASIS OF STRAIN WEDGE MODEL CHARACTERIZATION

The SW model parameters are related to an envisioned three-dimensional passive wedge of soil developing in front of the pile. The basic purpose of the SW model is to relate stress-strain-strength behavior of the soil in the wedge to one-dimensional BEF parameters. The SW model is, therefore, able to provide a theoretical link between the more complex three-dimensional soil-pile interaction and the simpler one-dimensional BEF characterization. The previously noted correlation between the SW model response and BEF characterization reflects the following interdependence:

- the horizontal soil strain (ε) in the developing passive wedge in front of the pile to the deflection pattern (y versus depth, x) of the pile;
- the horizontal soil stress change ($\Delta\sigma_h$) in the developing passive wedge to the soil-pile reaction (p) associated with BEF behavior; and
- the nonlinear variation in the Young's modulus ($E = \Delta\sigma_h/\varepsilon$) of the soil to the nonlinear variation in the modulus of soil subgrade reaction ($E_s = p/y$) associated with BEF characterization.

The analytical relations presented above reflect soil-pile interaction response characterized by the SW model that will be illustrated later. The reason for linking the SW model to BEF analysis is to allow the appropriate selection of BEF parameters to solve the following fourth-order ordinary differential equation to proceed.

$$EI\left(\frac{d^4 y}{d^4 x}\right)+ E_s(x)\, y + P_x\left(\frac{d^2 y}{d^2 x}\right)+ \left(\frac{d^2 M_R}{d^2 x}\right)=0 \qquad (5\text{-}1)$$

where M_R is the resisting bending moment per unit length induced along the shaft length (x) due to the vertical side shear (V_V) (Fig. 5-1). The closed form solution of the basic form of the above equation has been obtained by Matlock and Reese (1961) for the case of uniform soil. In order to appreciate the SW model's enhancement of BEF analysis, one should first consider the governing analytical formulations related to the passive wedge in front of the shaft, the soil's

stress-strain and the vertical side shear (t-z curve) formulations, and the related soil-pile interaction.

5.3 SOIL PASSIVE WEDGE CONFIGURATION

The SW model represents the mobilized passive wedge in front of the pile which is characterized by base angles, φ_m and β_m, the current passive wedge depth h, and the spread of the wedge fan angle, φ_m (the mobilized friction angle of soil). The horizontal stress change at the passive wedge face, $\Delta\sigma_h$, and side shear, τ, act as shown in Fig. 5-2. One of the main assumptions associated with the SW model is that the deflection pattern of the pile is taken to be linear over the controlling depth of the soil near the pile top resulting in a linearized deflection angle, δ, as seen in Fig. 5-3.

The SW model makes the analysis simpler because forces (F_1) on the opposite faces cancel, but the real zone of stress is like the dashed outline shown in Fig. 5-4b which includes side shear influence (ô) on the shape of the strained zone. However, the ô perpendicular to the face of the pile is still considered in the SW model analysis. As seen in Fig. 5-4c, the horizontal equilibrium in the SW wedge model is based on the concepts of the conventional triaxial test. The soil at the face of the passive wedge is represented by a soil sample in the conventional triaxial test where $\overline{s}_{vo}$ (i.e. K = 1) and the horizontal stress change, Äó$_h$, (from pile loading) are the confining and deviatoric stresses in the triaxial test, respectively.

The relationship between the actual (closed form solution) and linearized deflection patterns of long pile/shaft has been established by Norris (1986) (h/X_o = 0.69). As seen in 5-5, the relationship (h/X_o) between the actual and linearized deflection for the short shaft is equal to 1, and varies for the intermediate shafts from 0.69 at (L/T = 4) to 1 at (L/T = 2). As presented in Chapter 2, L is the embedded length of the shaft and T is the initial relative shaft stiffness.

It should be noted that the idea of the change in the full passive wedge (mobilized passive wedge at different levels of deflection) employed in the SW model has been shown experimentally by Hughes and Goldsmith (1978) and previously established by Rowe (1956).

Changes in the shape and depth of the upper passive wedge, along with changes in the state of loading and shaft/pile deflection, occur with change in the uniform strain (ε) in the developing passive wedge. As seen in Fig. 5-6, two mobilized (tip to tip) passive wedges are developed in soil in front of the short shaft. Because of the shaft straight-line deflection pattern with a deflection angle δ, the uniform soil strain (ε) will be the same in both (i.e. upper and lower) passive wedges.

As shown in Figs. 5-5 and 5-6, the deflection pattern is no longer a straight line for the intermediate shaft, and the lower passive wedge has a curved shape that is similar to the deflection pattern. Accordingly, the soil strain (ε_x) at depth x below the zero crossing will not be uniform and will be evaluated in an iterative method based on the associated deflection at that depth (Fig. 5-6c)

The lateral response of the short shaft is governed by both (upper and lower) developed passive wedges (Fig. 5-6). However, with the intermediate shaft, less soil strain (i.e. stress on soil) develops in the lower passive soil wedge (the inverted wedge below the point of zero crossing) compared to the upper one (Fig. 5-6). The non-uniform soil strain (ε_x) in the lower passive soil wedge (Fig. 5-6c) becomes much smaller compared to the strain in the upper soil wedge when the shaft deflection approaches the deflection pattern of the long shaft. Since the lateral deflection of the long pile/shaft below the zero crossing is always very small, the associated soil strain and developing passive wedge will be very small as well. Consequently, the developing upper passive soil wedge (and uniform strain therein) dominates the lateral response of the long pile/shaft; hence the adopted name “strain wedge” (SW).

As seen in Figs. 5-3 and 5-6, the configuration of the wedge at any instant of load and, therefore,base angle

$$\Theta_m = 45 - \frac{j_m}{2} \qquad (5\text{-}2)$$

mobilized friction angle, φ_m, and wedge depth, h, is given by the following equation:
or its complement

$$\beta_m = 45 + \frac{\phi_m}{2} \tag{5-3}$$

The width, $\overline{BC}$, of the wedge face at any depth is

$$\overline{BC} = D + (h - x)\, 2 \tan \beta_m \tan \phi_m \tag{5-4}$$

where x denotes the depth below the top of the studied passive wedge, and D symbolizes the width of the pile cross-section. It should be noted that the SW model is based upon an effective stress analysis of both sand and clay soils. As a result, the mobilized fanning angle, φ_m, is not zero in clay soil as assumed by Reese (1958, 1983).

The above equations are applied to the upper and lower passive wedges in the case of short and intermediate shafts where x for any point on the lower passive wedge (Fig. 5-6c) is measured downward from the zero crossing and replaces the term (h - x) in Eqn. 5-4. Therefore,

$$\varepsilon_x = \varepsilon\,(y_x / x) / \delta \quad = \quad \varepsilon\,(\frac{\delta_x}{\delta}) \tag{5-5}$$

where ε and δ are the uniform soil strain and linearized shaft deflection angle of the upper passive wedge, respectively. y_x and δ_x are the shaft deflection and secant deflection angle at depth x below the zero crossing (Fig. 5-6c).

5.4 STRAIN WEDGE MODEL IN LAYERED SOIL

The SW model can handle the problem of multiple soil layers of different types. The approach employed, which is called the multi-sublayer technique, is based upon dividing the soil profile and the loaded pile into sublayers and segments of constant thickness, respectively, as shown in Fig. 5-7. Each sublayer of soil is considered to behave as a uniform soil and have its own properties according to the sublayer location and soil type. In addition, the multi-sublayer technique depends on the deflection pattern of the embedded pile being continuous regardless of the variation of soil types. However, the depth, h, of the deflected portion of the pile is controlled by the stability analysis of the pile under the conditions of soil-pile interaction. The effects of the soil and pile properties are associated with the soil reaction along the pile by the

Young's modulus of the soil, the stress level in the soil, the pile deflection, and the modulus of subgrade reaction between the pile segment and each soil sublayer. To account for the interaction between the soil and the pile, the deflected part of the pile is considered to respond as a continuous beam loaded with different short segments of uniform load and supported by nonlinear elastic supports along soil sublayers, as shown in Fig. 5-8. At the same time, the point of zero deflection (X_o in Fig. 5-5) for a pile in a particular layered soil varies according to the applied load and the soil strain level.

The SW model in layered soil provides a means for distinguishing layers of different soil types as well as sublayers within each layer where conditions (ε_{50}, SL, φ_m) vary even though the soil and its properties ($\bar{\gamma}$, e or D_r, φ , etc.) remain the same. As shown in Fig. 5-9 , there may be different soil layers and a transition in wedge shape from one layer to the next, with all components of the compound wedge having in common the same depth h. In fact, there may be a continuous change over a given sublayer; but the values of stress level (SL) and mobilized friction angle (φ_m) at the middle of each sublayer of height, H_i, are treated as the values for the entire sublayer.

As shown in Fig. 5-9, the geometry of the compound passive wedge depends on the properties and the number of soil types in the soil profile, and the global equilibrium between the soil layers and the loaded pile. An iterative process is performed to satisfy the equilibrium between the mobilized geometry of the passive wedge of the layered soil and the deflected pattern of the pile for any level of loading.

While the shape of the wedge in any soil layer depends upon the properties of that layer and, therefore, satisfies the nature of a Winkler foundation of independent “soil” springs in BEF analysis, realize that there is forced interdependence given that all components of the compound wedge have the same depth (h) in common. Therefore, the mobilized depth (h) of the compound wedge at any time is a function of the various soils (and their stress levels), the bending stiffness (EI), and head fixity conditions (fixed, free, or other) of the pile. In fact, the developing depth of the compound wedge can be thought of as a retaining wall of changing height, h. Therefore, the resultant “soil” reaction, p, from any soil layer is really a “soil-pile” reaction that depends upon

the neighboring soil layers and the pile properties as they, in turn, influence the current depth, h. In other words, the p-y response of a given soil layer is not unique. The governing equations of the mobilized passive wedge shape are applied within each one- or two-foot sublayer i (of a given soil layer I) and can be written as follows:

$$\left(\Theta_m\right)_i = 45 - \frac{\left(\phi_m\right)_i}{2} \qquad (5\text{-}6)$$

$$\left(\beta_m\right)_i = 45 + \frac{\left(\phi_m\right)_i}{2} \qquad (5\text{-}7)$$

$$\left(\overline{BC}\right)_i = D + (h - x_i)\, 2 \left(\tan \beta_m\right)_i \left(\tan \phi_m\right)_i \qquad (5\text{-}8)$$

where h symbolizes the entire depth of the compound passive wedge in front of the pile and x_i represents the depth from the top of the pile or compound passive wedge to the middle of the sublayer under consideration. Equations 5-6 through 5-8 are applied at the middle of each sublayer. In the case of short and intermediate shafts, x_i is measured downward from the point of zero crossing and replaces the term $(h - x_i)$ in Eqn 5-8, as shown in Fig. 5-6, for analysis of the lower wedge.

5.5 SOIL STRESS-STRAIN RELATIONSHIP

The horizontal strain (ε) in the soil in the passive wedge in front of the pile is the predominant parameter in the SW model; hence, the name "strain wedge". Consequently, the horizontal stress change ($\Delta\sigma_h$) is constant across the width of the rectangle BCLM (of face width $\overline{BC}$ of the passive wedge), as shown in Fig. 5-4. The stress-strain relationship is defined based on the results of the isotropically consolidated drained (sand) or undrained (clay) triaxial test. These properties are summarized as follows:

- The major principle stress change ($\Delta\sigma_h$) in the wedge is in the direction of pile movement, and it is equivalent to the deviatoric stress in the triaxial test as shown in Fig. 5-4 (assuming that the horizontal direction in the field is taken as the axial direction in the triaxial test).
- The vertical stress change ($\Delta\sigma_v$) and the perpendicular horizontal stress change ($\Delta\sigma_{ph}$) equal zero, corresponding to the standard triaxial compression test where deviatoric stress

is increased while confining pressure remains constant.

- The initial horizontal effective stress is taken as

  $$\bar{\sigma}_{ho} = K\,\bar{\sigma}_{vo} = \bar{\sigma}_{vo}$$

  where K=1 due to pile installation effects. Therefore, the isotropic confining pressure in the triaxial test is taken as the vertical effective stress ($\bar{\sigma}_{vo}$) at the associated depth.
- The horizontal stress change in the direction of pile movement is related to the current level of horizontal strain (ε) and the associated Young's modulus in the soil, as are the deviatoric stress and the axial strain, to the secant Young's modulus ($E = \Delta\sigma_h/\varepsilon$) in the triaxial test.
- Both the vertical strain (ε_v) and the horizontal strain perpendicular to pile movement (ε_{ph}) are equal and are given as

  $\varepsilon_v = \varepsilon_{ph} = -\nu\varepsilon$

  where ν is the Poisson's ratio of the soil.

It can be demonstrated from a Mohr's circle of soil strain, as shown in Fig. 5-10, that shear strain, γ, is defined as

$$\frac{\gamma}{2} = \frac{1}{2}\left(\varepsilon - \varepsilon_v\right)\sin 2\Theta_m = \frac{1}{2}\varepsilon\left(1+\nu\right)\sin 2\Theta_m \qquad (5\text{-}9)$$

The corresponding stress level (SL) in sand (see Fig. 5-11) is

$$SL = \frac{\Delta\sigma_h}{\Delta\sigma_{hf}} = \frac{\tan^2\left(45+\phi_m/2\right)-1}{\tan^2\left(45+\phi/2\right)-1} \qquad (5\text{-}10)$$

where the horizontal stress change at failure (or the deviatoric stress at failure in the triaxial test) is

$$\Delta\sigma_{hf} = \bar{\sigma}_{vo}\left[\tan^2\left(45+\frac{\phi}{2}\right)-1\right] \qquad (5\text{-}11)$$

In clay,

$$SL = \frac{\Delta \sigma_h}{\Delta \sigma_{hf}} \; ; \qquad \Delta \sigma_{hf} = 2\, S_u \tag{5.12}$$

where S_u represents the undrained shear strength which may vary with depth. Determination of the values of SL and φ_m in clay requires the involvement of an effective stress analysis which is presented later in this chapter.

The relationships above show clearly that the passive wedge response and configuration change with the change of the mobilized friction angle (φ_m) or stress level (SL) in the soil. Such behavior provides the flexibility and the accuracy for the strain wedge model to accommodate both small and large strain cases. The above equations are applied for each soil sublayer along the shaft in order to evaluate the varying stress level in the soil and the geometry of the passive wedges.

A power function stress-strain relationship is employed in SW model analysis for both sand and clay soils. It reflects the nonlinear variation in stress level (SL) with axial strain (ε) for the condition of constant confining pressure. To be applicable over the entire range of soil strain, it takes on a form that varies in stages as shown in Fig. 5-12. The advantage of this technique is that it allows the three stages of horizontal stress, described in the next section, to occur simultaneously in different sublayers within the passive wedge.

5.5.1 Horizontal Stress Level (SL)

Stage I ($\varepsilon \le \varepsilon_{50\%}$)

The relationship between stress level and strain at each sublayer (i) in the first stage is assessed using the following equation,

$$SL_i = \frac{\lambda_i \varepsilon}{(\varepsilon_{50})_i} \exp\left(-3.707\, SL_i \right) \tag{5.13}$$

where 3.707 and λ (λ= 3.19) represent the fitting parameters of the power function relationship, and ε_{50} symbolizes the soil strain at 50 percent stress level at the associated confining pressure.

Stage II ($\varepsilon_{50\%} \leq \varepsilon \leq \varepsilon_{80\%}$)

In the second stage of the stress-strain relationship, Eqn. 5.13 is still applicable. However, the value of the fitting parameter λ is taken to vary in a linear manner with SL from 3.19 at the 50 percent stress level to 2.14 at the 80 percent stress level as shown in Fig. 5-12b.

Stage III ($\varepsilon \geq \varepsilon_{80\%}$)

This stage represents the final loading zone which extends from 80 percent to 100 percent stress level. The following equation is used to assess the stress-strain relationship in this range,

$$SL_i = \exp\left[\ln 0.2 + \frac{100\,\varepsilon_i}{(m\varepsilon_i + q_i)} \right] \quad ; \qquad SL_i \geq 0.80 \tag{5-14}$$

where m=59.0 and q=95.4 ε_{50} are the required values of the fitting parameters.

The three stages mentioned above are developed based on unpublished experimental results (Norris 1977). In addition, the continuity of the stress-strain relationship is maintained along the SL-ε curve at the merging points between the mentioned stages.

As shown in Fig. 5-13, if ε_{50} of the soil is constant with depth (x), then, for a given horizontal strain (ε), SL from Eqns 5-13 or 5-14 will be constant with x. On the other hand, since strength, $\Delta\sigma_{hf}$, varies with depth (e.g., see Eqns. 5-11 and 5-12), $\Delta\sigma_h$ (= SL $\Delta\sigma_{hf}$) will vary in a like fashion. However, ε_{50} is affected by confining pressure ($\bar{\sigma}_{vo}$) in sand and S_u in clay. Therefore, SL for a given ε will vary somewhat with depth.

The Young's modulus of the soil from both the shear loading phase of the triaxial test and the strain wedge model is

$$E_i = \frac{(\Delta\sigma_h)_i}{\varepsilon} = \frac{SL_i\,(\Delta\sigma_{hf})_i}{\varepsilon} \tag{5.15}$$

It can be seen from the previous equations that stress level, strain and Young's modulus at each sublayer (i) depend on each other, which results in the need for an iterative solution technique to satisfy the equilibrium between the three variables.

5.6 SHEAR STRESS ALONG THE PILE SIDES (SL_t)

Shear stress (τ) along the pile sides in the SW model (see Fig. 5-4) is defined according to the soil type (sand or clay).

5.6.1 Pile Side Shear in Sand

In the case of sand, the shear stress along the pile sides depends on the effective stress ($\overline{\sigma}_{vo}$) at the depth in question and the mobilized angle of friction between the sand and the pile (φ_s). The mobilized side shear depends on the stress level and is given by the following equation,

$$\tau_i = (\overline{\sigma}_{vo})_i \tan(\delta_s)_i; \qquad where \qquad \tan(\delta_s)_i = 2\tan(\delta_m)_i \tag{5-16}$$

In Eqn. 5-16, note that mobilized side shear angle, $\tan\varphi_s$, is taken to develop at twice the rate of the mobilized friction angle ($\tan\varphi_m$) in the mobilized wedge. Of course, φ_s is limited to the fully developed friction angle (φ) of the soil.

5.6.2 Pile Side Shear Stress in Clay

The shear stress along the pile sides in clay depends on the clay's undrained shear strength. The stress level of shear along the pile sides (SL_t) differs from that in the wedge in front of the pile. The side shear stress level is function of the shear movement, equal to the pile deflection (y) at depth x from the ground surface. This implies a connection between the stress level (SL) in the wedge and the pile side shear stress level (SL_t). Using the Coyle-Reese (1966) "t-z" shear stress transfer curves (Fig. 5-14), values for SL_t can be determined. The shear stress transfer curves represent the relationship between the shear stress level experienced by a one-foot diameter pile embedded in clay with a peak undrained strength, S_u, and side resistance, τ_{ult} (equal to ζ times the adhesional strength αS_u), for shear movement, y. The shear stress load transfer curves of Coyle-Reese can be normalized by dividing curve A ($0 < x < 3$ m) by $\zeta = 0.53$, curve B ($3 < x <$

6 m) by $\zeta = 0.85$, and curve C (x > 6 m) by $\zeta = 1.0$. These three values of normalization (0.53, 0.85, 1.0) represent the peaks of the curves A, B, and C, respectively, in Fig. 5-15a. Figure 5-15b shows the resultant normalized curves. Knowing pile deflection (y), one can assess the value of the mobilized pile side shear stress (τ) as

$$t_i = (SL_t)_i (t_{ult})_i \tag{5-17}$$

where

$$(t_{ult})_i = z\,(a\,S_u)_i \tag{5-18}$$

and α indicates the adhesion value after Tomlinson (1957).

The normalized shear stress load transfer curves can be represented by the following equations. For the normalized curves A (x < 3 m) and B (3 < x < 6 m),

$$SL_t = 12.9\,y\,D - 40.5\,y^2\,D^2 \tag{5-19}$$

For the normalized curve C (x > 6 m)

$$SL_t = 32.3\,y\,D - 255\,y^2\,D^2 \tag{5-20}$$

where y is in cm and D in m.

From the discussion above, it is obvious that SL_t varies nonlinearly with the pile deflection, y, at a given soil depth, x. Also, SL_t changes nonlinearly with soil depth for a given value of soil displacement/strain (see Fig. 5-15). These concepts are employed in each sublayer of clay.

5.7 SOIL PROPERTY CHARACTERIZATION IN THE STRAIN WEDGE MODEL

One of the main advantages of the SW model approach is the simplicity of the required soil properties necessary to analyze the problem of a laterally loaded pile. The properties required represent the basic and the most common properties of soil, such as the effective unit weight and the angle of internal friction or undrained strength.

The soil profile is divided into one or two foot sublayers, and each sublayer is treated as an independent entity with its own properties. In this fashion, the variation in soil properties or response (such as ε_{50} and φ in the case of sand, or S_u and $\bar{\varphi}$ in the case of clay) at each sublayer of soil can be explored. It is obvious that soil properties should not be averaged at the midheight of the passive wedge in front of the pile for a uniform soil profile (as in the earlier work of Norris 1986), or averaged for all sublayers of a single uniform soil layer of a multiple layer soil profile.

5.7.1 Properties Employed for Sand Soil

- Effective unit weight (total above water table, buoyant below), $\bar{\gamma}$
- Void ratio, e, or relative density, D_r
- Angle of internal friction, φ
- Soil strain at 50% stress level, ε_{50}

While standard subsurface exploration techniques and available correlations may be used to evaluate or estimate $\bar{\gamma}$, e or D_r, and φ, some guidance may be required to assess ε_{50}.

The ε_{50} represents the axial strain (ε_1) at a stress level equal to 50 percent in the ε_1-SL relationship that would result from a standard drained (CD) triaxial test. The confining (consolidation) pressure for such tests should reflect the effective overburden pressure ($\bar{\sigma}_{vo}$) at the depth (x) of interest. The ε_{50} changes from one sand to another and also changes with density state. In order to obtain ε_{50} for a particular sand, one can use the group of curves shown in Fig. 5-16 (Norris 1986) which show a variation based upon the uniformity coefficient, C_u, and void ratio, e. These curves have been assessed from sand samples tested with "frictionless" ends in CD tests at a confining pressure equal to 42.5 kPa (Norris 1977). Since the confining pressure changes with soil depth, ε_{50}, as obtained from Fig. 5-16, should be modified to match the existing pressure as follows:

$$\left(\varepsilon_{50}\right)_i = \left(\varepsilon_{50}\right)_{42.5} \left(\frac{\left(\bar{\sigma}_{vo}\right)_i}{42.5} \right)^{0.2} \qquad (5\text{-}21)$$

$$\left(\Delta \sigma_{hf}\right)_i = \left(\bar{\sigma}_{vo}\right)_i \left[\tan^2\left(45 + \frac{\phi_i}{2}\right) - 1\right] \quad (5\text{-}22)$$

where $\bar{\sigma}_{vo}$ should be in kPa.

5.7.2 The Properties Employed for Clay

- Effective unit weight $\bar{\gamma}$
- Plasticity index, PI
- Effective angle of friction, $\bar{\varphi}$
- Undrained shear strength, S_u
- Soil strain at 50% stress level, ε_{50}

Plasticity index, PI, and undrained shear strength, S_u, are considered the governing properties because the effective angle of internal friction, $\bar{\varphi}$, can be estimated from the PI based on Fig. 5-17. The ε_{50} from an undrained triaxial test (UU at depth x or CU with $\sigma_3 = \bar{\sigma}_{vo}$) can be estimated based on S_u as indicated in Fig. 5-18.

An effective stress (ES) analysis is employed with clay soil as well as with sand soil. The reason behind using the ES analysis with clay, which includes the development of excess porewater pressure with undrained loading, is to define the three-dimensional strain wedge geometry based upon the more appropriate effective stress friction angle, $\bar{\varphi}$. The relationship between the normally consolidated clay undrained shear strength, S_u, and $\bar{\sigma}_{vo}$ is taken as

$$S_u = 0.33\,\bar{\sigma}_{vo} \quad (5\text{-}23)$$

assuming that S_u is the equivalent undrained standard triaxial test strength. The effective stress analysis relies upon the evaluation of the developing excess porewater pressure based upon Skempton's equation (1954), i.e.

$$\Delta u = B\left[\Delta \sigma_3 + A_u\left(\Delta \sigma_1 - \Delta \sigma_3\right)\right] \quad (5\text{-}24)$$

where B equals 1 for saturated soil. Accordingly,

$$\Delta u = \Delta \sigma_3 + A_u \left(\Delta \sigma_1 - \Delta \sigma_3 \right) \tag{5-25}$$

Note that $\Delta\sigma_3 = 0$ both in the shear phase of the triaxial test and in the strain wedge. Therefore, the mobilized excess porewater pressure is

$$\Delta u = A_u \Delta \sigma_1 \tag{5-26}$$

where $\Delta\sigma_1$ represents the deviatoric stress change in the triaxial test and $\Delta\sigma_h$ in the field, i.e.

$$\Delta u = A_u \Delta \sigma_h \tag{5-27}$$

Therefore, using the previous relationships, the Skempton equation can be rewritten for any sublayer (i) as follows:

$$(\Delta u)_i = (A_u)_i SL_i (\Delta \sigma_{hf})_i = (A_u)_i SL_i 2 (S_u)_i \tag{5-28}$$

The initial value of parameter A_u is 0.333 and occurs at very small strain for elastic soil response. In addition, the value of parameter A_{uf} that occurs at failure at any sublayer (i) is given by the following relationship

$$(A_{uf})_i = \frac{1}{2}\left(1 + \frac{1/(S_u)_i}{(\bar{\sigma}_{vo})_i} - \frac{1}{\sin \bar{\phi}_i} \right) \tag{5-29}$$

after Wu (1966) as indicated in Fig. 5-19.

In Eqn. 5.29, $\bar{\varphi}$ symbolizes the effective stress angle of internal friction; and, based on Eqn. 5-23, $S_u / \bar{\sigma}_{vo}$ equals 0.33. However, A_u is taken to change with stress level in a linear fashion as

$$(A_u)_i = 0.333 + SL_i \left[(A_{uf})_i - 0.333 \right] \tag{5-30}$$

By evaluating the value of A_u, one can effectively calculate the excess porewater pressure, and then can determine the value of the effective horizontal stress, ($\bar{\sigma}_{vo} + \Delta\sigma_h - \Delta u$), and the effective confining pressure, ($\bar{\sigma}_{vo} - \Delta u$) at each sublayer, as shown in Fig. 5-19. Note that the mobilized effective stress friction angle, $\bar{\varphi}_m$, can be obtained from the following relationship.

$$\tan^2\left(45 + \frac{(\bar{\varphi}_m)_i}{2}\right) = \frac{(\bar{\sigma}_{vo} + \Delta\sigma_h - \Delta u)_i}{(\bar{\sigma}_{vo} - \Delta u)_i} \qquad (5\text{-}31)$$

The targeted values of $\bar{\varphi}_{mi}$ and SL_i in a clay sublayer and at a particular level of strain (ε) can be obtained by using an iterative solution that includes Eqns 5-12 through 5-14, and 5-28 through 5-31.

5.8 SOIL-PILE INTERACTION IN THE STRAIN WEDGE MODEL

The strain wedge model relies on calculating the modulus of subgrade reaction, E_s, which reflects the soil-pile interaction at any level of soil strain during pile loading. E_s also represents the secant slope at any point on the p-y curve, i.e.

$$E_s = \frac{p}{y} \qquad (5\text{-}32)$$

Note that p represents the force per unit length of the pile or the BEF soil-pile reaction, and y symbolizes the pile deflection at that soil depth. In the SW model, E_s is related to the soil's Young's modulus, E, by two linking parameters, A and ψ_s. It should be mentioned here that the SW model establishes its own E_s from the Young's modulus of the strained soil, and therefore, one can assess the p-y curve using the strain wedge model analysis. Therefore, E_s should first be calculated using the strain wedge model analysis to identify the p and y values.

Corresponding to the horizontal slice (a soil sublayer) of the passive wedge at depth x (see Figs. 5-2 and 5-4), the horizontal equilibrium of horizontal and shear stresses is expressed as

$$p_i = (\Delta\sigma_h)_i \overline{BC_i} S_1 + 2\tau_i D S_2 \qquad (5\text{-}33)$$

where S_1 and S_2 equal to 0.75 and 0.5, respectively, for a circular pile cross section, and equal to 1.0 each for a square pile (Briaud et al. 1984). Alternatively, one can write the above equation as follows:

$$A_i = \frac{p_i / D}{(\Delta \sigma_h)_i} = \frac{\overline{BC}_i S_1}{D} + \frac{2 \tau_i S_2}{(\Delta \sigma_h)_i} \tag{5-34}$$

where A symbolizes the ratio between the equivalent pile face stress, p/D, and the horizontal stress change, $\Delta\sigma_h$, in the soil. (In essence, it is the multiplier that, when taken times the horizontal stress change, gives the equivalent face stress.) From a different perspective, it represents a normalized width (that includes side shear and shape effects) that, when multiplied by $\Delta\sigma_h$ yields p/D. By combining the equations of the passive wedge geometry and the stress level with the above relationship, one finds that

$$A_i = S_1 \left(1 + \frac{(h - x_i)\, 2 (\tan \beta_m \tan \phi_m)_i}{D} \right) + \frac{2 S_2 (\bar{\sigma}_{vo})_i (\tan \delta_s)_i}{(\Delta \sigma_h)_i} \qquad \textit{in sand} \tag{5-35}$$

$$A_i = S_1 \left(1 + \frac{(h - x_i)\, 2 (\tan \beta_m \tan \bar{\phi}_m)_i}{D} \right) + \frac{S_2 (SL_t)_i}{SL_i} \qquad \textit{in clay} \tag{5-36}$$

Here the parameter A is a function of pile and wedge dimensions, applied stresses, and soil properties. However, given that $\Delta\sigma_h = E\varepsilon$ in Eqn. 2.33,

$$p_i = A_i D (\Delta \sigma_h)_i = A_i D E_i \varepsilon \tag{5-37}$$

For the upper passive wedge, ε represents the uniform soil strain and is replaced by ε_x for soil sublayers of the lower passive wedge. The second linking parameter, Ψ_s, relates the soil strain in the SW model to the linearized pile deflection angle, δ. Referring to the normalized pile deflection shape shown in Figs. 5-3 and 5-5

$$\delta = \frac{\gamma}{2} \tag{5-38}$$

$$\frac{\gamma}{2} = \frac{\gamma_{max}}{2} \sin 2\Theta_m \tag{5-39}$$

and

$$\frac{\gamma_{max}}{2} = \frac{\varepsilon - \varepsilon_v}{2} = \frac{(1+\nu)\varepsilon}{2} \tag{5-40}$$

where γ denotes the shear strain in the developing passive wedge. Using Eqns. 5-39 and 5.40, Eqn. 5-38 can be rewritten as

$$\delta = \frac{\varepsilon(1+\nu)\sin 2\Theta_m}{2} \tag{5-41}$$

Based on Eqn. 5-41, the relationship between ε and δ can expressed as

$$\Psi = \frac{\varepsilon}{\delta} \tag{5-42}$$

or

$$\Psi = \frac{2}{(1+\nu)\sin 2\Theta_m} \tag{5-43}$$

The parameter ψ varies with the Poisson's ratio of the soil and the soil's mobilized angle of internal friction (φ_m) and the mobilized passive wedge angle (Θ_m).

Poisson's ratio for sand can vary from 0.1 at a very small strain to 0.5 or lager (due to dilatancy) at failure, while the base angle, Θ_m, can vary between 45° (for $\varphi_m = 0$ at $\varepsilon = 0$) and 25° (for, say, $\varphi_m = 40°$ at failure), respectively. For this range in variation for ν and φ_m, the parameter Ψ for sand varies between 1.81 and 1.74 with an average value of 1.77. In clay soil, Poisson's ratio is assumed to be 0.5 (undrained behavior) and the value of the passive wedge base angle, Θ_m, can vary between 45° (for $\varphi_m = 0$ at $\varepsilon = 0$) and 32.5° (for, say, $\bar{\varphi}_m = 25°$ at failure). Therefore, the value of the parameter ψ will vary from 1.47 to 1.33, with an average value of 1.4.

It is clear from the equations above that employing the multi-sublayer technique greatly influences the values of soil-pile interaction as characterized by the parameter, A_i, which is

affected by the changing effective stress and soil strength from one sublayer to another. The final form of the modulus of subgrade reaction can be expressed as

$$\left(E_s\right)_i = \frac{p_i}{y_i} = \frac{A_i D \varepsilon E_i}{\delta\left(h - x_i\right)} = \frac{A_i}{\left(h - x_i\right)} D \Psi E_i \qquad (5\text{-}44)$$

It should be mentioned that the SW model develops its own set of non-unique p-y curves which are function of both soil and pile properties, and are affected by soil continuity (layering) as presented by Ashour et al. (1996). For the lower passive wedge, $(h - x_i)$ will be replaced by x_i that is measured downward from the point of zero crossing (Fig. 5-6).

5.9 PILE HEAD DEFLECTION

As mentioned previously, the deflection pattern of the pile in the SW model is continuous and linear. Based on this concept, pile deflection can be assessed using a simplified technique which provides an estimation for the linearized pile deflection, especially y_o at the pile head. By using the multi-sublayer technique, the deflection of the pile can be calculated starting with the base of the mobilized passive wedge and moving upward along the pile, accumulating the deflection values at each sublayer as shown in the following relationships and Fig. 5-20.

$$y_i = H_i \delta_i = H_i \frac{\varepsilon}{\Psi_s} \qquad (5\text{-}45)$$

$$y_o = \Sigma y_i \qquad i = 1 \text{ to } n \qquad (5\text{-}46)$$

where the ψ_s value changes according to the soil type (sand or clay), and H_i indicates the thickness of sublayer i and n symbolizes the current number of sublayers in the mobilized passive wedge.

The main point of interest is the pile head deflection which is a function of not only the soil strain but also of the depth of the compound passive wedge that varies with soil and pile properties and the level of soil strain.

5.10 ULTIMATE RESISTANCE CRITERIA IN STRAIN WEDGE MODEL

The mobilized passive wedge in front of a laterally loaded pile is limited by certain constraint criteria in the SW model analysis. Those criteria differ from one soil to another and are applied to each sublayer. Ultimate resistance criteria govern the shape and the load capacity of the wedge in any sublayer in SW model analysis. The progressive development of the ultimate resistance with depth is difficult to implement without employing the multi-sublayer technique.

5.10.1 Ultimate Resistance Criterion of Sand Soil

The mobilization of the passive wedge in sand soil depends on the horizontal stress level, SL, and the pile side shear resistance, τ. The side shear stress is a function of the mobilized side shear friction angle, φ_s, as mentioned previously, and reaches its ultimate value ($\varphi_s = \varphi$) earlier than the mobilized friction angle, φ_m, in the wedge (i.e. $SL_t \geq SL$). This causes a decrease in the rate of growth of sand resistance and the fanning of the passive wedge as characterized by the second term in Eqns 5-33 and 5-35, respectively.

Once the stress level in the soil of a sublayer of the wedge reaches unity ($SL_i = 1$), the stress change and wedge fan angle in that sublayer cease to grow. However, the width $\overline{BC}$ of the face of the wedge can continue to increase as long as ε (and, therefore, h in Eqn. 5-8) increases. Consequently, soil-pile resistance, p, will continue to grow more slowly until a condition of initial soil failure ($SL_i = 1$) develops in that sublayer. At this instance, $p = p_{ult}$ where p_{ult} in sand, given as

$$\left(p_{ult}\right)_i = \left(\Delta \sigma_{hf}\right)_i \overline{BC}_i S_1 + 2\left(\tau_f\right)_i D S_2 \qquad (5.47)$$

p_{ult} is "a temporary" ultimate condition, i.e. the fanning angle of the sublayer is fixed and equal to φ_i, but the depth of the passive wedge and, hence, BC continue to grow. The formulation above reflects that the near-surface "failure" wedge does not stop growing when all such sublayers reach their ultimate resistance at SL = 1 because the value of h at this time is not limited. Additional load applied at the pile head will merely cause the point at zero deflection and, therefore, h to move down the pile. More soil at full strength (SL = 1) will be mobilized to

the deepening wedge as BC, therefore, p_{ult} will increase until either flow around failure or a plastic hinge in the pile occurs.

Recognize that flow around failure occurs in any sublayer when it is easier for the sand at that depth to flow around the pile in a local bearing capacity failure than for additional sand to be brought to failure and added to the already developed wedge. However, the value at which flow failure occurs [$A_i = (A_{ult})_i$, $(p_{ult})_i = (\Delta\sigma_{hf})_i (A_{ult})_i D$] in sand is so large that it is not discussed here. Alternatively, a plastic hinge can develop in the pile when the pile material reaches its ultimate resistance at a time when $SL_i \leq 1$ and $A_i < (A_{ult})_i$. In this case, h becomes fixed, and $\overline{BC}_i$ and p_i will be limited when SL_i becomes equal to 1.

5.10.2 Ultimate Resistance Criterion of Clay Soil

The situation in clay soil differs from that in sand and is given by Gowda (1991) as a function of the undrained strength $(S_u)_i$ of the clay sublayer.

$$\left(p_{ult}\right)_i = 10\left(S_u\right)_i D\, S_1 + 2\left(S_u\right)_i D\, S_2 \tag{5-48}$$

Consequently,

$$\left(A_{ult}\right)_i = \frac{\dfrac{\left(p_{ult}\right)_i}{D}}{\left(\Delta \sigma_{hf}\right)_i} = \frac{\left(p_{ult}\right)_i}{D\, 2\left(S_u\right)_i} = 5\, S_1 + S_2 \tag{5-49}$$

A_{ult} indicates the limited development of the sublayer wedge geometry for eventual development of flow around failure ($SL_i = 1$) and, consequently, the maximum fanning angle in that sublayer becomes fixed, possibly at a value $\varphi_m \leq \bar{\varphi}$. If a plastic hinge develops in the pile at SL_i less than 1, then h will be limited, but $\overline{BC}$, and p_i will continue to grow until A_i is equal to A_{ult} or p_i is equal to $(p_{ult})_i$.

5.11 VERTICAL SIDE SHEAR RESISTANCE

As seen in Fig. 5-21, the vertical side shear stress distribution around the shaft cross section is assumed to follow a cosine function. It is assumed that there is no contact (active pressure) on the backside of the shaft due to the lateral deflection. The peak (q) of side shear stress develops at angle $\theta = 0$ and decreases to zero at angle $\theta = 90^o$. The total vertical side shear force (V_v) induced along a unit length of the shaft is expressed as

$$V_v = 2\int_0^{p/2} q\, r\cos\theta\, d\theta \;=\; 2q\,(r\sin\theta)_0^{p/2} \;=\; Dq \tag{5-50}$$

and the induced moment (M_{x-x}) per unit length of the shaft is given as

$$\begin{aligned} M_{x-x} &= 2\int_0^{p/2} (q\, r\cos\theta\, d\theta)\,(r\cos\theta) \;=\; 2qr^2\int_0^{p/2}\cos^2\theta\, d\theta \\ &= 2qr^2\int_0^{p/2}\frac{1}{2}\,(\cos 2\theta + 1)\, d\theta \\ &= qr^2\int_0^{p/2}(\cos 2\theta + 1)\, d\theta \\ &= qr^2\left(\frac{1}{2}\,(\sin 2\theta + \theta)\right)_0^{p/2} = \frac{q\,D^2\,\pi}{8} \end{aligned} \tag{5-51}$$

M_{x-x} represents the term M_R in Eqn. 5-1.

5.12 SHAFT BASE RESISTANCE

The soil shear resistance at the base of the shaft (V_b) that is shown in Fig. 5-1 is a function of the soil shear stress (τ_b) induced at the contact surface between the soil and shaft base. The shear stress (τ_b) varies with lateral deflection of the shaft base and the axial load delivered at the shaft base. Based on the failure mechanism at the shaft base for sand and clay that are presented in Chapter 3 and 4, Fig. 5-22 shows the shear tress (τ_b) that develops at the shaft base embedded in sand or clay soil. Unlike the clay case, the ultimate shear resistance at the base of the shaft increases with the axial load carried by the shaft base (Figs. 4-1 and 5-22).

The shear resistance at the shaft base can be determined as follows,

1. Using the lateral deflection at the shaft base (y_b) that is obtained from the lateral shaft analysis with no shaft base resistance, the soil shear strain at the base (γ_b) is calculated as,

$$\gamma_b = \frac{y_b}{2D} \tag{5-52}$$

where D is the shaft diameter, and the effective depth of the shear deformation is assumed to be equal to 2D

2. In the first step of analysis, assume the normal strain (ε_b) equal to the shear strain (γ_b). Based on the normal stress strain relationship presented in Section 5.5.1, the stress level (SL) can be evaluated and the associated Poisson's ratio (ν) is calculated as follows,

$$\nu = 0.1 + 0.4\,SL \tag{5-53}$$

It should be noted the $\Delta\sigma_{hf}$ used in Eqns. 5-10 through 5-12 is constant with clay ($\Delta\sigma_{hf} = 2S_u$) and varies with the load carried by the shaft base in the case of sand (Figs. 4-1 and 5-22), i.e.

$$\Delta\sigma_{hf} = (\bar{\sigma}_3)_{IV}\left[\tan^2\left(45 + \frac{\phi}{2}\right) - 1\right] \tag{5-54}$$

In sand soil, the increase of the shaft base load ($F_b = 0.6\ q_{net}\ A_b = \sigma_d\ A_b = SL\ \Delta\sigma_{hf}\ A_b$) results in the increase of the accompanying confining pressure $(\bar{\sigma}_3)_{IV}$.

3. The induced normal strain (ε_b) is recalculated as follows,

$$\varepsilon_b = \frac{\gamma_b}{(1+\nu)} \tag{5-55}$$

4. Repeat steps 2 and 3 to refine the value of ε_b by averaging the new and old values of ε_b until reaching the desired convergence.

5. Compute the associated soil shear stress that develops on the shaft base (τ_b) as follows:

$$\tau_b = SL\, S_u \qquad \text{(Clay)} \qquad (5\text{-}56a)$$

$$\tau_b = 0.5\, SL\ \Delta\sigma_{hf} \qquad \text{(Sand)} \qquad (5\text{-}56b)$$

$$V_b = \tau_b\ A_b \qquad (5\text{-}57)$$

where F_b and V_b are the axial load (as calculated in Chapter 4) and the shear resistance carried by the shaft base.

6. Analyze the laterally loaded shaft as a Beam on Elastic Foundations (Section 5-13) considering the effect of the base resistance. The base shear resistance is evaluated in each trial according to the lateral deflection induced at the shaft base.

5.13 STABILITY ANALYSIS IN THE STRAIN WEDGE MODEL

The objective of the SW model is to establish the soil response as well as model the soil-pile interaction through the modulus of subgrade reaction, E_s. The shape and the dimensions of the passive wedge in front of the pile basically depend on two types of stability which are the local stability of the soil sublayer and the global stability of the pile and the passive wedge. However, the global stability of the passive wedge depends, in turn, on the local stability of the soil sublayers.

5.13.1 Local Stability of a Soil Sublayer in the Strain Wedge Model

The local stability analysis in the strain wedge model satisfies equilibrium and compatibility among the pile segment deflection, soil strain, and soil resistance for the soil sublayer under consideration. Such analysis allows the correct development of the actual horizontal stress change, $\Delta\sigma_h$, pile side shear stress, τ, and soil-pile reaction, p, associated with that soil sublayer (see Figs. 5-2 and 5-4). It is obvious that the key parameters of local stability analysis are soil strain, soil properties, and pile properties.

5.13.2 Global Stability in the Strain Wedge Model

The global stability, as analyzed by the strain wedge model, satisfies the general compatibility among soil reaction, pile deformations, and pile stiffness along the entire depth of the developing passive wedge in front of the pile. Therefore, the depth of the passive wedge depends on the

global equilibrium between the loaded pile and the developed passive wedge. This requires a solution for Eqn. 5-1.

The global stability is an iterative beam on elastic foundation (BEF) problem that determines the correct dimensions of the passive wedge, the corresponding straining actions (deflection, slope, moment, and shear) in the pile, and the external loads on the pile. Satisfying global stability conditions is the purpose of linking the three-dimensional strain wedge model to the BEF approach. The major parameters in the global pile stability problem are pile stiffness, EI, and the modulus of subgrade reaction profile, E_s, as determined from local stability in the strain wedge analysis. Since these parameters are determined for the applied soil strain, the stability problem is no longer a soil interaction problem but a one-dimensional BEF problem. Any available numerical technique, such as the finite element or the finite difference method, can be employed to solve the global stability problem. The modeled problem, shown in Fig. 5-8c, is a BEF and can be solved to identify the depth, X_o, of zero pile deflection.

5.14 SUMMARY

The SW model approach presented here provides an effective method for solving the problem of a laterally loaded pile/shaft in layered soil. This approach assesses its own nonlinear variation in modulus of subgrade reaction or p-y curves. The SW model allows the assessment of the nonlinear p-y curve response of a laterally loaded pile based on the envisioned relationship between the three-dimensional response of a flexible pile in the soil to its one-dimensional beam on elastic foundation parameters. In addition, the SW model employs stress-strain-strength behavior of the soil as established from the triaxial test in an effective stress analysis to evaluate mobilized soil behavior.

The SW model accounts for the vertical side shear resistance that develops effectively with large diameter shafts. Such resistance enhances the performance of the large diameter shafts and increases with progressive lateral deflection. The evaluation of the vertical side shear resistance is based on the assessed t-z curve and affects the shape of the predicted p-y curve. The formulations of the t-z curve presented in Chapters 3 and 4 are employed in the SW model analysis and coupled with the shaft deformations.

Compared to empirically based approaches which rely upon a limited number of field tests, the SW approach depends on well known or accepted principles of soil mechanics (the stress-strain-strength relationship) in conjunction with effective stress analysis. Moreover, the required parameters to solve the problem of the laterally loaded pile are a function of basic soil properties that are typically available to the designer.

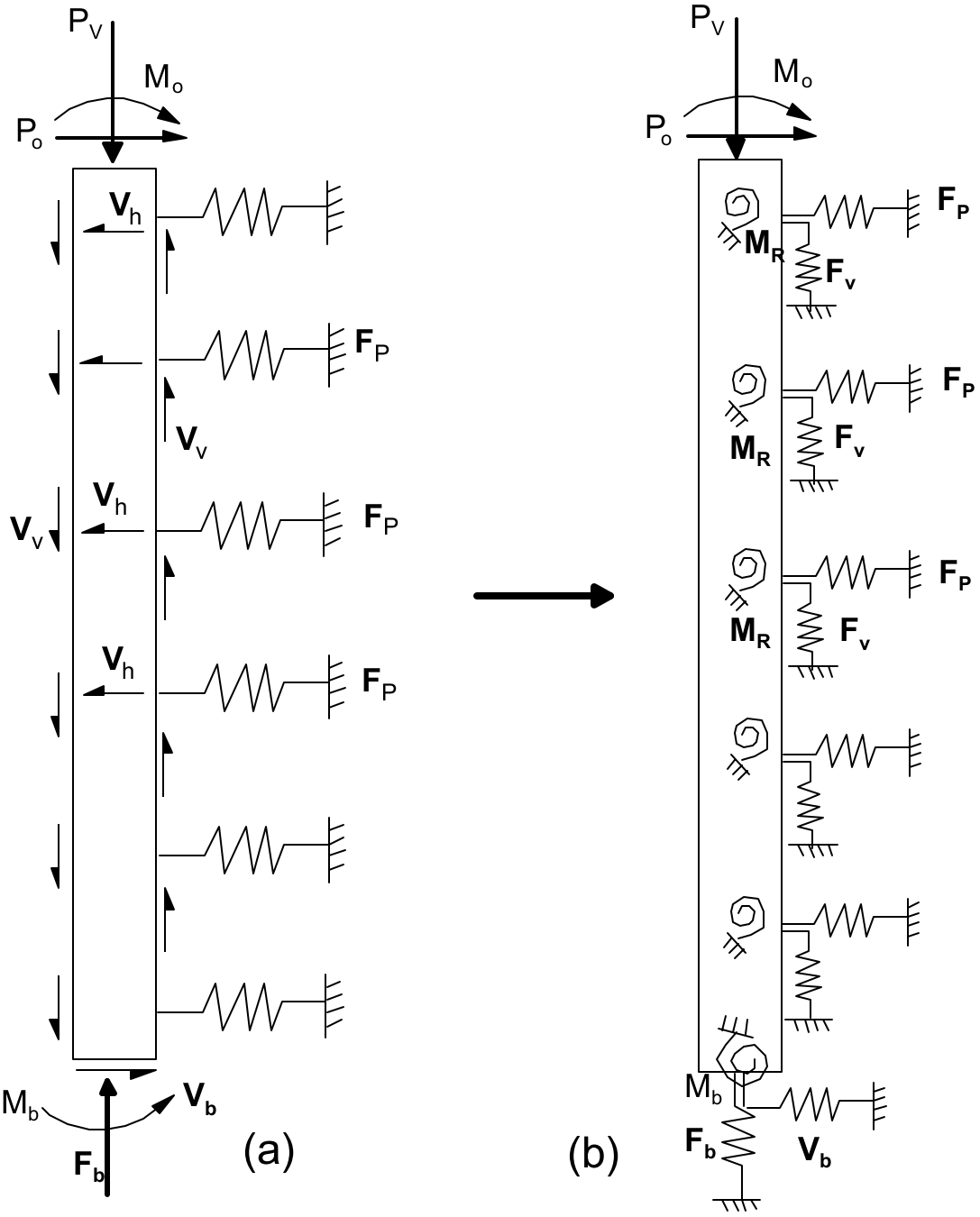

Fig. 5-1 Characterization of Large Diameter Long, Intermediate or Short Shafts In Terms of a) Forces and b) Nonlinear Springs

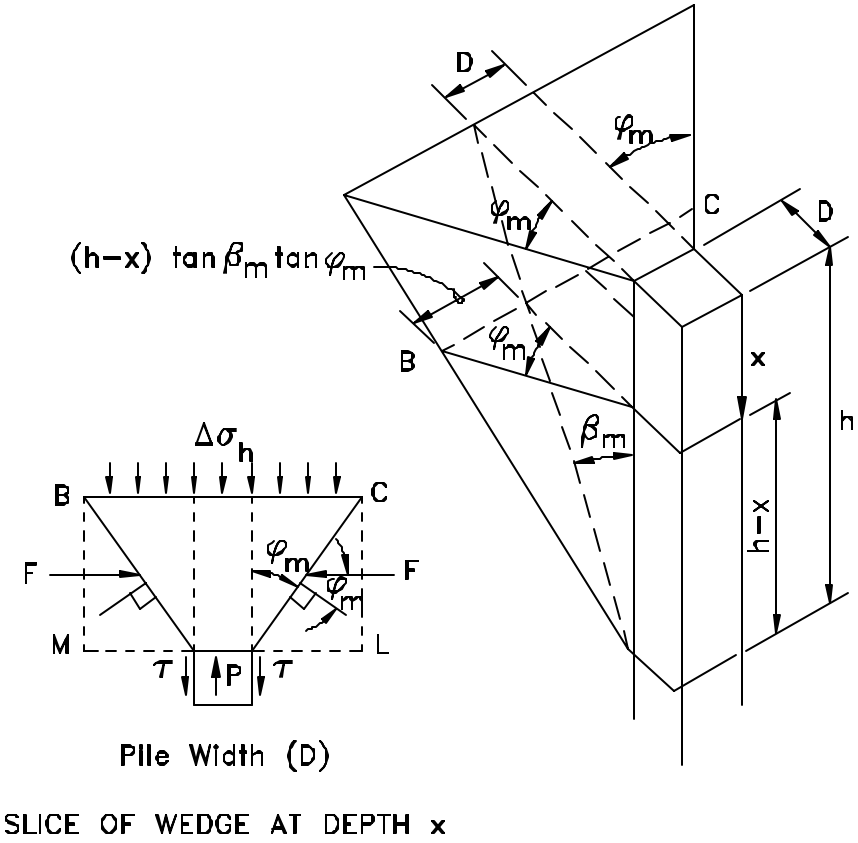

Fig. 5-2 The Basic Strain Wedge in Uniform Soil

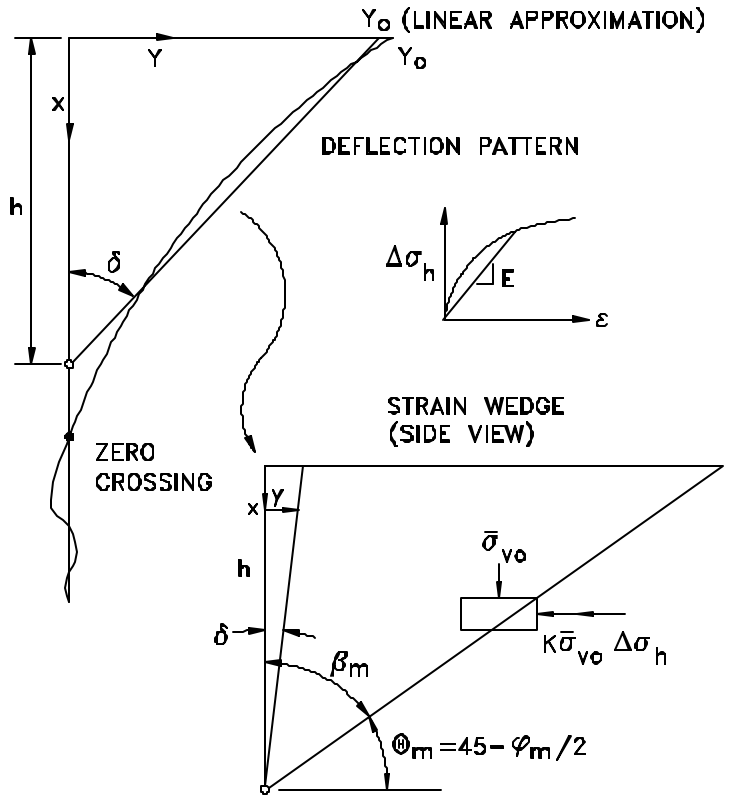

Fig. 5-3 Deflection Pattern of a Laterally Loaded Long Shaft/Pile and the Associated Strain Wedge

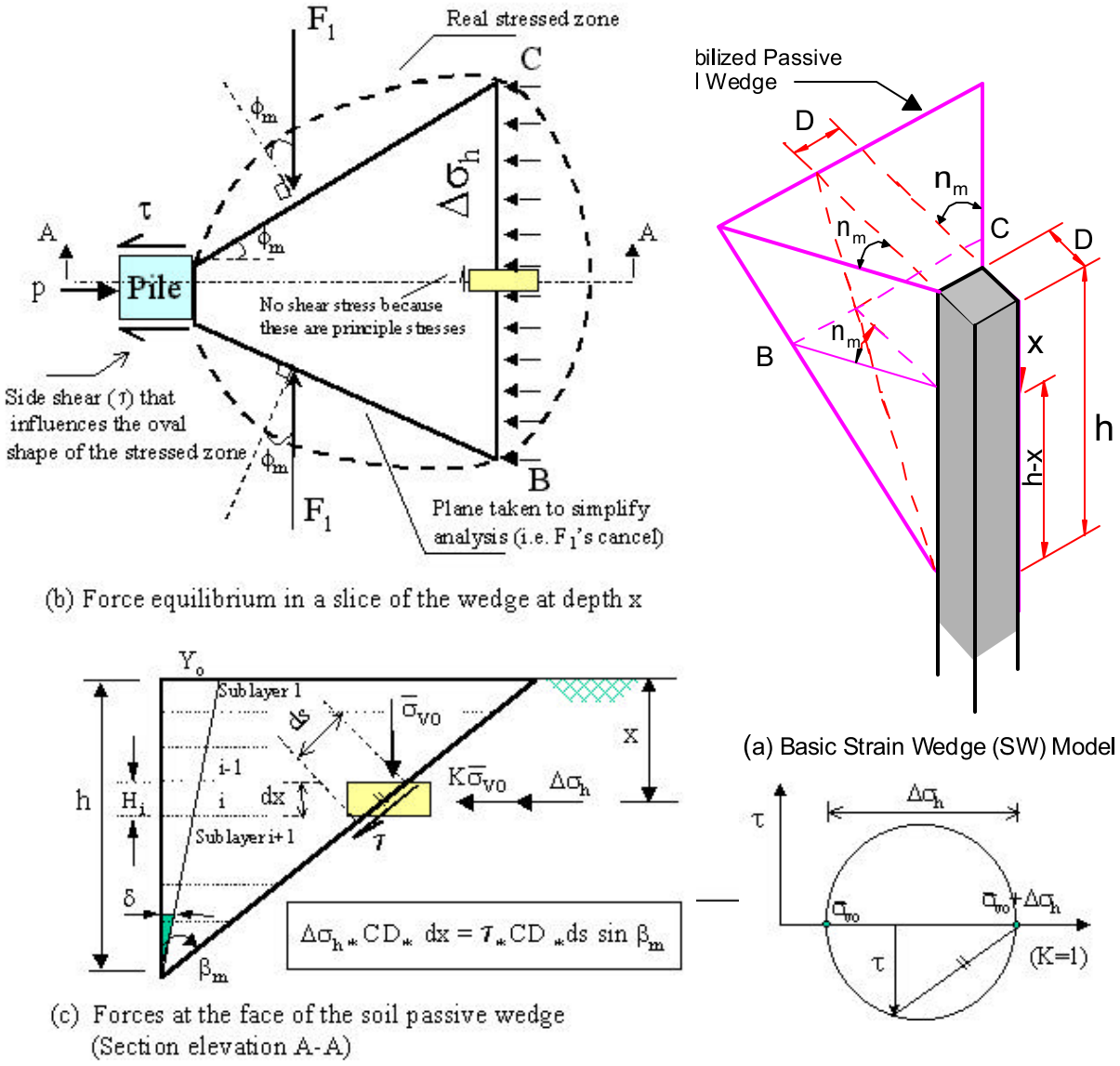

Fig. 5-4 Characterization and equilibrium of the SW model

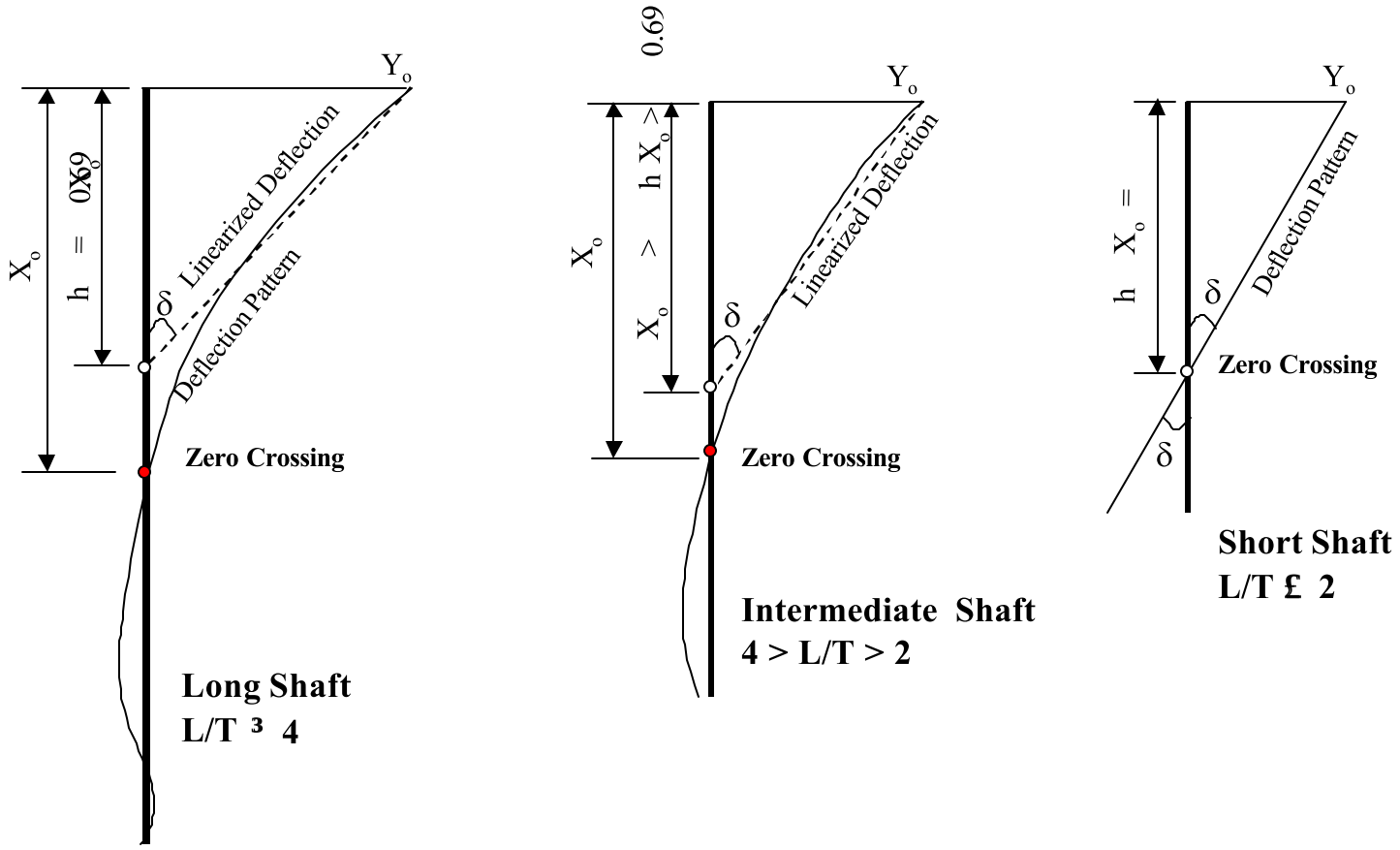

Fig. 5-5 Deflection Patterns of Long, Intermediate and Short Shafts

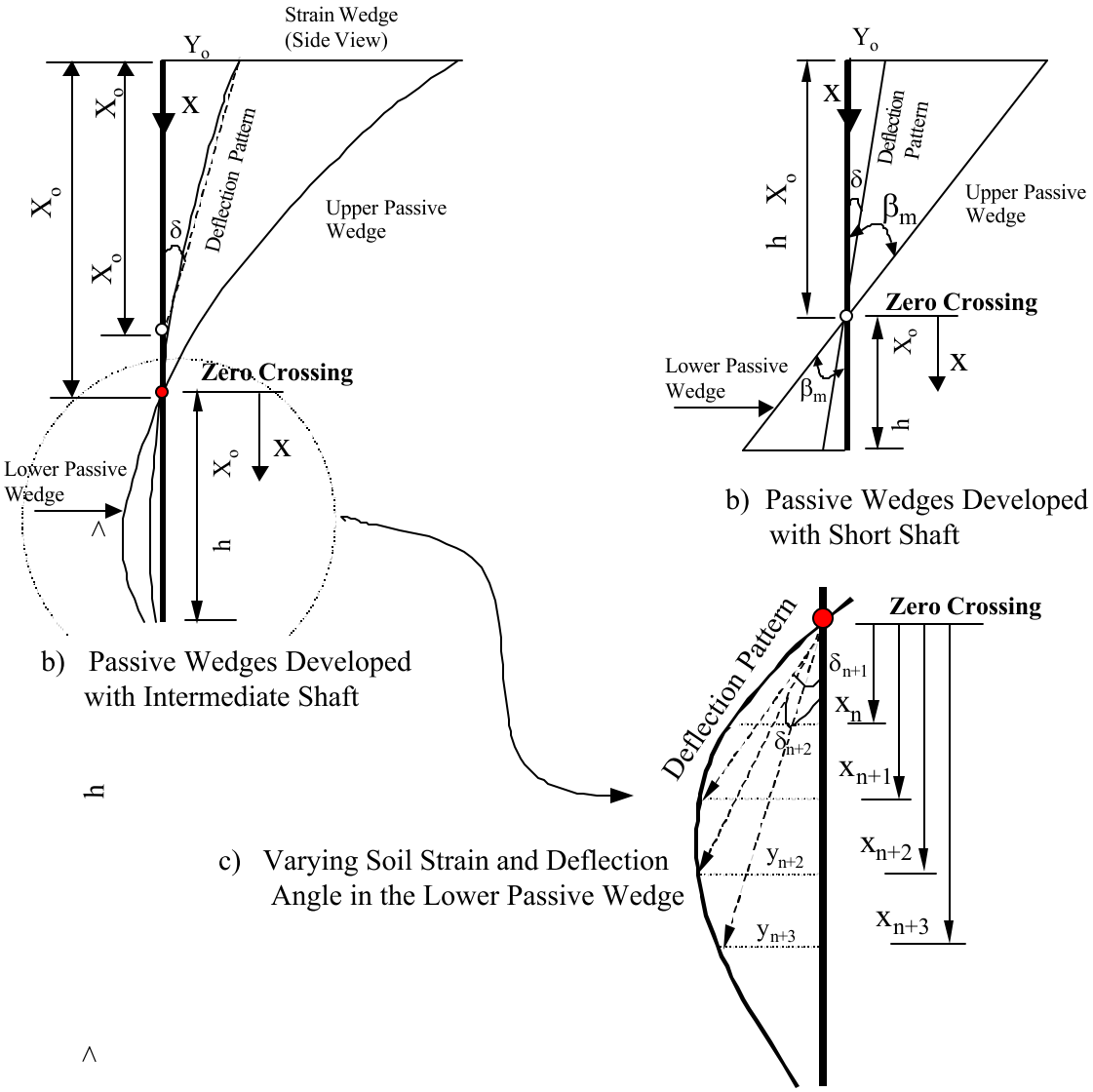

Fig. 5-6 Developed Passive Wedges with Short and Intermediate Shafts

0.69

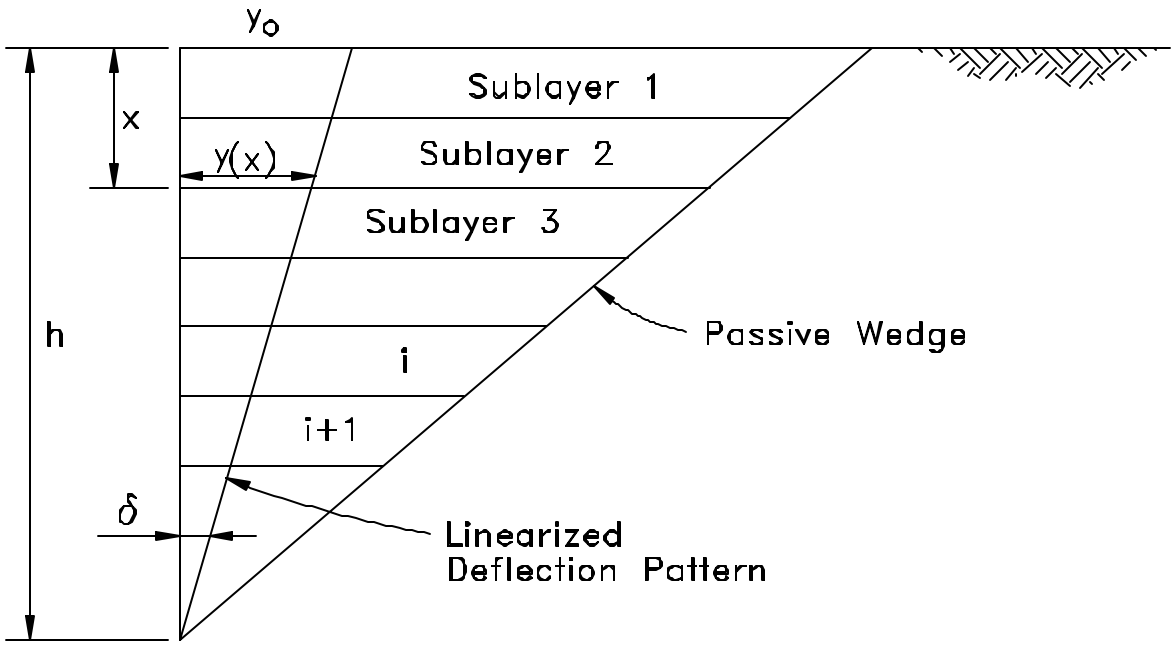

Fig. 5-7 The Linearized Deflection Pattern of a Pile/shaft Embedded in Soil Using the Multi Sublayer Strain Wedge Model

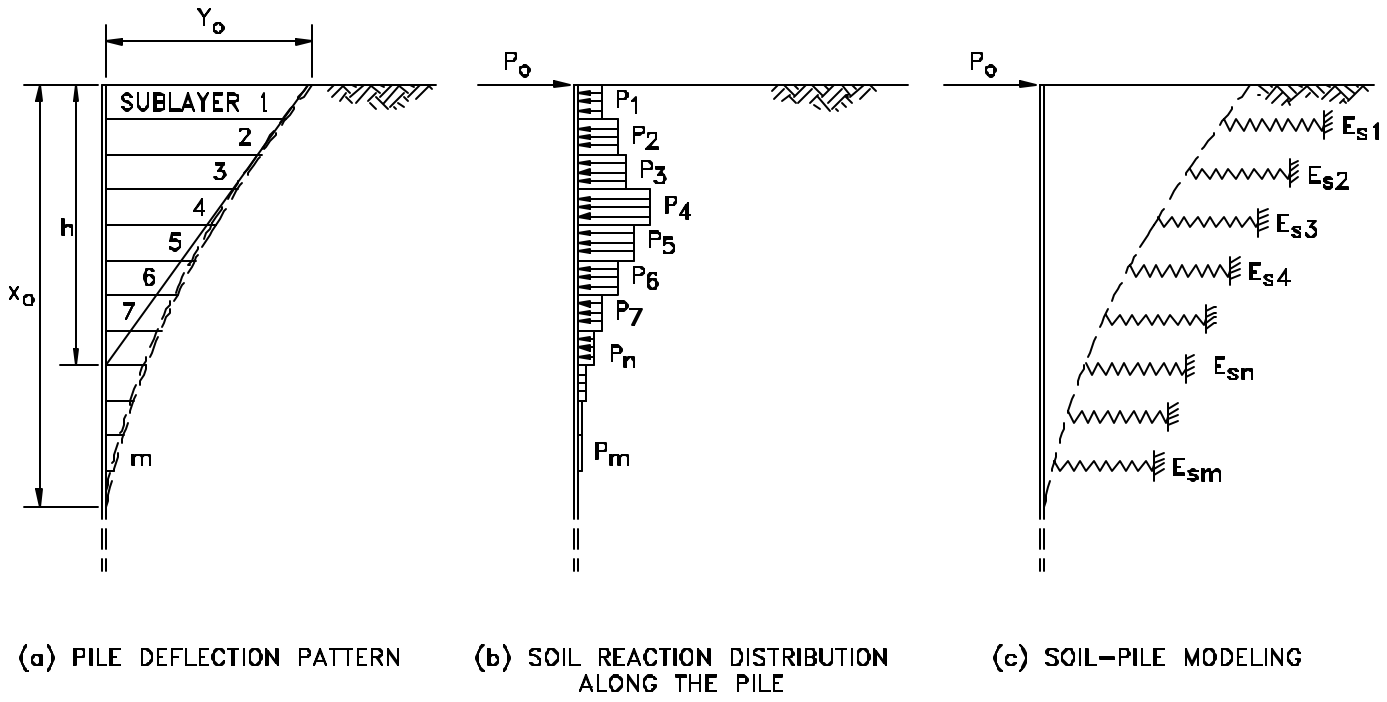

Fig. 5-8 Soil-Pile Interaction in the Multi-Sublayer Technique

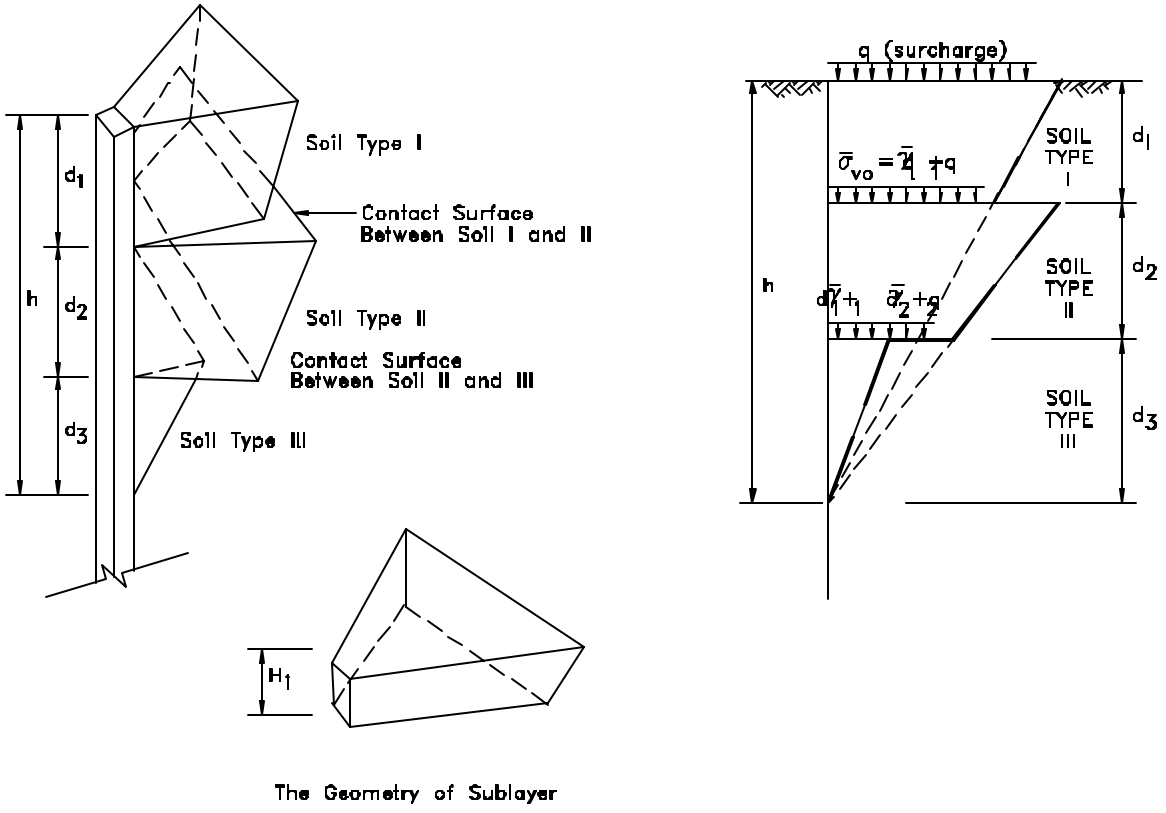

Fig. 5-9 The Proposed Geometry of the Compound Passive Wedge

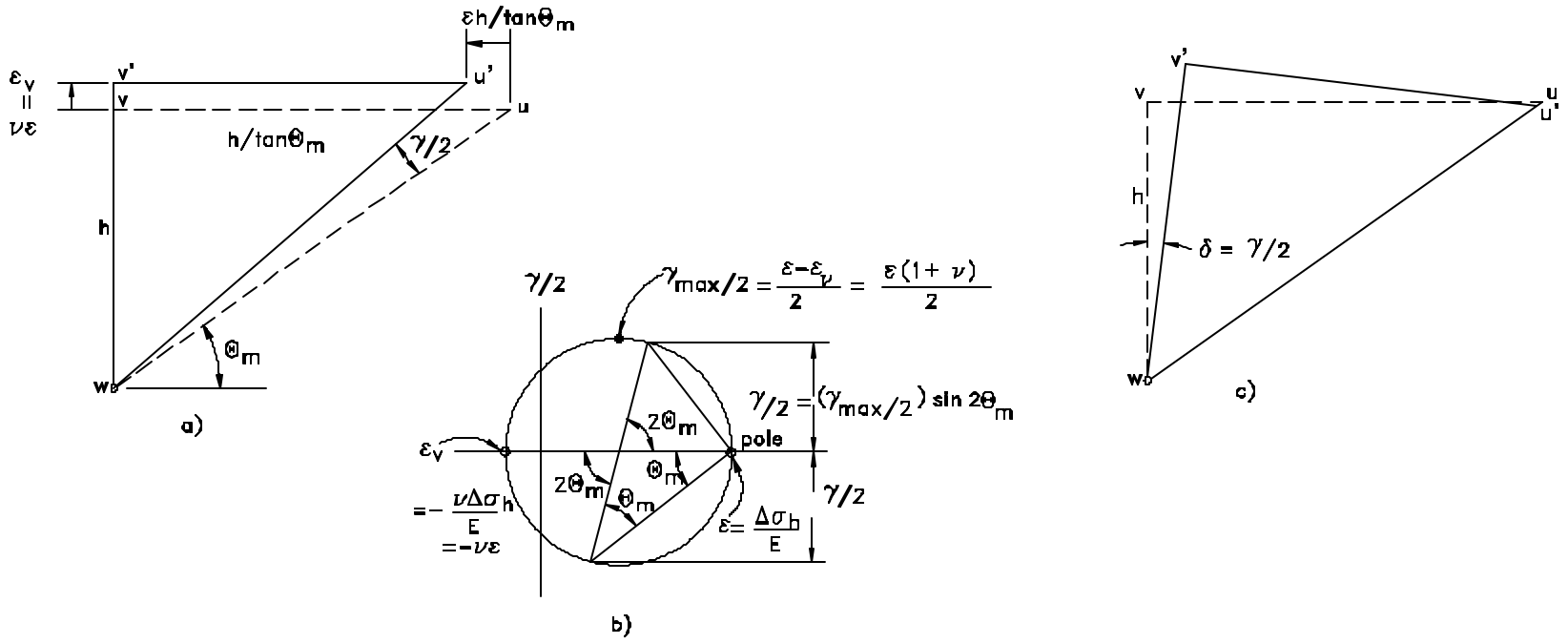

Fig. 5-10 Distortion of the Wedge a), The Associated Mohr Circle of Strain b), and the Relationship Between Pile Deflection and Wedge Distortion c)

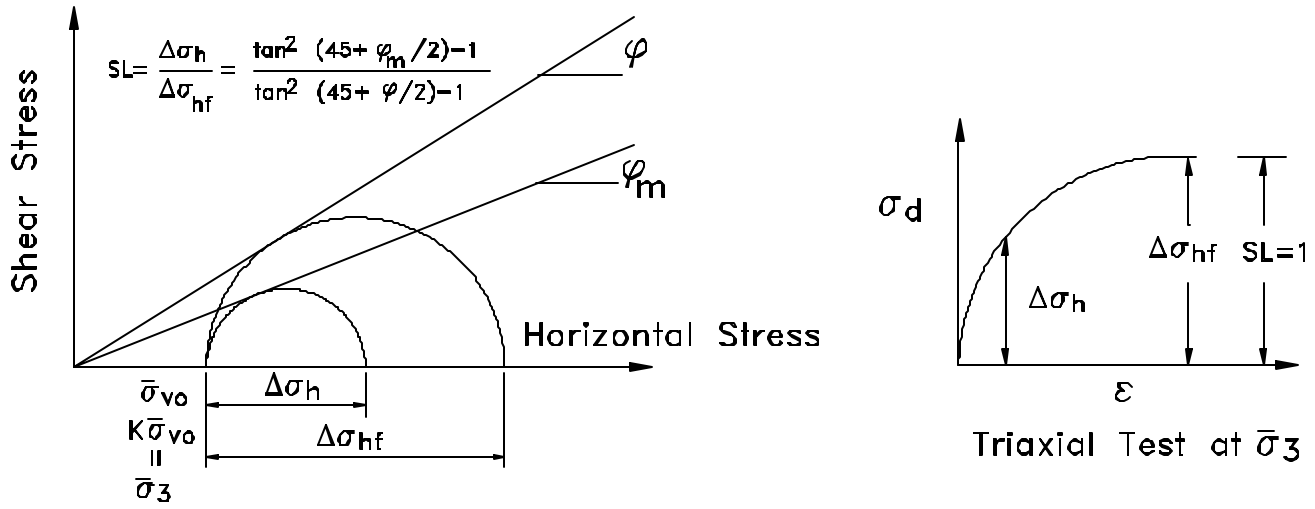

Fig. 5-11 Relationship Between Horizontal Stress Change, Stress Level, and Mobilized Friction Angle

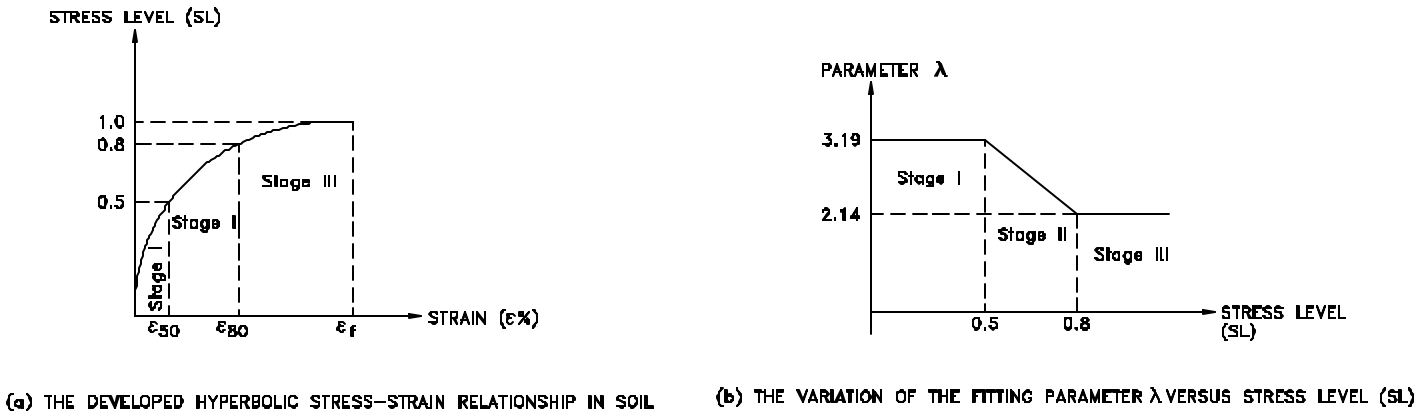

(a) THE DEVELOPED HYPERBOLIC STRESS–STRAIN RELATIONSHIP IN SOIL

(b) THE VARIATION OF THE FITTING PARAMETER λ VERSUS STRESS LEVEL (SL)

Fig. 5-12 The Developed Stress-Strain Relationship in Soil

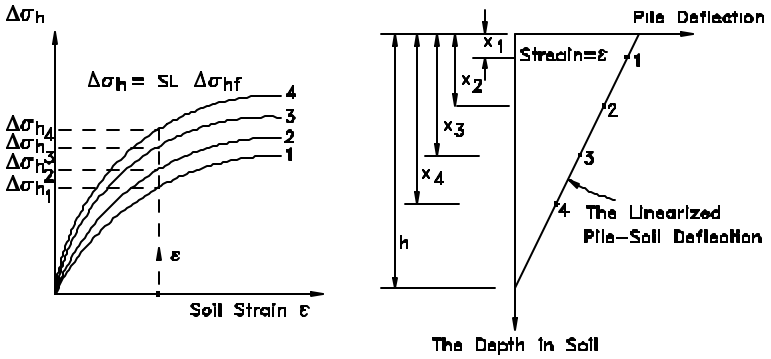

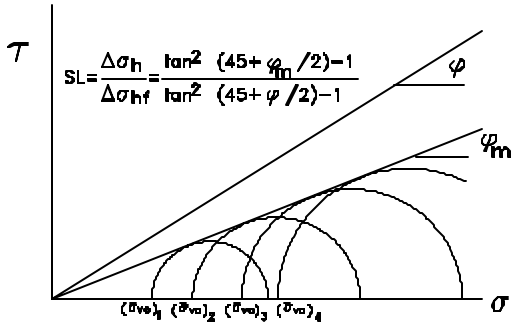

Fig. 5-13 The Nonlinear Variation of Stress Level Along the Depth of Soil at Constant Strain

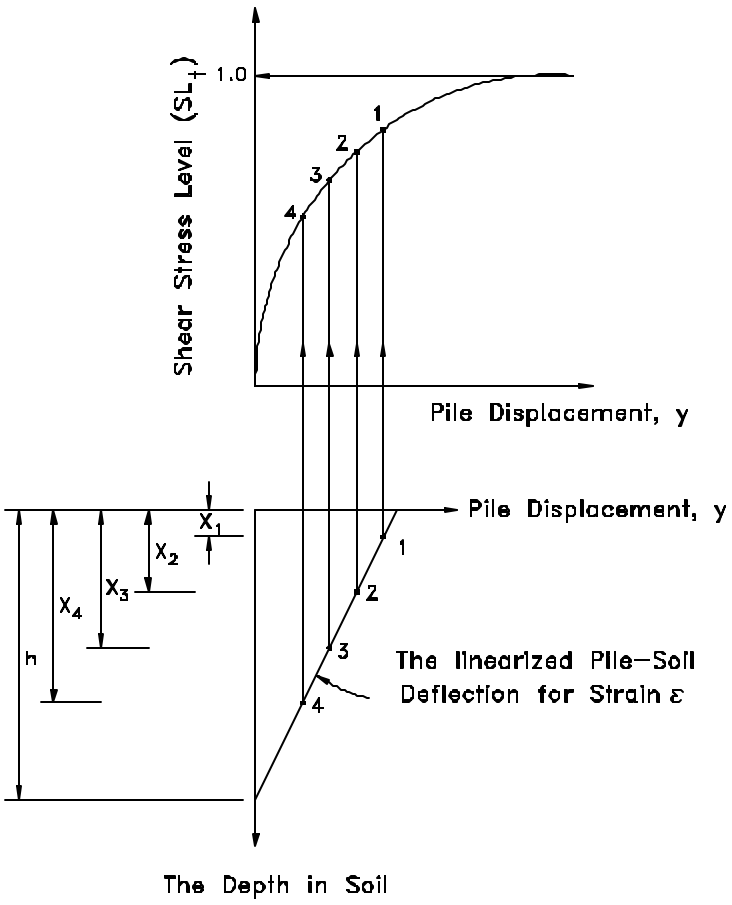

Fig. 5-14 The Employed Side Shear Stress-Displacement Curve in Clay

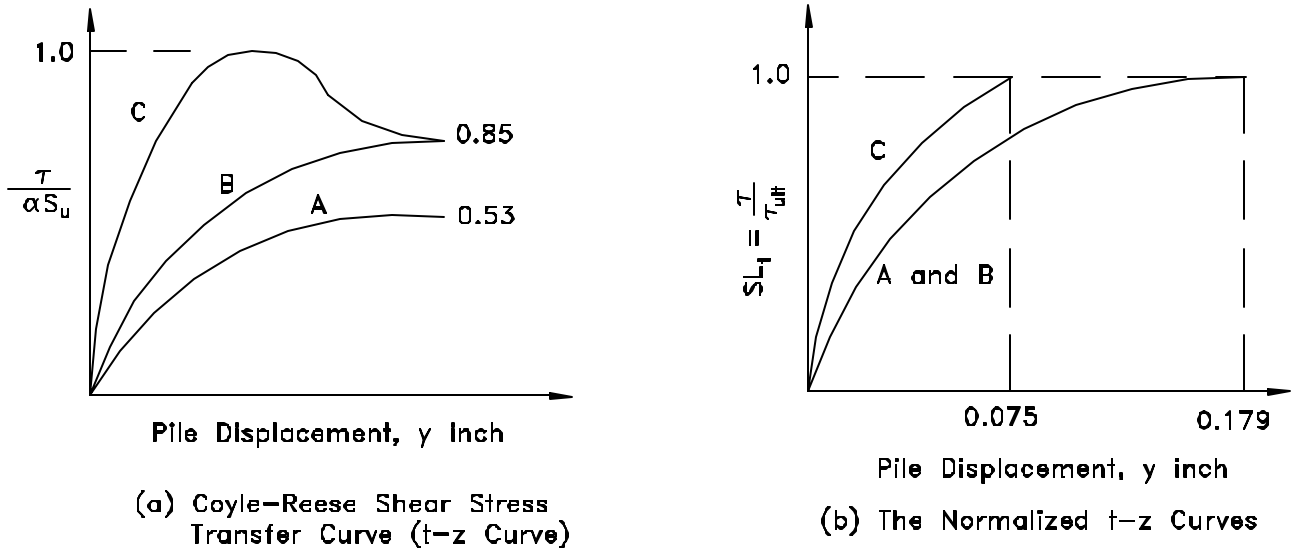

Fig. 5-15. The Nonlinear Variation of Shear Stress Level (SL_t) with depth in Clay

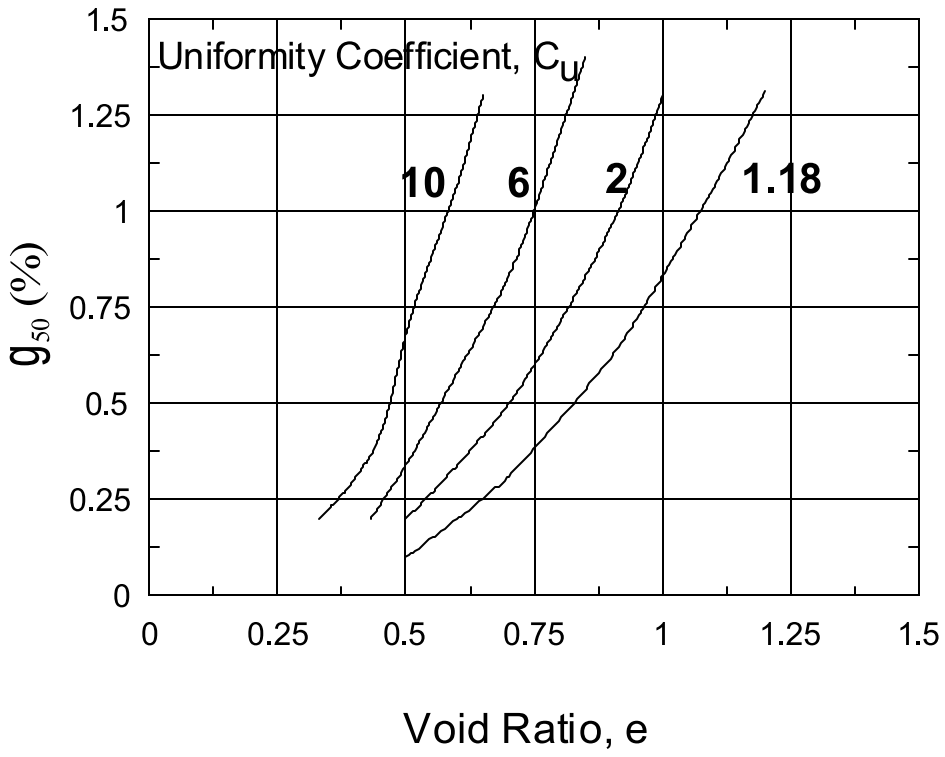

Fig. 5-16 Relationship Between e_{50}, Uniformity Coefficient (C_u) and Void Ratio (e) (Norris 1986)

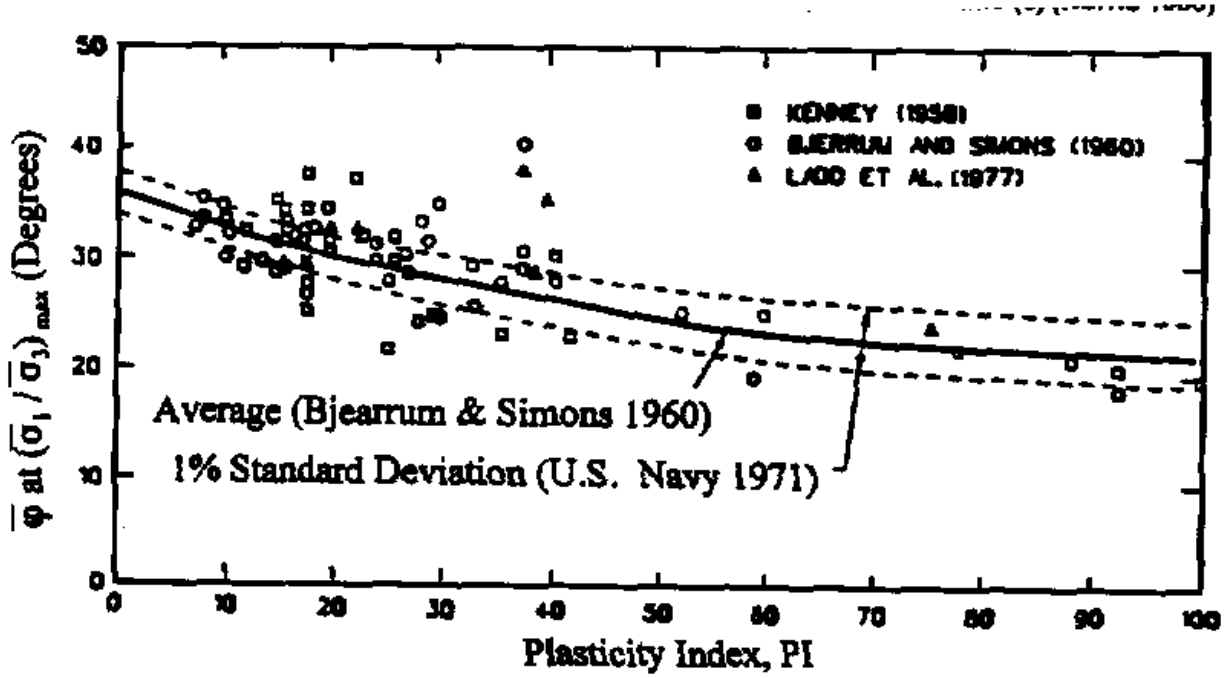

Fig. 5-17 Relationship Between Plasticity Index (PI) and Effective Stress Friction Angle (j) (US Army Corps of Engineers 1996)

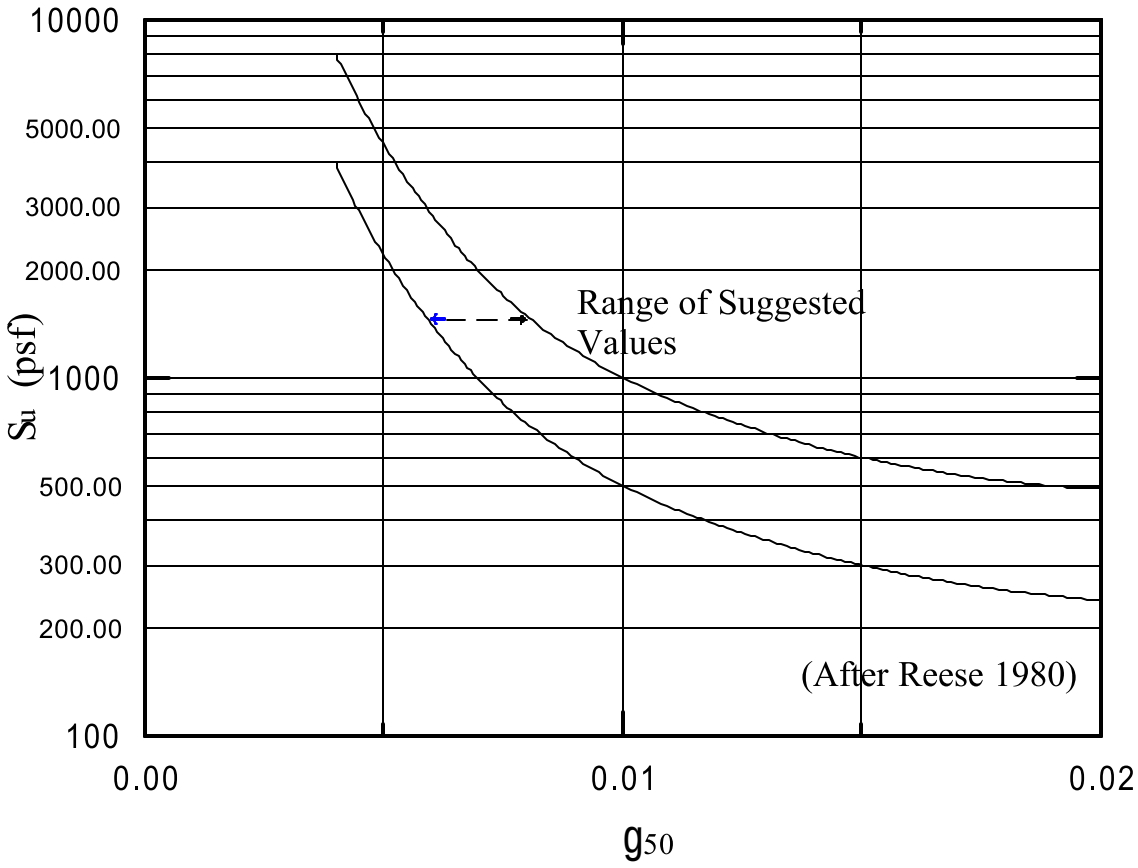

Fig. 5-18 Relationship Between ε_{50} and Undrained Shear Strength , S_u (Evans and Duncan 1982)

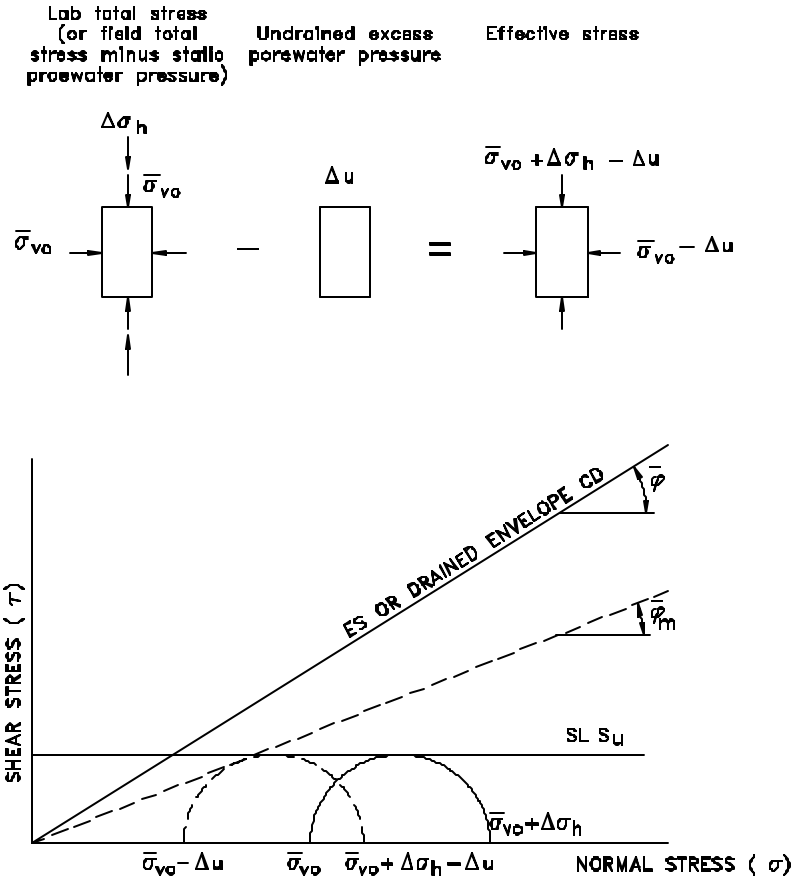

Fig. 5-19 Relationship Between Effective Stress and Total Stress Conditions

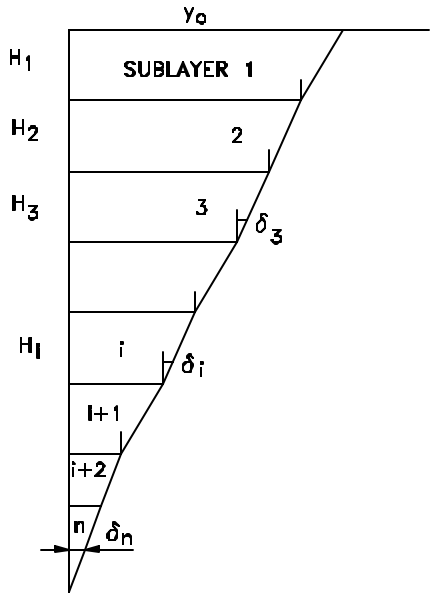

Fig. 5-20 The Assembling of Pile Head Deflection Using the Multi-Sublayer Technique

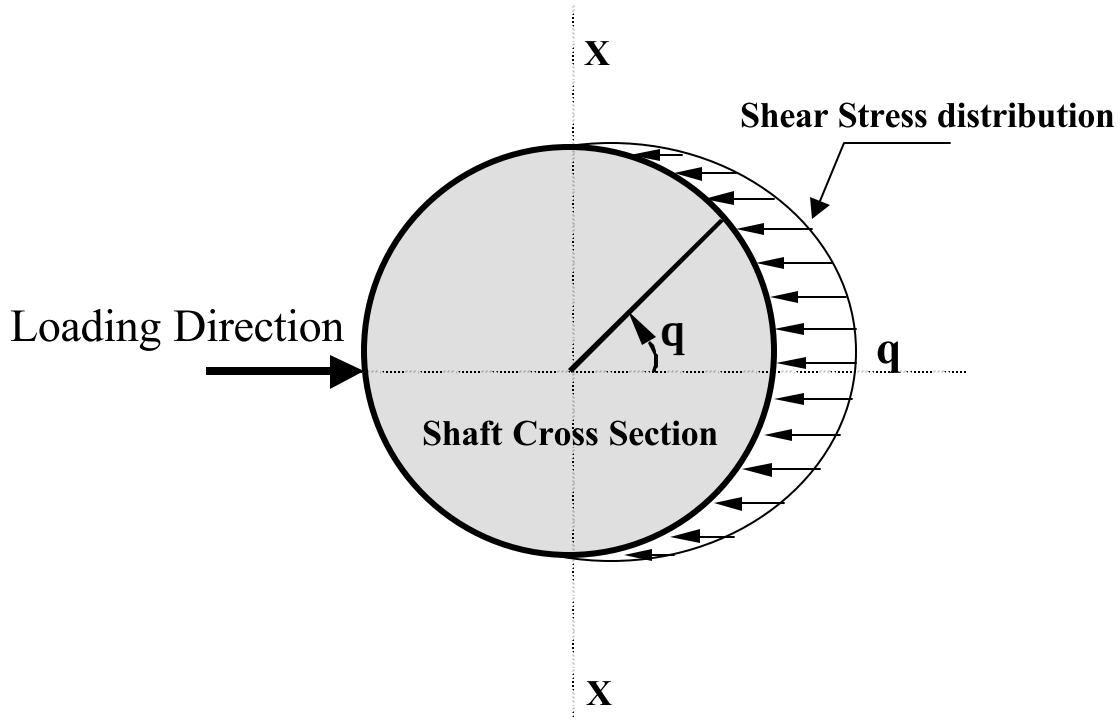

Fig. 5-21 Vertical Side Shear Stress Distribution on the Shaft Cross Section

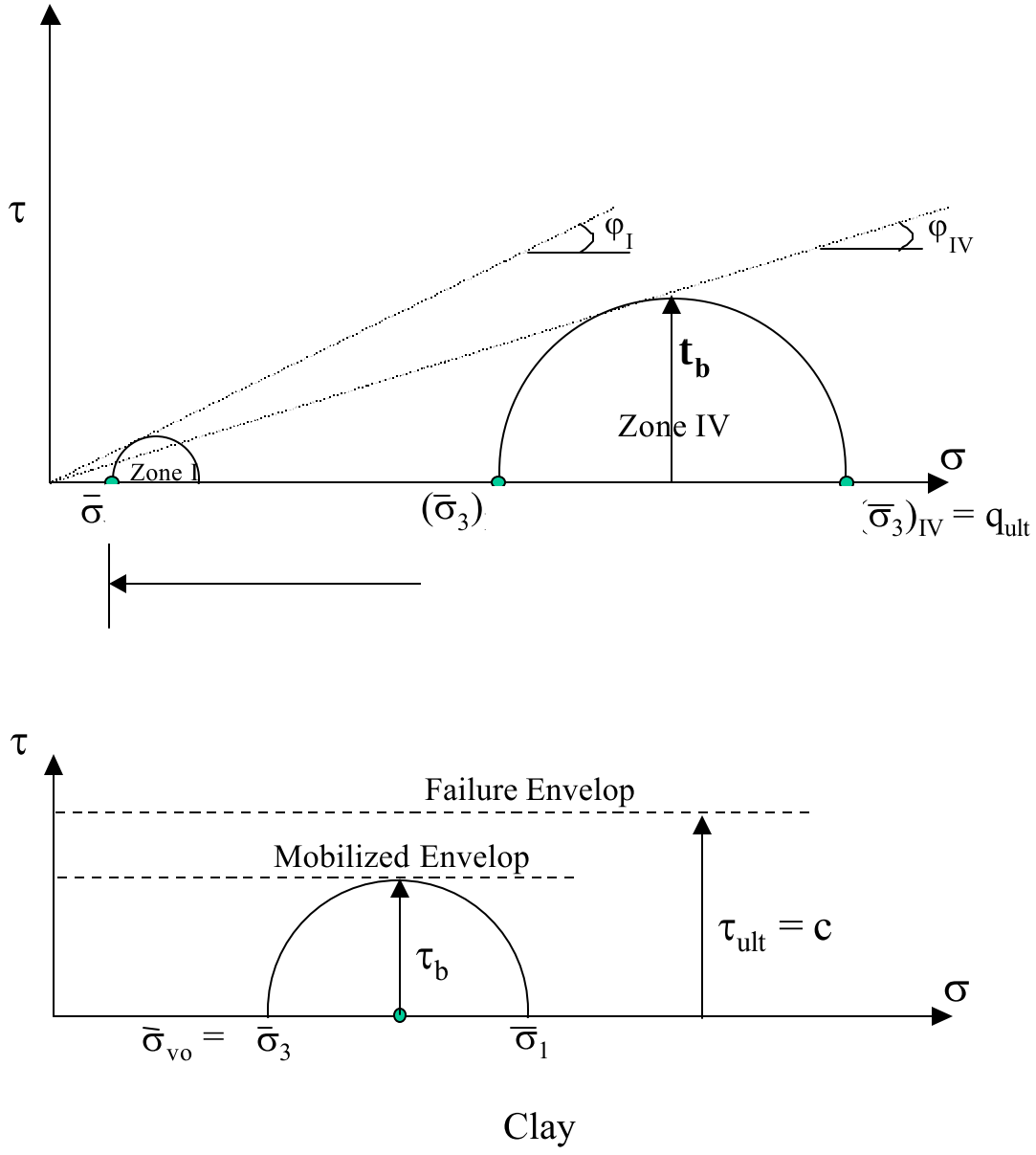

Fig. 5-22 Mobilized Shear Resistance at the Shaft Base in Sand and Clay

CHAPTER 6

SHAFTS IN LIQUEFIABLE SOILS

6.1 INTRODUCTION

This chapter presents the procedure developed to assess the response of the partially and completely liquefied granular soil as a post-liquefaction analysis. The SW model, initially developed to assess the relationship between one-dimensional beam on elastic foundation (BEF) or so called "p-y" curve behavior and three dimensional soil pile interaction, has been extended to include laterally loaded piles/shafts in liquefiable soil. Because the SW model relies on the undrained stress-strain characterization of the soil as occurs in the triaxial test, it is capable of treating one or more layers of soils that experience limited or full liquefaction. This chapter provides a methodology to assess the post-liquefaction response of an isolated pile/shaft in sand under an applied pile/shaft head load/moment combination assuming undrained conditions in the sand. The degradation in soil strength due to the free-field excess porewater ($u_{xs,ff}$), generated by the earthquake that results in developing or full liquefaction, is considered along with the near-field excess porewater pressure ($u_{xs,\ nf}$) generated by lateral loading from the superstructure.

Current design procedures assume slight or no resistance for the lateral movement of the pile in the liquefied soil which is a conservative practice. Alternatively, if liquefaction is assessed not to occur, some practitioners take no account of the increased $u_{xs,ff}$, and none consider the additional $u_{xs,\ nf}$ due to inertial interaction loading from the superstructure; a practice that is unsafe in loose sands. The paper characterizes the reduction in pile response and the changes in the associated p-y curves due to a drop in sand strength and Young's modulus as a result of developing liquefaction in the sand followed by inertial interaction loading from the superstructure.

The potential of soil to liquefy is one of the critical research topics of the last few decades. Several studies and experimental tests have been conducted for better understanding on the potential of soil to liquefy in both the free- and/or near-field soil regions. However, predicting the response of pile foundations in

liquefied soil or soil approaching liquefaction is very complex.

The procedure presented predicts the post-liquefaction behavior of laterally loaded piles in sand under developing or fully liquefied conditions. Due to the shaking from the earthquake and the associated lateral load from the superstructure, the free field $u_{xs,ff}$ and near-field $u_{xs,nf}$ develop and reduce the strength of loose to medium dense sand around a pile. The soil is considered partially liquefied or experiencing developing liquefaction if the excess porewater pressure ratio (r_u) induced by the earthquake shaking (i.e. $u_{xs,ff}$) is less than 1, and fully liquefied if $r_u = 1$. Therefore, the stress-strain response of the soil due to the lateral push from the pile as the result of superstructure load (and $u_{xs,nf}$) can be as shown in Fig. 6-1. Full-scale load tests on the post-liquefaction response of isolated piles and a pile group, performed at the Treasure Island and Cooper River Bridge (Ashford and Rollins 1999; and S&ME Inc. 2000) presented in Chapter 8, are the most significant related tests. However, the profession still lacks a realistic procedure for the design of pile foundations in liquefying or liquefied soil.

The most common practice employed is that presented by (Wang and Reese 1998) in which The traditional p-y curve for clay is used but based on the undrained residual strength (S_r) of the sand. As seen in Fig. 6-2 (Seed and Harder, 1990), S_r can be related to the standard penetration test (SPT) corrected blowcount, $(N_1)_{60}$. However, a very large difference between values at the upper and lower limits at a particular $(N_1)_{60}$ value affects the assessment of S_r tremendously. Even if an accurate value of S_r is available, S_r occurs at a large value of soil strain. In addition, a higher peak of undrained resistance is ignored in the case of the partially liquefied sand, while greater resistance at lower strain is attributed to the sand in the case of complete liquefaction. Such clay-type modeling can, therefore, be either too conservative (if $r_u < 1$) or unsafe (if $r_u = 1$). Furthermore, the p-y curve reflects soil-pile-interaction, not just soil behavior. Therefore, the effect of soil liquefaction (i.e. degradation in soil resistance) does not reflect a one-to-one change in soil-pile or p-y curve response.

The post-liquefaction stress-strain characterization of a fully or partially liquefied soil is still under investigation by several researchers. The current assessment of the resistance of a liquefied soil carries a

lot of uncertainty. This issue is addressed experimentally (Seed 1979; and Vaid and Thomas 1995) showing the varying resistance of saturated sands under undrained monotonic loading after being liquefied under cyclic loading corresponding to the free-field shaking of the earthquake (Fig. 6-3).

With lateral loading from the superstructure with a significant drop in the confining pressure following full liquefaction or partial liquefaction, the sand responds in a dilative fashion. However, a partially liquefied sand with a small drop in confining pressure may experience contactive behavior followed by dilative behavior under compressive monotonic loading. The post cyclic response of sand, particularly after full liquefaction, reflects a stiffening response, regardless of its initial (static) conditions (density or confining pressure). As seen in Fig. 6-4, there is no particular technique that allows the assessment of the p-y curve and its varying pattern in a partially or fully liquefied sand. Instead, the soil's undrained stress-strain relationship should be used in a true soil-pile interaction model to assess the corresponding p-y curve behavior. Because the traditional p-y curve is based on field data, a very large number of field tests for different pile types in liquefying sand would be required to develop a realistic, empirically based, p-y characterization.

6.2 METHOD OF ANALYSIS

Due to cyclic loading, excess porewater pressure ($\Delta u_c = u_{xs,ff}$) develops and reduces the effective consolidation confining pressure from $\bar{\sigma}_{3c}$ (= $\bar{\sigma}_{vo}$) to $\bar{\sigma}_{3cc}$. As given in Eqn. 6-1, if Δu_c is less than $\bar{\sigma}_{3c}$, sand will be "partially" liquefied and $\bar{\sigma}_{3cc} > 0$. Once Δu_c is equal to $\bar{\sigma}_{3c}$, the sand is completely liquefied ($r_u = 1$) and $\bar{\sigma}_{3cc} = 0$. $\bar{\sigma}_{3cc}$ is the post-cyclic effective confining stress.

$$\bar{\sigma}_{3cc} = \bar{\sigma}_{3c} - \Delta u_c \qquad (6\text{-}1)$$

The degradation in soil resistance due to earthquake shaking and the induced $u_{xs,ff}$ is based on the procedures proposed in (Seed et al. 1983). This $u_{xs,\,ff}$ reduces the effective stress and, therefore, the corresponding soil resistance for subsequent (post cyclic) undrained load application. This is followed by

the assessment of the $u_{xs,\ nf}$ in the near-field soil region induced by the lateral load from the superstructure. The variation in soil resistance (undrained stress-strain relationship) around the pile (near-field zone) is evaluated based on the undrained formulation for saturated sand presented in Ashour and Norris (2000).

The assessed value of the free-field excess porewater pressure ratio, r_u, induced by the earthquake is obtained using Seed's method (Seed et al. 1983). $u_{xs,\ ff}$ is calculated conservatively at the end of earthquake shaking corresponding to the number of equivalent uniform cycles produced over the full duration of the earthquake. Thereafter, the lateral load (from the superstructure) is applied at the pile head that generates additional porewater pressure ($u_{xs,\ nf}$) in the soil immediately around the pile, given the degradation in soil strength already caused by $u_{xs,\ ff}$. Note that $u_{xs,\ ff}$ is taken to reduce the vertical effective stress from its pre-earthquake state ($\bar{\sigma}_{vo}$), to $\bar{\sigma}_v = (1 - r_u)\ \bar{\sigma}_{vo}$. Thereafter, the behavior due to an inertial induced lateral load is assessed using the undrained stress-strain formulation presented in this chapter with the SW model (Ashour and Norris 1999 and 2001; and Ashour et al. 1998).

6.2.1 Free-Field Excess Pore Water Pressure, $u_{xs,\ ff}$

A simplified procedure for evaluating the liquefaction potential of sand for level ground conditions (Seed et al. 1998) is developed based on the sand's corrected SPT blow count, $(N_1)_{60}$. The $u_{xs,\ ff}$ in sand or silty sand soils due to the equivalent history of earthquake shaking can likewise be assessed. The procedure requires knowledge of the total and effective overburden pressure (σ_{vo} and $\bar{\sigma}_{vo}$ respectively) in the sand layer under consideration, the magnitude of the earthquake (M), the associated maximum ground surface acceleration (a_{max}) at the site, and the percentage of fines in the sand. The cyclic stress ratio, CSR [$(\tau_h)_{ave}$ / $\bar{\sigma}_{vo}$], induced by the earthquake at any depth is computed. If N cycles of CSR are induced, but N_L cycles are required to liquefy the sand at this same stress ratio, then the excess porewater pressure ratio (r_u) generated is given as a function of N/N_L. Given r_u, the $u_{xs,\ ff}$ generated and the resulting reduced vertical effective stress are expressed as

$$u_{xs,ff} = r_u \bar{\sigma}_{vo} \quad and \quad \bar{\sigma}_v = (1 - r_u)\ \bar{\sigma}_{vo} \tag{6-2}$$

It should be noted that the effect of the pore water pressure in the free field will be considered in the assessment of the t-z curve. As a result, the axial and lateral resistance of the shaft will be affected.

6.2.2 Near-Field Excess Pore Water Pressure, $u_{xs,\ nf}$

The technique developed by Norris et al. (1997) and formulated by Ashour and Norris (1999) employs a series of drained tests, with volume change measurements, on samples isotropically consolidated to the same confining pressure, $\bar{\sigma}_{3c}$, and void ratio, e_c, to which the undrained test is to be subjected. However, the drained tests are rebounded to different lower values of effective confining pressure, $\bar{\sigma}_3$, before being sheared. Such a technique allows the assessment of undrained behavior of isotropically consolidated sand at $\bar{\sigma}_{3c}$ and subjected to compressive monotonic loading (Fig. 6-5, no cyclic loading). During an isotopically consolidated undrained (ICU) test, the application of a deviatoric stress, σ_d, in compressive monotonic loading causes an additional porewater pressure, $\Delta u_d = u_{xs,\ nf}$, that results in a lower effective confining pressure (Fig. 6-5c), $\bar{\sigma}_{3,}$ i.e.

$$\bar{\sigma}_3 = \bar{\sigma}_{3c} - \Delta u_d \qquad \text{(No cyclic loading, near-field pore water pressure only)} \qquad (6\text{-}3)$$

and an associated isotropic expansive volumetric strain, $\varepsilon_{v,iso}$, the same as recorded in an isotropically rebounded drained triaxial test. However, in the undrained test, the volumetric change or volumetric strain must be zero. Therefore, there must be a compressive volumetric strain component, $\varepsilon_{v,\ shear}$, due to the deviatoric stress, σ_d. This shear induced volumetric strain, $\varepsilon_{v,\ shear}$, must be equal and opposite to $\varepsilon_{v,\ iso}$, so that the total volumetric strain, $\varepsilon_v = \varepsilon_{v,\ iso} + \varepsilon_{v,\ shear}$, in undrained response is zero. In the isotropically rebounded drained shear test, $\varepsilon_{v,\ iso}$ and then $\varepsilon_{v,shear}$ (to match $\varepsilon_{v,\ iso}$) are obtained separately and sequentially; in the undrained test, they occur simultaneously (Figs. 6-5a and 6-5b).

$$\varepsilon_{v,\ shear} = -\varepsilon_{v,\ iso} \qquad (6\text{-}4)$$

During drained isotropic expansion, the resulting axial strain, ε_1, is

$$\varepsilon_{1,iso} = \varepsilon_{2,iso} = \varepsilon_{3,iso} = \frac{1}{3}\varepsilon_{v,iso} \tag{6-5}$$

Based on Hooke's Law and effective stress concepts (Norris et al. 1998), the undrained axial strain due to shear (σ_d) and effective stress ($\bar{\sigma}_3$) changes can be related to the drained or effective stress strains as

$$(\varepsilon_1)_{undrained} = (\varepsilon_1)_{\sigma_d} + (\varepsilon_1)_{\Delta\bar{\sigma}_3} = (\varepsilon_1)_{drained} + \varepsilon_{1,iso} = (\varepsilon_1)_{drained} + \frac{1}{3}\varepsilon_{v,iso} \tag{6-6}$$

Therefore, with isotropically consolidated-rebounded drained triaxial tests available for different $\bar{\sigma}_3$, one can assume a value of $\bar{\sigma}_3$, find $\varepsilon_{v,iso}$ (Fig. 6-5b), enter the ε_v-ε_1 drained shear curves (Fig. 6-5a) at $\varepsilon_{v,shear}$ equal to $\varepsilon_{v,iso}$, and find the drained ε_1 and σ_d on the same confining pressure ($\bar{\sigma}_3$) ε_v-ε_1 and ε_1-σ_d curves. Then $(\varepsilon_1)_{undrained}$ is established according to Eqn. 6-6, and one point on the undrained σ_d-ε_1 curve can be plotted. The corresponding effective stress path ($\bar{p} = \bar{\sigma}_3 + \sigma_d/2$ versus $q = \sigma_d/2$) can also plotted as shown in Fig. 6-5c.

This technique is extended in this paper to incorporate the free-field excess porewater pressure induced by cyclic loading (Δu_c) and its influence on the undrained behavior of sands under the compressive monotonic loading whether the sand is partially or completely liquefied (Fig. 6-1). The following equations account for the pore water pressure in the free- and near-field ($u_{xs,ff}$ and $u_{xs,nf}$)

$$\bar{\sigma}_3 = (\bar{\sigma}_{3c} - \Delta u_c) - \Delta u_d = \bar{\sigma}_{3cc} - \Delta u_d$$

($\bar{\sigma}_{3cc} > 0$ and $r_u < 1$ partial liquefaction) (6-7)

$$\bar{\sigma}_3 = \bar{\sigma}_{3c} - \Delta u_c - \Delta u_d = -\Delta u_d$$

($\bar{\sigma}_{3c} = \Delta u_c$, i.e. $\bar{\sigma}_{3cc} = 0$ and $r_u = 1$ complete liquefaction) (6-8)

If $u_{xs,ff}$ is equal to $\bar{\sigma}_{3c}$ (i.e. $r_u = 1$), the sand will experience a fully liquefied state ($\bar{\sigma}_{3cc} = 0$) due to the

earthquake shaking . However, the sand is subjected to limited liquefaction when $r_u < 1$.

Based on experimental data obtained by several researchers for different sands, Ashour and Norris (1999) established a set of formulations that allows the assessment of the relationships seen in Figs. 6-5a and 6-5b. These formulations depend on the basic properties of sand and have been modified in this chapter to incorporate the initial effect of cyclic loading and the induced Δu_c on the post-liquefaction behavior of partially or completely liquefied sands.

A. Post-liquefaction Behavior of Partially Liquefied Sands

($\bar{\sigma}_{3cc} > 0$ or $\Delta u_c < \bar{\sigma}_{3c}$ because $r_u < 1$)

From ABC on the $\varepsilon_{v,\,shear}$-ε_1 curve (Fig. 6-8) and for $\bar{\sigma}_3 < \bar{\sigma}_{3cc}$ (associated with point r and the path r-s - $\bar{r}$ in Figs. 6-6a and 6-6b), the initial slope (S_A), $(\varepsilon_1)_B$ and $(\varepsilon_{v,shear})_{max}$ at point B, and $(\varepsilon_1)_C$ and $(\varepsilon_v)_C$ at point C are assessed based on Eqns. 6-9 through 6-14 (Ashour and Norris 1999).

$$(S_A)_{\bar{\sigma}_{3cc}} = \frac{1}{\exp(\beta^2 + Dr_c)} \tag{6-9}$$

$$(\varepsilon_{v,\,shear})_{B,\bar{\sigma}_{3cc}} = (\varepsilon_{v,shear})_{max,\bar{\sigma}_{3cc}} = 2\left[\frac{\varepsilon^2_{50}}{\exp(Dr_c)}\right]_{\bar{\sigma}_{3cc}} \tag{6-10}$$

$$(\varepsilon_1)_{B,\bar{\sigma}_{3cc}} = \frac{6(\varepsilon_{v,\,shear})_{max,\bar{\sigma}_{3cc}}}{\exp(\beta\, Dr_c)} \tag{6-11}$$

$$(\varepsilon_{v,\,shear})_{C,\bar{\sigma}_{3cc}} = (\varepsilon_{v,\,shear})_{max,\bar{\sigma}_{3cc}}\left[\frac{(\varepsilon_1)_{B,\bar{\sigma}_{3cc}}}{(\varepsilon_1)_{C,\bar{\sigma}_{3cc}}}\right]^{0.2}\left[1+(S_f)_{\bar{\sigma}_{3cc}}\right] \tag{6-12}$$

$$(\varepsilon_1)_{C,\bar{\sigma}_{3cc}} = 6(\varepsilon_{v,shear})_{max,\bar{\sigma}_{3cc}} \exp(\tan^2\phi) \tag{6-13}$$

$$(S_f)_{\bar{\sigma}_{3cc}} = -\,\rho^{0.5}\, Dr_c \tan^2 \phi \qquad (6\text{-}14)$$

Note that Dr_c (the relative density of consolidation in these equations) is a decimal value.

The empirically calculated slopes and coordinates at points A, B, and C on the ε_1-$\varepsilon_{v,\,shear}$ curve (Fig. 6-8) at $\bar{\sigma}_3 < \bar{\sigma}_{3cc}$ (OCR = $\bar{\sigma}_{3cc} / \bar{\sigma}_3$) are used in the determination of the constants (Eqns. 6-15 through 20 by Ashour and Norris 1999) of the binomial equation that describes the isotropically consolidated rebounded ε_1-$\varepsilon_{v,\,shear}$ curve. The following equations are associated with the path r-s- $\bar{r}$ as seen in Fig. 6-6a.

$$(S_A)_{\bar{\sigma}_3} = \frac{(S_A)_{\bar{\sigma}_{3cc}}}{OCR^{0.5}} \left[\frac{(\varepsilon_{v,shear})_{\max,\bar{\sigma}_3}}{(\varepsilon_{v,shear})_{\max,\bar{\sigma}_{3cc}}} \right]^{0.25} \qquad (6\text{-}15)$$

$$(\varepsilon_{v,\,shear})_{\max,\bar{\sigma}_3} = \frac{(\varepsilon_{v,shear})_{\max,\bar{\sigma}_{3cc}}}{OCR^{m}} \qquad (6\text{-}16)$$

$$m = \rho^{0.8} \exp\left[\frac{Dr\ \rho}{OCR} \right] \qquad (6\text{-}17)$$

where $OCR = \dfrac{\bar{\sigma}_{3cc}}{\bar{\sigma}_3}$ *for* $\bar{\sigma}_3 \le \bar{\sigma}_{3cc}$; $OCR = \dfrac{\bar{\sigma}_3}{\bar{\sigma}_{3cc}}$ *for* $\bar{\sigma}_3 \ge \bar{\sigma}_{3cc}$

$$(\varepsilon_1)_{B,\bar{\sigma}_3} = (\varepsilon_1)_{B,\sigma_{3c}} \left[\frac{(\varepsilon_{v,\,shear})_{\max,\bar{\sigma}_3}}{(\varepsilon_{v,shear})_{\max,\bar{\sigma}_{3cc}}} \right]^{0.5} \qquad (6\text{-}18)$$

$$\left(\varepsilon_{v,shear}\right)_{C,\bar{\sigma}_3} = \left(\varepsilon_{v,shear}\right)_{\max,\bar{\sigma}_3} \frac{\left(\varepsilon_{v,shear}\right)_{C,\bar{\sigma}_{3c}}}{\left(\varepsilon_{v,shear}\right)_{\max,\bar{\sigma}_{3c}}} \tag{6-19}$$

$$\left(e_1\right)_{C,\bar{\sigma}_3} = \left(e_1\right)_{C,\bar{\sigma}_{3cc}} \left[\frac{\left(e_1\right)_{B,\bar{\sigma}_3}}{\left(e_1\right)_{B,\bar{\sigma}_{3cc}}}\right]^{0.25} \tag{6-20}$$

$$\left(S_f\right)_{\bar{\sigma}_3} = \left(S_f\right)_{\bar{\sigma}_{3cc}} \tag{6-21}$$

As seen in the above equations, $\bar{\sigma}_{3cc}$ is undertaken as a reference value for OCR. ρ is the sand grain roundness parameter.

- **Isotropically Rebounded and Consolidated Volume Change of Partially Liquefied Sand ($\bar{\sigma}_3$ - $\varepsilon_{v,iso}$)**

The ($\bar{\sigma}_3$ - $\varepsilon_{v,iso}$) relationship seen in Fig. 6-5b is modified to assess the ($\bar{\sigma}_3$ - $\varepsilon_{v,iso}$) relationship for sand that has developed partial (limited) liquefaction as the result of cyclic loading (at point r) and been rebounded to point s in Figs. 6-6a and 6-6b. The value of $(\varepsilon_v)_c$ located on the backbone isotropic curve is calculated by Eqn. 6-22.

$$\left(\varepsilon_v\right)_c = I_7 = \varepsilon_{50} \exp\left[Dr_c\left(1+\rho\right)\right] \tag{6-22}$$

$$\varepsilon_{v,iso} = \left(\varepsilon_v\right)_c - \frac{\left(\varepsilon_v\right)_c}{OCR^h} \tag{6-23}$$

$$where \quad h = \frac{\rho^{0.1}}{4} \exp\left(0.5\,\rho\,Dr_c\right), and$$

$$OCR = \frac{\bar{\sigma}_{3cc}}{\bar{\sigma}_3} \quad for \quad \bar{\sigma}_3 \le \bar{\sigma}_{3cc}; \qquad OCR = \frac{\bar{\sigma}_3}{\bar{\sigma}_{3cc}} \quad for \quad \bar{\sigma}_3 \ge \sigma_{3cc}$$

The above procedure can be applied as long the excess porewater pressure ratio (r_u) induced by cyclic loading is less than 1 and the residual confining pressure ($\bar{\sigma}_3$) is greater than zero at point r (partially liquefied soil). Under monotonic loading, the partially liquefied sand may then experience a contractive response associated with a reduction in $\bar{\sigma}_3$ (from point r to point s in Figs. 6-6a and 6-6b) to reach the lowest value of $\bar{\sigma}_3$, and then rebound (dilate) with increasing $\bar{\sigma}_3$ until $\bar{\sigma}_3 = \bar{\sigma}_{3cc}$ again (point $\bar{r}$ in Figs. 6-6a and 6-6b). Sand continues to dilate beyond $\bar{\sigma}_{3cc}$ (Figs. 6-6a and 6-6b) with increasing $\bar{\sigma}_3$ and net negative porewater pressure. It should be noted that when $\bar{\sigma}_3 < \bar{\sigma}_{3cc}$, $\varepsilon_{v,iso}$ rebounds to point s and then recompresses. This is associated with an equal net compressive $\varepsilon_{v,shear}$. However, when $\bar{\sigma}_3 > \bar{\sigma}_{3cc}$, $\varepsilon_{v,iso}$ moves from $\bar{r}$ to $\bar{s}$ and an equal dilative $\varepsilon_{v,shear}$ develops simatanuously. In the undrained test, the volume change or volumetric strain must be zero such that at all times $\varepsilon_{v,iso} = -\varepsilon_{v,shear}$.

As applied in Fig. 6-5a, ε_1 associated with $\Delta\bar{\sigma}_3$ and $\varepsilon_{v,shear}$ represents the current drained axial strain. Based on Eqns. 6-5 and 6-6, the drained ε_1 is converted to the undrained ε_1. The associated deviator stress (σ_d) is determined as follows,

$$\sigma_d = SL(\sigma_d)_f = \bar{\sigma}_3\left[\tan^2\left(45 + \frac{\phi}{2}\right) - 1\right] \qquad (6\text{-}24)$$

The varying stress level (SL) is a function of ε_1, ε_{50}, and $\bar{\sigma}_3$ as presented by Ashour and Norris (1999).

B. Post-liquefaction Behavior of Completely (Fully) Liquefied Sands

(` $\sigma_{3cc}$ = 0 or $\Delta u_c$ =` σ_{3c} and r_u = 1)

Once the soil is completely liquefied (i.e. r_u =1, $\bar{\sigma}_3$ and σ_d are equal to zero) due to cyclic loading, the above procedure must be modified in order to handle a different type of behavior. As seen in Fig. 6-3, the completely liquefied soil loses its strength when the excess porewater pressure due to cyclic loading is equal

to the effective confining pressure ($u_{xs} = \Delta u_c = \bar{\sigma}_{3c}$) and the porewater pressure ratio (r_u) = 1. By applying monotonic loading thereafter, u_{xs} decreases and causes a growth in confining pressure (effective stress). This will be accompanied by a growth in sand resistance (σ_d).

As seen in Fig. 6-3 beyond a certain value of strain ($\varepsilon_1 = x_o$; $x_o \cong 20\%$ in the figure), u_{xs} decreases to zero and then to negative values. At $u_{xs} = 0$, sand exhibits resistance that is equal to that of initial loading at the same zero porewater pressure. Once u_{xs} becomes negative, $\bar{\sigma}_3$ will be larger than $\bar{\sigma}_{3c}$ and the undrained resistance will be greater than the drained strength.

Based on its Dr_c, the completely liquefied sand may experience a zero-strength transition zone with soil strain ($\varepsilon_1 \leq x_0$) and $r_u = 1$ before it starts to show some resistance, confining pressure ($\bar{\sigma}_3$) and dilative response (Fig. 6-3). This value of x_0 decreases with the increase of the sand relative density (D_r) and becomes approximately zero for dense sand.

As a result of the development of complete liquefaction by cyclic loading and the subsequent dilative response under an isotopically consolidated undrained (ICU) loading, two equal and opposite components of volume change (strain) develop in sand. In the undrained test, the total volumetric change or volumetric strain must be zero. Therefore, the shear induced volumetric strain, $\varepsilon_{v,\,shear}$, must be equal and opposite to $\varepsilon_{v,\,iso}$ (Eqn. 6-4). In the isotropically rebounded drained shear test, $\varepsilon_{v,\,iso}$ and then $\varepsilon_{v,\,shear}$ (to match $\varepsilon_{v,\,iso}$) are obtained separately and sequentially; in the undrained test, they occur simultaneously.

Figure 6-7 shows the drained dilative response of sand when $\varepsilon_{v,shear}$ is expansive and $\varepsilon_{v,\,iso}$ is compressive starting with $\bar{\sigma}_3 = 0$. As a result of the complete liquefaction under cyclic loading, $\bar{\sigma}_3 = \bar{\sigma}_{3cc} \cong 0$ (point r in Figs. 6-7a and 6-7b) and the associated $\varepsilon_{v,iso}$ at the start of undrained monotonic loading (point $\bar{r}$ in Figs. 6-7a and 6-7b). The change in the volumetric strain $\varepsilon_{v,\,iso}$ due the increase in $\bar{\sigma}_3$ is represented by the variation in $\varepsilon_{v,\,iso}$ (Fig. 6-7a) associated with $(\varepsilon_{v,shear})_{net\ dilative}$ in Fig. 6-7c. Equation 6-23 for $\varepsilon_{v,iso}$ is modified as follows:

$$\varepsilon_{v,iso} = \frac{(\varepsilon_v)_c}{OCR^h} - (\varepsilon_{v,iso})_a \qquad (6\text{-}25)$$

and

$$(\varepsilon_{v,iso})_a = \frac{(\varepsilon_v)_c}{(OCR^h)_{at\ Point\ \bar{r}}} \qquad where \quad OCR = \frac{\bar{\sigma}_{3c}}{\bar{\sigma}_3}$$

It should be noted that $\bar{\sigma}_3$ at point ($\bar{r}$) is approximately equal to zero. As observed experimentally and based on its relative density, the liquefied sand may experience a zero-resistance zone ($\bar{\sigma}_3 = 0$ and $\sigma_d = 0$) with a progressive axial strain (up to $\varepsilon_1 = x_0$) under the compressive monotonic loading. x_0 is determined from the drained rebounded ε_1-$\varepsilon_{v,shear}$ relationship at very small values of $\bar{\sigma}_3 \cong 0$ (Fig. 6-7). x_0 defines the end of complete liquefaction zone ($\Delta u_c = \bar{\sigma}_{3c}$) and indicates the subsequent growth in $\bar{\sigma}_3$ and σ_d, the degradation in the excess porewater pressure (Fig. 6-7a), and the development of dilative response (Fig. 6-7c). It should be noted that $\varepsilon_{v,shear}$ for the dilative sand represents the suppressed volume increase beyond the original volume of sand.

As seen in Fig. 6-7b, the resistance of completely liquefied sand under compressive monotonic loading lies on the failure envelope with stress level (SL) equal to 1. The variation of sand resistance after complete liquefaction due to its dilative response is a function of the varying $\bar{\sigma}_3$ and the full friction angle φ.

$$\sigma_d = SL(\sigma_d)_f = \bar{\sigma}_3 \left[\tan^2\left(45 + \frac{\varphi}{2} \right) - 1 \right] \qquad (6\text{-}26)$$

It should be noted that the values of the post-liquefaction response of sand depend on the magnitude of $\bar{\sigma}_3$ remaining after cyclic loading (Vaid and Thomas 1995).

6.3 CASE STUDIES

The approach developed here to assess the post-liquefaction behavior of liquefied sands has been verified through various comparisons to experimental results of different types of sands under monotonic loading

after being completely or partially liquefied by cyclic loading. The properties of these sands are presented in Table 6-1.

6.3.1 Post-Liquefaction Response of Completely Liquefied Nevada Sand

Figure 6-9 shows the good agreement between the measured and predicted post liquefaction resistance of Nevada sand under compressive monotonic loading. The sample tested was isotropically consolidated to $\bar{\sigma}_{3c}$ = 400 kPa at Dr_c = 15% and exhibited a drained $\varphi = 32^o$ and $\varepsilon_{50} = 0.0065$. The sample was completely liquefied by cyclic loading and then the undrained response shown in Fig. 6-9 was obtained (Nguyen 2002).

6.3.2 Post-Liquefaction Response of Completely Liquefied Ione Sand

Figure 6-10 shows the observed and predicted post-liquefaction response of Ione sand. Dr_c = 30%, for an isotropic consolidation pressure ($\bar{\sigma}_{3c}$) of 800 kPa and $\varphi = 29^o$ and $\varepsilon_{50} = 0.008$ in drained tests. Similar to Nevada sand, Ione sand was completely liquefied by cyclic loading and then subject to compressive monotonic loading (Nguyen 2002).

6.3.3 Post-liquefaction Response of Partially and Completely Liquefied Fraser River Sand

Vaid and Thomas (1995) performed a set of cyclic and then compressive monotonic loading tests to study the effect of residual confining pressure ($\bar{\sigma}_3$) on the post liquefaction behavior of a completely ($\bar{\sigma}_3 = 0$) and partially liquefied ($\bar{\sigma}_3 > 0$) Fraser sand. There is very good agreement between observed and predicted results in Fig. 6-11. The results shown in Fig. 6-11 for Fraser sand were obtained based on the completely liquefied status ($\bar{\sigma}_3 = 0$) for different Dr_c (Vaid and Thomas 1995).

Figure 6-12 shows the influence of partial or limited liquefaction induced by cyclic loading ($\bar{\sigma}_3 > 0$) on the post liquefaction behavior of 40% relative density samples of Fraser sand. The pre-cyclic consolidation pressure ($\bar{\sigma}_{3c}$) was 400 kPa, and the residual confining pressures induced by cyclic loading were 105 and 45 kPa, respectively.

6.4 UNDRAINED STRAIN WEDGE MODEL FOR LIQUEFIED SAND

The basic purpose of the SW model is to relate stress-strain-strength behavior of the soil in the wedge to one-dimensional Beam on Elastic Foundations (BEF) parameters. The SW model is, therefore, able to provide a theoretical link between the more complex three-dimensional soil-pile interaction and the simpler one-dimensional BEF characterization. As presented in Chapter 5, the SWM is based on the mobilized passive wedge in front of the pile (Fig. 6-13) which is characterized by base angle, β_m, the current passive wedge depth, h, and the spread of the wedge via the fan angle, φ_m (the mobilized effective stress friction angle). The horizontal stress change at the passive wedge face, $\Delta\sigma_h$, and side shear, τ, act as shown in Fig. 6-13.

The varying depth, h, of the deflected portion of the pile is controlled by the stability analysis of the pile under the conditions of soil-pile interaction. The effects of the soil and pile properties are associated with the soil-pile reaction along the pile via the Young's modulus of the soil (E), the stress level in the soil (SL), the pile deflection (y), and the modulus of subgrade reaction (E_s) between the pile segment and each soil sublayer (Chapter 5).

The shape of the wedge in any soil layer depends upon the properties of that layer and, therefore, would seem to satisfy the nature of a set of independent Winkler soil springs in BEF analysis. However, the mobilized depth (h) of the passive wedge at any time is a function of the various soils (and their stress levels) and the bending stiffness (EI) and head fixity condition of the pile. This, in turn, affects the resulting p-y response in a given soil layer; therefore, the p-y response is not a unique function of the soil alone. The governing equations of the mobilized passive wedge shape are applied within each soil sublayer (i) of a given deposit. The configuration of the wedge (Fig. 6-13) at any instant of load is a function of the stress level in the sublayer of sand and, therefore, its mobilized friction angle, φ_m. Note that

$$(\beta_m)_i = 45 + \frac{(\varphi_m)_i}{2}, \qquad \text{and}$$

$$\left(\overline{BC}\right)_i = D + (h - x_i)2\left(\tan\beta_m\right)_i\left(\tan\phi_m\right)_i \qquad (6\text{-}27)$$

where $\overline{BC}$ is the width of the wedge face at any depth. h symbolizes the current full depth of the passive wedge in front of the pile; x_i represents the depth from the top of the pile or passive wedge to the middle of the sublayer under consideration; and D indicates the width of the pile cross-section (Fig. 6-13). As presented in Chapter5, the geometry of the passive wedge(s) (short, intermediate or long shafts) is a function of the state of the soil. Consequently, the developing passive wedge in the liquefiable soil will be different from its original (as-is conditions) case under drained conditions.

Under undrained conditions, the major principal stress change ($\Delta\sigma_h$) in the wedge is in the direction of pile movement, and it is equivalent to the deviatoric stress (σ_d) in the isotropically consolidated undrained (ICU) triaxial test. Assuming that the horizontal direction in the field is taken as the axial direction in the triaxial test, the vertical stress change ($\Delta\sigma_v$) is zero and the perpendicular horizontal stress change ($\Delta\sigma_{ph}$) is taken to be the same. Corresponding to the (ICU) triaxial compression test, the deviatoric stress is increased, while the effective confining pressure decreases due to the positive induced excess porewater pressure, Δu_d. Note that Δu_d represents $u_{xs,nf}$ in the near-field region. The cycles of earthquake loading will generate excess porewater pressure in the free-field ($u_{xs,\,ff}$) that will reduce the effective stress in sand (Eqns. 6-1 and 6-2) according to its location below ground surface. Once the excess porewater pressure ($u_{xs,nf}$) increases due to the pile loading, the confining pressure in the sand around the pile reduces to

$$\overline{\sigma}_v = \overline{\sigma}_3 = (\sigma_{3c} - u_{xs,\,ff}) - u_{xs,nf} \qquad where \qquad \overline{\sigma}_h = \overline{\sigma}_v + \Delta\sigma_h \qquad (6\text{-}28)$$

$u_{xs,\,nf}$ (= Δu_d) is a function of stress level. Therefore, the assessment of the mobilized resistance of the sand ($\sigma_d = \Delta\sigma_h$) as a function of the axial strain (major strain) under undrained conditions allows the determination of the sand resistance and pile deformation at the associated undrained horizontal strain, ε_u. The current value of undrained Young's modulus in sand sublayer (i) which is associated with ε_u is given as

$$(E_u)_i = \left[\frac{\Delta \sigma_h}{\varepsilon_u}\right]_i = \left[\frac{\sigma_d}{\varepsilon_u}\right]_i \tag{6-29}$$

$$SL_i = \left[\frac{\Delta \sigma_h}{(\Delta \sigma_{hf})_{\bar{\sigma}_3}}\right]_i = \frac{(\sigma_d)_i}{(\bar{\sigma}_3)_i\left[\tan^2\left(45 + \frac{\varphi_i}{2}\right) - 1\right]}$$
$$= \frac{\tan^2\left(45 + \frac{(\varphi_m)_i}{2}\right) - 1}{\tan^2\left(45 + \frac{\varphi_i}{2}\right) - 1} \tag{6-30}$$

The major principal effective stress change, $\Delta\sigma_h$, in the passive wedge is in the direction of pile movement and is equivalent to the deviatoric stress change in the undrained triaxial test, σ_d (assuming that the horizontal direction in the field is taken as the axial direction in the triaxial test). The mobilized effective stress fanning angle, φ_m, of the passive wedge is related to the stress level or the strain in the sand. Knowing the soil strain, ε_u, the deviatoric stress, σ_d, and the associated instant effective confining pressure, $\bar{\sigma}_3$. φ_m can be determined from the associated effective stress-strain curve and effective stress path. Based on the approach presented in (Ashour and Norris 1999 and 2001), both the stress level, SL, and the mobilized angle of internal friction, φ_m, associated with the effective stress, $\bar{\sigma}_3$, and soil strain, ε_u, under undrained conditions can be calculated. Stress level (SL) relates σ_d (= $\Delta\sigma_h$) to σ_{df} (= $\Delta\sigma_{hf}$); where $\Delta\sigma_{hf}$ is the peak of the associated drained (i.e. current $\bar{\sigma}_3$) effective stress-strain curve.

The initial and subsequent values of confining pressure are not equal along the depth of the passive wedge of sand in front of the pile. Therefore, at the same value of horizontal soil strain (ε_u), the undrained resistance of the sand surrounding the pile varies throughout the depth of the passive wedge of sand providing different values of stress level. Such behavior requires the determination of the mobilized undrained resistance of the sand along the depth of the passive wedge. The SW model provides the means to divide the sand layer into equal-thickness sublayers in order to calculate the undrained sand response of each sublayer (i) according to the location and the properties of sand of that sublayer.

6.5 SOIL-PILE INTERACTION IN THE SW MODEL UNDER UNDRAINED CONDITIONS

By applying the drained SW model procedures for granular soil (Chapter 5), the modulus of subgarde reaction of sand under undrained conditions (E_{su}) at any sublayer (i) can be determined based on the associated values of E_u and SL. The SW model relies on calculating E_{su}, which reflects the soil-pile interaction at any level during pile loading or soil strain. By comparison with the drained E_s, in drained sand (Ashour et al. 1998), E_{su} is given in any sublayer (i) as

$$(E_{su})_i = \frac{p_i}{y_i} = \frac{D(A\varepsilon_u E_u)_i}{\delta(h - x_i)} = \frac{(A E_u)_i}{(h - x_i)} D(\Psi_u) \qquad (6\text{-}31)$$

Corresponding to a horizontal slice of (a soil sublayer) at a depth x (Fig. 6-13) under horizontal equilibrium, the soil-pile reaction, the undrained p_i (line load) is expressed as a function of $\Delta\sigma_h$ where $\Delta\sigma_h$ represents the mobilized undrained resistance in sand sublayer (i).

$$p_i = (\Delta\sigma_h)_i \overline{BC}_i S_1 + 2\tau_i D S_2 \qquad (6\text{-}32)$$

Shape factors S_1 and S_2 are equal to 0.75 and 0.5, respectively, for a circular pile cross section, and equal to 1.0 for a square pile; τ is shear stress along the sides of the pile. A is a parameter that governs the growth of the passive soil wedge and based on the concepts presented in Chapter 5. ψ_u is equal to 1.55 where the total stress Poisson's ratio for undrained sand is equal to 0.5. Equation 6-31 is based upon the undrained response of sand using the undrained stress-strain relationship (ε_u, σ_d and E_u). Once the values of E_{su} at any level of loading along the length of the deflected portion of the pile are calculated, the laterally loaded pile and the three-dimensional passive wedge in front of the pile can be transformed into a BEF problem and solved using a numerical technique such as the finite element method. The evaluation of E_{su}

as a function of soil and pile properties is the key point to the SW model analysis.

6.6 SUMMARY

The procedure presented yields the undrained lateral response of a laterally loaded pile/shaft in liquefiable soil incorporating the influence of both the developing excess porewater pressure in the free-field $u_{xs,\ ff}$ (due to ground acceleration) and the additional $u_{xs,\ nf}$ (due to the lateral load from the superstructure). The technique reflects the effect of soil liquefaction on the assessed (soil-pile reaction) p-y curves based on the reduced soil-pile interaction response (modulus of subgrade reaction). The capability of this procedure will (1) reduce the uncertainty of dealing with the behavior of laterally loaded piles in liquefiable soils and (2) allow estimation of realistic responses of laterally loaded piles in liquefiable soils based that properly account for local site conditions and shaft properties as demonstrated by the predictions for the Treasure Island and Cooper River Bridge load tests presented in Chapter 8.

Table 6-1. The properties of sands employed to demonstrate the approach presented

Material	Roundness (ρ)	e_{max}	e_{min}	C_u	Ref.
Nevada Sand (subrounded, clean, fine, white quartz, foundry sand)	0.45	0.856	0.548	1.6	Norris et al. (1995, 1997)
Ione Sand (subangular, clean, minerals, quartz, glass sand)	0.29	1.00	0.717	1.4	Norris et al. (1995, 1997)
Fraser River Sand (subangular to subrounded well graded quartz and feldspar sand)	0.4	1.00	0.68	1.5	Fukushima and Tatsuoka. (1984)

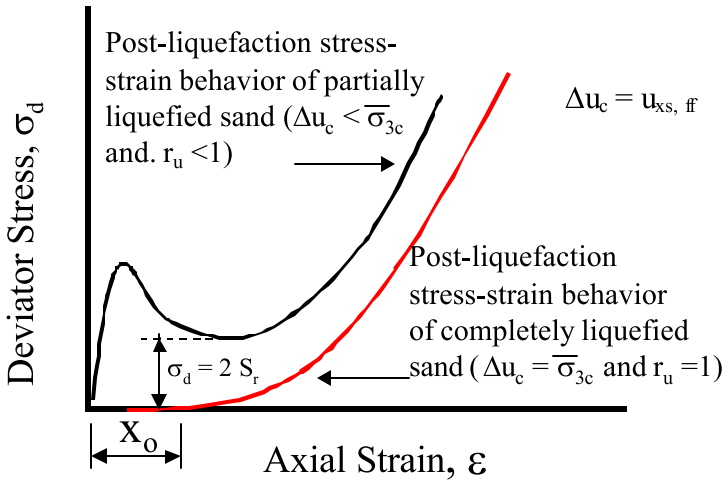

Fig. 6-1 Subsequent Undrained Stress-Strain Behavior of Sand that has Experienced Partial (r_u <1) or Complete (r_u =1) Liquefaction

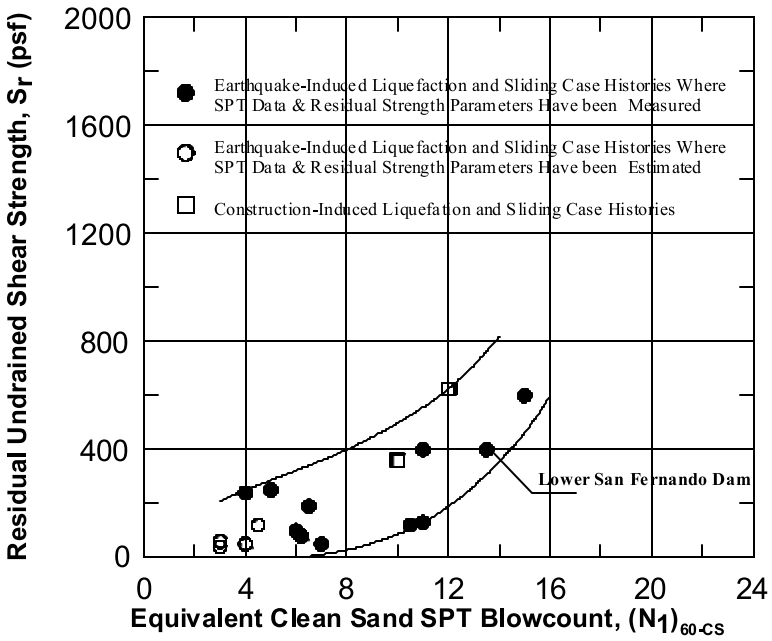

Fig. 6-2 Corrected Blowcount vs. Residual Strength (Seed and Harder, 1990)

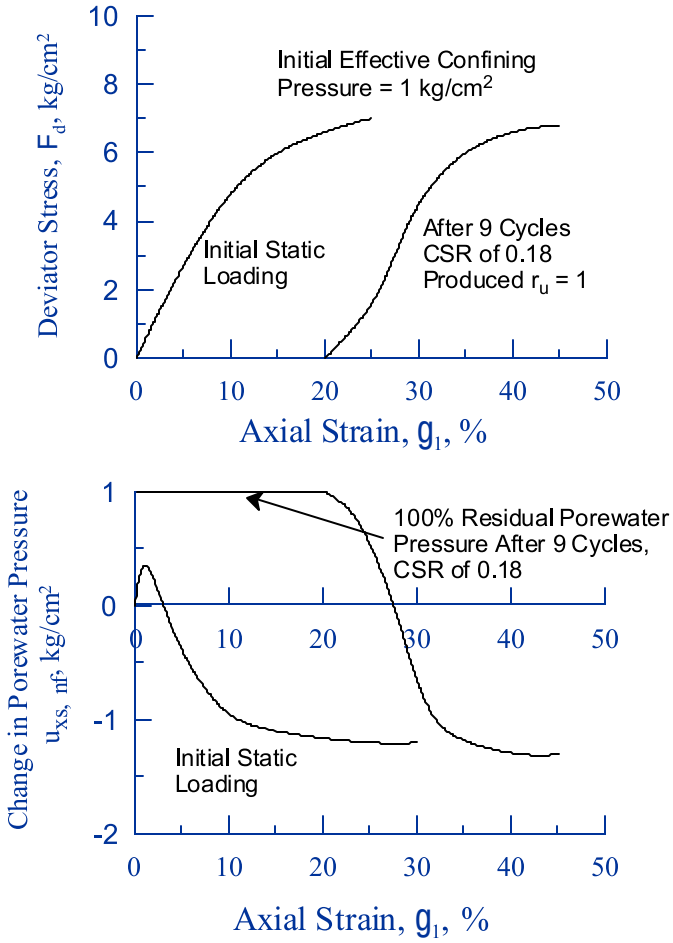

Fig. 6-3 Undrained Behavior of Sacramento Sand under Initial Static and Fully Liquefied Conditions (Seed 1979)

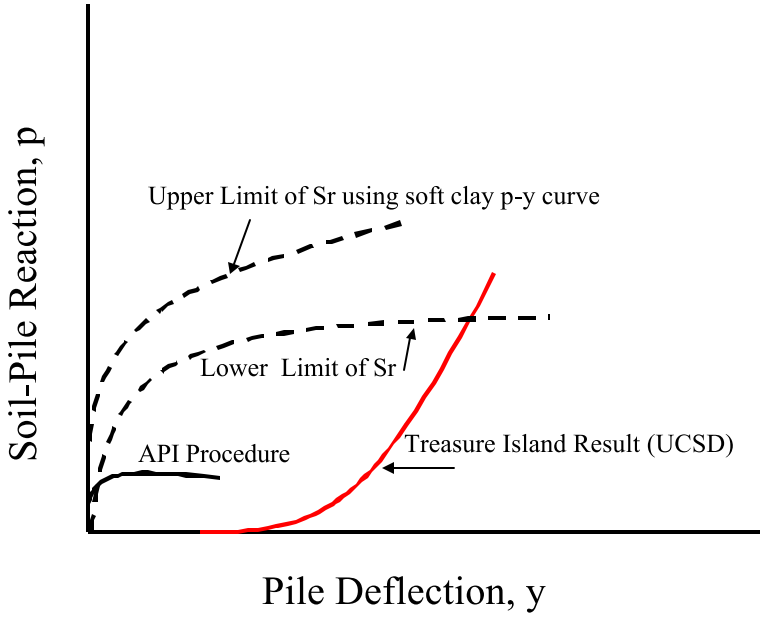

Fig. 6-4 Undrained p-y Curve in Liquefied Soil (Rollins et al. 2001)

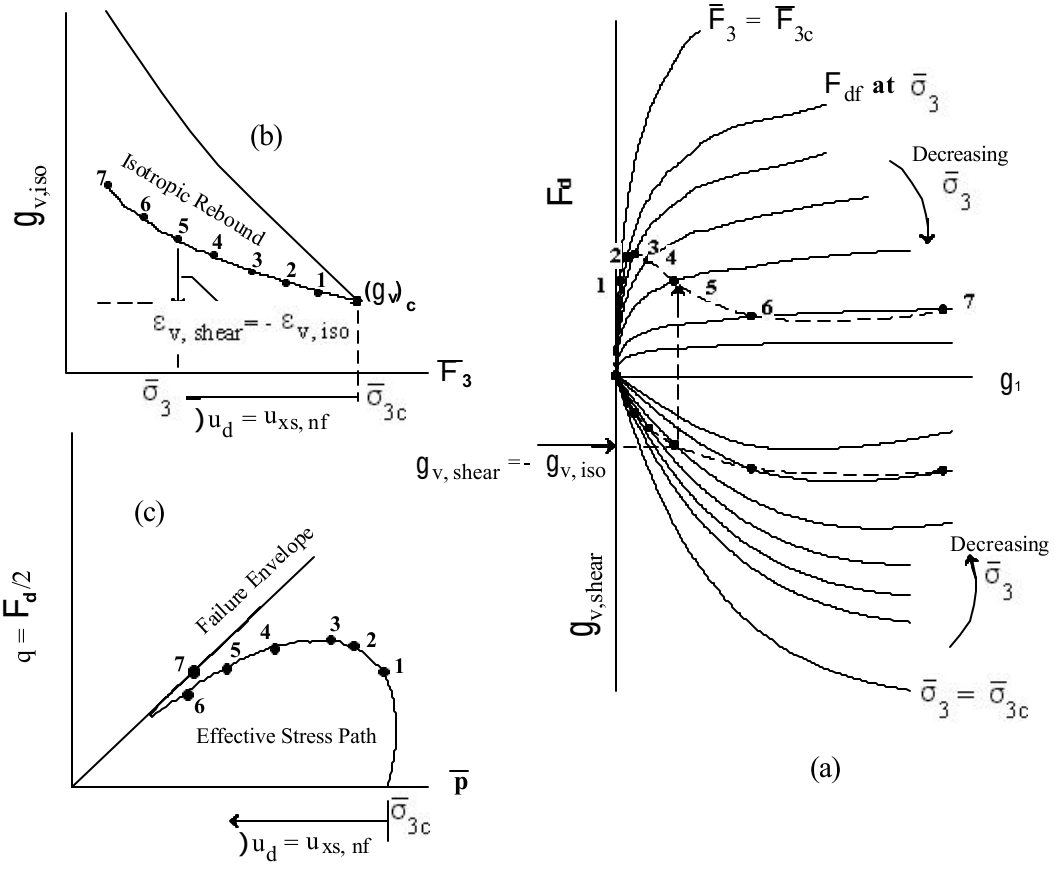

Fig. 6-5 Interrelationships Among
(a) Drained and Undrained Stress-Strain Behavior
(b) Isotropic Consolidation Rebound, and
(c) Undrained Effective Stress Path (Norris et al. 1997)

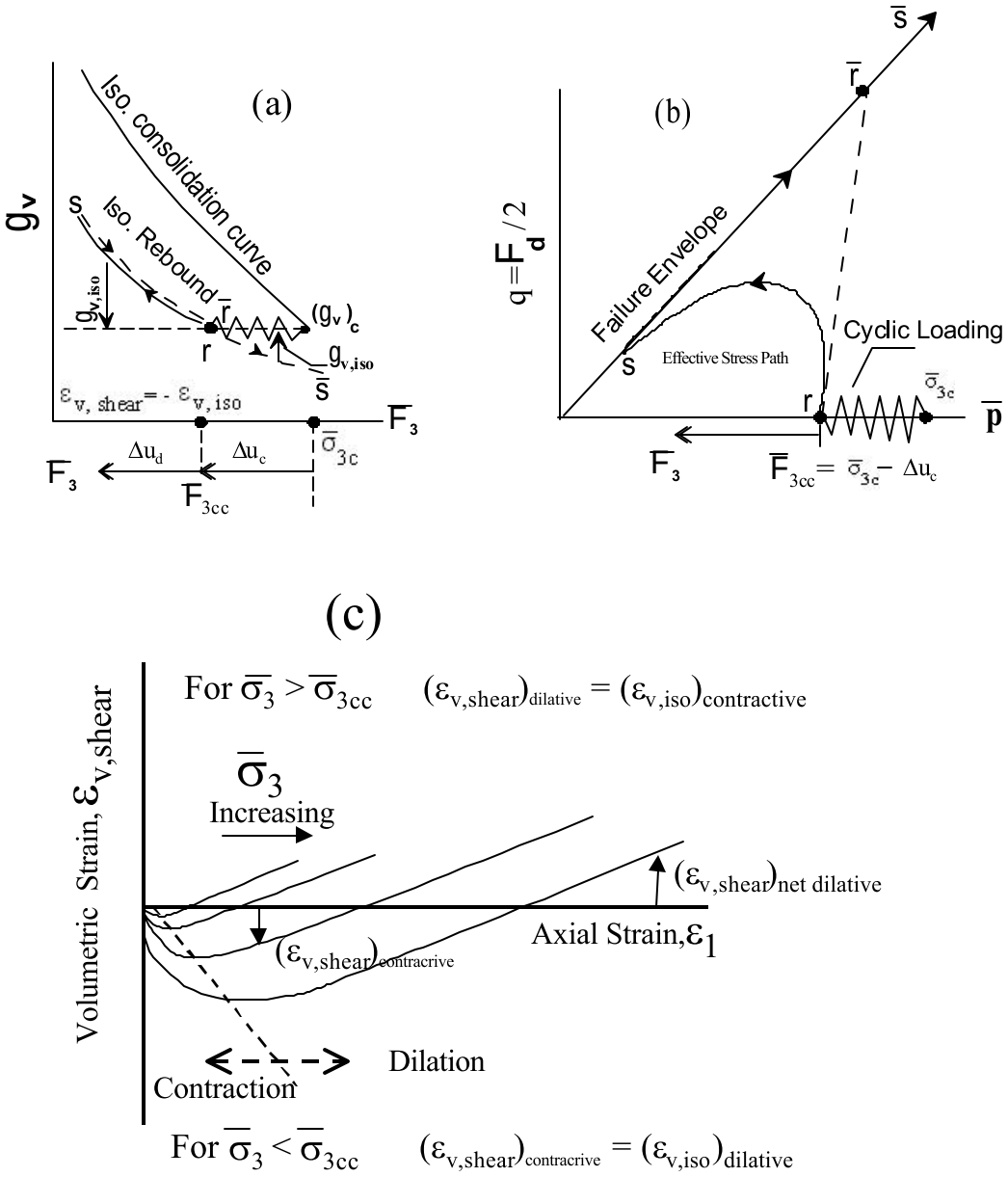

Fig. 6-6 Fully Liquefied Sand Interrelationships Among
(a) Isotropic Consolidation Followed by Cyclic Loading
(b) Undrained Effective Stress Path, and
(c) Drained Volumetric-Axia; Srain Behavior under Different Values of ` s 3

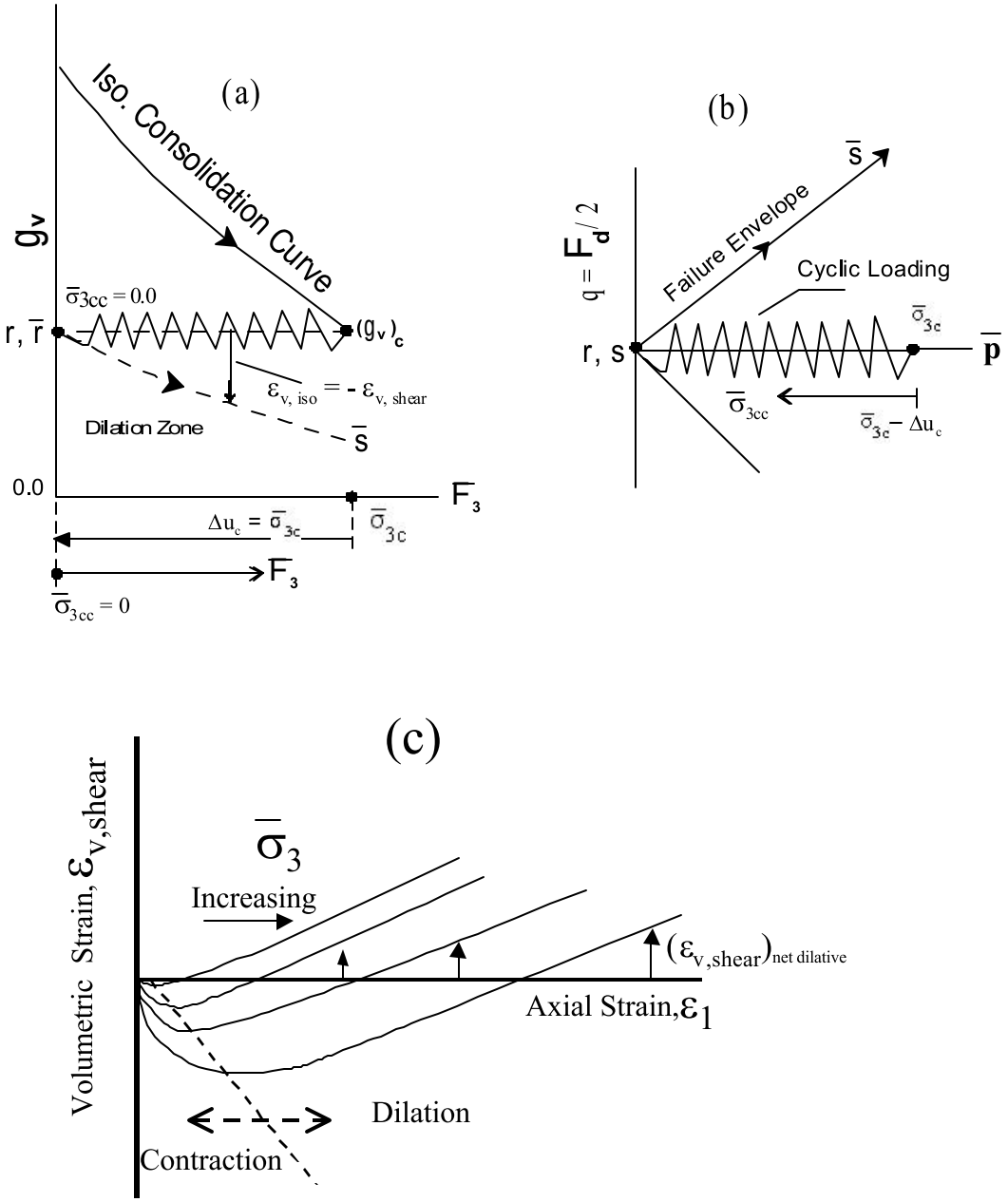

Fig. 6-7 Limited Liquefied Sand Interrelationships among
(a) Isotropic Consolidation Followed by Cyclic Loading (r_u <1)
(b) Undrained Effective Stress Path, and
(c) Drained Volumetric-Axial Strain Behavior under Different Values of Rebounded $\bar{s}_3$

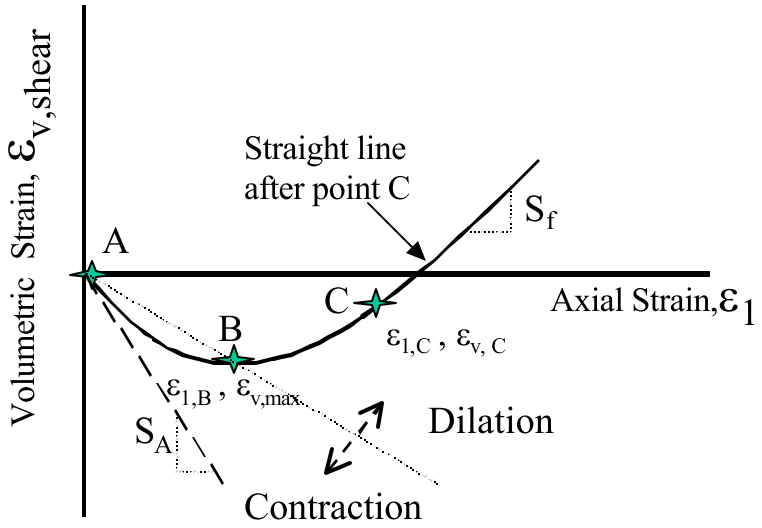

Fig. 6-8 Volumetric strain curve and its major points

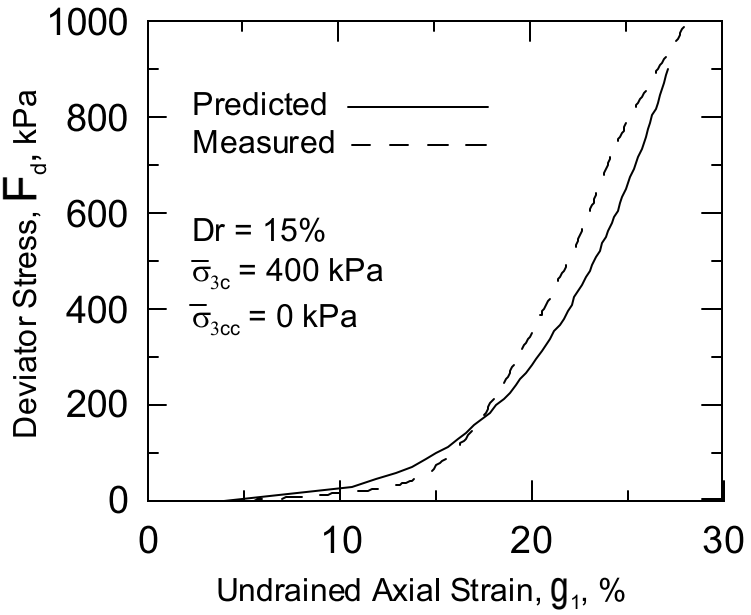

Fig. 6-9 Post-Liquefaction Undrained Stress-Strain Behavior of Completely Liquefied Nevada Sand

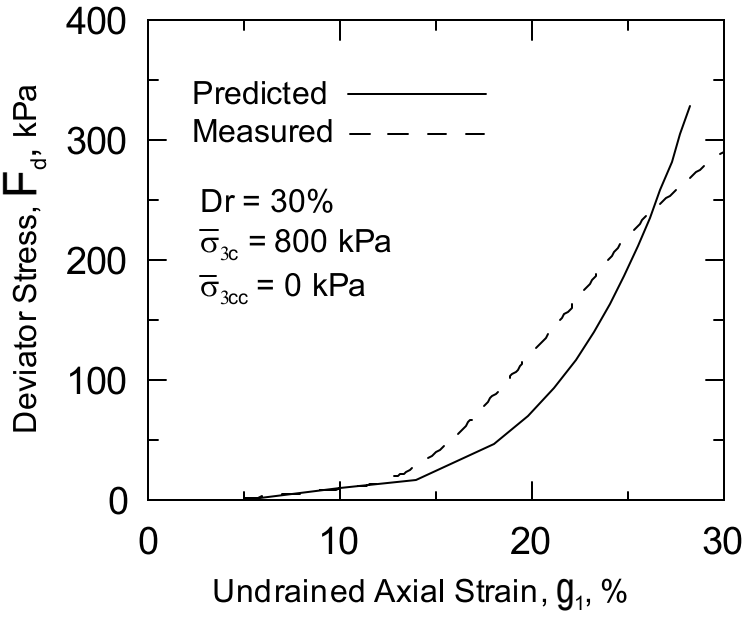

Fig. 6-10. Post-Liquefaction Undrained Stress-Strain Behavior of Completely Liquefied Ione Sand

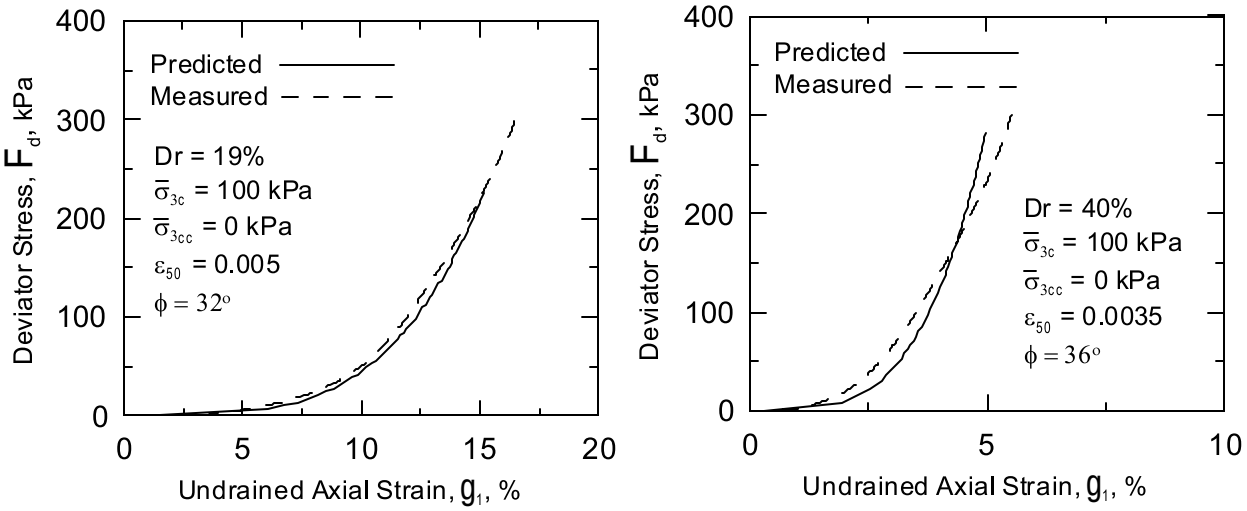

Fig. 6-11 Post-Liquefaction Undrained Stress-Strain Behavior of Completely Liquefied Fraser Sand

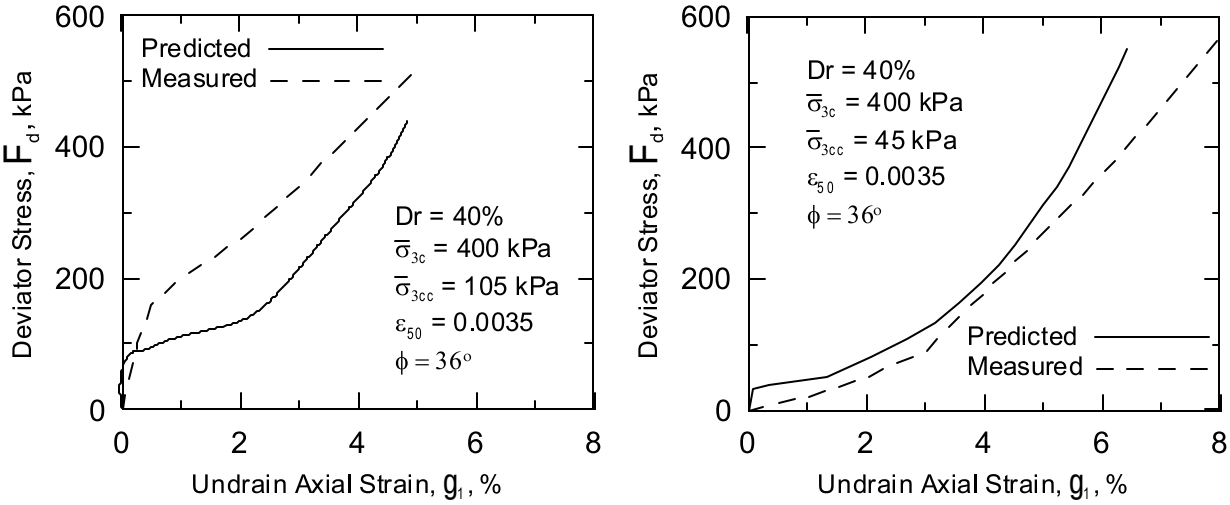

Fig. 6-12 Post-Liquefaction Undrained Stress-Strain Behavior of Partially Liquefied Fraser Sand

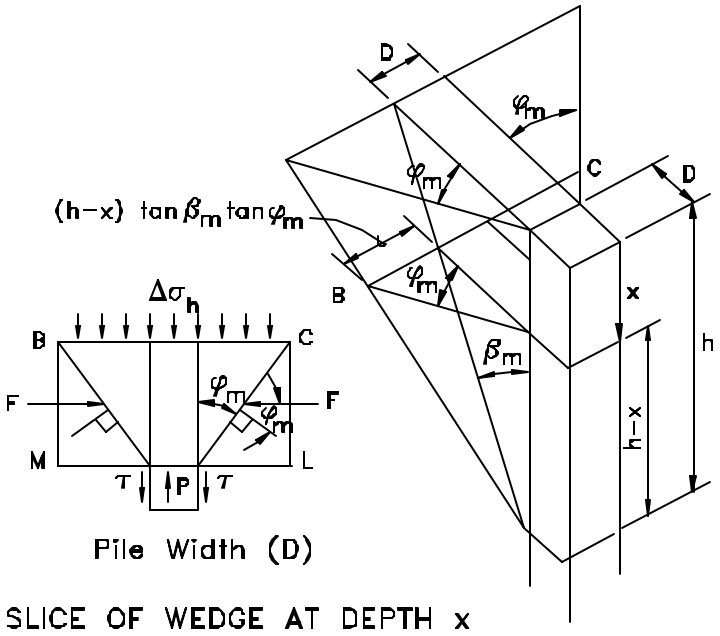

Fig. 6-13 Basic Characterization of the Strain Wedge Model (SW Model)

CHAPTER 7

FAILURE CRITERIA OF SHAFT MATERIAL

7.1 INTRODUCTION

Deformations in any structural element depend upon the characteristics of the load, the element shape and its material properties. With laterally loaded shafts and shafts, the flexural deformations are based on the applied moment and the flexural stiffness of the shaft at the cross section in question. In addition, the flexural stiffness (EI) of the shaft is a function of the Young's modulus (E), moment of inertia (I) of the shaft cross section and the properties of the surrounding soil. Given the type of material, concrete and/or steel, the properties of shaft material vary according to the level of the applied stresses.

Behavior of shafts under lateral loading is basically influenced by the properties of both the soil and shaft (shaft material and shape). The nonlinear modeling of shaft material, whether it is steel and/or concrete, should be employed in order to predict the value of the lateral load and the realistic associated bending moment and shaft deflection especially at large values of shaft-head deflection and the onset of shaft material failure. It is known that the variation in the bending stiffness (EI) of a laterally loaded shaft is a function of the bending moment distribution along the shaft (moment-curvature, M-Φ, relationship) as seen in Fig. 7-1. Consequently, some of the shaft cross sections which are subjected to high bending moment experience a reduction in bending stiffness and softer interaction with the surrounding soil. Such behavior is observed with drilled shafts and steel shafts at advanced levels of loading and has an impact on the lateral response and capacity of the loaded shaft. The shaft bending stiffnesses along the deflected shaft change with the level of loading, the M-Φ relationship of the shaft material, and the soil reaction which affects the pattern of shaft deflection. Therefore, the equilibrium among the distributions of shaft deflection, bending moment, bending stiffness, and soil reaction along the shaft should be maintained.

In the case of a steel shaft, the Young's modulus remains constant (elastic zone) until reaching the yield stress, f_y (indicating the initial yielding), at which time the steel starts to behave elastic-plastically with different values of the secant Young's modulus. Once a plastic hinge develops, the shaft cross section responds in plastic fashion under a constant plastic moment. But, in the case of a concrete shaft, the stress-strain relationship varies in a nonlinear fashion producing a simultaneous reduction in Young's modulus and, in turn, the stiffness of the shaft cross section. Furthermore, once it reaches a critical value of strain, the concrete ruptures catastrophically.

The technique suggested by Reese (1984), which employs the Matlock-Reese p-y curves, requires separate evaluation of the M-Φ relationship of the shaft cross section and then adoption of a reduced bending stiffness (EI_r) to replace the original shaft bending stiffness (EI). The suggested procedure utilizes this reduced bending stiffness (EI_r) over the full length of the shaft at all levels of loading. Assuming a reasonable reduction in bending stiffness, particularly with drilled shafts, is a critical matter that requires guidance from the literature which has only limited experimental data. At the same time, the use of one constant reduced bending stiffness for the shaft does not reflect the real progressive deformations and forces associated with the steps of lateral loading. However, this technique may work quite well with the steel H-pile which fails approximately once the shaft flange reaches the yielding stage (occurs rapidly). In general, the response of the shaft (shaft-head load vs. deflection, and shaft-head load vs. maximum moment) is assessed based on a constant bending stiffness (EI_r) and is truncated at the ultimate bending moment of the original shaft/drilled shaft cross section. The moment-curvature relationship, and thus the maximum bending moment carried by the shaft cross section should be evaluated first.

Reese and Wang (1994) enhanced the technique presented above by computing the bending moment distribution along the shaft and the associated value of EI at each increment of loading. Reese and Wang (1994) concluded that the bending moment along the shaft does not depend strongly on structural characteristics and that the moment differences due to EI variations are small. It should be noted that the effect of the varying EI on the bending moment values along the drilled shaft was not obvious because the

EI of the drilled shaft had no effect on the p-y curves (i.e. modulus of subgrade reaction) employed in their procedure. Therefore, it was recommended that a single value of EI of the cracked section (constant value) be used for the upper portion of the shaft throughout the analysis. Contrary to Reese and Wang's assumption, the variation in the value of EI has a significant effect on the nature of the p-y curve and modulus of subgrade reaction [Ashour and Norris (2000); Yoshida and Yoshinaka (1972); and Vesic (1961)] especially in the case of large diameter shafts.

The main purpose in this chapter is to assess the moment-curvature relationship (M-ϕ) of the loaded shaft in a convenient and simplified fashion considering the soil-shaft interaction. The prediction of the moment-curvature curve allows one to realistically determine the variation of shaft stiffness (EI) as a function of bending moment.

The SW model allows the designer to include the nonlinear behavior of the shaft material and, as a result, to find out the effect of material types on the shaft response and its ultimate capacity based on the concepts of soil-shaft interaction.

7.2 COMBINATION OF MATERIAL MODELING WITH THE STRAIN WEDGE MODEL

The bending moment distribution along the deflected length of a laterally loaded shaft varies as shown in Fig. 7-1. This profile of moment indicates the associated variation of shaft stiffness with depth if the stress-strain relationship of shaft material is nonlinear. The strain wedge model is capable of handling the nonlinear behavior of shaft material as well as the surrounding soil. The multi-sublayer technique, presented in Chapter 5, allows one to provide an independent description for each soil sublayer and the associated shaft segment. The effect of shaft material is considered with the global stability of the loaded shaft and the shape of the developing passive wedge of soil in front of the shaft. During the iteration process using the SW model, the stiffness of each shaft segment, which has a length equal to the depth of the soil sublayer, is a function of the calculated bending moment at the associated shaft segment, as seen in Fig. 7-1. Therefore,

the shaft is divided into a number of segments of different values of flexural stiffness under a particular lateral load.

In order to incorporate the effect of material non-linearity, numerical material models should be employed with the SW model. A unified stress-strain approach for confined concrete has been employed with the reinforced concrete shaft as well as the steel pipe shaft filled with concrete. In addition, steel is modeled using an elastic perfectly plastic uniaxial stress-strain relationship which is commonly used to describe steel behavior. The procedure presented provides the implementation of soil-shaft interaction in a fashion more sophisticated than that followed in the linear analysis with the SW model presented in Chapter 5.

The approach developed will allow one to load the shaft to its actual ultimate capacity for the desired lateral load and bending moment according to the variation of shaft material properties along the shaft length.

7.2.1 Material Modeling of Concrete Strength and Failure Criteria

Based upon a unified stress-strain approach for the confined concrete proposed by Mander et al. (1984 and 1988), a concrete model is employed with circular and rectangular concrete sections. The proposed model, which is shown in Fig. 7-2, has been employed for a slow strain rate and monotonic loading. The longitudinal compressive concrete stress f_c is given by

$$f_c = \frac{f_{cc}\, x\, r}{r - 1 + x^r} \qquad (7\text{-}1)$$

where f_{cc} symbolizes the compressive strength of confined concrete.

$$x = \frac{\varepsilon_c}{\varepsilon_{cc}} \tag{7-2}$$

where ε_c indicates the axial compressive strain of concrete.

$$\varepsilon_{cc} = \varepsilon_{co}\left[1 + 5\left(\frac{f_{cc}}{f_{co}} - 1\right)\right] \tag{7-3}$$

where ε_{cc} is the axial strain at the peak stress. f_{co} and ε_{co} represent the unconfined (uniaxial) concrete strength and the corresponding strain, respectively. Generally, ε_{co} can be assumed equal to 0.002, and

$$r = \frac{E_c}{E_c - E_{sec}} \tag{7-4}$$

where

$$E_c = 57{,}000\,(f_{co})^{0.5} \qquad (psi) \tag{7-5}$$

and

$$E_{sec} = \frac{f_{cc}}{\varepsilon_{cc}} \tag{7-6}$$

E_c denotes the initial modulus of elasticity of the concrete under slowly applied compression load.

As mentioned by Paulay and Priestly (1992), the strain at peak stress given by Eqn. 7-3 does not represent the maximum useful strain for design purposes. The concrete strain limits occur when transverse confining steel fractures. A conservative estimate for ultimate compression strain (ε_{cu}) is given by

$$\varepsilon_{cu} = 0.004 + \frac{1.4\,\rho_s\,f_{yh}\,\varepsilon_{sm}}{f_{cc}} \tag{7-7}$$

where ε_{sm} is the steel strain at maximum tensile stress (ranges from 0.1 to 0.15), and ρ_s is the volumetric ratio of confining steel. Typical values for ε_{cu} range from 0.012 to 0.05. f_{yh} represents the yield stress of the transverse reinforcement.

In order to determine the compressive strength of the confined concrete (f_{cc}), a constitutive model (Mander et al. 1988) is directly related to the effective confining stress (f_l) that can be developed at the yield of the transverse reinforcement.

$$f_{cc} = f_{co}\left[-1.254 + 2.254\left(1 + \frac{7.94\,f_l}{f_{co}}\right)^{0.5} - \frac{2\,f_l}{f_{co}}\right] \tag{7-8}$$

For circular and square section of concrete, f_l is given by

$$f_l = 0.95\ \rho_s f_{yh} \qquad (7\text{-}9)$$

- **Monotonic tensile loading**

Although concrete tension strength is ignored in flexural strength calculation, due to the effect of concrete confinement it would be more realistic if it were considered in the calculation. As suggested by Mander et al. (1988), a linear stress-strain relationship is assumed in tension up to the tensile strength (f_{tu}). The tensile stress is given by

$$f_t = E_c \varepsilon_c \qquad for \quad f_t \le f_{tu} \qquad (7\text{-}10)$$

and

$$\varepsilon_{tu} = \frac{f_{tu}}{E_c} \qquad (7\text{-}11)$$

where

$$f_{tu} = 9(f_{co})^{0.5} \qquad (psi) \qquad (7\text{-}12)$$

If tensile strain ε_t is greater than the ultimate tensile strain (ε_{tu}), f_t is assumed to be equal to zero.

7.2.2 Material Modeling of Steel Strength

There are different numerical models to represent the stress-strain relationship of steel. The model employed for steel in this study is linearly elastic-perfectly plastic, as shown in Fig. 7-3. The complexity of this numerical model is located in the plastic portion of the model which dose not include any strain hardening (perfectly plastic).

The elastic behavior of the steel is limited by the linearly elastic zone of this model at which the strain is less than the yield strain

$$\varepsilon_y = \frac{f_y}{E_{so}} \qquad (7\text{-}13)$$

where f_y is the yield stress of steel, and ε_y is the value of the steel strain at the end of the elastic zone where the stress is equal to f_y. E_{so} is the elastic Young's modulus of steel which is equal to 29,000 kips/inch^2.

When the value of steel stress (f_s) at any point on the cross section reaches the yield stress, the Young's modulus becomes less than E_{so} of the elastic zone. The initial yielding takes place when the stress at the farthest point from the neutral axis on the steel cross section (point A) becomes equal to the yield stress (f_y), as shown in Fig. 7-4a.

The initial yielding indicates the beginning of the elastic-plastic response of the steel section. By increasing the load, other internal points on the cross section will satisfy the yield stress to respond plastically under a constant yield stress (f_y), as seen in Figure 7-4b. Once all points on the steel section satisfy a normal stress (f_s) equal to the yield stress (f_y) or a strain value larger than the yield strain (ε_y), the steel section responds as a plastic hinge with an ultimate plastic moment (M_p) indicating the complete yielding of the steel section, as presented in Fig. 7-4c.

During the elastic-plastic stage (after the initial yielding and before complete yielding) some points on the steel section respond elastically ($f_s \leq f_y$) and the others respond plastically ($f_s = f_y$) with different values of Young's modulus (E_s) , as presented in Fig. 7-3. The values of normal strain are assumed to vary linearly over the deformed cross section of steel.

If the strain at any point on the steel cross section is larger than the yield strain (ε_y), the plastic behavior will be governed by the flow of the steel under a constant stress (f_y) at the point in question. Regardless of whether the section is under elastic, elastic-plastic or plastic states, the strain is linearly distributed over the whole steel section. In addition, the strain at any point is controlled by the values of strain at other locations in order to keep the strain distribution linear. Generally, the external and internal moments over the steel section should be in a state of equilibrium.

7.3 MOMENT-CURVATURE (M-F) RELATIONSHIP

The aim of developing the moment-curvature relationship of the shaft material is to determine the variation of the flexural stiffness (EI) at every level of loading. The normal stress (σ_x) at any cross section along the shaft length is linked to the bending moment (M) and curvature (ϕ) by the following equations:

$$EI \frac{d^2 y}{d x^2} = M \qquad (7\text{-}14)$$

$$EI \, \boldsymbol{f} = \frac{EI}{\boldsymbol{r}} = M \qquad (7\text{-}15)$$

$$\phi = \frac{d^2 y}{d x^2} = \frac{\varepsilon_x}{z} \tag{7-16}$$

$$\varepsilon_x = - \frac{z}{\rho_o} \tag{7-17}$$

where

$$\sigma_x = E \varepsilon_x = E \phi z \tag{7-18}$$

z = the distance from the neutral axis to the longitudinal fiber in question

ρ_o = the radius of curvature of the deflected axis of the shaft

ε_x = the normal strain at the fiber located z-distance from the neutral axis.

The above equations are based on the assumption of a linear variation of strain across the shaft cross section. In addition, the shaft cross section is assumed to remain perpendicular to the shaft axis before and after deforming, as shown in Fig. 7-5.

7.4 ANALYSIS PROCEDURE

The analysis procedure adopted consists of calculating the value of bending moment (M_i) at each cross section associated with a profile of the soil modulus of subgrade reaction which is induced by the applied load at the shaft top. Then, the associated curvature (ϕ), stiffness (EI), normal stress (σ_x) and normal strain (ε_x) can be obtained. This procedure depends on the shaft material. The profile of moment distribution

along the deflected portion of the shaft is modified in an iterative fashion along with the values of the strain, stress, bending stiffness and curvature to satisfy the equilibrium among the applied load and the associated responses of the soil and shaft. Based on the concepts of the SW model, the modulus of subgrade reaction (i.e. p-y curve) is influenced by the variations in the shaft bending stiffness at every shaft segment. This procedure guarantees the incorporation of soil-shaft interaction with the material modeling. The technique presented strives for a more realistic assessment of the shaft deflection pattern under lateral loading and due to the nonlinear response of shaft material and soil resistance.

7.4.1 Steel Shaft

Steel shafts involved in this study have circular cross sections, as seen in Fig. 7-6. The cross section of the steel shaft is divided into a number of horizontal strips (equal to a total of 2m) parallel to the neutral axis. Each strip has a depth equal to the thickness of the pipe shaft skin, as seen in Fig. 7-7. The moment applied over the cross section of the shaft segment (i) is M_i, and the normal stress at a strip (n) is $(f_s)_n$ ($1 \le n \le m$).

Using Eqns. 7-17 and 7-18, the stress and strain distributions over the cross section of each shaft segment can be determined as

$$\phi_i = \frac{M_i}{(E\,I)_i} \tag{7-19}$$

$$(\varepsilon_s)_n = z_n \phi_i \qquad 1 \le n \le m \tag{7-20}$$

$$\left(f_s \right)_n = \left(E_s \right)_n \left(\varepsilon_s \right)_n$$

(7-21)

where $E_s \leq E_{so}$; ϕ_i is the curvature at shaft segment (i) which is constant over the steel cross section at the current level of loading; z_n indicates the distance from the neutral axis to the midpoint of strip n; $(\varepsilon_s)_n$ represents the strain at strip n; $(EI)_i$ represents the initial stiffness of the shaft segment (i); I is the moment of inertia of the steel cross section of the shaft segment (i) which is always constant; and E_{so} symbolizes the elastic Young's modulus of the steel.

1. Elastic Stage

The Young's modulus of any strip of the steel section (i) is equal to the steel elastic modulus (29×10^6 psi) as long as the stress $(\varepsilon_s)_n$ is less or equal to the yield strain. Consequently, there is no change in the stiffness value of the shaft segment (i) if ε_s at the outer strip (n = 1) is less than or equal to ε_y. This stage is similar to the linear analysis (constant EI) of the SW model presented in Chapter 5.

2. The Elastic-Plastic Stage

Once the calculated strain at the outer strip based on Eqn. 7-20 is larger than ε_y, the stress $(f_s)_n$ determined at the outer strip (n = 1) using Eqn. 7-21 will be equal to the yield stress. Therefore, initial yielding occurs and the elastic-plastic stage begins. During the elastic-plastic stage, the strips of the steel cross section experience a combination of elastic and plastic responses with different values of the secant Young's modulus (E_s). Some strips behave elastically ($\varepsilon_s \leq \varepsilon_y$ and $f_s \leq f_y$) , and the others behave plastically ($\varepsilon_s > \varepsilon_y$ and $f_s = f_y$) with different values of the secant Young's modulus (E_s), as shown in Figs. 7-3, 7-4 and 7-8. The normal stresses on the steel cross section are redistributed in order to generate a resisting moment $(M_R)_i$ that balances the applied moment (M_i) and satisfies the following equation:

$$M_i = (M_R)_i = (M_e)_i + (M_y)_i \qquad (7\text{-}22)$$

where $(M_e)_i$ and $(M_y)_i$ represent the internal elastic and plastic moments induced over the steel cross section (i).

The internal elastic moment $(M_e)_i$ represents the internal moment exerted by the strips (m_1) which behave elastically and can be obtained as

$$(M_e)_i = \Sigma (f_s)_j A_j z_j \qquad (1 \le j \le m_1) \qquad (7\text{-}23)$$

The internal plastic moment $(M_y)_i$ is the moment generated by the yielded strips (m_2) which respond plastically and can be calculated using the following equation:

$$(M_y)_i = \Sigma f_y A_k z_k \qquad (1 \le k \le m_2) \qquad (7\text{-}24)$$

where A is the area of the steel strip, and

$$2m = m_1 + m_2 \qquad (4.25)$$

For the first iteration of the solution in this stage, the steel cross section experiences a resisting internal moment $(M_R)_i$ less than the external moment (M_i). Therefore, the steel cross section of the shaft segment (i) should maintain a modified stiffness value for the shaft segment in question, i.e. $(EI)_{i,mod}$. This reduced value of stiffness at shaft segment (i) is associated with an increase in the value of curvature such that the

$$(f_i)_{mod} = f_i \frac{M_i}{(M_R)_i} \qquad (7\text{-}26)$$

new value of curvature, $(\phi_i)_{mod}$, is

The modified stiffness value at shaft segment (i) can be computed using the following equation,

$$(EI)_{i,\mathrm{mod}} = \frac{M_i}{(f_i)_{\mathrm{mod}}} \qquad (7\text{-}27)$$

The above procedure should be performed with all the unbalanced segments along the deflected portion of the loaded shaft at each step of loading.

The global stability problem of the laterally loaded shaft is resolved under the same level of loading and soil resistance using the modified values of stiffness of the shaft segments (Eqn. 7-27). Consequently, the new moment distribution (M_i) along the shaft length is assessed during each iteration. The modification for shaft curvature and, therefore, stiffness values at the unbalanced segments continues until Eqn. 7-22 is satisfied over all the defelcted segments of the shaft.

3. Plastic Stage

The elastic-plastic stage continues until the steel cross section reaches a condition of complete yield. Thereafter, all strips of the steel section will be subjected to the yield stress (f_y) and strain values lager than ε_y , as presented in Fig. 7-9. At this level of shaft head load, the steel section exhibits a plastic moment (M_p) which represents the ultimate moment that can be carried by the steel section. Once the steel section reaches the plastic moment, a plastic hinge develops to indicate the beginning of the plastic stage at the shaft segment in question. The plastic moment is expressed as

$$M_p = \Sigma f_y A_n z_n \quad (7\text{-}28)$$

Equations 7-26 and 7-27 are employed in order to obtain the desired values of curvature and the associated stiffness at the plastic section is

$$(EI)_{i,\mathrm{mod}} = \frac{M_p}{(f_i)_{\mathrm{mod}}} \quad (7\text{-}29)$$

During the plastic stage, the moment capacity and the stress over the steel section are restricted to the plastic moment (M_p) and the yield stress (f_y), respectively. However, the strain and curvature values are free to increase in order to produce reduced stiffnesses with the higher level of loading.

The resisting moment of the completely yielded section (plastic hinge) is always equal to M_p. If the external moment (M_i) which is calculated from the global stability is larger than M_p, Eqns. 7-26, 7-28 and 7-.29 will be employed. The iteration process continues until satisfying an external moment value equal to the plastic moment at the shaft segment in question.

The development of the plastic hinge on the shaft does not mean the failure of the shaft but leads to a limitation for the shaft-head load. After the formation of the plastic hinge, the shaft deflects at a higher rate producing larger curvatures and smaller stiffnesses to balance the applied load. Therefore, another plastic hinge may develop at another location on the shaft. If the soil has not failed at the development of the plastic hinge, the shaft may exhibit a lateral load capacity slightly larger than the load associated with the plastic hinge formation due to increase in soil resistance. The laterally loaded shaft is assumed to fail when the outer strip at any shaft segment experiences a strain value larger than 0.15.

7.4.2 Reinforced Concrete Shaft

The reinforced concrete shaft has a circular cross section and to be divided into a total number of horizontal

strips of (2m) as seen in Fig. 7-10. Unlike the cross section of a steel shaft, the cross section of the reiforced concrete shaft is not symmetrical around the neutral axis as a result of the different behavior of concrete under tensile and compressive stresses. The incorporation of concrete tensile strength reflects the actual response of the reinforced concrete shaft. As presented in Section 7.2.1, the employment of concrete confinement has a significant influence on the concrete behavior (strength and strain values).

The resistance of the concrete cover (outside the confined core of concrete) is neglected. Therefore, the initial stiffness of the whole concrete cross section $(EI)_i$ represents the effective concrete section which is the confined concrete core. The curvature (ϕ_i) at the concrete section (i) is initially determined based on the applied external moment M_i and the initial stiffness of the reinforced concrete cross section $(EI)_I$, i.e.

$$f_i = \frac{M_i}{(EI)_i} \tag{7-30}$$

Based on a linear distribution of strain (ε) over the reinforced concrete cross section, the strain at any strip (n) can be obtained using Eqn. 7-20 and is expressed as

$$(e)_n = z_n f_i \qquad 1 \le n \le m \tag{7-31}$$

Eqns. 7-1 and 7-21, which represent the numerical models of the compressive stress of confined concrete and tensile stress of steel, respectively, are used to calculate the associated concrete stress (f_c) and steel stress (f_s) at each strip (n). In this study, the tensile stress (f_t) is assumed to be equal to the compressive stress (f_c) if the tensile strain $(\varepsilon_t)_n$ is less than ε_{tu}, which is more conservative than Eqn. 7-10. Therefore, the reinforced concrete cross section remains symmetric (the centerline represents the neutral axis) as long as ε_t at the outer strip (n = 1) is less than ε_{tu}. Under the conditions of a symmetric reinforced concrete section, the moment equilibrium and stiffness modification at any shaft segment (i) can be expressed as

$$\left(M_R\right)_i = \Sigma\, 2\left[\left(f_c A_c\right)_n z_n + \left(f_s A_s\right)_n z_n\right] \qquad \left(1 \le n \le m\right) \tag{7-32}$$

Once the value of the tensile strain at the outer strip of any shaft cross section exceeds ε_{tu}, the outer strip on the tension side fails and the cross section becomes unsymmetric. Thereafter, the neutral axis is shifted towards the compression side as shown in Fig. 7-10. In order to accurately estimate the new position of the neutral axis, the cross section should be in equilibrium under the compressive and tensile forces (F_{com} and F_{ten}) or

$$\left(F_{com}\right)_i = \left(F_{ten}\right)_i \tag{7-33}$$

where

$$\left(F_{com}\right)_i = \Sigma\left(A_c f_c + A_s f_s\right)_n \qquad 1 \le n \le n_1 \tag{7-34}$$

and

$$\left(F_{ten}\right)_i = \Sigma\left(A_c f_t + A_s f_s\right)_n \qquad 1 \le n \le n_2 \tag{7-35}$$

n_1 and n_2 are the numbers of strips in the compression and tension zones of the concrete cross section, respectively. At any strip in the tension zone, f_t is equal to zero when the tensile strain is greater than ε_{tu}.

Having the values of n_1 and n_2 ($2m = n_1 + n_2$) and using Eqns. 7-33 through 7-35, the location of the neutral axis can be identified, and the resisting moment can be determined as

where

$$(M_R)_i = (M_{com} + M_{ten})_i \tag{7-36}$$

$$(M_{com})_i = \Sigma\left[(f_c A_c + f_s A_s)_n (z_c)_n\right] \qquad (1 \le n \le n_1) \tag{7-37}$$

$$(M_{ten})_i = \Sigma\left[(f_t A_c + f_s A_s)_n (z_t)_n\right] \qquad (1 \le n \le n_2) \tag{7-38}$$

where z_c and z_t are the distance from the neutral axis to the strip in question in the compression and tension zones, respectively.

In addition, the behavior of steel bars in the compressive and tensile zones is subjected to the steel model presented in Section 7.2.2. Once the strain of any steel bar is greater than or equal to ε_y, f_s will be equal to f_y in Eqns. 7-34 through 7-38. The equations above are influenced by the ultimate values of concrete strength and strain (ε_{cu} and f_{cc}) that are associated with concrete confinement as presented in Section 7.2.1.

If the calculated moment $(M_R)_i$ is less than the external moment M_i, the cross section curvature will be modified to obtain new values for the curvature and stiffness to balance the applied moment, i.e.

$$(f_i)_{\text{mod}} = f_i \frac{M_i}{(M_R)_i} \tag{7-39}$$

The modified stiffness value at shaft segment (i) can be computed using the following equation,

$$(EI)_{i,\mathrm{mod}} = \frac{M_i}{(f_i)_{\mathrm{mod}}} \qquad (7\text{-}40)$$

By iteration, Eqns. 7-33 through 7-40 are emlpoyed to obtain the desired values of the curvature and the stiffness of the shaft segment (i) in order to generate a resisting moment $(M_R)_i$ equal to the external moment (M_i). The above procedure should be performed with all unbalanced segments along the deflected portion of the loaded shaft at each level of loading.

The global stability problem of the laterally loaded shaft is solved again under the same level of loading and using the modified values of stiffness of the shaft segments. Consequently, the bending moment (M_i) is redistributed along the shaft length.

Once any concrete strip under compressive stress reaches the ultimate strain ε_{cu} (Eqn. 7-7), the strip fails and is excluded from the resisting moment. The steel bars fail when the steel strain reaches a value of 0.15. The strength of a failed strip is assumed to be equal to zero in Eqn. 7-28. However, the shaft fails when the stiffness of any shaft segment diminishes to a small value that does not provide equilibrium between the external and the resisting moments. Therefore, the plastic moment of a concrete shaft represents the largest induced moment in the shaft that can be sustained before failure.

7.4.3 Concrete Shaft with Steel Case (Cast in Steel Shell, CISS)

In the current case, the shaft cross section is treated as a composite section similar to the reinforced concrete shaft. The shaft cross section (steel and concrete) is divided into a number of strips (equal to 2m) as shown in Fig. 7-9. The thickness of each strip is equal to the thickness of the steel shell (t_s). Both numerical material models presented in Section 7.2 are employed here using an iterative technique governed by the deformation criteria of the numerical models.

The normal strain is assumed to vary linearly over the shaft cross section which is perpendicular to the shaft

axis, as shown in Fig. 7-11. Therefore, the curvature is constant over the whole composite section. The applied bending moment (M_i) at shaft segment (i) generates initial values for curvature, stresses and strains in both the steel pipe and the concrete section as described in Section 4.2. Similar to the reinforced concrete section, the concrete resistance in the tension zone is considered. It should be noted that the steel pipe provides large concrete confinement resulting in large values of concrete strength and strain.

The composite cross section of shaft behaves symmetrically as long as the tensile strain at the outer strip of concrete (n = 2) is less than ε_{tu}. The strain values of steel and concrete are obtained using Eqns. 7-30 and 7-31. Then the associated stress values of concrete and steel are calculated based on Eqns. 7-1 and 7-21. Generally, the stiffness the composite cross section is modified according to the equilibrium between the external and internal moments as expressed by Eqn. 7-32 for the symmetric section.

When the tensile strain of the outer strip of concrete (n = 2) exceeds ε_{tu}, the composite cross section in no longer symmetric and the neutral axis location is shifted towards the compression zone and should be determined by using an iterative technique which includes Eqns. 7-36 through 7-39. It should be noted that the concrete tensile stress (f_t) at any failed strip in the tension zone is equal to zero. In addition, at any strip, the steel stress is equal to f_y if the strain is equal to or larger than ε_y. If the calculated resisting moment $(M_R)_i$ does not match the external moment (M_i), the stiffness of the shaft segment in question is modified using Eqn. 7-40.

The above procedure is performed with all shaft segments under the same level of loading. This procedure is repeated in an iterative way using the modified stiffness values to solve the problem of the laterally loaded shaft (global stability). The iteration process continues until there is equilibrium between the external and resisting moments at all shaft segments. The distribution of bending moment (M_i), along the length of the shaft, and the deflection pattern is based on the modified shaft stiffnesses and the resistance of the surrounding soil.

It should be noted that the concrete section will not fail before a plastic hinge develops. This occurs because the steel yields at a strain (ε_y) much less than the ultimate strain of concrete (ε_{cu}). However, the failed strips of concrete (in either the tension or compression zones) are subtracted from the composite section resulting in a faster drop in the stiffness of the shaft segment in question. It should be emphasized that there is no sudden failure for the concrete portion of the composite section because of the steel shell.

The stiffness of the loaded shaft and the effective area of the deflected shaft cross section vary according to the level of loading. Therefore, the actual moment-curvature relationship and the ultimate moment carried by a reinforced concrete shaft or a steel pipe shaft filled with concrete should be calculated using the technique presented.

7.4.4 Reinforced Concrete Shaft with Steel Case (Cast in Steel Shell, CISS)

Similar to the shaft cross section presented in Section 4.4.3, the shaft cross section is treated as a composite section. The shaft cross section (steel and reinforced concrete) is divided into a number of strips (equal to 2m) as shown in Fig. 7-12. The thickness of each strip is equal to the combined thickness of the steel shell (t_s) and the thickness equivalent to the longitudinal reinforcement, A_s [$t_r = A_s / 3.14 / (Z_s - t_s)$]. Both numerical material models presented in Section 7.2 are employed here using an iterative technique governed by the deformation criteria of the numerical models.

The normal strain is assumed to vary linearly over the shaft cross section which is perpendicular to the shaft axis, as shown in Fig. 7-12. Therefore, the curvature is constant over the whole composite section. The applied bending moment (M_i) at shaft segment (i) generates initial values for curvature, stresses and strains in both the steel pipe and the concrete section as described in Section 7-2. The current shaft cross section (Fig. 7-12) is analyzed by following the procedure applied to the CISS section presented in Section 7.4.3.

7.5 SUMMARY

A technique for the inclusion of nonlinear material modeling for steel, concrete, and composite steel concrete

shafts has been developed and demonstrated in this chapter. The strain wedge model exhibits the capability of predicting the response of a laterally loaded shaft based on the nonlinear behavior of shaft material. The technique presented allows the designer to evaluate the location of a plastic hinge developed in the shaft, and to determine the realistic values of the ultimate capacity and the associated deflection of the loaded shaft.

The nonlinear behavior of the shaft material has an influence on the lateral response and capacity of the shaft/shaft. This effect is dependent on the values of bending moment (level of loading). In turn, the modulus of subgrade reaction (i.e. the p-y curve) is affected by the changed bending moment, the reduced bending stiffnesses, and the changed deflection pattern of the shaft/shaft. Without the appropriate implementation of material modeling, the shaft/shaft capacity, and the associated deflection pattern and bending moment distribution will be difficult to predict with any degree of certainty.

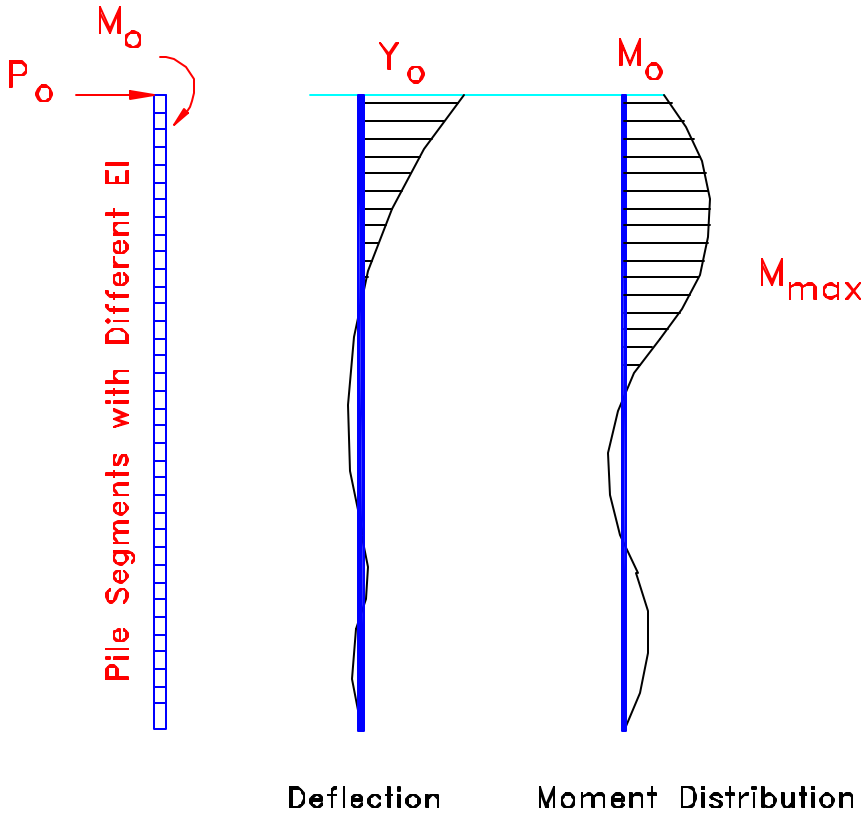

Fig. 7-1 Deflection and Moment Distributions in a Laterally Loaded Shaft

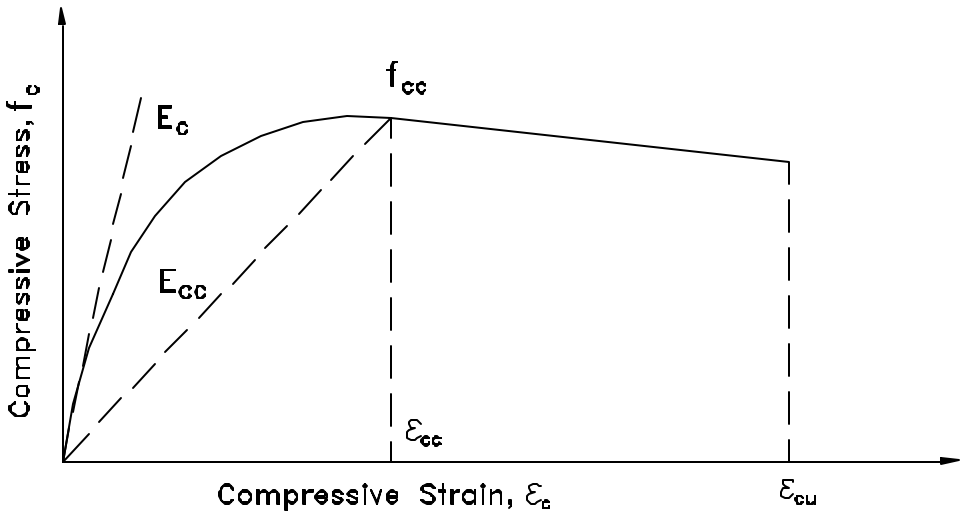

Fig. 7-2 Stress-Strain Model for Confined Concrete in Compression (Mander et al. 1984 and 1988)

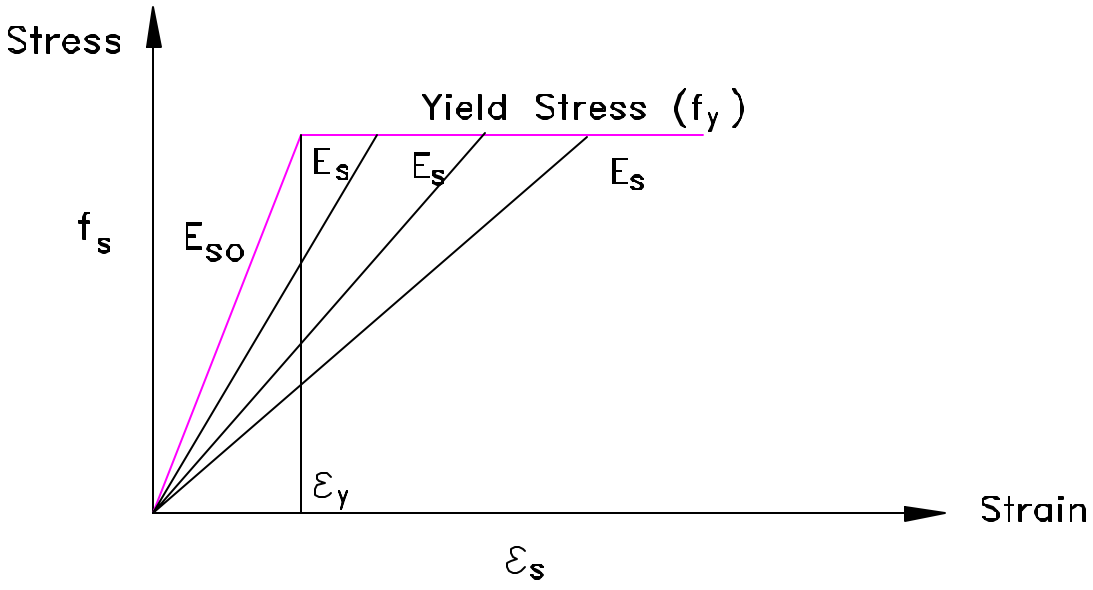

Fig. 7-3 Elastic-Plastic Numerical Model for Steel

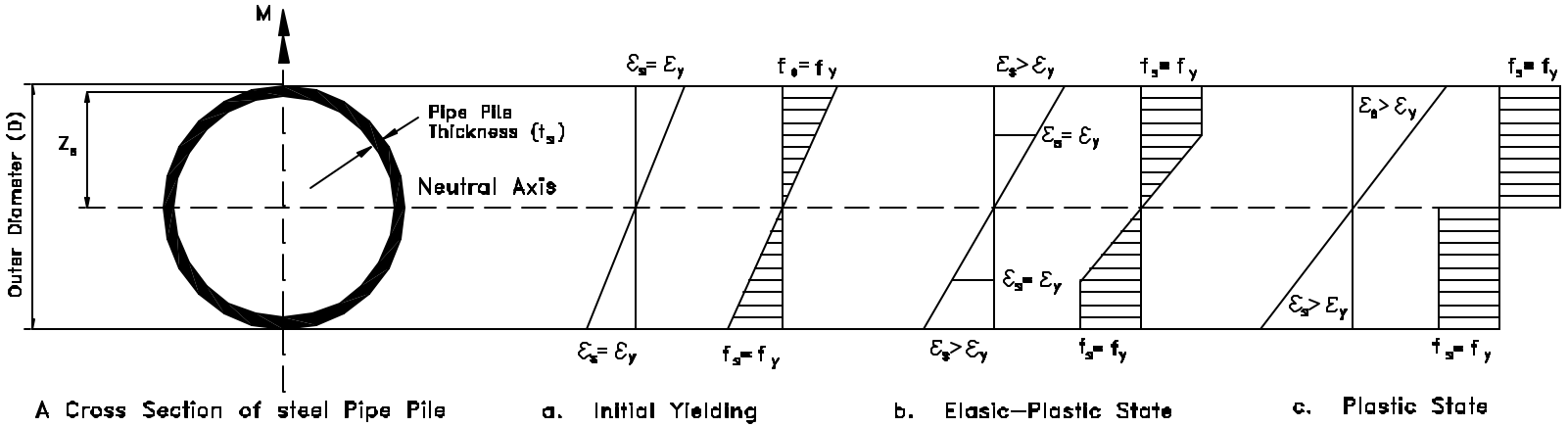

Fig. 7-4 Different stages of Normal Stresses over a Steel Section

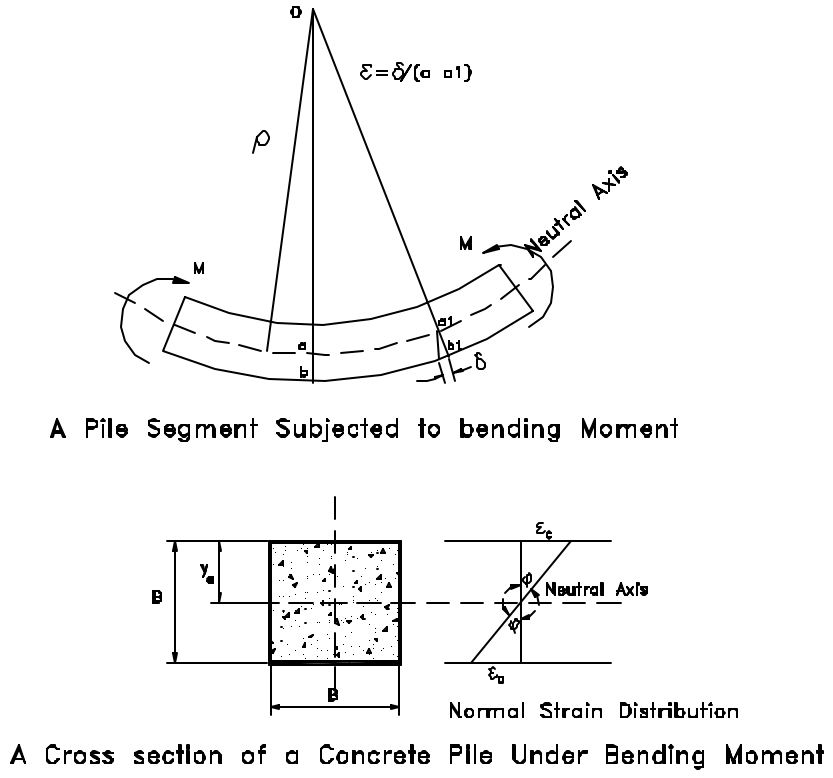

Fig. 7-5 Flexural Deformations of a Pile Segment subjected to Bending Moment

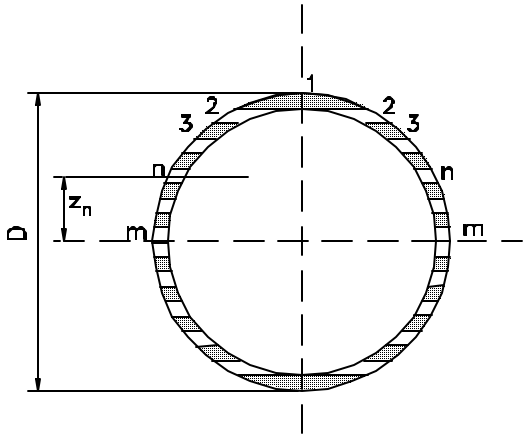

Fig. 7-6 A Cross Sections of Steel Shaft

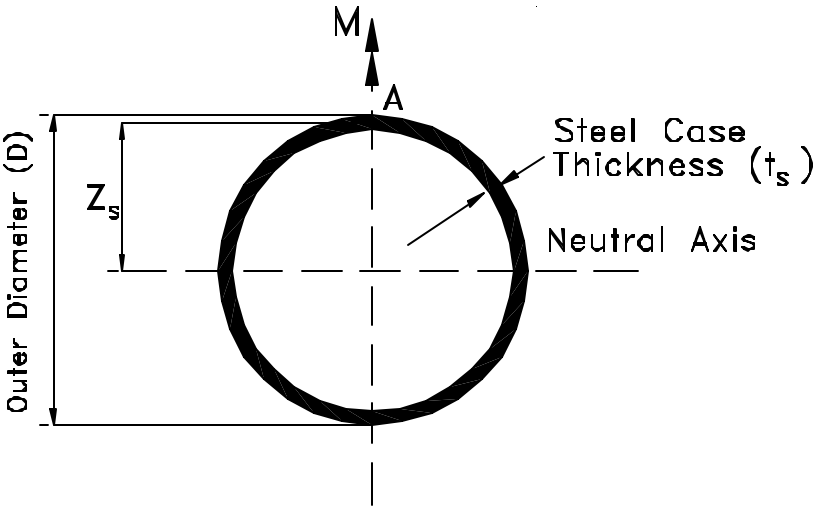

Fig. 7-7 Steel Sections Divided into Horizontal Strips

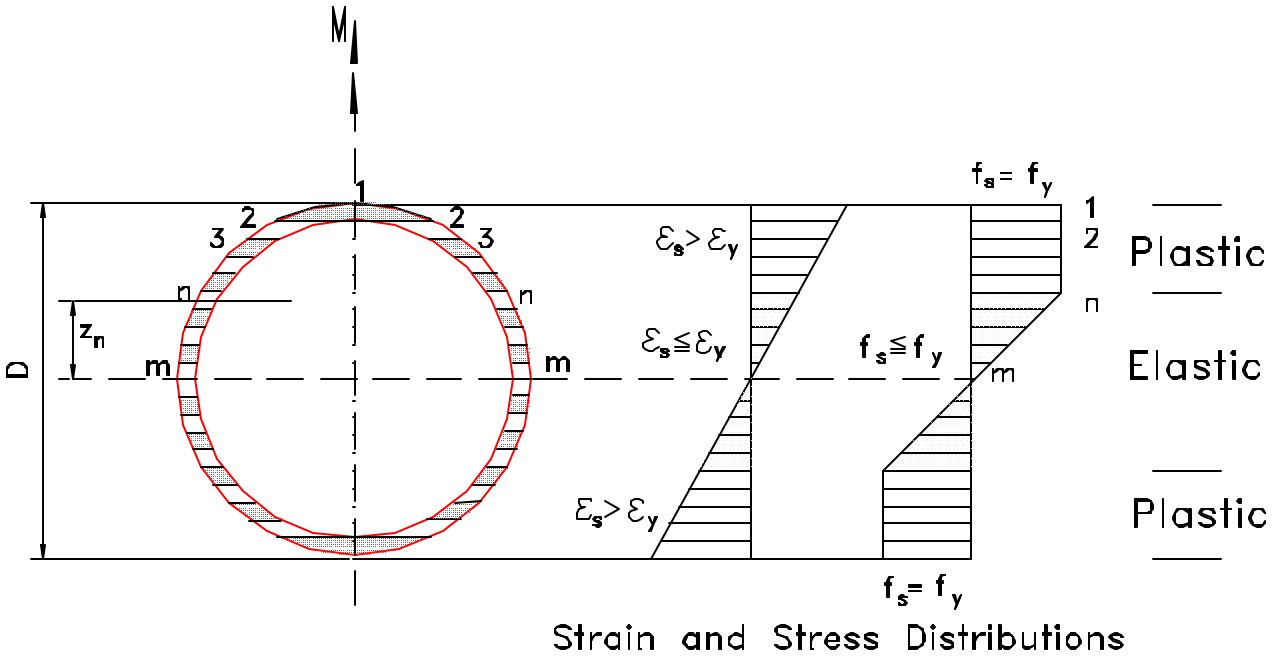

Fig. 7-8 Behavior of Steel Shaft Cross Section in the Elastic-Plastic Stage

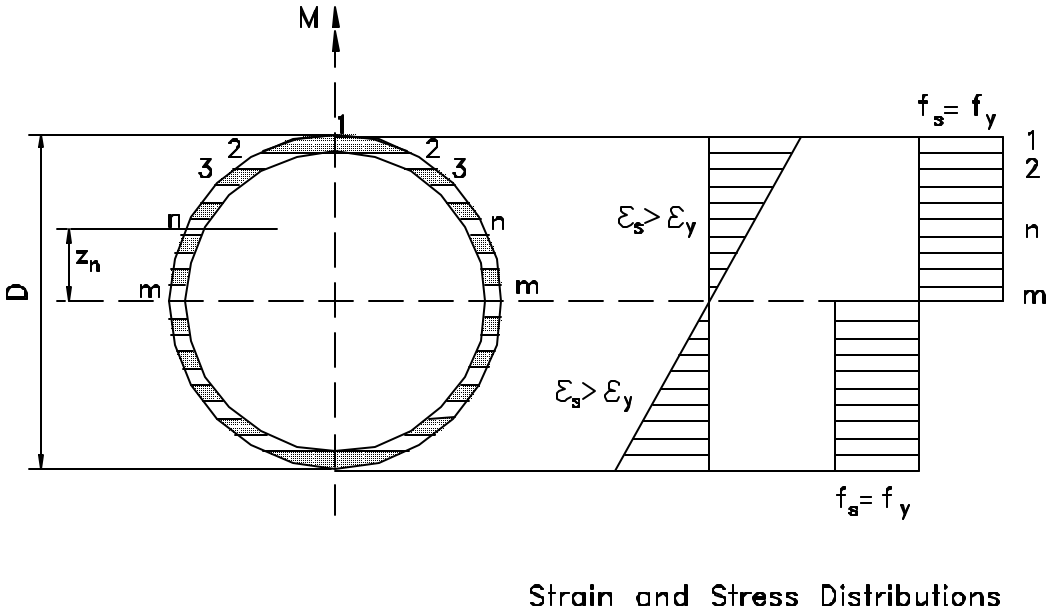

Fig. 7-9 Behavior of Steel Shaft Cross Section in the Plastic Stage

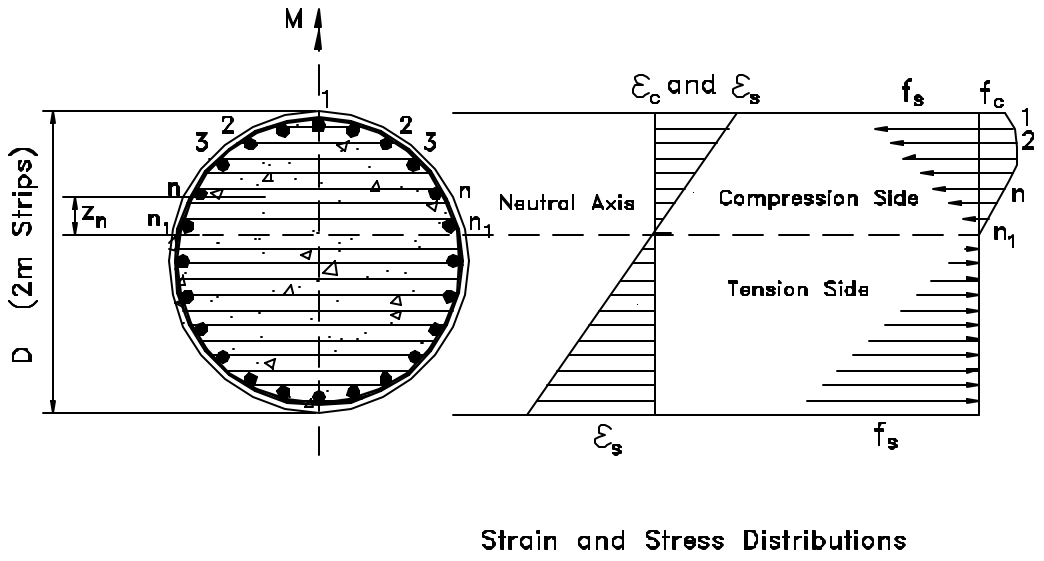

Fig. 7-10 Behavior of a Reinforced Concrete Shaft Cross Section Divided into Strips

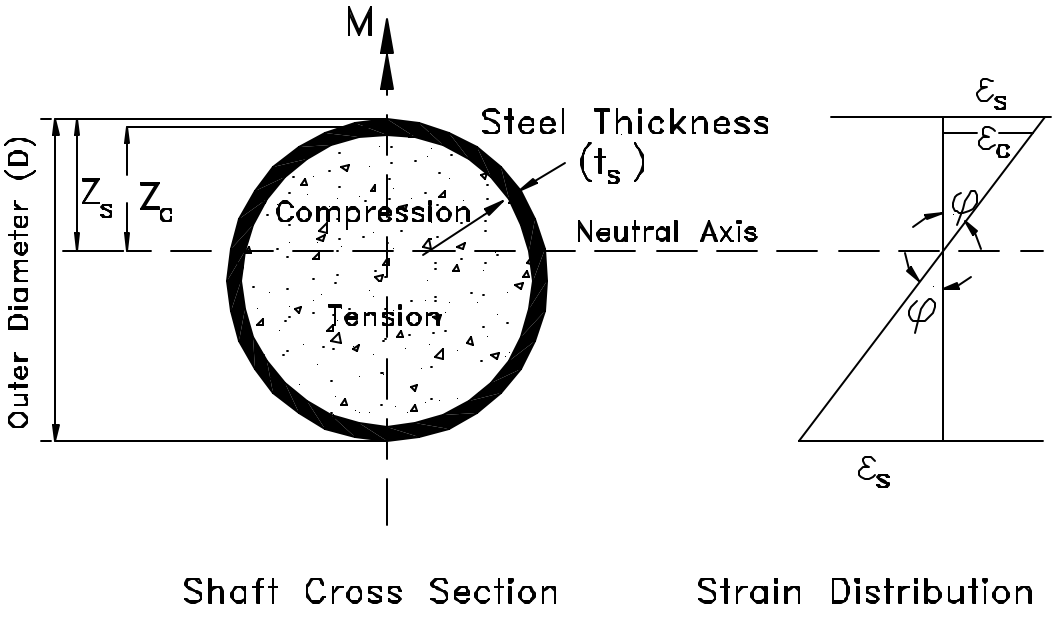

Fig. 7-11 Composite Cross Section of a Concrete Shaft with Steel Case (CISS)

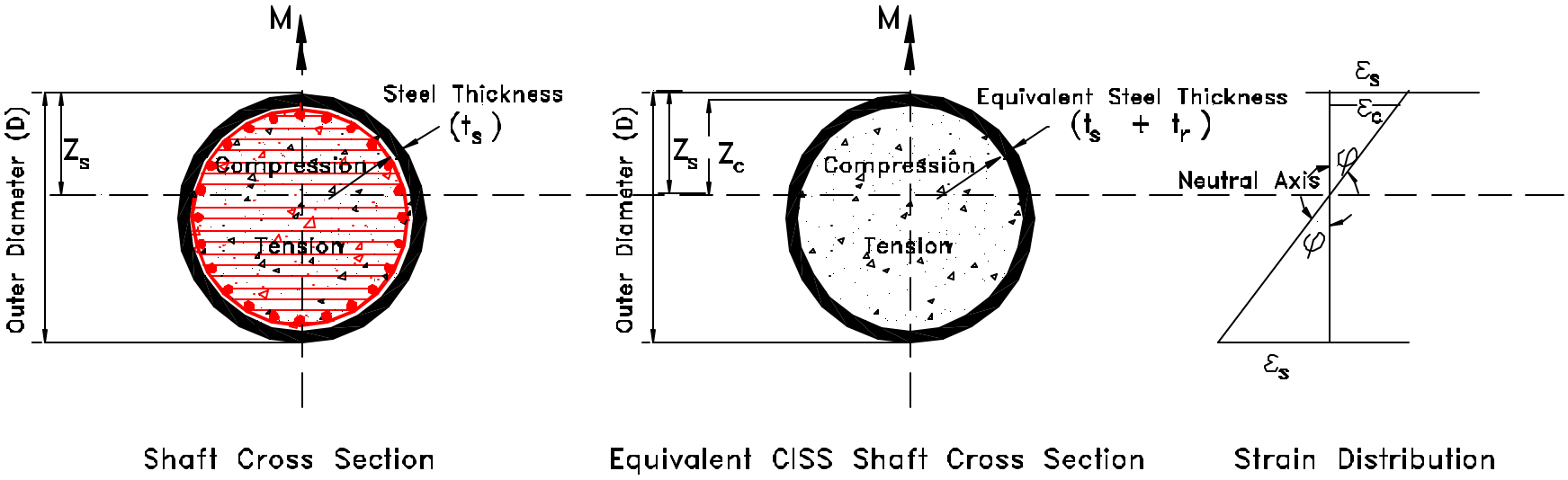

Fig. 7-12 A Shaft Cross Section of Reinforced Concrete Cast in Steel Shell

CHAPTER 8

VERIFICATIONS WITH FIELD LOAD TESTS

This chapter presents a number of example problems that reflect real applications for existing test projects. The SW model program input and output data will be summarized in tables. The data input will include the following sets of shaft and soil properties, shaft group geometry, and loads (shear and axial forces, and moment) applied at the top of the shaft.

8.1 INPUT DATA

8.1.1 Shaft Properties

- Shaft-head conditions (free head, fixed head, zero rotation or zero deflection)
- Behavior of shaft material (linear or nonlinear analysis)
- Shaft-head location above or below ground surface
- Shaft length
- Number of shaft segments (≥ 1)
- Length of shaft segment
- Diameter of shaft segment
- Uniaxial strength of concrete after 28 days (f_c)
- Longitudinal steel ratio(s) (A_s/A_c)
- Steel yield stress
- Thickness of steel casing, if present
- Steel yield stress of steel casing
- Thickness of concrete cover

Based on the ACI formula, the bending stiffness (EI) of the shaft cross-section is determined internally by the program S-Shaft.

8.1.2 Soil Properties

- Number of soil layers (starting from ground surface)

- Uniform surcharge at the ground surface (additional uniform loads at ground surface)
- Location of water table below ground surface
- Soil type of each soil layer
- Thickness of soil layer
- Effective unit weight of soil (γ)
- Friction angle (φ) for sand
- Undrained shear strength for clay (S_u)
- Unconfined compressive strength of rock mass (q_u)
- ε_{50}** of sand, clay, C-φ soil or rock (charts provided and can be determined by the program for default =0)

8.1.3 Liquefaction Analysis (for Saturated Sand)

- Corrected number of blowcounts, $(N_1)_{60}$
- Percentage of fines in sand
- Shape parameter (roundness) of sand grains

** ε_{50} = axial strain of soil at 50% of stress level (i.e. 50% of soil strength). ε_{50} can be calculated internally in the shaft program by typing 0 (program default). Also, a chart is provided in the program help to allow the designer to check the values of ε_{50}. However, it is recommended that the chart be used for sand if the uniformity coefficient (C_u) > 2 (from sieve analysis data). For the case of rock mass, the curve of S_u vs. ε_{50} is extrapolated to cover the rock mass strength ($q_u = 2\ S_u$).

8.1.4 Loads (shear force, moment and axial load)

- Axial load at shaft head
- Bending moment at shaft head
- Desired lateral load (shear force) at shaft head

8.1.5 Earthquake Excitation (Liquefaction)

- Magnitude of earthquake (M)
- Peak ground acceleration (a_{max})

8.2 LAS VEGAS FIELD TEST (SHORT SHAFT)

The Las Vegas test for large 8-foot diameter shaft represents an excellent case study for a short shaft (Zafir and Vanderpool, 1998). The soil data input for use with the programs FLPIER/COM624 was evaluated by the University of Florida team. The same soil data input has been used in the SW model program. The nonlinear modeling of shaft material (concrete and steel) is employed in both the FLPIER/COM624 and SW Model analyses.

The reinforced concrete drilled shaft tested was 8 feet in diameter and 32 feet in length with 1% longitudinal steel reinforcement. The uniaxial strength of concrete after 28 days (f_c) is assumed to be 5.0 ksi. Table 8-1 summarizes the detailed information for the soil profile as reported by the University of Florida team.

Table 8-1 - Soil Profile for the Las Vegas Test

Soil layer	Soil type	Thickness (ft)	γ (pcf)	ϕ (deg.)	k (pci)
Layer 1	Sand	2.5	120	33	15
Layer 2	Sand	6.5	120	37	30
Layer 3	Sand	3.0	120	32	11
Layer 4	Sand	1.5	120	36	26
Layer 5	Sand	7.5	120	45	62
Layer 6	Sand	2.0	120	40	43
Layer 7	Sand	3.5	120	45	63
Layer 8	Sand	6.0	120	40	44
Layer 9	Sand	1.0	120	32	10
Layer 10	Sand	2.0	120	37	32

γ = effective unit weight of soil

k = coefficient of subgrade reaction (F/L^3)

Compared to COM624/FLPIER, the SW model program provides very good prediction for the laterally loaded large diameter short shaft of the Las Vegas test (see Table 8-2 and Figs. 8-1 through 8-4). The nonlinear modeling of shaft material is used to show the program capability of predicting the response of a large diameter short shaft.

Table 8-2 Comparison of Measured Shaft Head Deflection and SW model and FLPIER/COM624P Predictions for Las Vegas Test

Load (kips)	Actual Shaft-Head Deflection, Yo, in	SW Model Deflection, Yo, in	FLPIER/COM624 Deflection, Yo, in
50	0.02	0.02	0.201
100	0.04	.05	0.402
150	0.07	.08	0.603
200	0.125	0.11	0.804
300	0.235	0.22	1.27
400	0.40	0.38	1.89
500	0.61	0.58	2.76
600	0.88	0.88	3.9
700	1.21	1.25	5.75
750	1.36	1.45	7.15

8.3 SOUTHERN CALIFORNIA FIELD TEST (SHORT SHAFT)

A number of cast-in-place drilled piers were constructed and tested in Southern California and reported by Bhushan et al. (1978). The piers were constructed at five different sites. One of these piers is an ideal short shaft with which to compare the predictive capability and reliability of computer programs such as LPILE/COM624P/FLPIER and SW model. Regardless of the predicted results, it should be mentioned again that the p-y curves employed in the programs LPILE, COM624P or FLPIER were established based on long small diameter piles that are not representative of large diameter shafts.

In short shaft case reported here, the pier tested was 4 feet in diameter and 16 feet in length. The pier was constructed in stiff clay with undrained shear strength (S_u) of 5500 psf and ε_{50} of 0.94% (Table 8-3). This data was reported by Bhushan et al. (1978) and used with COM624 by Reese (1983) [the developer of the program COM624 and LPILE]. Reese (1983) reported the results provided by the program COM624 and presented in Fig. 8-5 and Table 8-4. Compared to the measured data, COM624 provides very soft response. The results assessed using the SW model program are in good agreement with the field data. Figures 8-6 through 8-8 show the lateral response of the tested shaft using the SW model technique.

Table 8-3 - Soil Data for Southern California Test

Soil Layer	Soil Type	Thickness (ft)	γ (pcf)	ϕ (deg.)	S_u (psf)	ε_{50}**
Layer 1	Clay	22	130	34	5500	0.0095

Table 8-4 Comparison of Measured Shaft Head Deflection and SW model and COM624P Predictions for Southern California Test

Load (kips)	Actual shaft-head deflection, Yo, in	SW model Deflection, Yo, in	COM624 Deflection, Yo, in
50	0.1	0.094	0.20
100	0.25	0.2275	0.35
200	0.67	0.59	1.50
300	1.10	1.00	4.40
400	1.85	1.55	15.0

8.4 TREASURE ISLAND FULL-SCALE LOAD TEST ON PILE IN LIQUEFIED SOIL

A series of full-scale field tests in liquefied soil was performed at Treasure Island in San Francisco Bay (Ashford and Rollins 1999). The soil properties employed in the SWM analysis for the test site based on the reported data (Weaver et al. 2001) are described in Table 8-5. Soil and pile properties can be also seen in Fig. 8-9. In this analysis, the sand is assumed to contain 5% fines. The soil was liquefied by carrying out controlled blasts at that site without densifying the soil in the test area. Drained and undrained lateral loading tests were performed on a long isolated pipe pile filled with concrete (CISS) of 0.61 m diameter. The tested pile exhibited free-head conditions and was laterally loaded 1.0 m above ground surface. The test pile had bending stiffness EI = 448320 kN-m^2.

The observed and SW model predicted drained response of the pile compares favorably as seen in Fig. 8-10. Procedures followed in the Treasure Island test (liquefying the soil around the pile and then loading the pile laterally) subsequent to the static drained test are similar to those employed with the SW model analysis. The assessed undrained post-liquefaction behavior of the tested pile is based on the procedures presented herein, and includes the effect of free-field and near-field excess pore pressure ($u_{xs,ff} + u_{xs,nf}$). The pile head response shown in Fig. 8-10 is based on a peak ground acceleration (a_{max}) of 0.11g, and an earthquake magnitude (M) of 6.5.

The piles were cyclically loaded after the first blast at the site. The observed (field) undrained points (Ashford and Rollins 1999), which are shown in Fig. 8-10, represent the peaks of the cyclic undrained response of these piles. It should be mentioned that the good agreement between the measured and predicted undrained response is based on an assumed maximum ground acceleration, a_{max}, of 0.11g. This value of a_{max} generates high excess porewater pressures ($u_{xs,\ ff}$) in most of the sand layers. It should be noted that the value of a_{max} employed in the analysis causes an excess porewater pressure ratio (r_u) equal to 0.95 in most of the sand and the best match with the measured free-field excess porewater pressure pattern induced in the field (Ashford and Rollins 1999).

Table 8-5. Soil Properties Employed in the SWM Analysis for the Treasure Island Test

Soil Layer Thick. (m)	Soil Type	Unit Weight, $\overline{\gamma}$ (kN/m^3)	$(N_1)_{60}$	ö (degree)	å$_{50}$ %	S_u KN/m^2
0.5	Brown, loose sand (SP)	18.0	16	33	0.45	
4.0	Brown, loose sand (SP)	8.0	11	31	0.6	
3.7	Gray clay (CL)	7.0	4		1.5	20
4.5	Gray, loose sand (SP)	7.0	5	28	1.0	
5.5	Gray clay (CL)	7.0	4		1.5	20

The p-y curve comparisons in Fig. 8-11 show the capability of the SW model for predicting the p-y curves of a pile/shaft in fully or partially liquefied soils. The back-calculated (measured) p-y curves at different depths for the 0.61-m cast-in steel-shell (CISS) pile are from Weaver et al. (2001). Other techniques, such as the traditional p-y curve approach with a reduction multiplier, do not show the concave-upward pattern of the back-calculated p-y curves.

It was obvious from the $u_{xs,\ ff}$ distribution measured along the depth of the pile right after the blast that the upper 4.6 m was almost fully liquefied. The back-calculated (field) p-y curves shown in Fig. 8-11 were assessed after a few cycles of loading. As a result, the porewater pressure in the upper 4.5 m of soil reached 1.0. By increasing the peak ground acceleration (a_{max}) used in the SW model analysis from 0.11g to 0.15g, the whole soil profile completely liquefies and the pile head response (load-deflection curve) follows the concave-up shape (increasing slope) as seen in Fig. 8-12.

8.5 COOPER RIVER BRIDGE TEST AT THE MOUNT PLEASANT SITE, SOUTH CAROLINA SITE

Cyclic lateral load tests were performed on two large diameter long shafts at the Mount Pleasant site. Shaft MP-1 (Cast-in-Steel-Shell, CISS, bending stiffness (EI) = 2 x 10^8 kip-ft^2) was 8.33 ft in diameter while the shaft MP-2 (Cast-in-Drilled Hole, CIDH, EI = 1.38 x 10^8 kip-ft^2) was 8.5 ft in diameter, each with a one-inch thick steel shell. The lateral load in both cases was applied at a point 43-inches above the ground surface. The Mount Pleasant site soil profile consists of 40 ft of loose to medium dense, clean or silty or clayey sands overlaying a thick layer of the Cooper Marl (S & ME 2000). Table 8-6 summarizes the basic soil properties of the soil profile at the Mount Pleasant site used in the SW model analysis. Lateral static load tests were carried out on as-is conditions, and liquefied conditions induced by controlled blasting (Figs. 8-13 and 14) (S & ME). The blast successfully generated high porewater pressure (r_u =1) within most of the upper 38 ft as indicated by the piezometer data.

LPILE analyses for the load test for the project were carried out using (1) the traditional p-y curve for the 38 feet thick overburden consisting of sandy deposits of $\varphi = 35^o$ and $\gamma = 60$ pcf and (2) back calculated p-y curves for the Cooper Marl from O-cell tests as no traditional p-y curves representative of the Cooper Marl conditions were available. The LPILE results for pre- and post-liquefaction conditions based on the back-calculated p-y curve from the O-cell tests are shown in Figs. 8-13 and 14. In contrast, SW model predicted p-y curves for the Cooper Marl showed good agreement with the back-calculated p-y curve from the O-cell tests. The SW model results shown in Figs. 8-13 and 14 are based on the p-y curves predicted from the SW model analysis.

Table 8-6 Soil Properties Employed in the SW Model Analysis for the Cooper River Bridge Tests at Mt. Pleasant

Soil Layer Thick. (ft)	Soil Type	Unit Weight, $\bar{\gamma}$ (pcf)	$(N_1)_{60}$	Ö (degree)	å$_{50}$ %	S_u psf
4	Slightly clay sand (SP-SC)	120	19	34	0.004	
9	Sandy clay (CH)	62	7	30	0.008	
16	Very clayey sand (SC-CL)	62	10	32	0.006	
9	Silty sand (SM)	62	7	30	0.008	
80	Cooper Marl	65	20		0.002	4300

LPILE shaft responses for liquefied conditions were computed for various trial values of r_u different from the measured value in order to come up with a reasonable agreement of shaft response with the field test results. A constant value for r_u =0.7 for the upper 38 ft of overburden used in the LPILE analysis (for shaft MP-1) yields reasonable agreement with the field results Fig. 8-13). It should be noted that (1) r_u measured in the field was very close or equal to one and (2) use of r_u in the LPILE analysis only reduces the buoyant (effective) unit weight of soil thereby producing a softer shaft responses. r_u used with shaft MP-2 in LPILE analysis was not defined in the report (SM&E 2000).

The SW model analysis for a shaft in liquefied soil depends on several factors: earthquake magnitude (M); peak ground acceleration (a_{max}); and the soil properties to determine the values of r_u and the additional excess porewater pressure resulting from the superstructure lateral loading. An earthquake magnitude of 6.5 and a_{max} of 0.1g and 0.3g were used in the SW model analysis to obtain the shaft responses shown in Figs. 8-13 and 14. It should be noted that a_{max} of 0.3g develops complete liquefaction in the upper 38 ft of soil. Despite the diameter and EI of shaft MP-1, larger than those of shaft MP-2, shaft MP-2 experienced a post-liquefaction lateral response stiffer than that of shaft MP-1, as observed in the field test (Figs. 8-13 and 14). The use

of different values of a_{max} in the SWM analysis is to exhibit the varying shaft response. Knowing the seismic zone (i.e. M and a_{max}) and soil and shaft properties at a particular site, the designer will be able to assess the lateral response of a shaft/pile in liquefiable soils using the SW model computer program. No attempt was made by SM&E 2000 to back calculate the p-y curves.

8.6 UNIVERSITY OF CALIFORNIA, LOS ANGELES (UCLA) FULL-SCALE LOAD TEST ON LARGE DIAMETER SHAFT

A full-scale load test funded by Caltrans on a cast-in-drilled-hole (CIDH) shaft/column was conducted by UCLA (Janoyan et al. 2001). The 88-ft long shaft/column tested was 6.0 ft in diameter for the 40 ft above ground and 6.5 ft in diameter for the 48 ft below ground surface. The configuration of the tested shaft and its material (concrete/steel) properties are shown in Fig. 8-15. The testing was performed at a site with deep alluvial soils consisting of silty clay and silty, clayey sand. The soil properties employed in the SW model analysis are reported in Table. 8-7. The shaft/column tested was pushed laterally up to failure (the formation of a plastic hinge). It should be noted that the field results indicate that the shaft responded as an intermediate shaft which is consistent with the SW model program description.

Figure 8-16 provides a comparison between the experimental and computed moment curvature response for the 6-ft-diameter shaft cross section. Compared to the results of the X-Section program (used by Caltrans), the moment-curvature relationship assessed using the SW model program shows better agreement with the experimental results.

Table 8-7 - Soil Data for the UCLA Test

Soil layer	Soil type	Thickness (ft)	γ (pcf)	S_u (psf)	ε_{50}
Layer 1	Stiff Clay	6	130	4000	0.003
Layer 2	Stiff Clay	18	130	2500	0.005
Layer 3	Stiff Clay	40	130	3000	0.004

Figure 8-17 shows a comparison between the measured shaft response and the computed one using LPILE, SWM6.0 and the current shaft program. To obtain good match with field data, a sand soil profile was used with LPILE (as reported by Caltrans). The data obtained using LPILE based on the original soil profile shown in Table 8-7 and given in the UCLA report did not provide good agreement with the measured data. As seen in Fig. 8-16, the same column/shaft

was previously analyzed using the older SW model program (SWM6.0) for a long piles/shaft that does not account for the vertical side shear resistance and shaft classification.

8.7 FULL-SCALE LOAD TEST ON A BORED PILE IN LAYERED SAND AND CLAY SOIL

A bored 1.5-m-diameter reinforced concrete pile was installed to a depth 34 m below ground surface in the town of Chaiyi in the west central coastal plain of Taiwan (Fig. 8-18 by Brown et al. 2001). The pile tested with free-head conditions was laterally loaded at 0.5 m above ground. As reported by Brown et al (2001), relatively poor comparisons with the measured results were obtained using the traditional p-y curves for sand (Reese et al. 1974) and clay (Matlock 1970) with the program FLPIER (McVay et al. 1996). The traditional p-y curves were modified to a very large extent in the upper 12 m (see the modified p-y curves by Brown et al. 2001 in Fig. 8-19) in order to obtain good agreement with the measured data for the isolated pile.

Using the original soil properties given by Brown et al. (2001) shown in Fig. 8-18, the SW model provides an assessed response in good agreement with the measured response of the single free head pile (Fig. 8-20). A nonlinear model for pile material behavior (reinforced concrete) incorporated in the SW model analysis is employed in this analysis. It should be noted that none of the given (original) soil and pile properties was modified for the SW model analysis.

As presented by Brown et al. (2001) FLPIER (McVay et al. 1996) provides excellent agreement with the measured response by using deduced (adjusted) (site specific) modified p-y curves shown in Fig. 8-19. The nonlinear modeling of pile material played an important role in the results obtained by FLPIER and the SW model analyses. Significant recommendations and comments were made by Brown et al. (2001) relative to a p-multiplier to be used with the traditional p-y curves.

8.8 SUMMARY

This chapter has demonstrated via comparison with field test results, the capability of the SW model shaft analysis relative to various applications. The SW model analyses were undertaken using the unmodified soil and pile properties reported in the literature. Comparable LPILE/COM24/FLPIER assessments using the traditional p-y curves required moderate to significant modifications of such data in order to obtain reasonable agreement with overall field test results. Even so, traditional p-y curves for liquefied sand do not show the concave-upward

shape that is predicted by the SW model analysis and noted back-calculated curves from the Treasure Island tests.

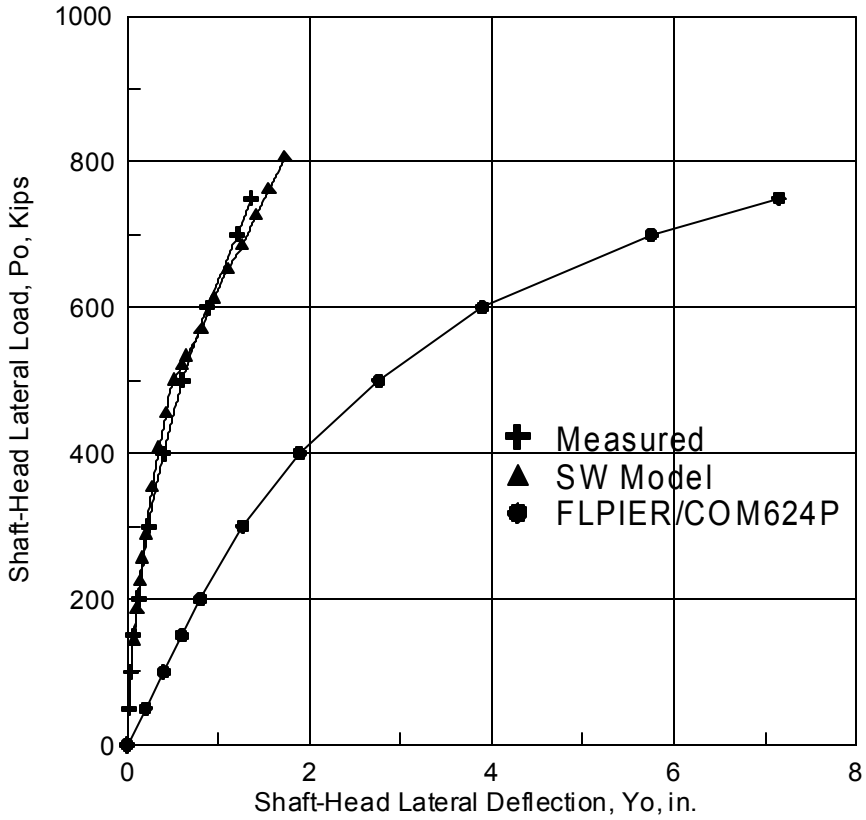

Fig. 8-1 Measured and Computed Shaft Response of the Las Vegas Test

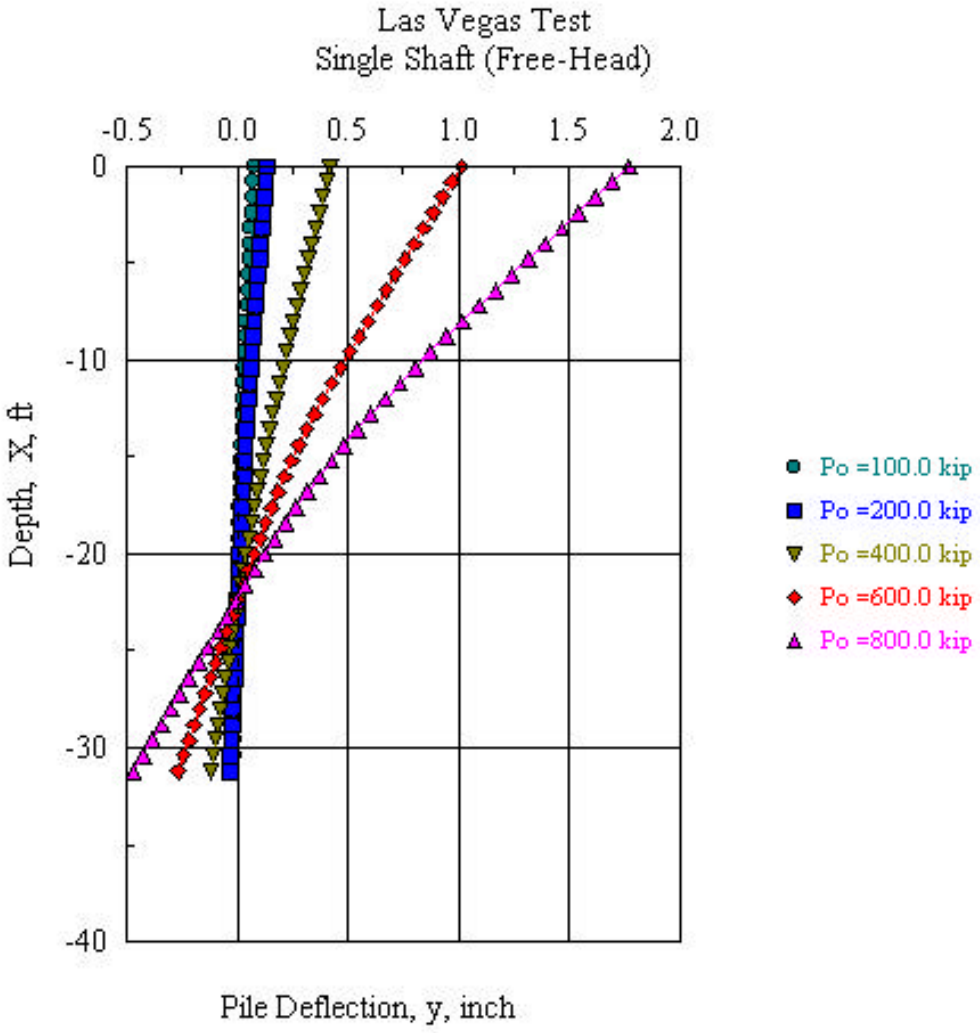

Fig. 8-2 Computed Lateral Deflection of the Shaft at Various Loads in the Las Vegas Test

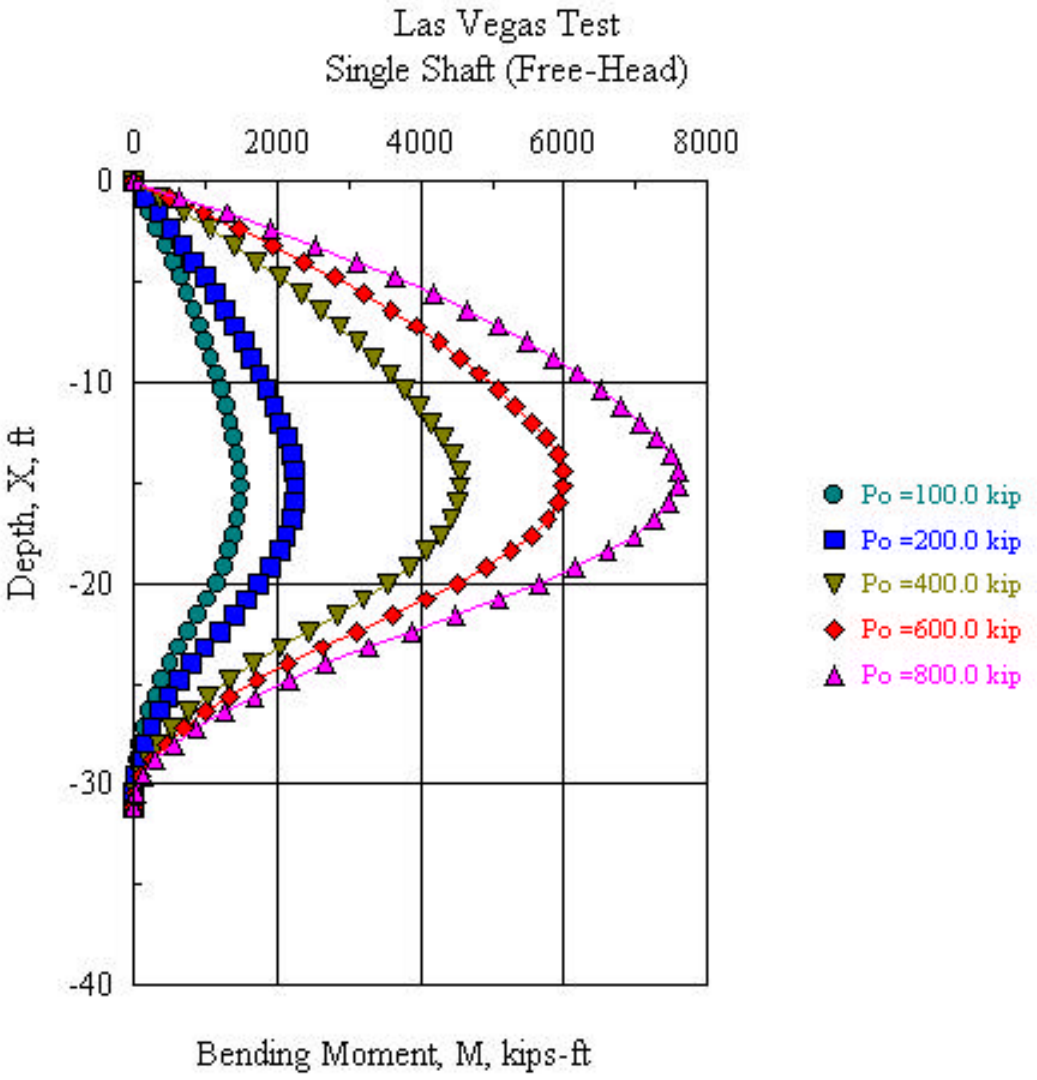

Fig. 8-3 Computed Bending Moment Distribution in the Shaft in the Las Vegas Test

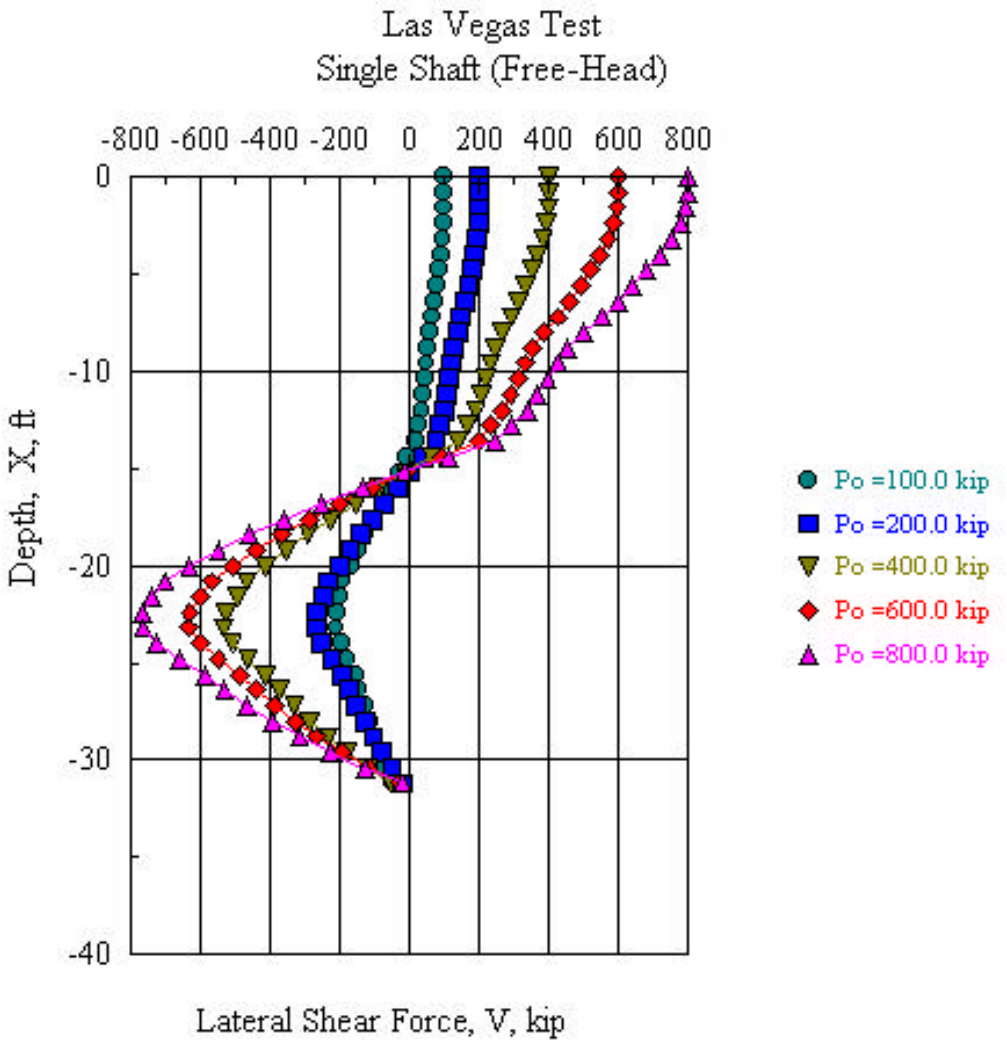

Fig. 8-4 Computed Shear Force Distribution in the shaft in the Las Vegas Test

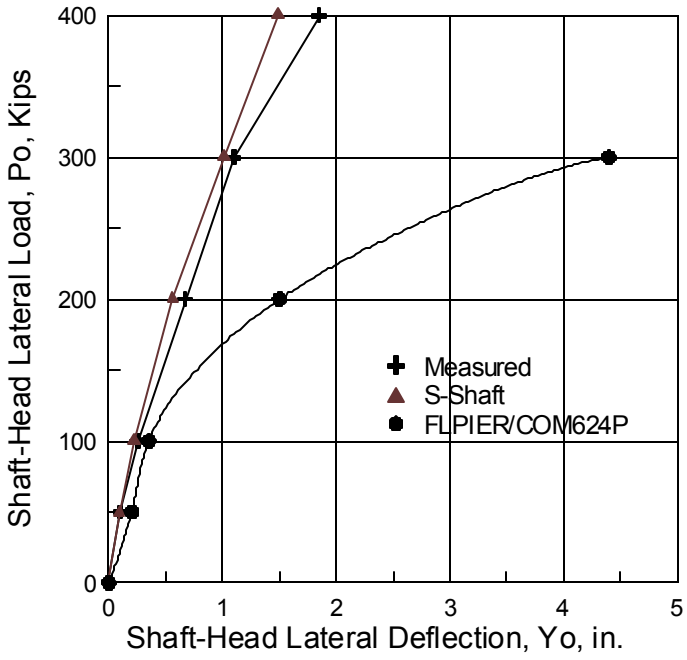

Fig. 8-5 Measured and Predicted Shaft Response of the Southern California Test (Pier 1)

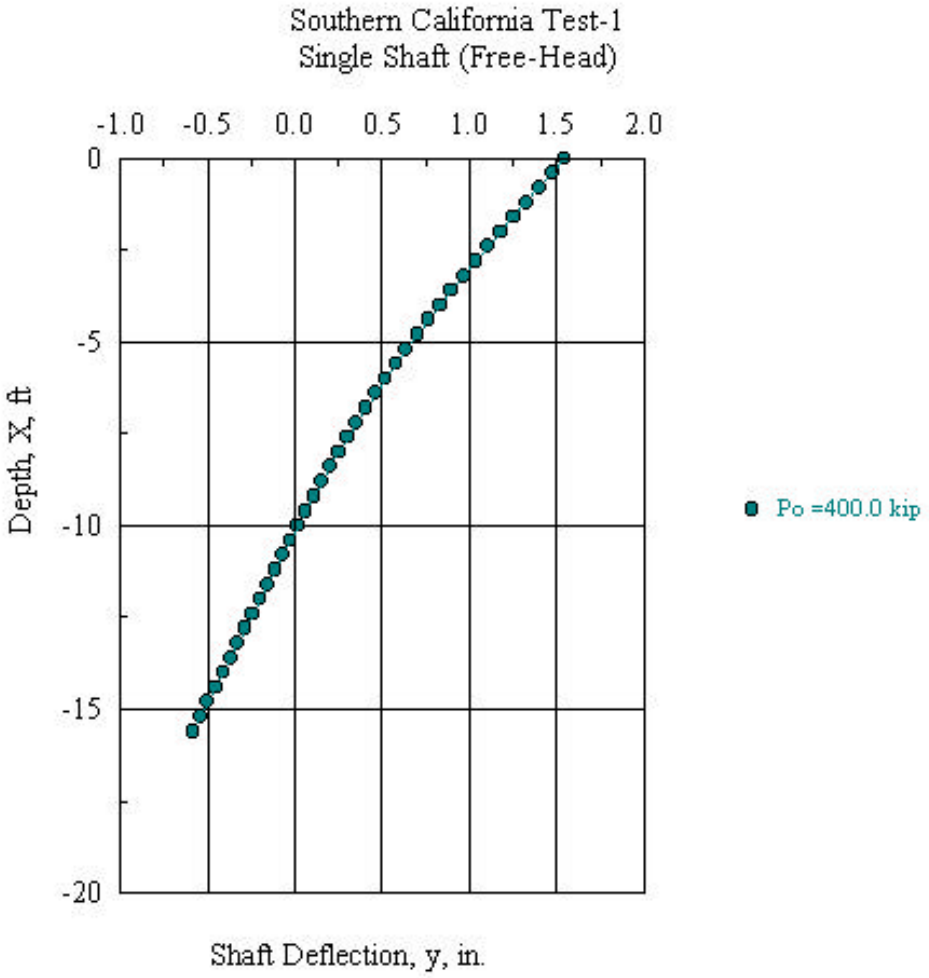

Fig. 8-6 Computed Lateral Deflection for at the Southern California Test

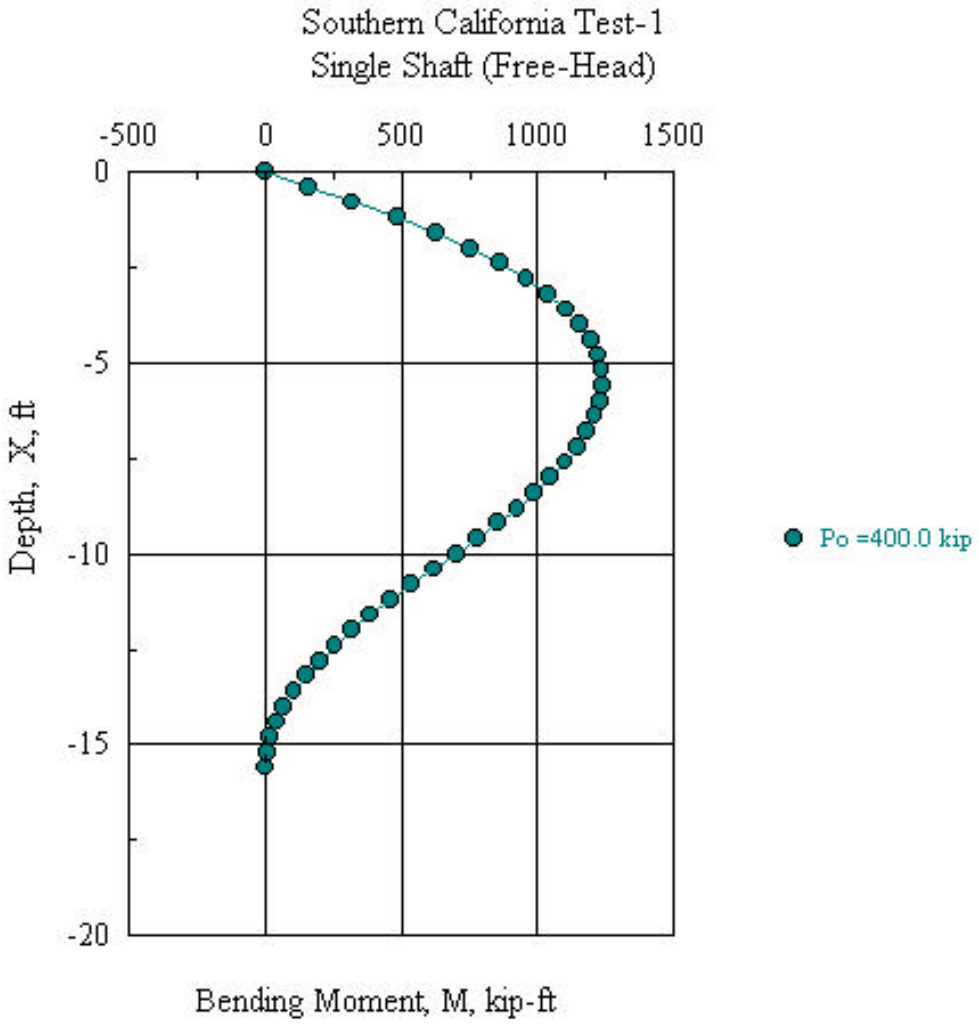

Fig. 8-7 Computed Bending Moment Distribution for the Southern California Test

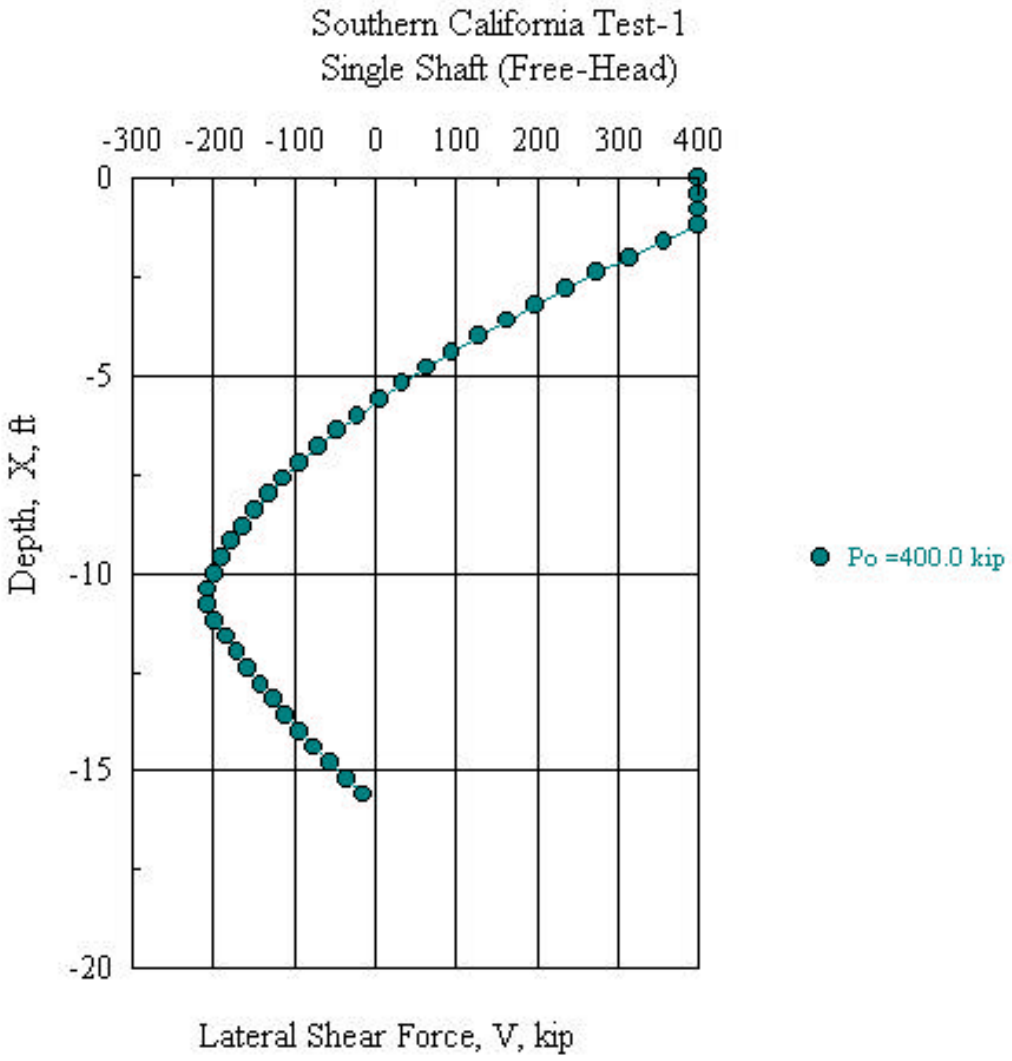

Fig. 8-8 Computed Shear Force in the Shaft in the Southern California Test

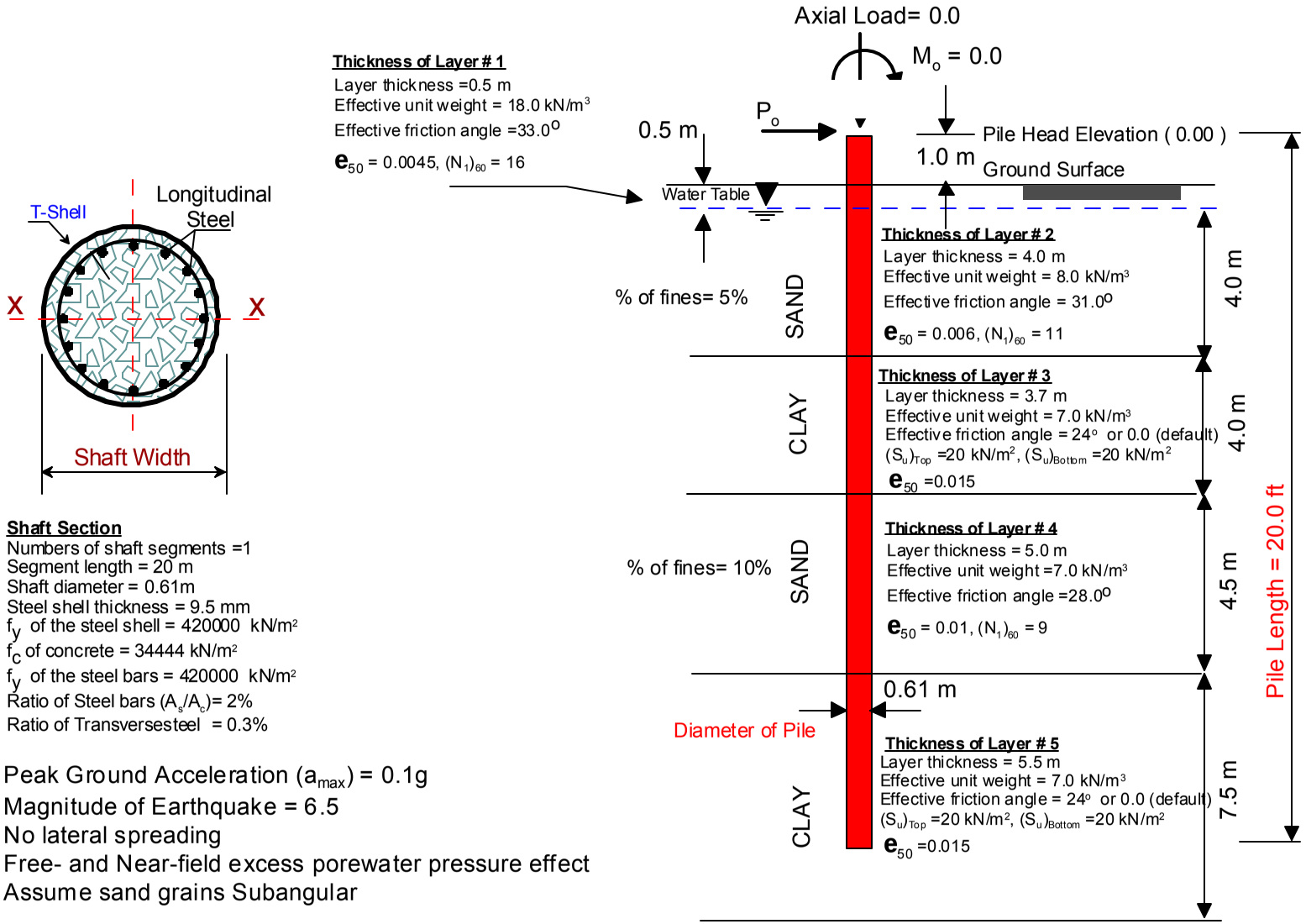

Fig. 8-9 Soil and Pile Properties of the Test Performed at Treasure Island.

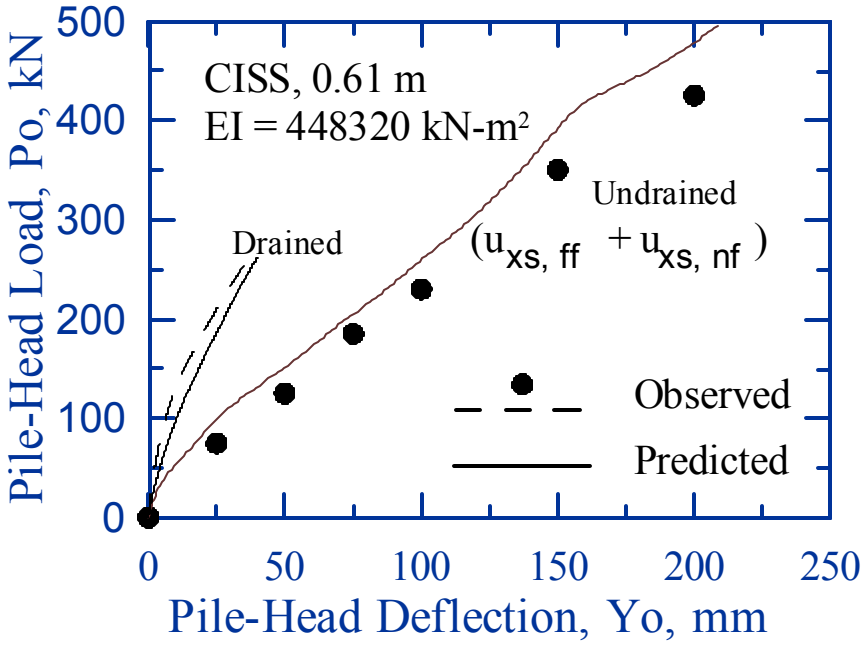

Fig. 8-10 Post-Liquefaction Pile Head Response of the Treasure Island Test

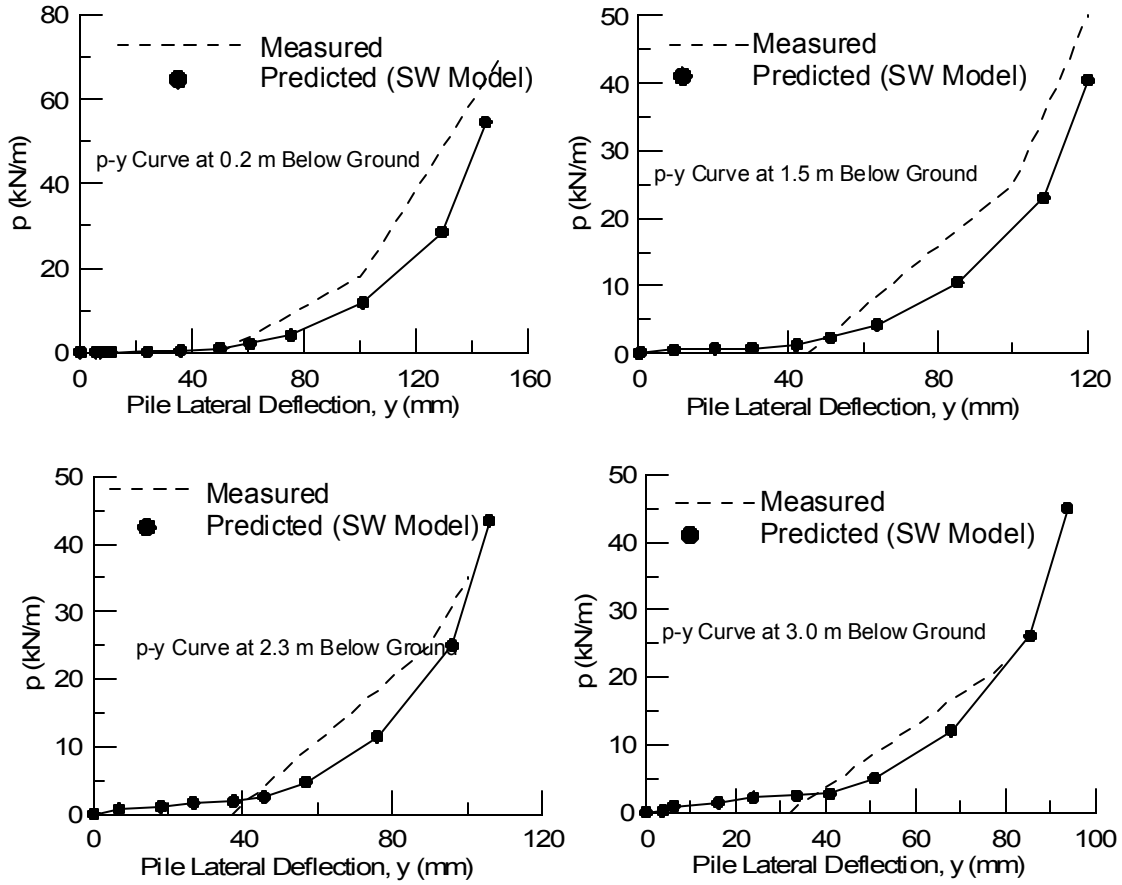

Fig. 8-11. Predicted p-y Curves Using the SWM vs. the Observed Ones from Treasure Island Test.

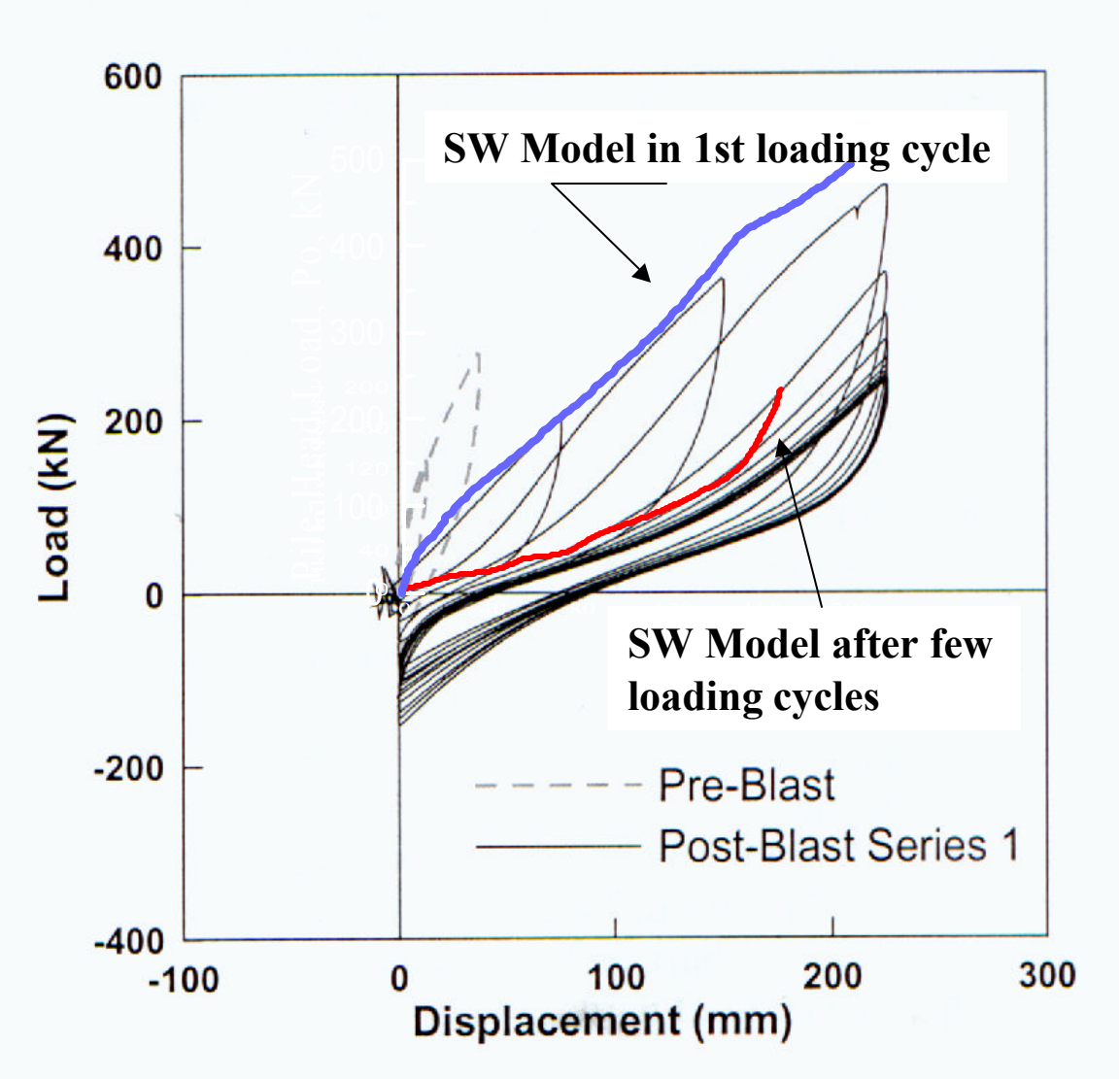

Fig. 8-12. Effect of Loading Cycles on Pile Head Response after Liquefying the Upper Soil Layers (0.61 m Diameter)

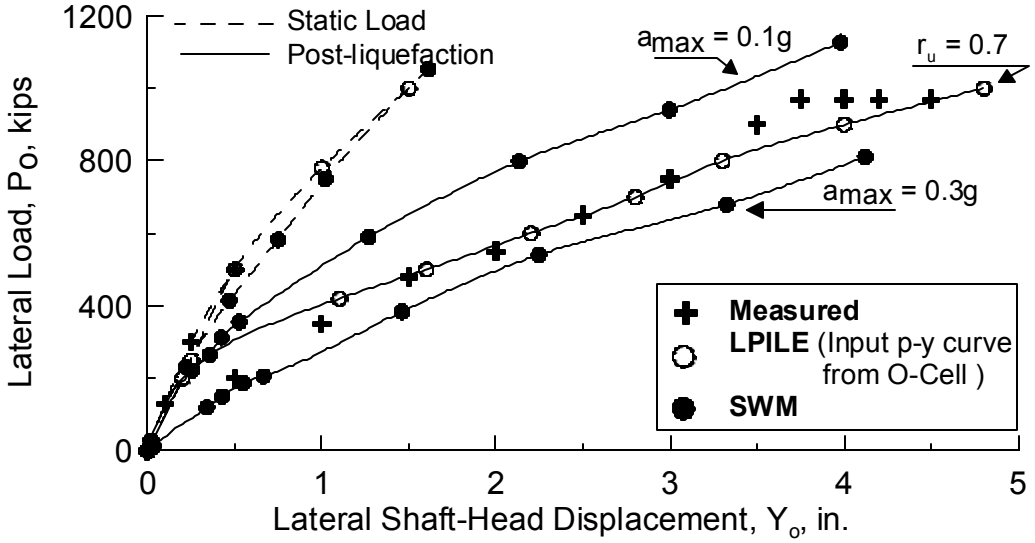

Fig. 8-13. Lateral Response of Shaft MP-1 at Mount Pleasure Test Site (Cooper River Bridge)

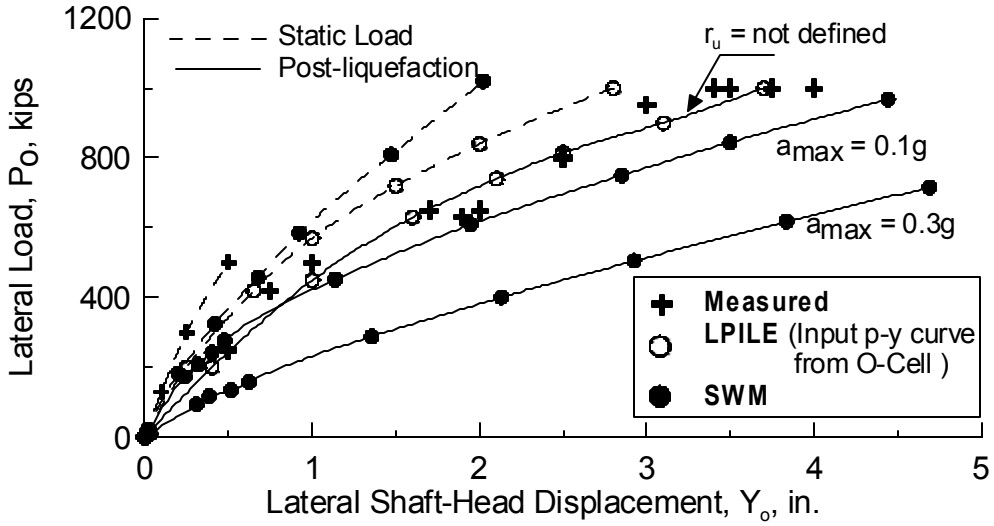

Fig. 8-14 Lateral Response of Shaft MP-2 at Mount Pleasure Test Site (Cooper River Bridge)

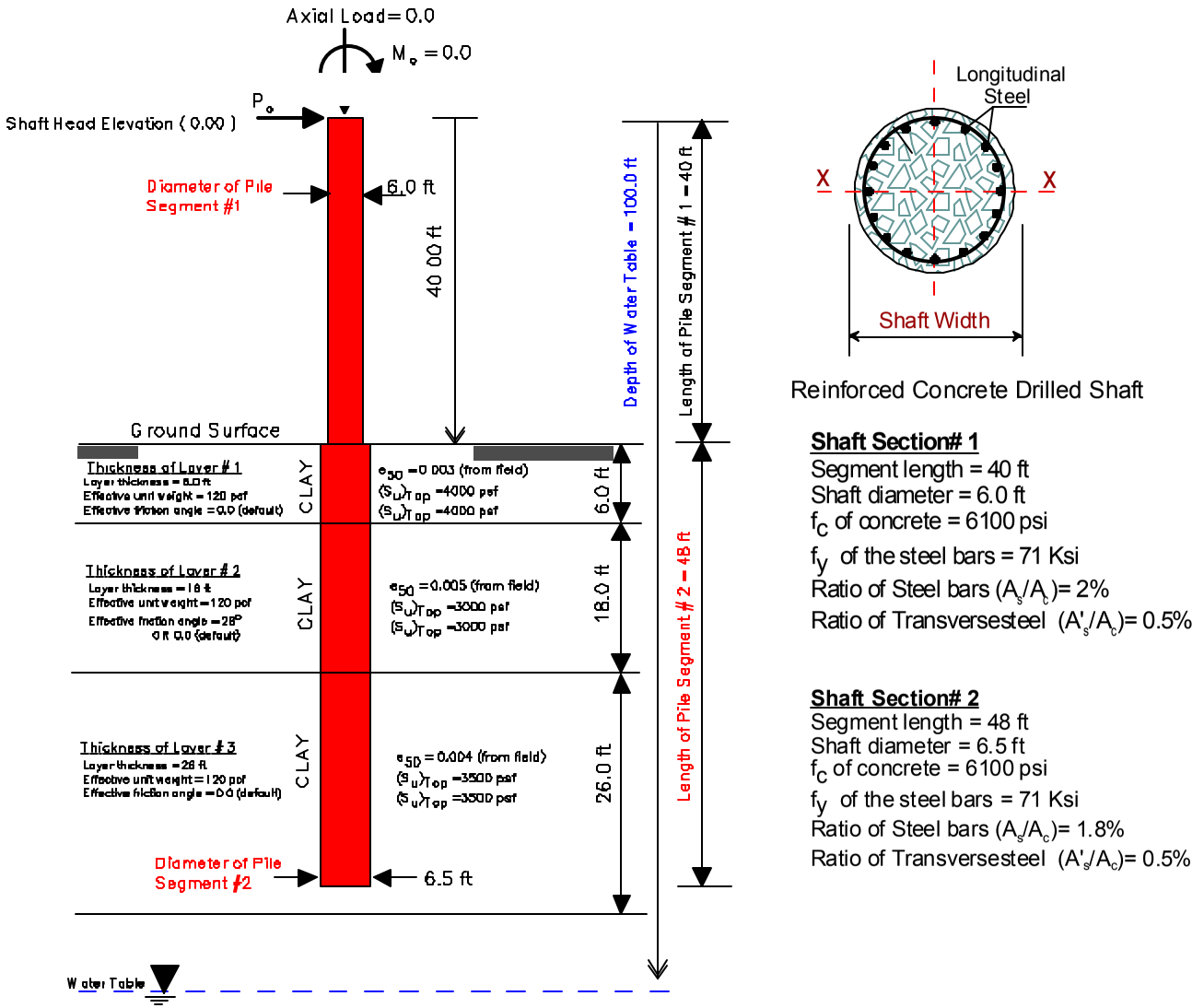

Fig. 8-15 Soil and Shaft Properties of the Column/Shaft Test Performed by the UCLA

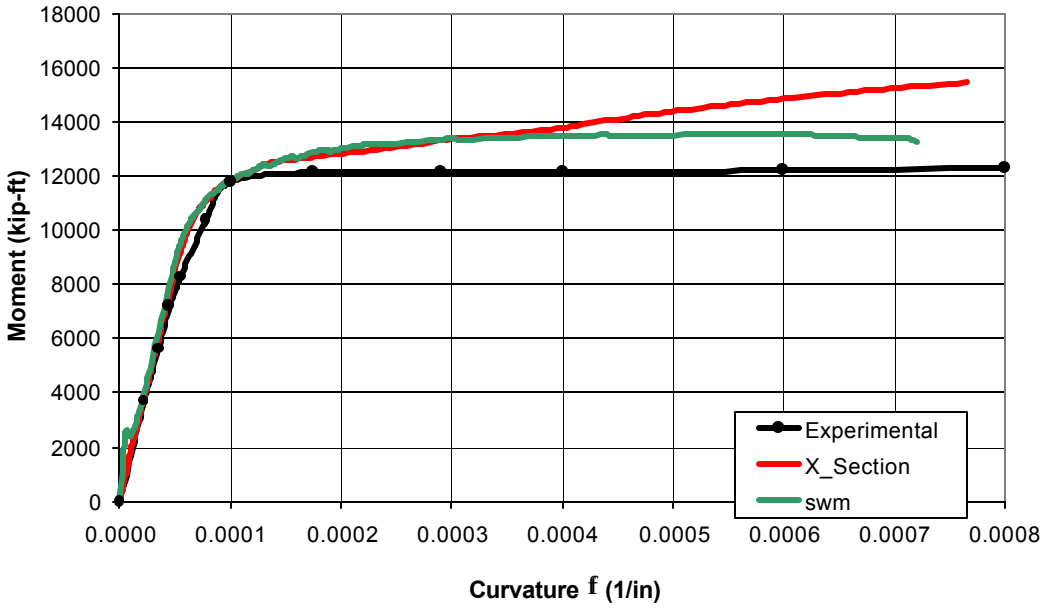

Fig. 8-16 Moment-Curvature Relationship of the 6-ft-Diamter Cross-Section

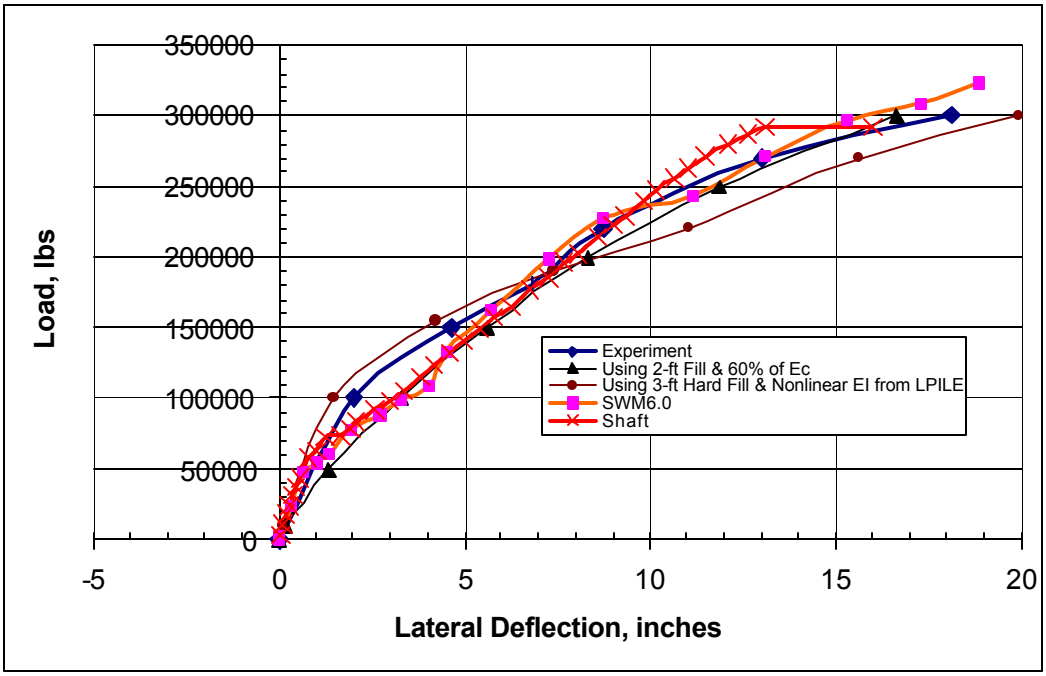

Fig. 8-17 Comparison Between Measured and Computed Lateral Deflection of the shaft tested at UCLA

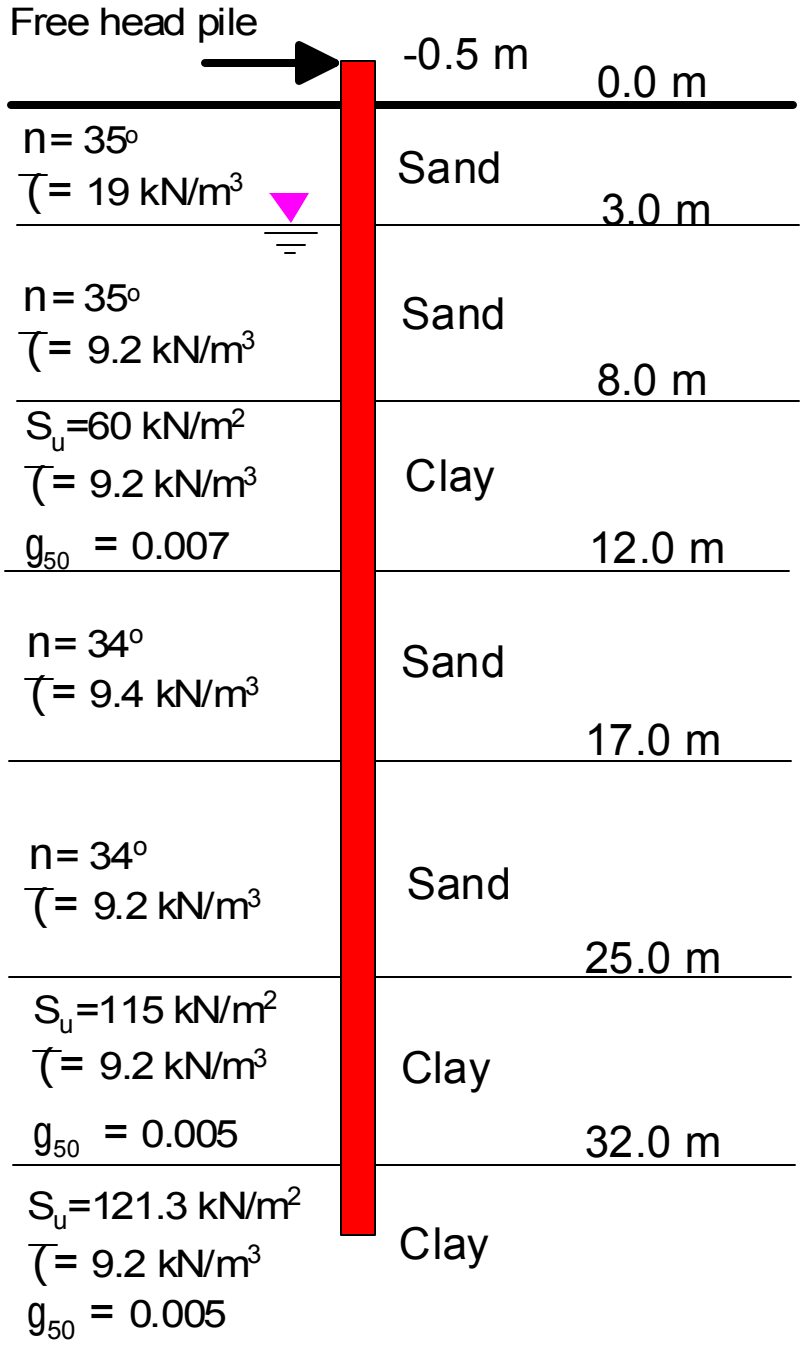

Fig. 8-18 Original Soil Profile and Pile Tested at the Chaiyi Test, Taiwan (Brown et al. 2001)

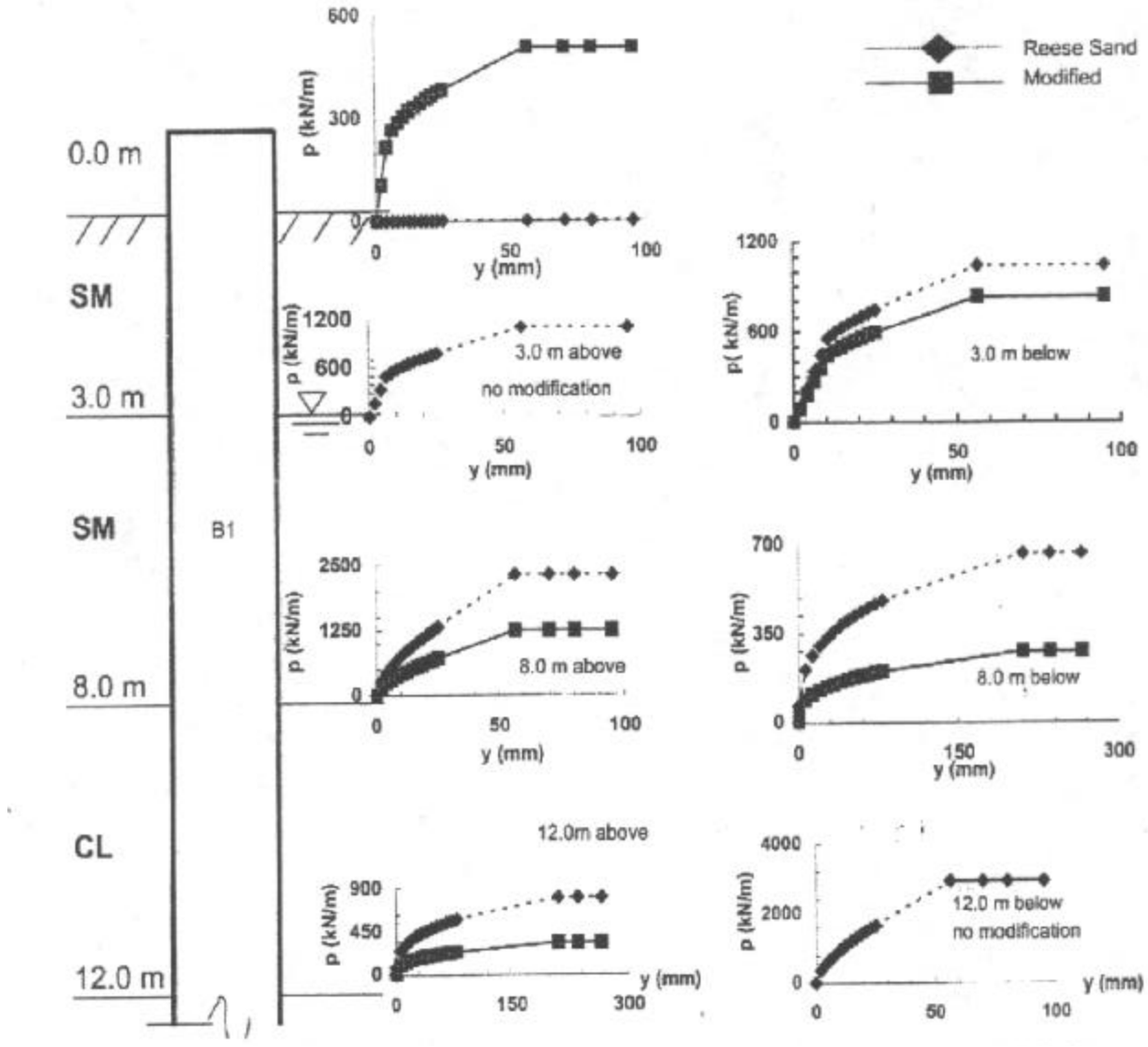

Fig. 8-19 Traditional p-y Curves Modified to Obtain Good Match with Field Data (Chaiyi Test, Brown et al. 2001)

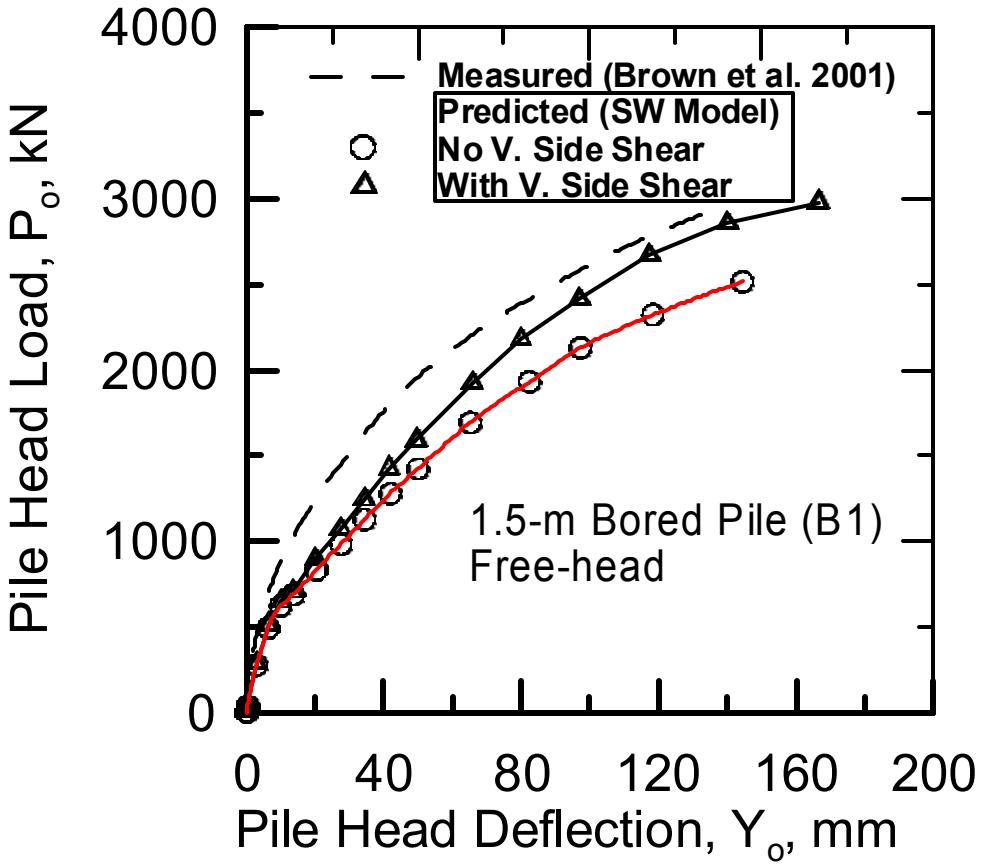

Fig. 8-20 Measured Vs. Computed Pile-Head Deflections and the Effect of Vertical Side Shear

REFERENCES:

Ashford, S. A., and Rollins, K. (1999). "Full-scale behavior of laterally loaded deep foundations in liquefied sands." Report No. TR-99/03, Struct. Engg Dept., University of Calif., San Diego

Ashour, M. and Norris, G. (2000). "Modeling Lateral Soil-Pile Response Based on Soil-Pile Interaction." Journal of Geotechnical and Geoenvironmental Engineering, ASCE, Vol. 126, No. 5, pp. 420-428.

Ashour, M. and Norris, G. 1999. "Liquefaction and undrained response evaluation of sands from drained formulation@ J. of Geotech. Engg, ASCE, Vol. 125, No. 8, pp. 649-658.

Ashour, M., Norris, G. M., Bowman, S., Beeston, H, Billing, P. and Shamsabadi, A. (2001). "Modeling Pile Lateral Response in Weathered Rock.." Proceeding 36st Engineering Geology and Geotechnical Engineering Symposium, Las Vegas, Nevada, March 26-29.

Ashour, M., Norris, G., and Pilling, P. (1998). "Lateral Loading of a Pile in Layered Soil Using the Strain Wedge Model." Journal of Geotechnical and Geoenvironmental Engineering, ASCE, Vol. 124, No. 4, pp. 303-315.

Ashour, M., Pilling, P., Norris, G., and Perez, H.. (1996). "Development of Strain Wedge Model Program for Pile Group Interference and Pile Cap Contribution Effects." CCEER, Report No. 96-4, Civil Engrg Dept., University of Nevada, Reno.

Ashour, M. and Norris, G. M. (2001). "Pile Group Program for Full Material Modeling and Progressive Failure." Report No. CCEER-01-02, Civil Engineering Dept. University of Nevada, Reno, Contract No. 59A0160, Submitted to State of California Department of transportation (CalTrans)

Ashour, M. and Norris, G. M. (2000). "Undrained Lateral Pile and Pile Group Response in Saturated Sand." Report No. CCEER-00-01, Civil Engineering Dept. University of Nevada, Reno, Federal Study No. F98SD01, Submitted to State of California Department of Transportation (CalTrans)

Ashour, M. and Norris, G. M. (1999). "Refinement of the Strain wedge Model Program." Report No. CCEER-99-8, Civil Engineering Dept. University of Nevada, Reno, Federal Study No. F99STD21, Submitted to State of California Department of transportation (CalTrans)

Norris, G. M., and Ashour, M. "Liquefaction and Undrained Response Evaluation of Sands From Drained Formulation." Report No. CCEER-98-2, Civil Engineering Dept., University of Nevada, Reno, May 1998, Project No. DACW39-94-M-5638 (Army Corps of Engineers)

Bhushan, K., Haley, S. C., and Fong, P. T. (1979). "Lateral Load Tests on Drilled Piers in Stiff Clays." Journal of Geotechnical Engineering, ASCE, Vol. 105, No. GT8, pp. 969-985.

Bolton, M. D. (1986). 'The Strength and Dilatancy of Sand." Geotechnique, 36 (1), pp 65-78.

Briaud, J. L., Smith, T., and Mayer, B. (1984). "Laterally Loaded Piles and the Pressuremeter: Comparison of Existing Methods." Laterally Loaded Deep Foundations, ASTM, STP 835, pp. 97-111.

Butterfield, R. and Banerjee, P. K. (1971). "The Elastic Analysis of Compressible Piles and Pile Groups." Geotechnique, London, England, Vol. 21, pp. 43-60.

Coyle, H. M. and Reese, L. C. (1966). "Load Transfer for Axially Loaded Piles in Clay." Journal of Soil Mechanics and Foundations Division, ASCE, Vol. 92, NO. SM2.

Design Manual 7.1 (DM 7.1) (1986). "Soil Mechanics." Naval Facilities Engg. Command, 200 Stovall str., Alexandria, Virginia 22332-2300.

Design Manual 7.2 (DM 7.2) (1986). "Foundations and Earth Structures." Naval Facilities Engg. Command, 200 Stovall str., Alexandria, Virginia 22332-2300.

Elfass, S. (2001). "A New Approach For Estimating The Axial Capacity of Driven Piles In Sand Up To True Soil Failure," Ph.D. Thesis, University of Nevada, Reno.

Gowda, P. (1991). "Laterally Loaded Pile Analysis for Layered Soil Based on the Strain Wedge Model." M. S. Thesis, University of Nevada, Reno.

Grosch, J. J. and Reese, L. C. (1980). "Field Tests of Small-Scale Pile Segments in a Soft Clay Deposit under Repeated Loading." Proceedings, 12th offshore Technology Conference, Houston, TX, Vol. 4, pp. 143-151

Holmquist, D. V. and Matlock, H. (1976). "Resistance-Displacements Relationships for Axially Loaded Piles in Soft Clay." Proceedings, 8th offshore Technology Conference, Houston, TX, Vol. 1, pp. 553-569

Janoyan, K., Stewart, J. P. and Wallace, J. W. (2001). "Preliminary Test Results for Full Scale Drilled Shaft Under Cyclic Lateral Loading." Report to Caltrans No. 59A0183, Civil Eng. Dept., UC Los Angeles.

Kraft, L. M., Richard, P. R. And Kagawa, T. (1981). "Theoretical t-z Curves." J. of Geotech. Engg. Division,. ASCE, Vol. 107, GT11, pp. 1543-1561.

Mander, J. B., Briestley, M. J. N., and Park, R. (1988). "Theoretical Stress-Strain Model for Confined Concrete." Journal of Structural Engineering, ASCE, Vol. 114, No. 8, pp. 1804-1826.

Matlock, H. (1970). "Correlations for Design of Laterally Loaded Piles in Soft Clay." The 2nd Annual Offshore Technology Conference, Houston, Texas, OTC 1204, pp. 577-607.

Matlock, H. and Reese, L. C. (1961). "Generalized Solution for Laterally Loaded Piles." Journal of Soil Mechanics and Foundations Division, ASCE, Vol. 86, No. SM5, pp. 673-694.

Meyerhof, G. G. (1956). "Penetration Tests and Bearing Capacity of Cohesionless Soils." ASCE J., Foundation Division 89, No. SM1, Paper 866, pp. 5-10.

NAVFAC (1982). "Foundations and Earth Retaining Structures Design manual." Dept. of navy, DM 7.2, Alexandria, VA.

Nguyen, T. Q. 2002. "Sand Behavior from Anisotropic and Isotropic Static and Dynamic Triaxial Tests." Ph.D. Dissertation, Civil Engg. Dept., Univ. of Nevada, Reno, January.

Norris, G. M. (1977). "The Drained Shear Strength of Uniform Quartz Sand as Related to Particle Size and Natural Variation in Particle Shape and Surface Roughness." Ph.D. Thesis, University of California , Berkeley, 523 pp.

Norris, G. M. (1986). "Evaluation of the Nonlinear Stabilized Rotational Stiffness of Pile Groups." Proceedings of the 37th Annual Highway Geology Symposium, Montana Dept. of Highways, Helena, Montana.

Norris, G. M. (1986). "Theoretically Based BEF Laterally Loaded Pile Analysis." Third International Conference on Numerical Methods in Offshore Piling, Nantes, France, pp. 361-386.

Norris, G., Siddharthan, R., Zafir, Z., and Madhu, R. 1997. "Liquefaction and residual strength of sands from drained triaxial tests.@ J. of Geotech. Engg, ASCE, Vol. 123, No. 3, pp. 220-228.

Norris, G., Zafir, Z., and Siddharthan, R. 1998. "An effective stress understanding of liquefaction behavior." Journal of Environmental & Engineering Geoscience, Vol. 4, No. 1 pp. 93-101.

Paulay, T., and Priestley, M. J. N. (1992). "Seismic Design of Reinforced Concrete and Masonry." Johen Wiley and Sons, New York, N.Y., pp. 95-157.

Poulos, H. G. and Davis, E. H. (1968). "The Settlement Behavior of Single, Axially

Loaded Incompressible Piles and Piers." Geotechnique, London, England, Vol. 18, pp. 351-371.

Randolph, M. F. and Worth, C. P. (1978). "Analysis of Deformation of Vertically Loaded Piles." J. of Geotech. Engg. Division,. ASCE, Vol. 104, GT12, pp. 1465-1488.

Reese, L. C. (1958). "Discussion of Soil Modulus for Laterally Loaded Piles." by Bramlette McClelland and John A. Focht, Jr., Transactions, ASCE, Vol. 123, pp. 1071.

Reese, L. C. (1977). "Laterally Loaded Piles: Program Documentation." Journal of Geotechnical Engineering, ASCE, Vol. 103, No. GT4, pp. 287-305.

Reese, L. C. (1983). "Behavior of Piles and Pile Groups Under Lateral Load." Report to the U.S. Department of Transportation, Federal Highway Administration, Office of Research, Development, and Technology, Washington, D.C.

Reese, L. C. (1984). "Handbook on Design of Piles and Drilled Shafts under Lateral Load." Geotechnical Engineering Center, Bureau of Engineering Research, University of Texas at Austin., Report No. FHWA-IP-84-11

Reese, L. C. (1987). "Documentation of The Computer Program LPILE1." Ensoft Inc., Post Office Box 180348, Texas 78718.

Reese, L. C. and Wang S. T. (1994). "Analysis of piles under lateral loading with nonlinear flexural rigidity." U.S. FHWA Int. Conf. On Design and Construction of Deep Foundation, FHWA, Washington, D.C.

Richart, E. F. (1975). "Some Effects of dynamic Soil Properties on Soil-Structure Interaction." J. of Geotech. Engg. Division,. ASCE, Vol. 101, GT12, pp. 1197-1240.

Robinsky, E. I. And Morrison, C. E. (1964). "Sand Displacement and Compaction Around Model Friction Piles." Canadian Gotech. J., Vol. 1, No. 2, p. 81.

S&ME Inc. (2000). "Cooper River Bridge replacement project, Charleston, South Carolina."Report prepared by S $ ME, Inc., 840 Low Country Blvd, Mt. Pleasant, SC 29464.

Schnertmann, J. H. (1970). "Static Cone to Compute Static Settlement Over Sand.". J. of Geotech. Engg. Division,. ASCE, Vol. 96, SM3, pp. 1011-1043.

Schnertmann, J. H., Hartman, J. P. And Brown, P. R. (1979). "Improved Strain Influence Factor Diagram." J. of Geotech. Engg. ASCE, Vol. 105, No. GT6, pp. 715-726.

Seed, H. B. 1979. "Considerations in the earthquake-resistance design of earth and rockfill dams." Geotechnique 29, No. 3, pp. 215-263.

Seed, H. B. And Reese, L. C. (1957). "The action of Soft Clay along Friction Piles." Transactions, ASCE, Vol. 122.

Seed, R. B. and Harder, L. F. 1990. "SPT-based analysis of cyclic pore pressure generation and undrained residual strength.@ Vol. 2, BiTech Publishers Ltd, Vancouver, B. C., Canada.

Skempton, A. W. (1951). "The Bearing capacity of Clays." Proceedings, Bldg, Research Congress, Inst. Og Civil Engineering, London, Eng., 1951, Vol. I.

Skempton, A. W. (1954). "The Pore Pressure Coefficients A and B." Geotechnique, 4, pp. 148.

Terzaghi, K. (1955). "Evaluation of Coefficients of Subgrade Reaction." Geotechnique, Vol. 5, No. 4, pp. 297-326.

The 2nd Annual Offshore Technology Conference, Houston, Texas, OTC 1204, pp. 577-
Thesis, University of California , Berkeley, 523 pp.

Tomlinson, M. J. (1957). "The Adhesion of Piles Driven in Clay Soils." Proceedings of Fourth International Conf. on Soil mechanics and Foundation Engrg, Vol. II, London, pp. 66-71.

Triaxial Tests." Ph.D. Dissertation, Civil Engg. Dept., Univ. of Nevada, Reno, January.
Vaid, Y. P. And Thomas, J. 1995. "Liquefaction and post-liquefaction of behavior of sand." J. of Geotech. Engg, ASCE, Vol. 121, No. 2, pp. 163-173.

Vesic, A. (1961). "Bending of Beams Resting on Isotropic Elastic Solid." Journal, ASCE, Engineering Mechanics Div., Vol. 87, SM 2, pp. 35-53.

Vesic, A. S. (1970). "Tests on Instrumented Piles, Ogeechee River Site." Journal of Soil Mechanics and Foundations Division, ASCE, Vol. 96, No. SM2, pp. 561-584.

Weaver, T. J., Ashford, S. A. and Rollins, K. M. (2001). "Development of p-y curves for a 0.6-m CISS pile in liquefied sand." The 6th Caltrans Seismic Research Workshop Program, June 12th-13th, Paper No. 5-104

Wu, T. H. (1966). Soil Mechanics, Boston, Allyn and Bacon Inc., pp. 169.

Zafir, Z. and Vanderpool, W. (1998). "Lateral Response of Large Diameter Drilled Shafts: I-15/US 95 Load Test Program." 33rd Engineering Geology and Geotechnical Engineering Symposium, March 25-27, Reno, Nevada, pp. 161-176.

Hughes, J. M. O., Goldsmith, P. R., and Fendall H.D.W. 1978. "The Behavior of Piles to Lateral Loads." Civil Engg. Dept., Univ. of Auckland, Auckland, New Zealand, Report No. 178.

Rowe, P. W. (1956). “The Single Pile Subject to Horizontal Force.” Geotechnique, Vol. 6.